Lehigh University
Lehigh Preserve

Theses and Dissertations

2013

Device Engineering for Internal Quantum Efficiency Enhancement and Efficiency Droop Issue in III-Nitride Light-Emitting Diodes

Guangyu Liu
Lehigh University

Follow this and additional works at: http://preserve.lehigh.edu/etd

Part of the Electrical and Computer Engineering Commons

Recommended Citation
Liu, Guangyu, "Device Engineering for Internal Quantum Efficiency Enhancement and Efficiency Droop Issue in III-Nitride Light-Emitting Diodes" (2013). *Theses and Dissertations.* Paper 1543.

This Dissertation is brought to you for free and open access by Lehigh Preserve. It has been accepted for inclusion in Theses and Dissertations by an authorized administrator of Lehigh Preserve. For more information, please contact preserve@lehigh.edu.

Device Engineering for Internal Quantum Efficiency Enhancement and Efficiency Droop Issue in III-Nitride Light-Emitting Diodes

by

Guangyu Liu

Presented to the Graduate and Research Committee
of Lehigh University
in Candidacy for the Degree of
Doctor of Philosophy

in

Electrical Engineering

Lehigh University

September 2013

Dissertation Signature Sheet

Approved and recommended for acceptance as a dissertation in partial fulfillment of the requirements for the degree of Doctor of Philosophy.

____

Date

____

Prof. Nelson Tansu
(Ph.D. Advisor)

____

Accepted Date

Committee Members:

____

Prof. Nelson Tansu
(Committee Chair)

____

Prof. Filbert J. Bartoli

____

Prof. Yujie Ding

____

Prof. Michael J. Stavola

Acknowledgements

This report would not have been possible without the essential and continuous support from my advisor, the committee members, my previous and current colleagues, my family and friends.

Firstly, I want to express my great gratitude to my PhD advisor, Prof. Nelson Tansu, for his strong desire of helping the students maximizing the potentials and advancing our technical and non-technical capabilities. His expectation for the graduate students is high, and it sets a high standard for me to move forward at fast pace. Prof. Tansu is always passionate about the research and teaching. He has endless energy in teaching me with great details, inspiring me with various ideas, and preparing me for the future successful career. I also want to thank Prof. Tansu for bringing many good people into the group who I have great time working with.

I would like to acknowledge my committee members, Prof. Filbert J. Bartoli, Prof. Yujie Ding, and Prof. Michael J. Stavola for taking the time to read this dissertation, to join the defense, and to offer inspiring discussions and valuable comments of the research works.

This report has included the multidiscipline works from different collaborators. I want to thank Jonathan Poplawsky and ByungGook Lyu (Physics at Lehigh University), Joo Hyung Park (Electrical Engineering at University of Wisconsin-Madison), and Tanya Paskova (Kyma Technologies) for their contributions to this dissertation. I also want to express my gratitude to Prof. Luke J. Mawst at University of Wisconsin-Madison for the great collaboration experience.

I would like to express my sincere gratitude to our clean room manager, Tony Jeffers, for his detailed training of the clean room operations and equipments. His consistent support of my research activities greatly helped the advances of my research work.

I am deeply grateful for my research mates for their supports during my PhD study. I would like to thank the past postdoctoral fellows, Dr. Gensheng Huang, Dr. Renbo Song and Dr. M. Jamil for the training and the strong support in the maintenance of our sophisticated equipments and facilities. I want to thank Dr. Ronal A. Arif for his impactful guidance during our one-week overlap. I want to thank Dr. Yik-Khoon Ee for his contribution of setting up and maintaining the MOCVD laboratory, and for his outstanding professionalism from which I learned a great deal. I want to

thank Dr. Hua Tong for his creativity in assisting the experimental setup and his kindness of offering helps without asking anything in return. Not only did I learn the technical skills from them, but also I developed the problem-solving capabilities with their supports. I would like to express my great gratitude to Dr. Hongping Zhao who is a faculty in Case Western Reserve University for her guidance and teaching of the theoretical and experimental backgrounds of the research work, which brings me to a higher academic level. I also would like to extend my appreciation to Dr. Jing Zhang for sharing ideas and laughter in the past four years in the group. Gratitude also goes to the current graduate students Chee Keong Tan and Peifen Zhu, previous graduate students Tidapan Sursattayawong, Takahiro Toma, Xiaohang Li, Vincent Handara, and Joseph B. Mulhern for their kindness and support when we are or were working together. I would also like to thank our visiting scientists for inspiring conversations: Dr. Juan A. Herbsommer, and Dr. Marco Mastrapasqua. I feel extremely lucky having the chance to work with all of them.

Finally and most importantly, I would like to express my utmost gratitude to my family and my friends. I am deeply indebted to my family. It was a long and extremely tough journey for my beloved parents, Huizu Liu and Fangfang Shen, to bring up their two daughters. Their unconditional love for me is the strongest support that brings me this far. My father's sacrifice for the whole family has been the motivation that carries me forward, and his optimistic attitude towards life always cheers me up. My mother is a fighter against difficulties in life. She takes very good care of the whole family, and shares the huge responsibility of providing the best possible futures to the two kids with my father. My parents have dedicated everything they have to encourage and support the growths and education of my sister and me, while I have put them through many days and nights of missing and worrying about their little daughter. Here I also want to thank my dearest sister, Guangting Liu. She has always been by the side of our elderly parents, looking after them for me. She has been supporting her younger sister without any complaints. My family means everything to me, and I want to dedicate all that I have achieved to them. Besides, my special thanks go to my friends who are always ready to listen to me, sharing my happiness, joy, excitement, sadness, fear and frustration. Because of them, my life becomes such a colorful one.

Table of Contents

List of Tables ix

List of Figures x

Abstract 1

Chapter 1: Introduction of III-Nitrides 3

1.1 Nitride Semiconductors and Their Applications

1.1.1 III-Nitride based Light-emitting Diode for Solid State Lighting

1.1.2 III-Nitride based Laser Diodes

1.1.3 Concentrated Photovoltaic Cells

1.1.4 Power Electronics

1.1.5 Other applications

1.2 Research Objectives of High-Efficiency III-Nitride based Optoelectronics

1.2.1 Research Works Accomplished

1.2.2 Future Works

1.3 Report Organization

Chapter 2: Challenges and Solutions of III-Nitride LEDs for Solid State Lighting 18

2.1 Low efficiency of Green LEDs

2.1.1 Green Gap Issue

2.1.2 Approaches for High-Efficient Green LED

2.1.3 Large-overlap Design for IQE Enhancement

2.2 Efficiency Droop Phenomenon

2.2.1 Introduction and Possible Cause

2.2.2 Solution of Efficiency Droop Suppression

2.2.3 Novel Barrier Design

2.3 Low Extraction Efficiency

Chapter 3: Numerical Simulations and Analysis of InGaN QW LEDs with Carrier Transport Effect 32

3.1 Introduction to the Numerical Methods – Drift Diffusion Equations

3.1.1 Flow Chart of Simulations

3.1.2 Parameters and Equations Used in the Simulation

3.2 Simulation and Related Issues of InGaN/GaN QW LEDs

3.2.1 Current Crowding Effect

3.2.2 Single QW versus Multiple QWs

3.2.3 Efficiency Droop

Chapter 4: Novel Device Designs of InGaN QW LEDs for Efficiency Enhancement **57**
4.1 Novel Barrier Designs for Efficiencies Droop Suppression
4.1.1 Concept of Efficiencies and Efficiency Droop Issue in InGaN QW LEDs
4.1.2 Analysis of Novel Barrier Design for Droop Suppression
4.2 Characteristics of InGaN QW LEDs with Different Thin Barrier Designs
4.2.1 Analytical Simulations of InGaN QW LEDs with Large-Bandgap Thin Barrier
4.2.2 Numerical Simulations of InGaN QW LEDs with AlGaInN Thin Barrier
4.2.3 Effect of Lattice-Matched AlInN Thin Barrier Thickness
4.2.4 Effect of Lattice-Matched AlInN Thin Barrier Positioning
4.3 Novel QW Designs of InGaN-Delta-InN QW LEDs for Green, Yellow and Red Emission
4.3.1 InGaN-Delta-InN QW LEDs with Different InN Thickness
4.3.2 InGaN-Delta-InN QW LEDs with Different InN Positioning

Chapter 5: Metalorganic Vapor Phase Epitaxy and Device Fabrication **81**
5.1 Introduction to MOVPE system
5.1.1 Configurations and Design of MOVPE P75 Reactor
5.1.2 Growth Parameters in Epitaxy
5.2 MOVPE of (In, Al)GaN on Sapphire Substrate
5.2.1 MOVPE Processes
5.2.2 Growth of GaN Template on Sapphire Substrate
5.3 Device Fabrication
5.3.1 Typical Device Structures
5.3.2 Photolithography Process in Device Fabrication
5.3.3 Process of Device Fabrication

Chapter 6: Metalorganic Vapor Phase Epitaxy of Lattice-Matched AlInN Compounds and InN Alloy **96**
6.1 Applications and Growth Challenges of AlInN Alloys
6.1.1 Applications of AlInN Alloys
6.1.2 Challenges of AlInN Alloy Epitaxy
6.2 AlInN Alloys with Various Indium Content on GaN / Sapphire Virtual Templates
6.2.1 MOVPE of AlInN Alloys on GaN Templates
6.2.2 XRD Characterization of AlInN Alloys with Various In-contents on GaN Templates
6.3 Growth Optimizations of Nearly-lattice-matched AlInN on GaN / Sapphire Templates
6.3.1 Growth Optimizations to Obtain Lattice-Matched AlInN Alloy
6.4 Electrical Characteristics of AlInN on GaN Templates
6.5 Growth of Nearly-Lattice-Matched AlInN Alloy on GaN Native Substrate

6.5.1 Growth of Nearly-lattice-matched AlInN Alloy on GaN Native Substrate
6.5.2 Morphology Comparison of AlInN on GaN substrates and GaN/sapphire virtual templates
6.6 Photoluminescence Measurements of AlInN / GaN Heterostructures
6.7 MOVPE of InN Alloy by Pulsed Growth Mode

Chapter 7: Device Characterizations of InGaN-AlInN QWs LEDs for Efficiency Droop Suppression and LEDs with Large-Overlap Design for Green LEDs 119
7.1 Fabrication of InGaN QW LEDs with AlInN Thin Barrier
7.2 Characterizations of InGaN-AlInN QW LEDs
7.2.1 Power-Dependent Cathodoluminescence Measurement
7.2.2 Electroluminescence Measurement
7.3 Fabrication of InGaN MQWs LEDs with Large-overlap Designs
7.3.1 Growth of Staggered InGaN MQWs LED
7.3.2 Discussion of InGaN-Delta-InN QW LEDs Growth
7.4 Characterizations of InGaN MQWs LEDs with Large-overlap Designs
7.4.1 Luminescence Measurements at Room Temperature
7.4.2 Time-Resolved Photoluminescence for Carrier Lifetime
7.4.3 Temperature Dependent Electroluminescence

Chapter 8: Analysis of InGaN QW LEDs with Different Polarity 133
8.1 Introduction of Polarity of InGaN QW LEDs
8.2 Analysis of Ga-polar and N-polar InGaN QW LEDs

Chapter 9: P-type III-Nitrides Doping Sensitivity of InGaN QW LED Device Characteristics 140
9.1 Motivation of Sensitivity Study for Industrial Production
9.2 Effect of LEDs with Different P-type Doping Levels in Each Layer
9.3 Effect of LEDs with Activation Level

Chapter 10: Fabrications and Characterizations of InGaN Quantum Dots Using Selective Area Epitaxy 151
10.1 Introduction of InGaN based Quantum Dots
10.1.1 Motivation of Pursuit of Quantum Dots Nanostructure
10.1.2 Fabrication Methods of InGaN based Quantum Dots
10.2 Fabrication of Ultra-high density and Highly Uniformed InGaN QDs
10.2.1 Selective Area Epitaxy of InGaN QDs by Diblock Copolymer Lithography

10.2.2 Procedure of Selective-Area Epitaxy of InGaN Quantum Dots
10.3 Structural and Morphology Characterizations
10.4 Photoluminescence Studies and Discussion

Chapter 11: Summary and Future Outlook **168**
11.1 Summary
11.1.1 Novel Barrier Design for Efficiency-Droop Suppression
11.1.2 Novel Quantum Well Design for LEDs Emitting at Long Wavelength Regime
11.1.3 Novel Quantum Dot Active Region Fabrication for High-efficiency Optoelectronics
11.2 Future Outlook

Curriculum Vitae-Guangyu Liu **173**

List of Tables

Page

Table 3-1 Material parameters of binaries GaN, AlN and InN for band structure calculations. 45

Table 3-2 Parameters for the calculation of material properties of ternary InGaN, AlGaN and AlInN. 46

Table 5-1 Parameter List of a, b, temperature T and corresponding P_{vapor} and $P_{bubbler}$ for MO sources. 84

Table 6-1 XRD rocking curve FWHM and intensity for AlInN thin films on GaN / sapphire templates. 100

Table 6-2 Hall measurement results of Al1-xInxN alloy on GaN / sapphire templates. 106

List of Figures

Page

Figure 1-1 LED revenue split by application 3

Figure 1-2 Energy bandgap diagram and lattice structure of III-nitride semiconductors. 4

Figure 1-3 Approaches for generating white light from LEDs and representative power. spectra US Department of Energy Solid State Lighting (SSL)-LEDs lamp targets 5

Figure 1-4 Market size of GaN power electronics devices predicted by analysts at market research firm Yole Développement in Lyon. 9

Figure 2-1 External quantum efficiency of LEDs with various emission wavelength (dash line) and the luminous eye response curve, V(λ) (solid line). 19

Figure 2-2 The electron-hole wavefunctions overlap ($\Gamma_{e\text{-}hh}$) for InGaN QW as a function of Indium content with d_{QW} = 2nm and 3nm, and the corresponding emission wavelengths are shown. 19

Figure 2-3 Schematics of the (a) conventional $In_zGa_{1-z}N$ / GaN QW; (b) two-layer staggered $In_xGa_{1-x}N$ / $In_yGa_{1-y}N$ QW; and (c) three-layer staggered $In_yGa_{1-y}N$ / $In_xGa_{1-x}N$ / $In_yGa_{1-y}N$ QW structures. 21

Figure 2-4 Band structures and wavefunctions calculated for (a) conventional $In_{0.25}Ga_{0.75}N$ QW emitting at 506 nm and (b) $In_{0.25}Ga_{0.75}N$ / InN / $In_{0.25}Ga_{0.75}N$ QW emitting at 636 nm with enhanced $\Gamma_{e\text{-}h}$. 22

Figure 2-5 External quantum efficiency and light output at different dc forward currents for blue and green InGaN-GaN QW-based TFFC LEDs with the size of 1 mm^2. 23

Figure 3-1 The process flow of numerical simulation. 33

Figure 3-2: (a) A representative schematic for the 2-D mesh structure for InGaN-based QW LEDs in lateral LED configuration, and (b) the enlarged mesh structures near the active regions of the LEDs. 34

Figure 3-3 Energy bandgap diagram of III-Nitride alloys. 36

Figure 3-4 Schematics of (a) compressive strain and (b) tensile strain induced by lattice mismatch between the substrate and the thin film on top. 38

Figure 3-5 Schematics of InGaN/GaN MQW LED with (a) lateral configuration and (b) vertical configurations. 47

Figure 3-6 (a) Electron concentration and (b) hole concentration in the last QW active region of the lateral LEDs and the vertical LED at J = 100 A/cm^2 along lateral direction (x-direction). The length of p-contact in lateral LEDs, L_p, varies from 100 μm to 400 μm. 48

Figure 3-7 Lattice temperature gradient map of (a) lateral LEDs wth L_p = 100 μm, (b) lateral LEDs wth L_p = 400 μm and (c) vertical LED at J = 100 A/cm^2. 49

Figure 3-8 I-V curves of the four lateral LEDs wth different L_p and lateral LEDs. 50
Figure 3-9 Band lineups and carrier distributions of MQW LED with four periods of 3 nm $In_{0.25}Ga_{0.75}N$ QWs / 10 nm GaN barriers where (a) shows the conduction band structure and electron concentration and (b) shows the valence band structure and hole concentration at J = 100 A/cm^2. 51
Figure 3-10 Band lineups and carrier distributions of SQW LED with 3 nm $In_{0.25}Ga_{0.75}N$ single QW surrounded by 10 nm GaN barriers at J = 100 A/cm^2. 52
Figure 3-11 Radiative recombination rates of (a) MQW LED and (b) SQW LED at J = 100 A/cm^2. The emission wavelengths of both QWs are 490 nm. 52
Figure 3-12 Light output power as a function of current density for both SQW LED and MQW LED with the extraction efficiency of 70%, SRH recombination rate of $10^6 s^{-1}$ and Auger recombination rate of 10^{-34} cm^{6}s^{-1}. 53
Figure 3-13 Internal quantum efficiency (IQE) of four investigated LEDs emitting at 490 nm including lateral LEDs with L_p=100 μm and 400 μm, and vertical LEDs with MQW and SQW. 54
Figure 3-14 IQE of vertical SQW LEDs emitting at 490 nm as a function of current density for different Auger recombination coefficient C. C varies from 10^{-34} cm^{6}s^{-1}, 10^{-32} cm^{6}s^{-1}, 10^{-31} cm^{6}s^{-1}, and 10^{-30} cm^{6}s^{-1}. 54
Figure 4-1 Illustration of band structures and current/carrier flow of (a) nonpolar InGaN/GaN QW and (b) polar InGaN/GaN QW. 58
Figure 4-2 Internal quantum efficiency (IQE) (η_{IQE}), radiative efficiency ($\eta_{Radiative}$) and current injection efficiency ($\eta_{Injection}$) of 24-Å $In_{0.28}Ga_{0.72}N$ QW surrounded by 10-nm GaN barrier (λ = 480 nm) at 300 K as a function of total current density. 59
Figure 4-3 Schematic of (a) conventional c-plane InGaN QW with GaN barrier and (b) InGaN QW structure inserted with large bandgap thin barriers. 60
Figure 4-4 Injection efficiency as a function of total current density for 24 Å $In_{0.28}Ga_{0.72}N$/GaN QW, 24 Å $In_{0.28}Ga_{0.72}N$/15 Å $Al_{0.1}Ga_{0.9}N$ QW and 24 Å $In_{0.28}Ga_{0.72}N$/15 Å $Al_{0.83}In_{0.17}N$ QW. 61
Figure 4-5 IQE as a function of total current density for 24-Å $In_{0.28}Ga_{0.72}N$/GaN QW, 24-Å $In_{0.28}Ga_{0.72}N$/15-Å $Al_{0.1}Ga_{0.9}N$ QW and 24-Å $In_{0.28}Ga_{0.72}N$/15-Å $Al_{0.83}In_{0.17}N$ QW. 62
Figure 4-6 Schematics of five investigated InGaN QW LEDs. The inserted table summarizes the material composition and corresponding bandgaps of the thin AlGaInN barrier used in the study. 63
Figure 4-7 (a) Conduction band structures and electron concentrations and (b) valence band structures and hole concentrations of 3 nm $In_{0.28}Ga_{0.72}N$ QW LEDs with five different barrier designs at J= 250 A/cm^2. 64
Figure 4-8 Radiative recombination rates across the active regions of the five LEDs at

J= 250 A/cm^2. 65

Figure 4-9 (a) Electron concentrations in last GaN barriers and (b) the electron current densities ($J_{electron}$) and hole current densities (J_{hole}) across the active region of LED (A)-(E) at J = 250 A/cm^2. 66

Figure 4-10 Light output powers and (b) IQE (η_{IQE}) for 3 nm $In_{0.28}Ga_{0.72}N$ QW LEDs with five barrier designs of (A) GaN barriers, (B) $Al_{0.19}Ga_{0.77}In_{0.04}N$ thin barriers, (C) $Al_{0.37}Ga_{0.55}In_{0.08}N$ thin barriers, (D) $Al_{0.56}Ga_{0.32}In_{0.12}N$ thin barriers and (E) $Al_{0.82}In_{0.18}N$ thin barrier as a function of current density. 67

Figure 4-11 IQE (η_{IQE}) for LED (A)-(E) as a function of current density. 67

Figure 4-12 (a) Conduction band structures and electron concentrations and (b) valence band structures and hole concentrations of 3 nm $In_{0.28}Ga_{0.72}N$ QW LEDs with 1 nm (E1), 1.5 nm (E1.5) and 2 nm (E2) $Al_{0.82}In_{0.18}N$ thin barriers at J= 250 A/cm^2. 69

Figure 4-13 The electron current densities ($J_{electron}$) and hole current densities (J_{hole}) across the active region of LED (A), (E1), (E1.5) and (E2) at J = 250 A/cm^2. 69

Figure 4-14 (a) Light output powers and (b) IQE (η_{IQE}) for 3 nm $In_{0.28}Ga_{0.72}N$ QW LEDs with GaN barrier (A), 1 nm (E1), 1.5 nm (E1.5) and 2 nm (E2) $Al_{0.82}In_{0.18}N$ thin barriers as a function of current density. The insertion in (a) shows the schematic of InGaN QW LED with $Al_{0.82}In_{0.18}N$ thin barriers. The maximum current density is extended to 500 A/cm^2. 70

Figure 4-15 Band Lineups and corresponding quasi Fermi levels of (a) LED (E) with 1 nm $Al_{0.82}In_{0.18}N$ thin barriers on both sides of 3 nm $In_{0.28}Ga_{0.72}N$ QW, (b) LED (ER) with 1 nm $Al_{0.82}In_{0.18}N$ thin barrier on the right-hand side of $In_{0.28}Ga_{0.72}N$ QW and (c) LED (EL) with 1 nm $Al_{0.82}In_{0.18}N$ thin barrier on the left-hand side of $In_{0.28}Ga_{0.72}N$ QW at J= 250 A/cm^2. 71

Figure 4-16 (a) Light output power and (b) IQE (η_{IQE}) of LED (A) with GaN barrier, LED (E) with $Al_{0.82}In_{0.18}N$ thin barriers on both sides, LED (ER) with $Al_{0.82}In_{0.18}N$ thin barriers on the right-hand side and LED (EL) with $Al_{0.82}In_{0.18}N$ thin barriers on the left-hand side of 3 nm $In_{0.28}Ga_{0.72}N$ QW, respectively. 72

Figure 4-17 Band lineups and corresponding wavefunctions of (a) conventional (CV) 30 Å $In_{0.25}Ga_{0.75}N$ QW LED, (b) 15 Å $In_{0.25}Ga_{0.75}N$ / 3 Å InN / 15 Å $In_{0.25}Ga_{0.75}N$ QW LED and (c) 15 Å $In_{0.25}Ga_{0.75}N$ / 6 Å InN / 15 Å $In_{0.25}Ga_{0.75}N$ QW LED at J = 50 A/cm^2. 75

Figure 4-18 (a) Electron concentration in conduction band and (b) hole concentration in valence band for CV InGaN QW LED, InGaN QW LED with 3 Å delta-InN layer and InGaN QW LED with 6 Å delta-InN layer at J = 50 A/cm^2. 75

Figure 4-19 Spontaneous emission spectrum of CV InGaN QW LED, InGaN QW LED with 3 Å delta-InN layer and InGaN QW LED with 6 Å delta-InN layer at

J = 50 A/cm^2 and 100 A/cm^2. 76
Figure 4-20 Band lineups and corresponding wavefunctions of QW designs that consist of (a) 10 Å $In_{0.25}Ga_{0.75}N$ / 6 Å InN / 20 Å $In_{0.25}Ga_{0.75}N$ (denoted as LED 10:20), (b) 15 Å $In_{0.25}Ga_{0.75}N$ / 6 Å InN / 15 Å $In_{0.25}Ga_{0.75}N$ (denoted as LED 15:15) and (c) 20 Å $In_{0.25}Ga_{0.75}N$ / 6 Å InN / 10 Å $In_{0.25}Ga_{0.75}N$ (denoted as LED 20:10) at J = 50 A/cm^2. 77
Figure 4-21 (a) Electron concentration in conduction band and (b) hole concentration in valence band of CV InGaN QW LED and three InGaN QW LEDs with different positions of 6 Å delta-InN layer at J = 50 A/cm^2. InGaN QW LED is included as a reference. 77
Figure 4-22 Spontaneous emission spectrum of of CV InGaN QW LED and three InGaN QW LEDs with different positions of 6 Å delta-InN layer at J = 50 A/cm^2. 78
Figure 4-23 Light output power as a function of current density for the three investigated LED designs in this study. The emission wavelength are around 658 nm to 668 nm. 78
Figure 5-1 Schematics of Veeco P75 MOVPE reactor system. 82
Figure 5-2 Smoke flow patterning in rotation disc system. 83
Figure 5-3 Schematics of bubbler configuration (a) without and (b) with double dilution. TEGa and TMIn are using (a) and TMGa and TMAl are using (b). 84
Figure 5-4 Comparison of the temperature profile controlled by the thermocouple (T/C) and filament current. 86
Figure 5-5 Processes occurring during the metal-organic vaper phase deposition (MOVPE) of III-nitride material. 87
Figure 5-6 The growth profile of GaN template growth on sapphire substrates with different stages of (a)-(f). 89
Figure 5-7 The process flow of (a) high temperature cleaning, (b) low temperature GaN growth, (c) formation of 3D islands, (d) 3D growth mode, (e) coalescence process and (f) high temperature GaN growth. 89
Figure 5-8 Schematic of InGaN/GaN based MQW LEDs with (a) square-shaped bottom-emitting configuration and (b) hexagonal-shaped top-emitting configuration. 90
Figure 5-9 Illustration of photolithography processes in cleanroom. 92
Figure 5-10 Mask design of n-contact, mesa, p-contact and transparent metal for (a) square-shaped bottom-emitting devices, (b) hexagonal-shaped bottom-emitting devices, (c) square-shaped top-emitting devices and (d) hexagonal-shaped top-emitting devices. 93
Figure 5-11 Process flow of III-nitride device fabrication 94
Figure 6-1 Normalized XRD ω-2θ scans of AlInN epilayers on GaN/sapphire templates with the indication of nearly-lattice-matched condition. 99

Figure 6-2 Lattice mismatch ratio of AlInN grown on GaN templates along c-axis and a-axis as a function of the In-contents. The insert shows the wurtzite crystal structure of nitride material system. 101
Figure 6-3 Microscope image comparison of two AlInN samples on GaN/sapphire templates with (a) In-content=0.38% and (b) In-content=16.44%. The insets show the XRD ω-2θ scans of corresponding AlInN alloys on GaN / sapphire templates. 102
Figure 6-4 Growth rate and indium content of nearly-lattice-matched AlInN alloys versus the growth pressure for AlInN alloys grown on GaN / sapphire template. The insets show SEM images of the sample surface morphology for the different growth pressures. 103
Figure 6-5 Surface roughness versus growth pressure for AlInN alloys grown on GaN/sapphire template. The inserts show AFM images of the surface morphology of AlInN grown with the different growth pressures. 104
Figure 6-6 Growth rate and indium content of nearly-lattice-matched AlInN alloys as a function of V/III ratio for AlInN alloys grown on GaN / sapphire template. The insets show the corresponding SEM images for the respective V/III ratio. 105
Figure 6-7 Surface roughness of AlInN grown on GaN/ sapphire template versus the V/III ratio. The insets show the corresponding AFM images for the respective growth pressures and V/III ratio. 105
Figure 6-8 Surface roughness as a function of: (a) growth pressure and (b) V/III ratio for AlInN grown on free-standing GaN substrate on sample surface roughness with the insets show the corresponding SEM images for the respective growth pressures and V/III ratio. 107
Figure 6-9 SEM images of surface morphology of 0.2-μm-thick nearly-lattice-matched AlInN thin film grown on: (a) GaN / sapphire template (#1804) and (b) GaN free-standing substrate (#1805). 109
Figure 6-10 XRD ω-2θ scans for nearly-lattice-matched AlInN on GaN / sapphire template (#1804) and on GaN free-standing substrate (#1805). 110
Figure 6-11 Reciprocal space map around the (105) reflection of the nearly-lattice-matched AlInN on (a) GaN /sapphire template (#1804) and (b) GaN free-standing substrate. 110
Figure 6-12 PL spectra measured for lattice-matched AlInN on GaN/ sapphire template and GaN substrate at T = (a) 4.5 K and (b) 300 K. 112
Figure 6-13 The integrated PL intensities as a function of the temperature for AlInN alloy grown on GaN / sapphire substrate. 112
Figure 6-14 TMIn and NH_3 profile of InN pulse growth mode with ON:OFF = 36s:18s. 113
Figure 6-15 The effect of growth condition on the surface morphology of InN thin film on GaN template. 114
Figure 7-1 Schematics of fabricated InGaN QWs LEDs with three different barrier designs

of a) 10 nm GaN barrier (sample #1 of conventional InGaN QWs LEDs), b) direct 1 nm AlInN thin barrier followed by 10 nm GaN barrier (sample #2 of InGaN-AlInN QWs LEDs) and c) 0.5 nm GaN spacer followed 1 nm AlInN thin barrier and 10 nm GaN barrier (sample #3 of InGaN-GaN-AlInN QWs LEDs). 119
Figure 7-2 Real growth temperature profile of InGaN-AlInN QWs LEDs with 48 sec pressure grading and InGaN-GaN-AlInN QWs LEDs with the growth of 0.5 nm GaN spacer layer. 120
Figure 7-3 Comparison of CL measurements results of InGaN-AlInN QWs (sample #2) and conventional InGaN/GaN QWs (sample #3) at T=300K: (a) the CL spectra at different current CL current and (b) normalized CL intensity for both samples. 121
Figure 7-4 Comparison of CL measurements results of InGaN-AlInN QWs (sample #2) and conventional InGaN/GaN QWs (sample #1) at T=300K: (a) the CL spectra at different current CL current; (b) normalized CL intensity for both samples. 121
Figure 7-5 Comparison of EL spectra of InGaN-AlInN LEDs (sample #2) and conventional InGaN LEDs (sample #1) under CW operation at T= 300K with various current injection. The device area is 510 μm x 510 μm. 122
Figure 7-6 Normalized output power as a function of current density plotted for InGaN-AlInN LEDs (sample #2) and conventional InGaN LEDs (sample #1) with emission wavelength round 500 nm and 440 nm, respectively. 123
Figure 7-7 (a) The schematic and (b)-(d) the growth profile of three-layer staggered InGaN QWs. The graded growth temperature profile, constant TMIn flow rate and staggered In-content structure are shown in (b), (c) and (d), respectively. 124
Figure 7-8 Schematics of the growth temperature, TMIn-flow rate, and In-content for the linearly-shaped staggered InGaN QW [(a), (b), (c)] and the corresponding real growth temperature profiles [(d), (e), (f)]. 124
Figure 7-9 (a) EL spectra and (b) the EL output power as a function of current density for conventional InGaN QW and three-layer staggered InGaN QW LEDs emitting at 520-525 nm with the device size of 510 μm x 510 μm. 126
Figure 7-10 Integrated CL intensity of conventional, LS-1 staggered, LS-2 staggered, and LS-3 staggered InGaN QW versus CL excitation currents at T = 300K. 127
Figure 7-11 The total carrier life time measurement for conventional InGaN QWs and three-layer staggered InGaN QWs emitting at 520-525 nm at T = 300 K. 128
Figure 7-12 The total carrier lifetime as a function of carrier density for conventional InGaN QW and staggered InGaN QW at monomolecular coefficient A = 1.6×10^{7} s^{-1} and Auger coefficient C = 5×10^{-33} $cm^{6}s^{-1}$. 129
Figure 7-13 Schematic of the setup of temperature-dependent / power-dependent EL measurement. 130

Figure 7-14: Integrated EL intensity of three-layer staggered InGaN QW LEDs emitting at 500 nm as a function of the inverse of temperature at (a) J=7.71 A/cm^2 and (b) J= 30.86 A/cm^2 under CW operation. 131
Figure 8-1 Schematics and band structures of (a) Ga-polar GaN based InGaN QW LEDs and (b) Ga-polar GaN based InGaN QW LEDs under bias. 133
Figure 8-2 Band structures and Fermi levels of Ga-polar and N-polar InGaN single quantum well (SQW) LEDs at equilibrium. 134
Figure 8-3 (a) Conduction bands, quasi-Fermi level for electrons and electron concentrations, and (b) valence bands, quasi-Fermi level for holes and hole concentrations of Ga-polar and N-polar InGaN QW LEDs at J =100 A/cm^2. 135
Figure 8-4 Spontaneous emission rate of (a) Ga-polar GaN based InGaN QW LEDs and (b) Ga-polar GaN based InGaN QW LEDs under bias. 136
Figure 8-5 Electron and hole current densities across the active region of N-polar and Ga-polar InGaN QW LEDs. 137
Figure 8-6 Devices characteristics of Ga-polar InGaN SQW LEDs at different current density. (a) shows the light output power and voltage and (b) shows the IQE. 137
Figure 9-1 (a) Schematics of the device structure and doping levels in the simulation, and (b) band structures of InGaN QW LEDs at J = 200 A/cm^2. 141
Figure 9-2 (a) Conduction band and electron concentration and (b) valence band and hole concentration of the last QW of LEDs with p-AlGaN doping level of 3x10^{17} cm^{-3} and 5x10^{18} cm^{-3} at J= 200A/cm^2. 142
Figure 9-3 (a) Light output power-current density-voltage characteristics and (b) internal quantum efficiency (IQE) of LEDs with different p-AlGaN doping levels. 143
Figure 9-4 (a) Light output power at J= 100A/cm^2 and 200A/cm^2 as a function of p-AlGaN doping level, N_a(p-AlGaN). The calculation of doping sensitivity of output power (D-P sensitivity) is illustrated. (b) P-AlGaN D-P sensitivity at J= 100A/cm^2 and 200A/cm^2. 144
Figure 9-5 (a) IQE at J= 100A/cm^2 and 200A/cm^2 as a function of p-AlGaN doping level, N_a(p-AlGaN). The calculation of doping sensitivity of IQE (D-IQE sensitivity) is illustrated. (b) P-AlGaN D-IQE sensitivity at J= 100A/cm^2 and 200A/cm^2. 145
Figure 9-6 (a) The light output power, (b) D-P sensitivity, (c) IQE and (d) D-P sensitivity at J= 200A/cm^2 as the doping levels of p-GaN (green line) and p+-GaN doping level (orange line) changes. 146
Figure 9-7 (a) Light output power-voltage-current density characteristics and (b) IQE of LEDs with different activation levels. 147
Figure 9-8 (a) Light output power and (b) IQE at J=200A/cm2 as a function of p-layer activation levels from LEDs with different QW numbers. 148

Figure 10-1 Schematics of material growth evolution of Stranski-Krastanow growth mode. 153
Figure 10-2 AFM measurements of MOCVD-grown self-assembled InGaN QDs by employing the Stranski-Krastanow growth mode. 153
Figure 10-3 The electron-hole envelop function overlap in the $In_{0.2}Ga_{0.8}N$ quantum dot device with different wetting layer thicknesses. 154
Figure 10-4 MOCVD process flow of InGaN/GaN QDs SAE with dielectric patterns defined by the self-assembled diblock copolymer. 156
Figure 10-5 Schematic of two groups of QD samples with the structures of: (A) 1.5-nm InGaN sandwiched between 1 GaN layers (Sample A); (B) 3 nm InGaN sandwiched between 2-nm GaN layers (Sample B). 157
Figure 10-6 SEM image of diblock copolymer nanopatterns on SiN_x with the hexagonal array of openings after the UV exposure. 158
Figure 10-7 SEM images of SAE-grown InGaN/GaN QDs with SiN_x layer for both samples investigated: (a) sample A; (b) sample B. 158
Figure 10-8 SEM images of SAE-grown InGaN/GaN QDs after removal of SiN_x layer for both samples investigated: (a) sample A; (b) sample B. 159
Figure 10-9 AFM measurement using Dimension 3000 for SAE-grown InGaN/GaN QDs arrays on sample A after removal of SiN_x: (a) AFM scan with the scale of 0.5μm x 0.5μm; (b) the corresponding height and size of the cross-sectional profiles. 160
Figure 10-10 AFM measurement using Agilent 5500 for SAE-grown InGaN/GaN QDs arrays on sample A after removal of SiN_x: (a) AFM scan with the scale of 0.6 μm x 0.6 μm; (b) the corresponding height and size of the cross-sectional profiles. 161
Figure 10-11 AFM image of SAE-grown InGaN/GaN QDs on samples B measured by Dimension 3000 after removal of SiN_x on 1 μm x 1 μm area. 162
Figure 10-12 PL comparison of planar SQW grown on (1) GaN with no surface treatment, (2) GaN with HF wet etching, and (3) GaN with SiNx deposition and HF etching. 163
Figure 10-13 PL comparison of (1) planar InGaN QW on GaN template that has been treated with SiN_x deposition and HF etching, and (2) InGaN QD sample with the same InGaN and GaN layer thickness. 164
Figure 10-14 PL enhancement study of SQW with different growth condition treatments. 164

Abstract

Over the past few decades, III-nitride semiconductors have found the tremendous impacts in solid state lighting, power electronics, photovoltaics and thermoelectrics. In particular, III-nitride based light-emitting diodes (LEDs) with long lifetime and eco-friendliness are fundamentally redefining the concepts of light generation due to the superior material properties of direct bandgap, efficient light emission and robustness. The industry of LED based solid state lighting is fulfilling the potential of reducing the 20% of the total US energy consumed by lighting to half of this usage. However, several major obstacles are still hindering the further development of LEDs for general illuminations. They include efficiency droop phenomenon at high operating current, low efficiency in green spectrum, and low extraction efficiency due to the large difference in refractive index. The report will present both experimental and theoretical works on III-nitride semiconductor materials and devices for solid state lighting, including 1) novel barrier design for efficiency-droop suppression, 2) novel active region design for radiative efficiency enhancement, and 3) fabrication of ultrahigh density and highly uniform III-nitride based quantum dots (QDs) for high efficiency optoelectronics and photovoltaic cells. In addition to the three main topics, a new topic on the p-type III-nitrides doping sensitivity will be investigated in the latter part of this report.

Firstly, the use of large bandgap thin barrier layers surrounding the InGaN QWs in LEDs will be proposed for efficiency droop suppression. The efficiency of LED devices suffers from reduction at high current injection, which is referred as efficiency droop phenomenon. Although the origin is still inconclusive up till now, the carrier leakage issue is widely considered as one of the major reasons. The increased effective barrier heights from the use of a thin ($d < 2$ nm) lattice-matched AlGaInN barriers are shown to improve current injection efficiency and internal quantum efficiency. The optimization of epitaxial conditions of lattice-matched AlInN material has been carried out by metal-organic chemical vapor deposition (MOCVD) for the fabrication of InGaN QW LEDs with the insertion of AlInN thin barrier. The device characterizations of cathodoluminescence and electroluminescence show the great potential of the InGaN-AlInN design in addressing the efficiency droop issue at high current density.

Secondly, the staggered InGaN QW and InGaN-delta-InN QW are investigated for the high

efficiency LEDs emitting at green or longer emission spectrum region to provide solutions for greengap challenge. The introduction of energy local minima in QW region by the novel structures of staggered InGaN QWs enables the spatial shift of electron and hole wavefunction towards the center of active region. Therefore, the approach leads to the enhancement of electron-hole wavefunction overlap and thus the radiative recombination rate and optical gain. The analysis of InGaN-delta-InN QW LED with the potential of effectively extending the emission wavelength without sacrificing the radiative recombination rates will also be presented.

Thirdly, the sensitivity study of the doping levels of p-type layers in InGaN/GaN MQW LEDs will be discussed for industrial application. Due to the difficulty in activating the acceptor magnesium in III-nitrides, thermal annealing process is employed to increase the hole concentration in p-type semiconductors. The uniform temperature distributions in the annealing chambers will lead to non-uniformity in p-type doping levels. The effect of doping levels on LED device performance will be examined, and the doping sensitivity of light output power and internal quantum efficiency will be investigated in this report. The results will provide guidance for the parameter optimization of the fabrication process for commercial product line to increase the yield.

Fourthly, the growths of ultra-high density and highly uniform InGaN QDs on GaN/ sapphire template as an important alternative active region for high-efficiency optoelectronic devices will be discussed. The growths of ultra-high density and highly uniform InGaN QDs by employing selective area epitaxy were realized on nanopatterned GaN template fabricated by diblock copolymer lithography. It results in well-defined QD density in the range of $8x10^{10}$ cm^{-2}, which represents the highest QD density reported for nitride-based QDs. In comparison, the InGaN QD density by the prevailing Stranski–Krastanow (S-K) growth mode is around mid 10^9 cm^{-2} with non-uniformity in dot sizes and distributions. The availability of highly-uniform and ultra-high density InGaN QDs formed by this approach has significant and transformational impacts on developing high-efficiency light-emitting diodes for solid state lighting, ultra-low threshold current density visible diode lasers, and intermediate-band nitride-based solar cells.

Chapter 1 Introduction

1.1 Nitride Semiconductors and Their Applications

In the past few decades, the semiconductor of III-nitride materials, including GaN, AlN and InN, find the tremendous impacts in our daily life. With the superior material property and device capabilities, III-nitrides are fundamentally redefining the concepts of light generation and control of electrical power. The great promise of III-nitride-based semiconductor devices are clearly impacting various applications of solid state lighting, laser diodes, photovoltaic, power electronics, thermoelectric, terahertz photonics and many other fields.

1.1.1 III-Nitride based Light-emitting Diode for Solid State Lighting

Solid state lighting brings a revolution as the energy-efficient solution for addressing the general illumination applications. The high efficiency, long lasting life-time, environmental-friendly materials, high controllability and many other advantages of these solid-state lighting sources, such as light-emitting diodes (LEDs) as compared to the conventional incandescence and florescence enable the transformational change in our lighting infrastructure. Figure 1-1 illustrates the LED revenue split by application [1]. The market size is expected to grow from $12.5 billion in 2013 to $17.1 billion in 2018, and the dominant driving force of the increase will shift from backlighting for TVs and monitors to general lighting application.

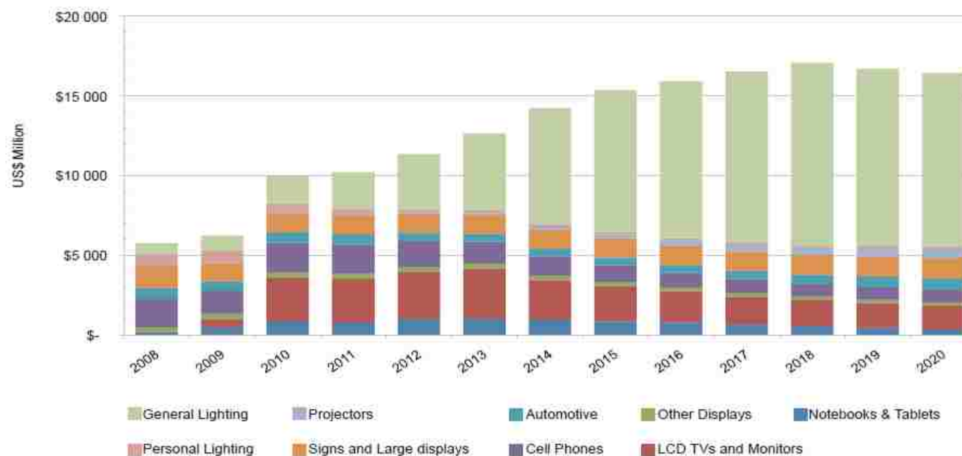

Figure 1-1: *LED revenue split by application [1].*

Human eyes in general are able to detect the light emission with the wavelength from 360 nm to 770 nm, which is considered as the visible light spectrum regime. The III-nitride semiconductor compounds of InGaN alloys has energy bandgap covering from 0.7 eV (InN) up to 3.4 eV (GaN) with decreasing In-content from 100% to 0%, corresponding to emission wavelength from 365 nm to 1.77 μm, as shown in figure 1-2. Hence, the InGaN material covers the whole visible spectrum regime, which is the foremost motivation to pursue GaN based solid state lighting [2-6]. To satisfy the light quality requirements for solid state lighting and accent the color of various objects, the high color rendering is very important for designing the light-emitting diodes (LEDs) for general illumination. Three metrics used to define the effect of a light source on objects are spectral power distribution, correlated color temperature and color rendering index.

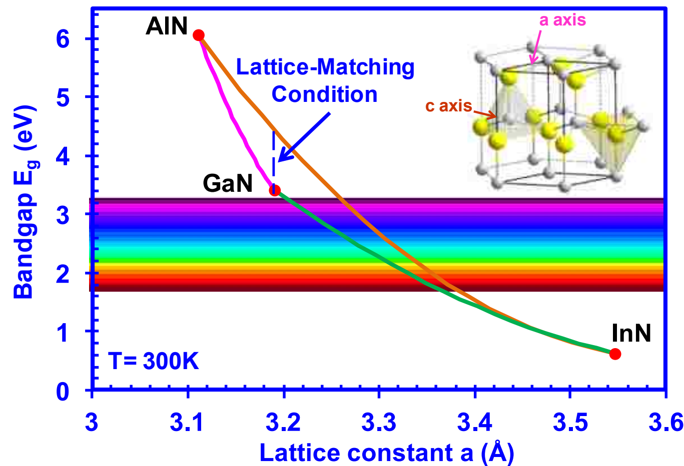

Figure 1-2: *Energy bandgap diagram and lattice structure of III-nitride semiconductors.*

In addition, the luminous efficacy of a light source is another key metric for energy savings considerations. It is a measurement of how well the light source produces visible light with the unit of lumens/Watt. This efficacy is obtained by taking the ratio of total luminous flux of the source devices and the electrical input power that the device has consumed. The average luminous efficacy of the commercially available white light solid state lighting devices have already achieved ~46 lm/W reported by The Department of Energy (DOE) in 2011 [7]. Cree's XLamp XM-L LEDs can even deliver 100 lumens per watt at their full power of 10 watts on average, and up to 160 lumens/watt at around 2 watts input power on average [8]. For comparison, the incandescence and florescence light bulbs typically produce ~15-20 lm/W and

60-80 lm/W, respectively [9]. Thus, the steadily increasing efficacy of LED based solid state lighting lamps has currently surpassed that of the incandescent and is comparable to that of fluorescents. Considering that ~22% of the total energy currently consumed by US is used for lighting applications with a great portion of the consumption wasted as heat or via other inefficient processes, the employment of long-lifetime, low maintenance requirement, environmentally friendly and energy efficient solid state light would significantly contribute to the saving of the energy and protection of the environment.

Significant progress has been achieved on the investigation and commercialization of GaN material based lighting devices for artificial white light sources. The current chip configurations include LED-plus-phosphors-based module, hybrid LED-phosphors-based module and multi-LED-based module [2, 3]. Figure 1-2 shows several examples of the approaches of white light generation from LEDs and the corresponding power spectrums [2]. The first R_BG_BB system employs a blue LED to pump red and green phosphors while the second RG_BB system employed a red AlGaInP based LED plus a InGaN based blue LED with the pumping green. In contrast, the last four-color RYGB (red, yellow, green, blue) all-LED system utilizes only high efficient LED to generate white light with high controllability of the color temperature and color rendering index. However, the challenges exist in obtaining high quality LED chips in green to yellow emission region, which will be further discussed later.

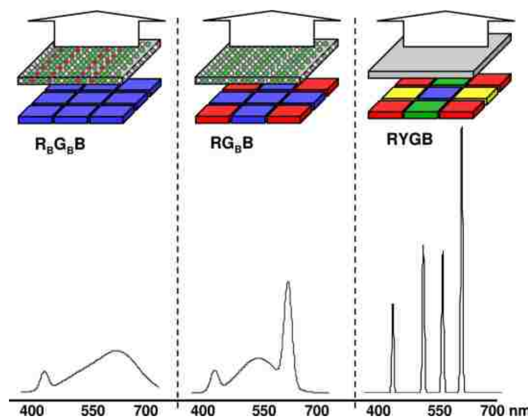

Figure 1-3: *Approaches for generating white light from LEDs and representative power spectra [2].*

1.1.2 III-Nitride based Laser Diodes

GaN materials are good material candidate for light emitter due to the direct bandgap properties. In additional to LED, another important category of GaN based light generating devices is laser diodes emitting at visible spectral region [10-24]. After the realization of the first efficient blue laser diodes using AlGaInN material by Nakamura in 1996 [12], the GaN based laser diodes have found the great opportunities in high speed and high density optoelectronic data storage and processing, medical diagnostics, environmental monitoring, telecommunications and display applications. Important advances have been achieved in improving the performance of GaN based blue laser diodes (LDs) with higher output power, longer lifetime and continuous-wave (CW) operation at higher temperature [13-15]. However, it is still very challenging to extend the lasing wavelength of III-nitride laser diodes to green or beyond. The challenges include high misfit dislocation density as a result of poor material quality, phase separation of high In-content InGaN and charge separation due to the strong polarization field. Several approaches have been employed to increase the optical gain for green GaN laser diode, including the employment of 1) nonpolar and semipolar InGaN QWs [16, 17], 2) GaN free standing substrate [18, 19], 3) AlGaN δ-layer in InGaN QW [20], 4) strain-compensated InGaN–AlGaN QW [21, 22], 5) type-II InGaN–GaNAs QW [10, 23], 5) triangular InGaN QW [24], 6) staggered InGaN QW [11] and 7) InGaN ternary substrate [25].

The cutting edge of semiconductor based laser diodes have been extending to ultraviolet (UV) where the LEDs and lasers can be implemented in the applications of biosensors, water purification, sterilization, and non-line-of-sight atmospheric communications [26-32]. The large bandgap ternary AlGaN or quaternary AlInGaN alloys are employed as the active region of III-nitride based UV laser. However, it is proven that it is not an easy task to fabricate electrical injected laser diodes at UV and deep UV spectrum region. With increasing Al-content in the AlGaN alloy, several issues started to play important roles: 1) increasing nonradiative recombination process due to the poor material quality; 2) decreasing refractive index difference leading to larger light leakage; 3) difficulty in obtaining ohmic contact from the high Al-content AlGaN surface and 4) lack of understanding in gain characteristics. Compared to LEDs, UV

lasers are even harder to obtain due to the more complex heterostructure, higher operation current density and the stringent requirements on the confinement of light. The electrical injected AlGaN QW LDs were obtained in the wavelength range of 320 nm to 380 nm with the output power from several mWs to several hundred mWs [26-30]. Recently, the crossover of the HH/LH and CH bands was reported for the high-Al content AlGaN QWs as the gain medium for deep UV LDs, which results in the polarization shift of the emission [31]. The AlGaN-delta-GaN QW structure was proposed to enhance the optical gain for mid UV and deep UV lasers [32].

Recently, GaN based quantum cascade lasers (QCLs) emitting at near-infrared (near-IR) spectrum regime has attracted much attention [33-40]. In contrast to the traditional laser diode using interband transition, the QCL active region utilizes the intersubband transition of the QWs or heterostructures, and the applications include a wide range of astrophysics, biological and medical sciences, security screening and illicit material detection, communications technology, and ultrafast spectroscopy [34]. The QCL structure was first and has been mainly implemented using III-V compound semiconductor, such as GaAs, InP and InSb [41]. Up till now, hundreds of miliwatts power has been achieved in far-IR, IR and mid-IR with CW and pulse-wave (PW) operation at low and room temperature. However, these technologies cannot access to near IR regime, which requires the employment of larger band offset materials. Significant advances on the pursuit of intersubband QW optoelectronics in the near IR regime have occurred by employing AlN / GaN material systems. In addition to larger bandgap of GaN material, GaN based laser diodes are able to have a higher operation temperature due to the large phonon energy in GaN material of 92 meV which is 2.56 times larger than that of GaAs (~36 meV) and about 3.5 times larger than thermal energy at room temperature (~26 meV). However, these advances are still lagging due to: 1) challenges in growing high-quality AlN / GaN superlattices, and 2) limited design consideration from AlN / GaN QW structures. Thus, the III-nitride based QCL design is of great interests for the near-IR applications [42].

1.1.3 Concentrated Photovoltaic Cells

The increasing demand for energy and reducing fossil fuels significantly stimulates the pursuit of renewable energy technology for electrical generation, such as solar energy, wind, geothermal

energy and biofuel. Photovoltaic cells are becoming one of the most rapidly developing areas with an averaging 20% growing rate in energy production in the past decade [43]. The prevailing solar cells in market nowadays are low-cost silicon based solar cells and high-efficiency GaAs/Ge based multi-junction tandem solar cells. III-nitrides are gaining attention due to the following reasons. First of all, the direct-bandgap III-nitride alloys nearly cover the whole solar spectral from 310 nm to 1.8 μm, which makes it possible to fabricate PV devices from this material system. Secondly, the favorable properties of InGaN alloys including superior radiation hardness, high light absorption, high thermal conductivity, the potential of integration into the current silicon technology give rise to many researches in realizing and optimizing the InGaN based solar cells [44-56]. Up till now, the active region structure of p-i-n InGaN bulk [44-49], InGaN/GaN MQW or/and superlattice [50-55], III-nitride nanowires [57] have been extensively investigated. Both MOCVD and MBE techniques are employed for the growth of active region on planar sapphire substrate, patterned sapphire substrate and GaN native substrate. So far, the most efficient solar cells own the bandgap around 1.5 eV where the photons of visible spectral regime with smaller energy near the peak of the solar spectrum will be absorbed. This energy level corresponds to the In-content around 57% of InGaN bulk, which is not experimentally feasible up till now [48]. The highest conversion efficiency of III-nitride based PV cells so far is around 3% from 30%-In-content InGaN / GaN QWs [55]. Research works on how to improve the material quality of high In-content InGaN, novel device structure for high light absorption and the employment of InGaN QDs are still ongoing for achieving high efficiency III-nitride based photovoltaic devices.

1.1.4 Power Electronics

The high efficiency and robust III-nitride based power electronics can potentially improve the energy efficiency and serve as the building blocks of smart grid in electrical systems. According to *The Economist*, the standby electrical power accounts for 5-10% of annual energy consumption in the home due to the power consumption of the inefficient power supplies even when the devices is not in use [57]. In addition, the smart grid with more intelligent processes of monitoring and managing the energy generation and consumption are required to be introduced

into the current electrical power delivery network [58]. The wide bandgap semiconductors, such as GaN, can play an important role in forming solid-state power controlling devices for the transformation of the electric power grid from electromechanically controlled system to electronic controlled network.

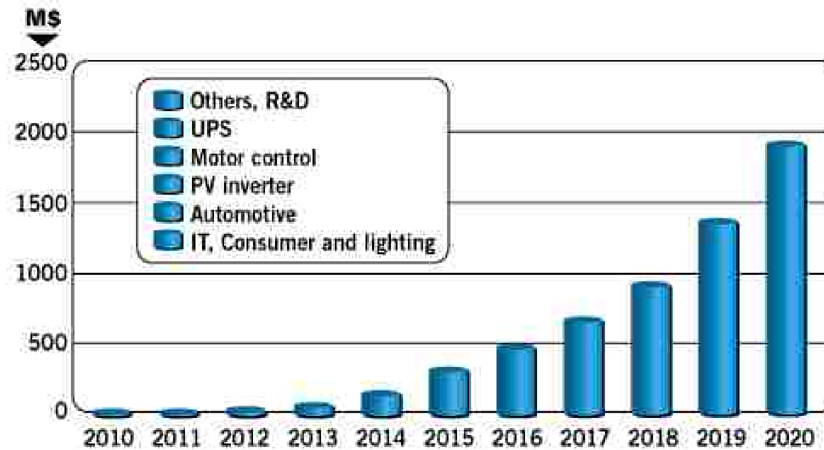

Figure 1-4 *Market size of GaN power electronics devices predicted by analysts at market research firm Yole Développement in Lyon [60].*

Besides the wide bandgap, a large critical breakdown electric field (~3 MV/cm) and a high electron mobility (~1500 $cm^2/(V*s)$ at T=300K) enable GaN to form electronic devices with low on-state resistance, low switching losses, high temperature performance and high power conversion efficiencies [59, 60]. The heterjunction of AlGaN/GaN based devices include Schottky diodes for high efficient switching, field effect transistors (FET), heterojunction bipolar transistors (HBT) with D.C. or R.F. operation and high-electron mobility transistor (HEMT) have been widely studied. Figure 1-4 shows the estimated market size of GaN based power electronic devices predicted by *Yole Développement* in Lyon [61]. The GaN power device industry only generated less than $2.5M (estimated) revenues in 2011. However, the total available market is expected to grow from $10 million in 2012 to $50 million in 2013, and may exceed $1 billion by 2019 [61].

1.1.5 Other Applications

Due to the tunable direct bandgap as well as strong physical and chemical damage resistance, Group-III Nitrides exhibit significant impact in photon-detection of UV, solar blind and visible,

where the high responsive, low noise, and increasingly efficient detectors have been demonstrated [62-64]. In addition, the electrical properties of III-nitrides was found to be very sensitive to the exposure of volatile organic compound (VOC) or combustible gases, such as butane, propane, and carbon monoxide and alcohol (C_2H_5OH). Thus, another arising field of application for III-nitrides is the toxic gas detection [65, 66].

III-nitrides play an important role in green energy applications, not only for energy efficient appliance, such as LEDs and LDs, but also for the renewable energy generation devices, such as concentrated photovoltaic cells. Some other important applications of GaN based devices in green energy aspects are thermoelectrics [67-69] and solar H_2 generation [70, 71]. The thermoelectric effect describes the energy conversion between heat and electricity, and it can be utilized to generate electrical power, measure temperature and change temperature of targeted objects. From our experiments, we found that the AlInN alloy exhibits excellent thermoelectric property with figure of merit Z*T value as high as 0.5 at room temperature from $Al_{0.83}In_{0.17}N$. Together with the capability of being grown lattice-matched to GaN with significantly reduced dislocations and defects, AlInN alloy shows promising potential as thermoelectric material in device integration with GaN based technologies. III-nitrides are also being explored as active region of photoelectrochemical cell to split water into H_2 and O_2 gas through photoelectrochemical hydrolysisas process. This clean and low-cost approach of solar energy storage via H_2 gas generation would have great potential for future green energy applications.

1.2 Research Works Accomplished - High-Efficiency III-Nitride based Optoelectronics

Several important challenges still exist despite the significant advances of III-nitride material in solid state lighting. The issues of low radiative efficiency in longer emission wavelength regime, the efficiency droop phenomenon at high current density operation and low light extraction efficiencies of the InGaN based LEDs are three major limitations hindering the further development of III-nitride based LEDs and laser diodes. In this report, the device engineering of

novel active region design for radiative efficiency enhancement, novel barrier design for efficiency-droop suppression and the InGaN based quantum dots approach for high efficiency optoelectronic devices will be presented.

1.2.1 Novel Barrier Design for Efficiency-Droop Suppression in Nitride LEDs

As indicated previously, the efficiency droop issue in nitride-based LEDs significantly hinders the development of high power and high brightness InGaN based solid state lighting. The previous analytical model indicated that the reduction of injection efficiency contributes to the existence of efficiency droop phenomenon. This report would discuss the novel barrier design of the use of large-bandgap thin barrier, for instance, AlGaInN or AlInN, sandwiching the InGaN QWs for increasing the effective barrier heights, reducing carrier leakage and suppressing the efficiency droop issue. The theoretical analysis using numerical methods with the consideration of carrier transport effect is presented, and the results show promising potential of the use of ~ 2 nm lattice-matched $Al_{0.72}In_{0.18}N$ in suppression of efficiency reduction at high current density in InGaN based QW LEDs.

The growth of lattice matched AlInN alloy is crucial for various applications as discussed in the earlier sections. The growth optimization of AlInN with various In composition will be presented. The growth parameter as well as the effect of the substrates on the morphology of the AlInN thin film will be discussed in details. In addition, the fabrication of InGaN-AlInN QW LED for efficiency droop suppression will be presented. The characterization measurements are carried out to investigate the feasibility of the novel barrier design in enhancing the device characteristics.

1.2.2 Novel Active Region Design for Radiative Efficiency Enhancement in III-Nitride LEDs

The low radiative efficiency and light output power of InGaN QW LED emitting at green and yellow spectrum region leads to the green gap issue of solid state lighting. The severe charge separation issue of conventional InGaN QWs results in the low electron-hole wavefunction overlap and thus low radiative recombination rate. The QW structure engineering of introducing an energy local minimum inside the InGaN QW, specifically by linearly-shaped staggered InGaN QWs and InGaN-delta-InN QWs in this report, would shift the electron-hole wavefunction towards the center of active region. The approaches of novel InGaN QWs LEDs with green and yellow

emission will be discussed.

1.2.3 Selective Area Epitaxy of InGaN based Quantum Dot Nanostructures

The efficiencies of III-nitride based LEDs and solar cells can be further enhanced by nanostructure engineering. The three-dimensional quantum confinement of carriers from the quantum dot structures could potentially enhance the quantum efficiency of InGaN based devices. However, the state-of-the-art InGaN QDs have relatively low dot density (~ mid 10^9 cm^{-3}) or uniform dot distributions from S-K growth mode, selective area epitaxy or etching techniques. The work on Selective area epitaxy of ultra-high density InGaN quantum dots by diblock copolymer lithography will be discussed. The low-cost approach is applicable for large-scale production and it results in the uniform InGaN QD with high density of high 10^{10} cm^{-3}.

1.3 Report Organization

The organization of this report is presented as follow. The brief introduction of III-nitride materials and the applications will be presented in Chapter 1. The current challenges of III-nitride based LEDs for high power and high efficiency solid state lighting applications will then be discussed in Chapter 2. The report will introduce the numerical simulation methods of APSYS using the conventional InGaN/GaN MQWs LED as an example in Chapter 3. Chapter 4 will focus on the theoretical investigation of novel barrier design for efficiency droop suppression and novel QW design for green LEDs.

After providing the motivation of the device engineering, the report will move to the discussion of experimental works. Chapter 5 will introduce the general concept of MOCVD growth and device fabrication process and Chapter 6 will emphasis on the growth study of novel III-nitride materials for device applications. The device fabrication and characterization of InGaN-AlInN MQWs LEDs for efficiency droop suppression as well as InGaN MQWs LEDs with large-overlap designs will be presented in Chapter 7 while Chapter 8 will describe the fabrication process for the alternative novel structure of high density InGaN based QDs for high efficiency optoelectronics. The future works and tentative timeline would be presented in Chapter 9.

References for Chapter 1

1. Yole Développement, “Status of the LED Industry”, August, 2012.
2. M. H. Crawford, "LEDs for Solid-State Lighting: Performance Challenges and Recent Advances," *IEEE J. Sel. Top. Quantum Electron.,* vol. 15, pp. 1028-1040, 2009.
3. E. F. Schubert and J. K. Kim, "Solid-state light sources getting smart," *Science,* vol. 308, pp. 1274-1278, May 27 2005.
4. M. R. Krames, O. B. Shchekin, R. Mueller-Mach, G. O. Mueller, L. Zhou, G. Harbers, and M. G. Craford, "Status and future of high-power light-emitting diodes for solid-state lighting," *Journal of Display Technology,* vol. 3, pp. 160-175, Jun 2007.
5. N. Tansu, H. P. Zhao, G. Y. Liu, X. H. Li, J. Zhang, H. Tong, and Y. K. Ee, "III-Nitride Photonics," *IEEE Photonics Journal,* vol. 2, pp. 241-248, Apr 2010.
6. H. P. Zhao, G. Y. Liu, J. Zhang, J. D. Poplawsky, V. Dierolf, and N. Tansu, "Approaches for high internal quantum efficiency green InGaN light-emitting diodes with large overlap quantum wells," *Optics Express,* vol. 19, pp. A991-A1007, Jul 4 2011.
7. DOE Solid-State Lighting CALiPER Program Summary of Results: Round 12 of Product Testing, U.S. Department of Energy, June 2011.
8. http://www.cree.com/led-components-and-modules/products/xlamp/discrete-directional/xlamp-xml
9. Philips Product Catalog
10. R. A. Arif, H. P. Zhao, and N. Tansu, "Type-II InGaN-GaNAs quantum wells for lasers applications," *Appl. Phys. Lett.,* vol. 92, Jan 7 2008.
11. H. P. Zhao and N. Tansu, "Optical gain characteristics of staggered InGaN quantum wells lasers," *J. Appl. Phys.,* vol. 107, Jun 1 2010.
12. S. Nakamura, M. Senoh, S.-i. Nagahama, N. Iwasa, T. Yamada, T. Matsushita, H. Kiyoku, Y. Sugimoto, T. Kozaki, H. Umemoto, M. Sano, and K. Chocho, "Continuous-wave operation of InGaN/GaN/AlGaN-based laser diodes grown on GaN substrates," *Appl. Phys. Lett.,* vol. 72, pp. 2014-2016, 1998.
13. A. C. Tamboli, E. D. Haberer, R. Sharma, K. H. Lee, S. Nakamura, and E. L. Hu, "Room-temperature continuous-wave lasing in GaN/InGaN microdisks," *Nature Photonics,* vol. 1, pp. 61-64, Jan 2007.
14. T. C. Lu, C. C. Kao, H. C. Kuo, G. S. Huang, and S. C. Wang, "CW lasing of current injection blue GaN-based vertical cavity surface emitting laser," *Appl. Phys. Lett.,* vol. 92, Apr 7 2008.
15. C. Skierbiszewski, M. Siekacz, H. Turski, G. Muziol, M. Sawicka, A. Feduniewicz-Zmuda, J. Smalc-Koziorowska, P. Perlin, S. Grzanka, Z. R. Wasilewski, R. Kucharski, and S. Porowski, "InGaN laser diodes operating at 450--460 nm grown by rf-plasma MBE," *Journal of Vacuum Science & Technology B: Microelectronics and Nanometer Structures,* vol. 30, p. 02B102, 2012.
16. Y. Enya, Y. Yoshizumi, T. Kyono, K. Akita, M. Ueno, M. Adachi, T. Sumitomo, S.

Tokuyama, T. Ikegami, and K. Katayama, "531 nm Green Lasing of InGaN Based Laser Diodes on Semi-Polar (2021) Free-Standing GaN Substrates," *Appl. Phys. Express,* vol. 2, p. 82101, 2010.

17. A. Tyagi, R. M. Farrell, K. M. Kelchner, C. Y. Huang, P. S. Hsu, D. A. Haeger, M. T. Hardy, C. Holder, K. Fujito, D. A. Cohen, H. Ohta, J. S. Speck, S. P. DenBaars, and S. Nakamura, "AlGaN-Cladding Free Green Semipolar GaN Based Laser Diode with a Lasing Wavelength of 506.4 nm," *Appl. Phys. Express,* vol. 3, 2010.

18. T. Miyoshi, S. Masui, T. Okada, T. Yanamoto, T. Kozaki, S. Nagahama, and T. Mukai, "510-515 nm InGaN-Based Green Laser Diodes on c-Plane GaN Substrate," *Appl. Phys. Express,* vol. 2, Jun 2009.

19. D. Queren, A. Avramescu, G. Bruderl, A. Breidenassel, M. Schillgalies, S. Lutgen, and U. Strauss, "500 nm electrically driven InGaN based laser diodes," *Appl. Phys. Lett.,* vol. 94, Feb 23 2009.

20. S.-H. Park, J. Park, and E. Yoon, "Optical gain in InGaN/GaN quantum well structures with embedded AlGaN delta layer," *Appl. Phys. Lett.,* vol. 90, p. 023508, 2007.

21. H. P. Zhao, R. A. Arif, Y. K. Ee, and N. Tansu, "Optical gain analysis of strain-compensated InGaN-AlGaN quantum well active regions for lasers emitting at 420-500 nm," *Optical and Quantum Electronics,* vol. 40, pp. 301-306, Apr-May 2008.

22. H. P. Zhao, R. A. Arif, Y. K. Ee, and N. Tansu, "Self-Consistent Analysis of Strain-Compensated InGaN-AlGaN Quantum Wells for Lasers and Light-Emitting Diodes," *Ieee Journal of Quantum Electronics,* vol. 45, pp. 66-78, Jan-Feb 2009.

23. H. Zhao, R. A. Arif, and N. Tansu, "Self-consistent gain analysis of type-II `W' InGaN--GaNAs quantum well lasers," *J. Appl. Phys.,* vol. 104, p. 043104, 2008.

24. Z. Yang, R. Li, Q. Wei, T. Yu, Y. Zhang, W. Chen, and X. Hu, "Analysis of optical gain property in the InGaN/GaN triangular shaped quantum well under the piezoelectric field," *Appl. Phys. Lett.,* vol. 94, p. 061120, 2009.

25. J. Zhang and N. Tansu, "Improvement in spontaneous emission rates for InGaN quantum wells on ternary InGaN substrate for light-emitting diodes," *J. Appl. Phys.,* vol. 110, Dec 1 2011.

26. M. Kneissl, D. W. Treat, M. Teepe, N. Miyashita, and N. M. Johnson, "Continuous-wave operation of ultraviolet InGaN/InAlGaN multiple-quantum-well laser diodes," *Appl. Phys. Lett.,* vol. 82, pp. 2386-2388, 2003.

27. M. Kneissl, Z. Yang, M. Teepe, C. Knollenberg, O. Schmidt, P. Kiesel, N. M. Johnson, S. Schujman, and L. J. Schowalter, "Ultraviolet semiconductor laser diodes on bulk AlN," *J. Appl. Phys.,* vol. 101, p. 123103, 2007.

28. H. Yoshida, Y. Yamashita, M. Kuwabara, and H. Kan, "A 342-nm ultraviolet AlGaN multiple-quantum-well laser diode," *Nature photonics,* vol. 2, pp. 551-554, Sep 2008.

29. H. Yoshida, M. Kuwabara, Y. Yamashita, Y. Takagi, K. Uchiyama, and H. Kan, "AlGaN-based laser diodes for the short-wavelength ultraviolet region," *New Journal of Physics,* vol. 11, Dec 17 2009.

30. H. Yoshida, M. Kuwabara, Y. Yamashita, K. Uchiyama, and H. Kan, "Radiative and

nonradiative recombination in an ultraviolet GaN/AlGaN multiple-quantum-well laser diode," *Appl. Phys. Lett.,* vol. 96, p. 211122, 2010.

31. J. Zhang, H. P. Zhao, and N. Tansu, "Effect of crystal-field split-off hole and heavy-hole bands crossover on gain characteristics of high Al-content AlGaN quantum well lasers," *Appl. Phys. Lett.,* vol. 97, Sep 13 2010.

32. J. Zhang, H. P. Zhao, and N. Tansu, "Large optical gain AlGaN-delta-GaN quantum wells laser active regions in mid-and deep-ultraviolet spectral regimes," *Appl. Phys. Lett.,* vol. 98, Apr 25 2011.

33. C. Gmachl, H. M. Ng, S. N. G. Chu, and A. Y. Cho, "Intersubband absorption at lambda similar to 1.55 mu m in well- and modulation-doped GaN/AlGaN multiple quantum wells with superlattice barriers," *Appl. Phys. Lett.,* vol. 77, pp. 3722-3724, Dec 4 2000.

34. B. S. Williams, "Terahertz quantum-cascade lasers," *Nature photonics,* vol. 1, pp. 517-525, 2007.

35. C. Gmachl, H. M. Ng, and A. Y. Cho, "Intersubband absorption in degenerately doped GaN/AlxGa1-xN coupled double quantum wells," *Appl. Phys. Lett.,* vol. 79, pp. 1590-1592, Sep 10 2001.

36. C. Gmachl and H. M. Ng, "Intersubband absorption at lambda similar to 2.1 mu m in A-plane GaN/AlN multiple quantum wells," *Electronics Letters,* vol. 39, pp. 567-569, Mar 20 2003.

37. H. Sodabanlu, J. S. Yang, M. Sugiyama, Y. Shimogaki, and Y. Nakano, "Strain effects on the intersubband transitions in GaN/AlN multiple quantum wells grown by low-temperature metal organic vapor phase epitaxy with AlGaN interlayer," *Appl. Phys. Lett.,* vol. 95, Oct 19 2009.

38. W. Terashima and H. Hirayama, "Design and fabrication of terahertz quantum cascade laser structure based on III-nitride semiconductors," *physica status solidi (c),* vol. 6, pp. S615-S618, 2009.

39. K. Kishino, A. Kikuchi, H. Kanazawa, and T. Tachibana, "Intersubband transition in (GaN)(m)/(AlN)(n) superlattices in the wavelength range from 1.08 to 1.61 mu m," *Appl. Phys. Lett.,* vol. 81, pp. 1234-1236, Aug 12 2002.

40. K. Driscoll, Y. T. Liao, A. Bhattacharyya, L. Zhou, D. J. Smith, T. D. Moustakas, and R. Paiella, "Optically pumped intersubband emission of short-wave infrared radiation with GaN/AlN quantum wells," *Appl. Phys. Lett.,* vol. 94, Feb 23 2009.

41. J. Faist, F. Capasso, D. L. Sivco, C. Sirtori, A. L. Hutchinson, and A. Y. Cho, "Quantum Cascade Laser," *Science,* vol. 264, pp. 553-556, Apr 22 1994.

42. G. Y. Liu, H. Zhao, and N. Tansu, “Electron-Phonon and Electron-Photon Intersubband Scattering Rates in Asymmetric AlN / GaN Coupled Quantum Wells,” in Proc. of the SPIE Photonics West 2010, Physics and Simulation of Optoelectronics Devices XVIII, San Francisco, CA, Jan 2010.

43. http://en.wikipedia.org/wiki/Renewable_energy#cite_note-jr2010-47

44. X. M. Cai, S. W. Zeng, and B. P. Zhang, "Favourable photovoltaic effects in InGaN pin homojunction solar cell," *Electronics Letters,* vol. 45, pp. 1266-U104, Nov 19 2009.

45. B. R. Jampana, A. G. Melton, M. Jamil, N. N. Faleev, R. L. Opila, I. T. Ferguson, and C. B. Honsberg, "Design and Realization of Wide-Band-Gap (similar to 2.67 eV) InGaN p-n Junction Solar Cell," *Ieee Electron Device Letters,* vol. 31, pp. 32-34, Jan 2010.

46. O. Jani, I. Ferguson, C. Honsberg, and S. Kurtz, "Design and characterization of GaN/InGaN solar cells," *Appl. Phys. Lett.,* vol. 91, Sep 24 2007.

47. X. Chen, K. D. Matthews, D. Hao, W. J. Schaff, and L. F. Eastman, "Growth, fabrication, and characterization of InGaN solar cells," *Physica Status Solidi a-Applications and Materials Science,* vol. 205, pp. 1103-1105, May 2008.

48. C. J. Neufeld, N. G. Toledo, S. C. Cruz, M. Iza, S. P. DenBaars, and U. K. Mishra, "High quantum efficiency InGaN/GaN solar cells with 2.95 eV band gap," *Appl. Phys. Lett.,* vol. 93, p. 143502, 2008.

49. J. J. Wierer, A. J. Fischer, and D. D. Koleske, "The impact of piezoelectric polarization and nonradiative recombination on the performance of (0001) face GaN/InGaN photovoltaic devices," *Appl. Phys. Lett.,* vol. 96, Feb 1 2010.

50. K. Y. Lai, G. J. Lin, Y.-L. Lai, Y. F. Chen, and J. H. He, "Effect of indium fluctuation on the photovoltaic characteristics of InGaN/GaN multiple quantum well solar cells," *Appl. Phys. Lett.,* vol. 96, p. 081103, 2010.

51. J. Y. Wang, F. J. Tsai, J. J. Huang, C. Y. Chen, N. Li, Y. W. Kiang, and C. C. Yang, "Enhancing InGaN-based solar cell efficiency through localized surface plasmon interaction by embedding Ag nanoparticles in the absorbing layer," *Optics Express,* vol. 18, pp. 2682-2694, Feb 1 2010.

52. S. Y. Bae, J. P. Shim, D. S. Lee, S. R. Jeon, and G. Namkoong, "Improved Photovoltaic Effects of a Vertical-Type InGaN/GaN Multiple Quantum Well Solar Cell," *Japanese J. Appl. Phys.,* vol. 50, Sep 2011.

53. C. C. Yang, J. K. Sheu, C. H. Kuo, M. S. Huang, S. J. Tu, F. W. Huang, M. L. Lee, Y. H. Yeh, X. W. Liang, and W. C. Lai, "Improved Power Conversion Efficiency of InGaN Photovoltaic Devices Grown on Patterned Sapphire Substrates," *Ieee Electron Device Letters,* vol. 32, pp. 536-538, Apr 2011.

54. G. J. Lin, K. Y. Lai, C. A. Lin, and J. H. He, "Solar energy harvesting scheme using syringe-like ZnO nanorod arrays for InGaN/GaN multiple quantum well solar cells," *Optics Letters,* vol. 37, pp. 61-63, Jan 1 2012.

55. R. Dahal, J. Li, K. Aryal, J. Y. Lin, and H. X. Jiang, "InGaN/GaN multiple quantum well concentrator solar cells," *Appl. Phys. Lett.,* vol. 97, p. 073115, 2010.

56. Y. Dong, B. Tian, T. J. Kempa, and C. M. Lieber, "Coaxial Group III−Nitride Nanowire Photovoltaics," *Nano Letters,* vol. 9, pp. 2183-2187, 2009/05/13 2009.

57. http://www.lbl.gov/today/2006/Mar/14-Tue/standby.html

58. M. Amin and J. Stringer, "The electric power grid: Today and tomorrow," *MRS Bulletin,* vol. 33, pp. 399-407, Apr 2008.

59. J. Wuerfl, E. Bahat-Treidel, F. Brunner, E. Cho, O. Hilt, P. Ivo, A. Knauer, P. Kurpas, R. Lossy, M. Schulz, S. Singwald, M. Weyers, and R. Zhytnytska, "Reliability issues of GaN based high voltage power devices," *Microelectronics Reliability,* vol. 51, pp. 1710-1716,

Sep-Nov 2011.

60. Technology of Gallium Nitride Cystal Growth, Chapter 1, Springer

61. http://www.electroiq.com/articles/sst/2012/03/led-makers-could-diversify-with-gan-power-electronics-production.html

62. D. Walker, V. Kumar, K. Mi, P. Sandvik, P. Kung, X. Zhang, and M. Razeghi, "Solar-blind AlGaN photodiodes with very low cutoff wavelength," *Appl. Phys. Lett.,* vol. 76, p. 403, 2000.

63. E. Monroy, F. Omnes, and F. Calle, "Wide-bandgap semiconductor ultraviolet photodetectors," *Semiconductor Science and Technology,* vol. 18, p. R33, 2003.

64. Z. T. Chen, S. X. Tan, Y. Sakai, and T. Egawa, "Improved performance of InAlN-based Schottky solar-blind photodiodes," *Appl. Phys. Lett.,* vol. 94, p. 213504, 2009.

65. W. Y. Weng, S. J. Chang, T. J. Hsueh, C. L. Hsu, M. J. Li, and W. C. Lai, "AlInN resistive ammonia gas sensors," *Sensors and Actuators B: Chemical,* vol. 140, pp. 139-142, 2009.

66. D. S. Lee, J. H. Lee, Y. H. Lee, and D. D. Lee, "GaN thin films as gas sensors," *Sensors and Actuators B-Chemical,* vol. 89, pp. 305-310, Apr 1 2003.

67. J. Zhang, H. Tong, G. Y. Liu, J. A. Herbsommer, G. S. Huang, and N. Tansu, "Characterizations of Seebeck coefficients and thermoelectric figures of merit for AlInN alloys with various In-contents," *J. Appl. Phys.,* vol. 109, Mar 1 2011.

68. H. Tong, J. Zhang, G. Y. Liu, J. A. Herbsommer, G. S. Huang, and N. Tansu, "Thermoelectric properties of lattice-matched AlInN alloy grown by metal organic chemical vapor deposition," *Appl. Phys. Lett.,* vol. 97, p. 112105, Sep 13 2010.

69. J. Zhang, S. Kutlu, G. Y. Liu, and N. Tansu, "High-temperature characteristics of Seebeck coefficients for AlInN alloys grown by metalorganic vapor phase epitaxy," *J. Appl. Phys.,* vol. 110, Aug 15 2011.

70. J. Li, J. Y. Lin, and H. X. Jiang, "Direct hydrogen gas generation by using InGaN epilayers as working electrodes," *Appl. Phys. Lett.,* vol. 93, pp. 162107-162107-3, 2008.

71. K. Aryal, B. Pantha, J. Li, J. Lin, and H. Jiang, "Hydrogen generation by solar water splitting using p-InGaN photoelectrochemical cells," *Appl. Phys. Lett.,* vol. 96, p. 052110, 2010.

Chapter 2 Challenges and Solutions of III-Nitride LEDs for Solid State Lighting

Despite the advantages of GaN based light-emitting diodes (LEDs) and the great potential of III-nitrides for solid state lighting applications, there are several major obstacles hindering the further development of solid state lighting for general illuminations. Green gap in the emission spectra, efficiency droop phenomenon at high operating current and the difficulty of extracting light out to the free space from the high index cavity are among the most challenging issues.

2.1 Low efficiency of Green LEDs

2.1.1 Green Gap Issue

As discussed in Chapter 1, the optimal white light source consists of multiple emitters with different wavelengths. As shown in figure 2-1, high efficient LEDs can be obtain at orange and red using AlGaInP materials and at violet and blue using InGaN materials, respectively [1]. However, the green and yellow LEDs which have the highest luminous eye response own the low quantum efficiency from the plot. This phenomenon is referred as ‘green gap’ issue in solid state lighting. To extend the emission spectrum into green and yellow region, the approach of reducing the bandgap of AlGaInP is not feasible due to the crossover of direct-bandgap to indirect-bandgap of the alloys. Thus, the high efficient green LED would be possibly available by utilizing InGaN/GaN quantum well (QW) system with increased QW thickness or high In-content InGaN active region. However, both approaches are huge challenges in material growth and would result in significant compromises in material quality. Specifically, with the increasing In-content and thickness of InGaN QWs, the strain misfit dislocation density from the mismatched lattice constants of InGaN and GaN layers are increasing. Besides, the severe phase separation in high-In content InGaN QW leads to compositional inhomogeneity in the QW.

In addition to the growth difficulty in obtain high quality materials, a more profound challenge, the charge separation issue is also a severe limitation of extending the InGaN based LED wavelength. The strong polarization in III-nitride material leads to significant tilting of

bandstructure of InGaN/GaN QWs, which results in the shift of electron and hole wavefunctions away from the center of active region. Therefore, the radiative recombination rate of InGaN QW would be reduced as a result of the wavefunction overlap according to Fermi's Golden Rule. To illustrate the concept, figure 2-2 plots the electron-hole wavefunction overlap ($\Gamma_{e\text{-}hh}$) and emission wavelength as a function of the indium-content and thickness of InGaN active region from reference 2 [2]. The $\Gamma_{e\text{-}hh}$ reduces significantly as one tries to push the emission wavelength of a conventional InGaN QW to longer spectra regimes by increasing the Indium content and layer thickness of the InGaN QW region. Thus, it is very challenging to realize green-emitting InGaN based LEDs with high-efficiency.

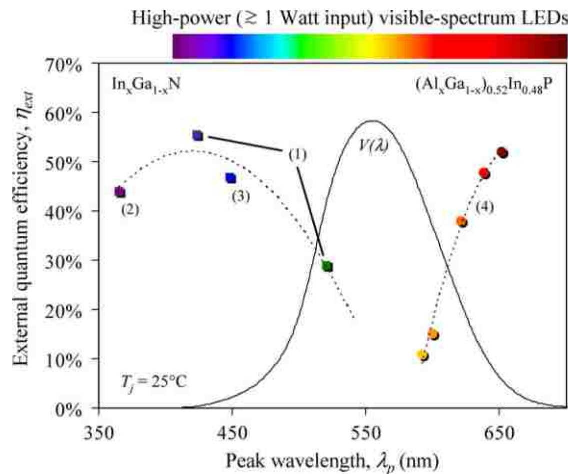

Figure 2-1 *External quantum efficiency of LEDs with various emission wavelength (dash line) and the luminous eye response curve, V (λ) (solid line) (from [1])*

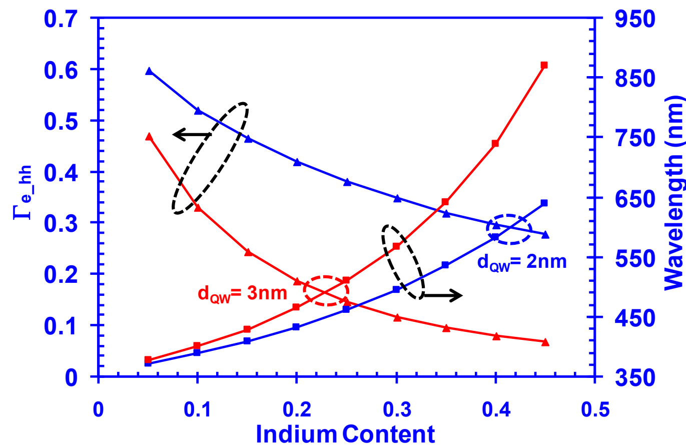

Figure 2-2 *The electron-hole wavefunctions overlap ($\Gamma_{e\text{-}hh}$) for InGaN QW as a function of Indium content with d_{QW} = 2nm and 3nm, and the corresponding emission wavelengths are shown.*

2.1.2 Approaches for High-Efficient Green LED

Various approaches have been investigated to increase the luminescence and efficiency from InGaN based LEDs. Extensive studies has been carried out to improve the material quality for the reduction of dislocations and thus nonradiative recombination centers [3, 4]. Ultimately, the charge separation issues need to be addressed to solve the low efficiency issue from InGaN/GaN based LED emitting at green spectrum regime. The employment of nonpolar or semipolar InGaN QW was proposed to eliminate or suppress the effect of polarization field in material, respectively [5-8]. Significant progress has been accomplished by researchers in the fields of non-polar or semi-polar InGaN QW LEDs. However, the further development of nonpolar InGaN QWs still require significant optimization in epitaxy as well as the reduction of the high cost of the non-polar or semi-polar GaN substrate.

On the other hand, the nanostructure engineering on c-plane InGaN QW increase in both spontaneous emission rate and optical gain has been investigated. The approaches include InGaN QW embedded with AlGaN-δ-layer [9, 10], type-II InGaN QW [11-13], strain-compensated QWs [14, 15] InGaN-delta-InN QWs [2] and staggered InGaN QWs [16-25] and other types of QW structure engineering [26]. Specifically, the use of staggered InGaN QWs and InGaN-delta-InN QWs enables one to enhance the electron-hole wavefunction overlap by introducing an energy local minima inside the active region. Hence, the electron and hole distribution are shifted towards the center of the QW, leading to the increase of optical matrix element and radiative recombination.

2.1.3 Large-overlap Design for IQE Enhancement

As a result of the strong polarization field, the conventional InGaN/GaN QW LEDs suffer from the spatial separation of electron and hole distributions due to the low electron-hole wavefunction overlap. This charge separation issue can be addressed by the QW structure engineering. Two types of structures are going to be extensively studied in this report, including staggered InGaN QW LEDs and InGaN-delta-InN QW LEDs. Figure 2-3 shows the schematics of (a) a

conventional $In_zGa_{1-z}N$ QW; (b) a two-layer staggered $In_xGa_{1-x}N$ / $In_yGa_{1-y}N$ QW and (c) a three-layer staggered $In_yGa_{1-y}N$ / $In_xGa_{1-x}N$ / $In_yGa_{1-y}N$ QW structures with $x > y$, which are surrounded by the GaN barriers [19, 24]. According to the simulation results by 6-band $\boldsymbol{k \cdot p}$ methods, by optimizing the In content and thickness of each sublayer, the electron-hole wavefuncion overlap of the staggered InGaN QW can be doubled as compared to conventional InGaN QW. The enhancement ratio of the total spontaneous recombination rate can be as high as 4 times for two-layer staggered InGaN QW and 5.86 times for three-layer staggered InGaN QW, respectively [19]. The detailed computation studies had been presented in reference 19, and the experimental realization as well as the characterizations will be presented in Chapter 7.

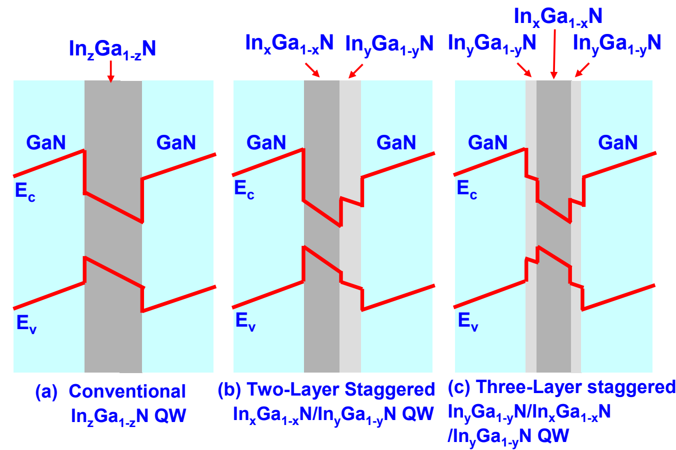

Figure 2-3 *Schematics of the (a) conventional $In_zGa_{1-z}N$ / GaN QW; (b) two-layer staggered $In_xGa_{1-x}N$ / $In_yGa_{1-y}N$ QW; and (c) three-layer staggered $In_yGa_{1-y}N$ / $In_xGa_{1-x}N$ / $In_yGa_{1-y}N$ QW structures [19, 24].*

Another interesting structure for the IQE enhancement is InGaN QW with the insertion of a low-bandgap delta-layer for the effective shift of the electron hole wavefunction while LED emission to yellow and red spectra regime. Figure 2-4 shows the band structures and wavefunctions of (a) conventional $In_{0.25}Ga_{0.75}N$ QW emitting at 492 nm and (b) $In_{0.25}Ga_{0.75}N$ / InN / $In_{0.25}Ga_{0.75}N$ QW emitting at 590 nm by the employment of self-consistent 6 band $\boldsymbol{k \cdot p}$ methods [2]. The introduction of low-bandgap delta-layer inside the InGaN QW enables the extension of the emission wavelength while enhancing the radiative recombination rate. The challenge lies in the experimental realization of LED devices with precise control of the delta layer growth.

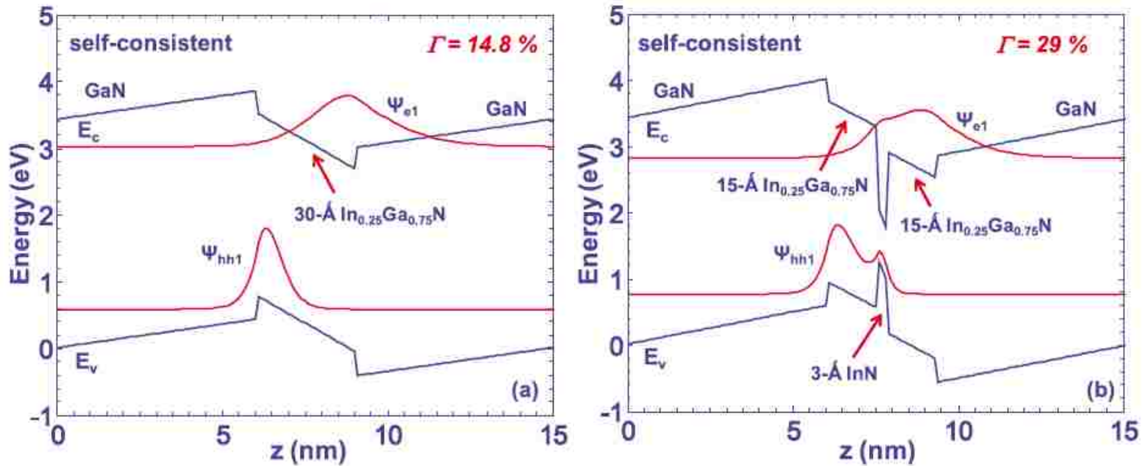

Figure 2-4 *Band structures and wavefunctions calculated for (a) conventional* $In_{0.25}Ga_{0.75}N$ *QW emitting at 506 nm and (b)* $In_{0.25}Ga_{0.75}N$ / InN / $In_{0.25}Ga_{0.75}N$ *QW emitting at 636 nm with enhanced* $\Gamma_{e\text{-}h}$ *[2].*

2.2 Efficiency Droop Phenomenon

2.2.1 Introduction and Possible Cause

To obtain high brightness of the lamps, devices are required to be operated at certain high power level. For instant, a current density (J) of 200 A/cm^2 or beyond is typically needed for general purpose. Furthermore, the chip sizes are expected to reduce for the cost effective purposes. In another word, to achieve some amount of light output power from a smaller device require the higher efficiency from the devices as well as higher operational current. However, the quantum efficiencies of nitride LEDs reduce significantly at J > 10-70 A/cm^2 [1, 27]. Figure 2-5 depicts the external quantum efficiency (EQE) and light output power as functions of dc forward currents for blue and green InGaN-GaN QW-based TFFC LEDs from reference 1, and the so-called “efficiency droop” phenomenon can be clearly observed. It occurs at both PW and CW operation, meaning that device heating is not the only reason or major issue causing this phenomenon. In addition, it has been proven that the LEDs with longer wavelength tends to suffer more from efficiency reduction as compared to the LEDs with shorter wavelength, which adds up to the already lower efficiency from green LEDs. Many proposals have been reported to investigate the origin and the solution to this problem. However, the mechanisms leading to the

existence of efficiency droop are still controversial and inclusive. One of the mechanism is the carrier escape. The internal quantum efficiency comprises of radiative efficiency and injection efficiency, where the injection efficiency defines as the ratio of injected current that recombine in the active region to total injected current. The conventional InGaN QW surrounded by GaN barrier exhibits great band-bending due to the strong polarization fields in III-nitride materials. Thus, the carrier leakage would increase due to reduction in effective barrier height, especially at high injection level.

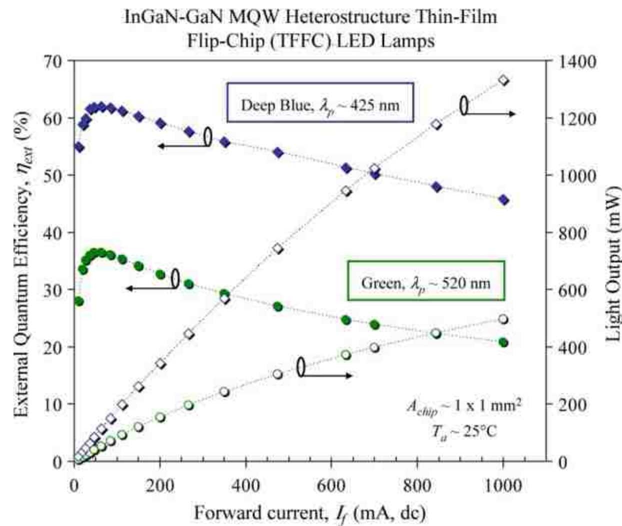

Figure 2-5 *External quantum efficiency and light output at different dc forward currents for blue and green InGaN-GaN QW-based TFFC LEDs with the size of 1 mm^2 [1].*

So far, various mechanisms have been investigated to account for the existence of efficiency droop phenomenon in nitride LEDs including: 1) carrier leakage [28-34], 2) Auger recombination processes [35-38], 3) hole transport impediment [39-41], 4) junction heating and other temperature related effects [42, 43], 5) large dislocation density [44], 6) decreased carrier localization at In-rich regions [45] and 7) current crowding effect [46-49]. Though the origin of the efficiency-droop phenomenon in InGaN-based LEDs remains controversial and inconclusive up till now, the primary reasons accounting for this issue have been mainly focused on the carrier density related mechanisms including large Auger recombination and large carrier leakage in III-nitrides. The Auger recombination coefficient C has been theoretically calculated and experimentally estimated for InGaN bulk materials as well as InGaN/GaN QW systems [35-38,

50]. A huge discrepancy of reported C values ranging from 10^{-34} to 10^{-30} cm^6s^{-1} indicates the inconclusive effect of Auger recombination on the performance of InGaN based LEDs. On the other hand, the carrier escape processes have been investigated for the reduction of efficiencies at high current density [31-34]. The injection efficiency at high current density is observed to experience reduction and hence the assumption of unity injection efficiency at all current density is not valid.

2.2.2 Approaches for Efficiency Droop Suppression

Various novel device configurations have been explored to enhance the injection efficiency for c-plane InGaN QW LEDs up till now. The suppression of efficiency droop using different designs of barrier layers, electron blocking layers and QW regions are due to reasons including the modification of polarization field [28, 51-55], the uniform current density distribution across the active region [48, 49, 56], the enhancement of hole injection [57-60] and the suppression of carrier leakage [31]. Specifically, in previous studies, the large bandgap materials were used as thick barrier surrounding the QW region (~ 12 nm) [28, 51, 52, 56, 61], or as the thick electron blocking layers (~ 20 nm) [53-55, 59]. However, the employment of thick layers of AlGaN or AlGaInN is difficult to realize in device fabrication and is hard to implement for industrial applications with the concern of defects and dislocations.

2.2.3 Novel Barrier Design

Recently, our works on the analytical simulation of current injection efficiency on the performances of InGaN QWs LEDs suggested that the use of thin large bandgap barrier layers sandwiching the InGaN QWs have the potential to suppress the efficiency-droop in the LEDs up to high current density [31]. The increased effective barrier height from the insertion of a thin low-Al content AlGaN or lattice-matched AlGaInN barrier surrounding InGaN QW were shown to significantly suppress the thermionic carrier leakage process in the active region, which in turn leads to improved current injection efficiency and internal quantum efficiency. Similar approaches have been employed for InGaAs QW and InGaAsN QW for the suppression of carrier leakage [62-65]. In addition, the polarization-matched AlGaInN materials were employed for the reduction

of efficiency droop issue previously [27, 50, 51]. However, the use of thin layer of large bandgap barrier for the carrier leakage suppression has not been extensively studied and optimized yet for enhancing the nitride LED quantum efficiency in device configuration. Detailed theoretical and experimental investigation of this novel barrier design for efficiency droop study will be presented in Chapter 4 and 7, respectively.

2.2.4 Employment of N-polar InGaN Quantum Well

The c-plane InGaN QW LED is typically Ga-polar, i.e., gallium atoms is a fist layer of atoms deposited on top of sapphire substrate in metal-organic chemical vapor deposition (MOCVD) growth. On the other hand, the N-polar III-nitrides have been investigated recently for AlGaN/GaN and InGaN/GaN heterostructures [70-72]. The potential for efficiency droop reduction will be discussed.

2.3 Low Extraction Efficiency

Due to large refractive index contrast of GaN (n~2.5) to air (n~1), the conventional planar InGaN QW LEDs suffers from small extraction efficiency. The extraction efficiency is defined as the ratio of photons that escape out of the cavity into free space to the total photons that have been generated in the active region. For the case of planar InGaN QWs LEDs, only the photons inside the narrow escape cone (~23.5°) can be extracted out, leading to only 4% extraction efficiency. Approaches to increase the extraction of photons includes surface roughening [66-69], photonic crystals [73, 74], graded refractive index materials [75, 76], and microlens array of SiO_2/Polystyrene and TiO_2/Polystyrene for better light coupling and light extraction [77-80].

References for Chapter 2

1. M. R. Krames, O. B. Shchekin, R. Mueller-Mach, G. O. Mueller, L. Zhou, G. Harbers, and M. G. Craford, "Status and future of high-power light-emitting diodes for solid-state lighting," *Journal of Display Technology,* vol. 3, pp. 160-175, Jun 2007.
2. H. P. Zhao, G. Y. Liu, and N. Tansu, "Analysis of InGaN-delta-InN quantum wells for light-emitting diodes," *Appl. Phys. Lett.,* vol. 97, Sep 27 2010.

3. Y. K. Ee, J. M. Biser, W. J. Cao, H. M. Chan, R. P. Vinci, and N. Tansu, "Metalorganic Vapor Phase Epitaxy of III-Nitride Light-Emitting Diodes on Nanopatterned AGOG Sapphire Substrate by Abbreviated Growth Mode," *IEEE J. Sel. Top. Quantum Electron.,* vol. 15, pp. 1066-1072, Jul-Aug 2009.
4. Y. K. Ee, X. H. Li, J. Biser, W. J. Cao, H. M. Chan, R. P. Vinci, and N. Tansu, "Abbreviated MOVPE nucleation of III-nitride light-emitting diodes on nano-patterned sapphire," *J. Crys. Growth,* vol. 312, pp. 1311-1315, Apr 1 2010.
5. T. Koyama, T. Onuma, H. Masui, A. Chakraborty, B. A. Haskell, S. Keller, U. K. Mishra, J. S. Speck, S. Nakamura, S. P. DenBaars, T. Sota, and S. F. Chichibu, "Prospective emission efficiency and in-plane light polarization of nonpolar m-plane In[sub x]Ga[sub 1 - x]N/GaN blue light emitting diodes fabricated on freestanding GaN substrates," *Appl. Phys. Lett.,* vol. 89, pp. 091906-3, 2006.
6. Y. Enya, Y. Yoshizumi, T. Kyono, K. Akita, M. Ueno, M. Adachi, T. Sumitomo, S. Tokuyama, T. Ikegami, and K. Katayama, "531 nm Green Lasing of InGaN Based Laser Diodes on Semi-Polar (2021) Free-Standing GaN Substrates," *Appl. Phys. Express,* vol. 2, p. 82101, 2010.
7. A. Tyagi, R. M. Farrell, K. M. Kelchner, C. Y. Huang, P. S. Hsu, D. A. Haeger, M. T. Hardy, C. Holder, K. Fujito, D. A. Cohen, H. Ohta, J. S. Speck, S. P. DenBaars, and S. Nakamura, "AlGaN-Cladding Free Green Semipolar GaN Based Laser Diode with a Lasing Wavelength of 506.4 nm," *Appl. Phys. Express,* vol. 3, 2010.
8. R. M. Farrell, E. C. Young, F. Wu, S. P. DenBaars, and J. S. Speck, "Materials and growth issues for high-performance nonpolar and semipolar light-emitting devices," *Semiconductor Science and Technology,* vol. 27, p. 024001, 2012.
9. J. Park and Y. Kawakami, "Photoluminescence property of InGaN single quantum well with embedded AlGaN delta layer," *Appl. Phys. Lett.,* vol. 88, p. 202107, 2006.
10. S.-H. Park, J. Park, and E. Yoon, "Optical gain in InGaN/GaN quantum well structures with embedded AlGaN delta layer," *Appl. Phys. Lett.,* vol. 90, p. 023508, 2007.
11. R. A. Arif, H. P. Zhao, and N. Tansu, "Type-II InGaN-GaNAs quantum wells for lasers applications," *Appl. Phys. Lett.,* vol. 92, Jan 7 2008.
12. H. P. Zhao, R. A. Arif, and N. Tansu, "Self-consistent gain analysis of type-II 'W' InGaN-GaNAs quantum well lasers," *J. Appl. Phys.,* vol. 104, Aug 15 2008.
13. S. H. Park, D. Ahn, B. H. Koo, and J. E. Oh, "Optical gain improvement in type-II InGaN/GaNSb/GaN quantum well structures composed of InGaN/and GaNSb layers," *Appl. Phys. Lett.,* vol. 96, Feb 1 2010.
14. H. P. Zhao, R. A. Arif, Y. K. Ee, and N. Tansu, "Optical gain analysis of strain-compensated InGaN-AlGaN quantum well active regions for lasers emitting at 420-500 nm," *Optical and Quantum Electronics,* vol. 40, pp. 301-306, Apr-May 2008.
15. H. P. Zhao, R. A. Arif, Y. K. Ee, and N. Tansu, "Self-Consistent Analysis of Strain-Compensated InGaN-AlGaN Quantum Wells for Lasers and Light-Emitting Diodes," *IEEE J. Quantum Electron.,* vol. 45, pp. 66-78, Jan-Feb 2009.
16. R. A. Arif, Y. K. Ee, and N. Tansu, "Polarization engineering via staggered InGaN quantum wells for radiative efficiency enhancement of light emitting diodes," *Appl. Phys. Lett.,* vol. 91,

Aug 27 2007.

17. R. A. Arif, Y. K. Ee, and N. Tansu, "Nanostructure engineering of staggered InGaN quantum Wells light emitting diodes emitting at 420-510 nm," *Physica Status Solidi a-Applications and Materials Science,* vol. 205, pp. 96-100, Jan 2008.

18. R. A. Arif, H. P. Zhao, Y. K. Ee, and N. Tansu, "Spontaneous emission and characteristics of staggered InGaN quantum-well light-emitting diodes," *IEEE J. Quantum Electron.,* vol. 44, pp. 573-580, May-Jun 2008.

19. H. P. Zhao, R. A. Arif, and N. Tansu, "Design Analysis of Staggered InGaN Quantum Wells Light-Emitting Diodes at 500-540 nm," *IEEE J. Sel. Top. Quantum Electron.,* vol. 15, pp. 1104-1114, Jul-Aug 2009.

20. H. P. Zhao, G. Y. Liu, X. H. Li, R. A. Arif, G. S. Huang, J. D. Poplawsky, S. T. Penn, V. Dierolf, and N. Tansu, "Design and characteristics of staggered InGaN quantum-well light-emitting diodes in the green spectral regime," *Iet Optoelectronics,* vol. 3, pp. 283-295, Dec 2009.

21. H. P. Zhao, G. Y. Liu, X. H. Li, G. S. Huang, J. D. Poplawsky, S. T. Penn, V. Dierolf, and N. Tansu, "Growths of staggered InGaN quantum wells light-emitting diodes emitting at 520-525 nm employing graded growth-temperature profile," *Appl. Phys. Lett.,* vol. 95, Aug 10 2009.

22. H. P. Zhao and N. Tansu, "Optical gain characteristics of staggered InGaN quantum wells lasers," *J. Appl. Phys.,* vol. 107, Jun 1 2010.

23. C. T. Liao, M. C. Tsai, B. T. Liou, S. H. Yen, and Y. K. Kuo, "Improvement in output power of a 460 nm InGaN light-emitting diode using staggered quantum well," *J. Appl. Phys.,* vol. 108, Sep 15 2010.

24. H. P. Zhao, G. Y. Liu, J. Zhang, J. D. Poplawsky, V. Dierolf, and N. Tansu, "Approaches for high internal quantum efficiency green InGaN light-emitting diodes with large overlap quantum wells," *Optics Express,* vol. 19, pp. A991-A1007, Jul 4 2011.

25. S. H. Park, D. Ahn, J. Park, and Y. T. Lee, "Optical Properties of Staggered InGaN/InGaN/GaN Quantum-Well Structures with Ga- and N-Faces," *Japanese J. Appl. Phys.,* vol. 50, Jul 2011.

26. K. P. O'Donnell, M. A. D. Maur, A. Di Carlo, K. Lorenz, and S. Consortium, "It's not easy being green: Strategies for all-nitrides, all-colour solid state lighting," *Physica Status Solidi-Rapid Research Letters,* vol. 6, pp. 49-52, Feb 2012.

27. J. Q. Xie, X. F. Ni, Q. Fan, R. Shimada, U. Ozgur, and H. Morkoc, "On the efficiency droop in InGaN multiple quantum well blue light emitting diodes and its reduction with p-doped quantum well barriers," *Appl. Phys. Lett.,* vol. 93, Sep 22 2008.

28. M.-H. Kim, M. F. Schubert, Q. Dai, J. K. Kim, E. F. Schubert, J. Piprek, and Y. Park, "Origin of efficiency droop in GaN-based light-emitting diodes," *Appl. Phys. Lett.,* vol. 91, p. 183507, 2007.

29. W. W. Chow, M. H. Crawford, J. Y. Tsao, and M. Kneissl, "Internal efficiency of InGaN light-emitting diodes: Beyond a quasiequilibrium model," *Appl. Phys. Lett.,* vol. 97, p. 121105, 2010.

30. J. Piprek and S. Li, "Electron leakage effects on GaN-based light-emitting diodes," *Optical and Quantum Electronics,* vol. 42, pp. 89-95, Jan 2010.

31. H. P. Zhao, G. Y. Liu, R. A. Arif, and N. Tansu, "Current injection efficiency induced efficiency-droop in InGaN quantum well light-emitting diodes," *Solid-State Electronics,* vol. 54, pp. 1119-1124, Oct 2010.

32. G.-B. Lin, D. Meyaard, J. Cho, E. F. Schubert, H. Shim, and C. Sone, "Analytic model for the efficiency droop in semiconductors with asymmetric carrier-transport properties based on drift-induced reduction of injection efficiency," *Appl. Phys. Lett.,* vol. 100, p. 161106, 2012.

33. I. E. Titkov, D. A. Sannikov, Y.-M. Park, and J.-K. Son, "Blue light emitting diode internal and injection efficiency," *AIP Advances,* vol. 2, p. 032117, 2012.

34. J. Wang, L. Wang, L. Wang, Z. Hao, Y. Luo, A. Dempewolf, M. Muller, F. Bertram, and J. Christen, "An improved carrier rate model to evaluate internal quantum efficiency and analyze efficiency droop origin of InGaN based light-emitting diodes," *J. Appl. Phys.,* vol. 112, p. 023107, 2012.

35. N. F. Masse, A. R. Adams, and S. J. Sweeney, "Experimental determination of the band gap dependence of Auger recombination in InGaAs/InP multiple quantum well lasers at room temperature," *Appl. Phys. Lett.,* vol. 90, p. 161113, 2007.

36. J. Hader, J. V. Moloney, B. Pasenow, S. W. Koch, M. Sabathil, N. Linder, and S. Lutgen, "On the importance of radiative and Auger losses in GaN-based quantum wells," *Appl. Phys. Lett.,* vol. 92, p. 261103, 2008.

37. E. Kioupakis, P. Rinke, A. Schleife, F. Bechstedt, and C. G. Van de Walle, "Free-carrier absorption in nitrides from first principles," *Physical Review B,* vol. 81, Jun 2 2010.

38. E. Kioupakis, P. Rinke, K. T. Delaney, and C. G. Van de Walle, "Indirect Auger recombination as a cause of efficiency droop in nitride light-emitting diodes," *Appl. Phys. Lett.,* vol. 98, p. 161107, Apr 18 2011.

39. X. F. Ni, Q. Fan, R. Shimada, U. Ozgur, and H. Morkoc, "Reduction of efficiency droop in InGaN light emitting diodes by coupled quantum wells," *Appl. Phys. Lett.,* vol. 93, Oct 27 2008.

40. J. Xie, X. Ni, Q. Fan, R. Shimada, U. Ozgur, and H. Morkoc, "On the efficiency droop in InGaN multiple quantum well blue light emitting diodes and its reduction with p-doped quantum well barriers," *Appl. Phys. Lett.,* vol. 93, p. 121107, 2008.

41. D. S. Meyaard, G.-B. Lin, Q. Shan, J. Cho, E. F. Schubert, H. Shim, M.-H. Kim, and C. Sone, "Asymmetry of carrier transport leading to efficiency droop in GaInN based light-emitting diodes," *Appl. Phys. Lett.,* vol. 99, pp. 251115-3, 2011.

42. A. Efremov, N. Bochkareva, R. Gorbunov, D. Lavrinovich, Y. Rebane, D. Tarkhin, and Y. Shreter, "Effect of the joule heating on the quantum efficiency and choice of thermal conditions for high-power blue InGaN/GaN LEDs," *Semiconductors,* vol. 40, pp. 605-610, 2006.

43. W. W. Chow, M. H. Crawford, J. Y. Tsao, and M. Kneissl, "Internal efficiency of InGaN light-emitting diodes: Beyond a quasiequilibrium model," *Appl. Phys. Lett.,* vol. 97, Sep 20 2010.

44. M. F. Schubert, S. Chhajed, J. K. Kim, E. F. Schubert, D. D. Koleske, M. H. Crawford, S. R. Lee, A. J. Fischer, G. Thaler, and M. A. Banas, "Effect of dislocation density on efficiency droop in GaInN/GaN light-emitting diodes," *Appl. Phys. Lett.,* vol. 91, p. 231114, 2007.

45. S. F. Chichibu, T. Azuhata, M. Sugiyama, T. Kitamura, Y. Ishida, H. Okumura, H. Nakanishi, T. Sota, and T. Mukai, "Optical and structural studies in InGaN quantum well structure laser diodes," *Journal of Vacuum Science & Technology B,* vol. 19, pp. 2177-2183, Nov-Dec 2001.

46. X. Guo and E. F. Schubert, "Current crowding in GaN/InGaN light emitting diodes on insulating substrates," *J. Appl. Phys.,* vol. 90, pp. 4191-4195, Oct 15 2001.

47. V. K. Malyutenko, S. S. Bolgov, and A. D. Podoltsev, "Current crowding effect on the ideality factor and efficiency droop in blue lateral InGaN/GaN light emitting diodes," *Appl. Phys. Lett.,* vol. 97, Dec 20 2010.

48. Y. Y. Kudryk and A. V. Zinovchuk, "Efficiency droop in InGaN/GaN multiple quantum well light-emitting diodes with nonuniform current spreading," *Semiconductor Science and Technology,* vol. 26, Sep 2011.

49. H. Y. Ryu and J. I. Shim, "Effect of current spreading on the efficiency droop of InGaN light-emitting diodes," *Optics Express,* vol. 19, pp. 2886-2894, Feb 14 2011.

50. J. Hader, J. V. Moloney, B. Pasenow, S. W. Koch, M. Sabathil, N. Linder, and S. Lutgen, "On the importance of radiative and Auger losses in GaN-based quantum wells," *Appl. Phys. Lett.,* vol. 92, Jun 30 2008.

51. M. F. Schubert, J. Xu, J. K. Kim, E. F. Schubert, M. H. Kim, S. Yoon, S. M. Lee, C. Sone, T. Sakong, and Y. Park, "Polarization-matched GaInN/AlGaInN multi-quantum-well light-emitting diodes with reduced efficiency droop," *Appl. Phys. Lett.,* vol. 93, Jul 28 2008.

52. J. Y. Chang and Y. K. Kuo, "Influence of polarization-matched AlGaInN barriers in blue InGaN light-emitting diodes," *Optics Letters,* vol. 37, pp. 1574-1576, May 1 2012.

53. H. J. Kim, S. Choi, S. S. Kim, J. H. Ryou, P. D. Yoder, R. D. Dupuis, A. M. Fischer, K. W. Sun, and F. A. Ponce, "Improvement of quantum efficiency by employing active-layer-friendly lattice-matched InAlN electron blocking layer in green light-emitting diodes," *Appl. Phys. Lett.,* vol. 96, Mar 8 2010.

54. S. Choi, H. J. Kim, S. S. Kim, J. Liu, J. Kim, J. H. Ryou, R. D. Dupuis, A. M. Fischer, and F. A. Ponce, "Improvement of peak quantum efficiency and efficiency droop in III-nitride visible light-emitting diodes with an InAlN electron-blocking layer," *Appl. Phys. Lett.,* vol. 96, May 31 2010.

55. Y. K. Kuo, J. Y. Chang, and M. C. Tsai, "Enhancement in hole-injection efficiency of blue InGaN light-emitting diodes from reduced polarization by some specific designs for the electron blocking layer," *Optics Letters,* vol. 35, pp. 3285-3287, Oct 1 2010.

56. Y. K. Kuo, T. H. Wang, J. Y. Chang, and M. C. Tsai, "Advantages of InGaN light-emitting diodes with GaN-InGaN-GaN barriers," *Appl. Phys. Lett.,* vol. 99, Aug 29 2011.

57. J. Y. Chang, M. C. Tsai, and Y. K. Kuo, "Advantages of blue InGaN light-emitting diodes with AlGaN barriers," *Optics Letters,* vol. 35, pp. 1368-1370, May 1 2010.

58. C. H. Wang, S. P. Chang, W. T. Chang, J. C. Li, Y. S. Lu, Z. Y. Li, H. C. Yang, H. C. Kuo, T. C. Lu, and S. C. Wang, "Efficiency droop alleviation in InGaN/GaN light-emitting diodes by graded-thickness multiple quantum wells," *Appl. Phys. Lett.,* vol. 97, Nov 1 2010.

59. C. H. Wang, C. C. Ke, C. Y. Lee, S. P. Chang, W. T. Chang, J. C. Li, Z. Y. Li, H. C. Yang, H. C. Kuo, T. C. Lu, and S. C. Wang, "Hole injection and efficiency droop improvement in

InGaN/GaN light-emitting diodes by band-engineered electron blocking layer," *Appl. Phys. Lett.,* vol. 97, Dec 27 2010.

60. Y. K. Kuo, T. H. Wang, and J. Y. Chang, "Blue InGaN Light-Emitting Diodes With Multiple GaN-InGaN Barriers," *IEEE J. Quantum Electron.,* vol. 48, pp. 946-951, Jul 2012.
61. P. M. Tu, C. Y. Chang, S. C. Huang, C. H. Chiu, J. R. Chang, W. T. Chang, D. S. Wuu, H. W. Zan, C. C. Lin, H. C. Kuo, and C. P. Hsu, "Investigation of efficiency droop for InGaN-based UV light-emitting diodes with InAlGaN barrier," *Appl. Phys. Lett.,* vol. 98, May 23 2011.
62. N. Tansu and L. J. Mawst, "The role of hole leakage in 1300-nm InGaAsN quantum-well lasers," *Appl. Phys. Lett.,* vol. 82, pp. 1500-1502, Mar 2003.
63. N. Tansu, J. Y. Yeh, and L. J. Mawst, "Experimental evidence of carrier leakage in InGaAsN quantum-well lasers," *Appl. Phys. Lett.,* vol. 83, pp. 2112-2114, Sep 15 2003.
64. N. Tansu and L. J. Mawst, "Current injection efficiency of InGaAsN quantum-well lasers," *J. Appl. Phys.,* vol. 97, Mar 1 2005.
65. J. Y. Yeh, L. J. Mawst, and N. Tansu, "The role of carrier transport on the current injection efficiency of InGaAsN quantum-well lasers," *Ieee Photonics Technology Letters,* vol. 17, pp. 1779-1781, Sep 2005.
66. C. Huh, K. S. Lee, E. J. Kang, and S. J. Park, "Improved light-output and electrical performance of InGaN-based, light-emitting diode by microroughening of the p-GaN surface," *J. Appl. Phys.,* vol. 93, pp. 9383-9385, Jun 1 2003.
67. T. Fujii, Y. Gao, R. Sharma, E. L. Hu, S. P. DenBaars, and S. Nakamura, "Increase in the extraction efficiency of GaN-based light-emitting diodes via surface roughening," *Appl. Phys. Lett.,* vol. 84, pp. 855-857, Feb 9 2004.
68. H. W. Huang, J. T. Chu, C. C. Kao, T. H. Hseuh, T. C. Lu, H. C. Kuo, S. C. Wang, and C. C. Yu, "Enhanced light output of an InGaN/GaN light emitting diode with a nano-roughened p-GaN surface," *Nanotechnology,* vol. 16, pp. 1844-1848, Sep 2005.
69. C. F. Lin, Z. H. Yang, J. H. Zheng, and J. H. Dai, "Enhanced light output in nitride-based light-emitting diodes by roughening the mesa sidewall," *Ieee Photonics Technology Letters,* vol. 17, pp. 2038-2040, Oct 2005.
70. [1] O. Ambacher, J. Smart, J. R. Shealy, N. G. Weimann, K. Chu, M. Murphy, W. J. Schaff, L. F. Eastman, R. Dimitrov, L. Wittmer, M. Stutzmann, W. Rieger, and J. Hilsenbeck, "Two-dimensional electron gases induced by spontaneous and piezoelectric polarization charges in N- and Ga-face AlGaN/GaN heterostructures," J. Appl. Phys., vol. 85, pp. 3222-3233, 1999.
71. S. H. Park, D. Ahn, J. Park, and Y. T. Lee, "Optical Properties of Staggered InGaN/InGaN/GaN Quantum-Well Structures with Ga- and N-Faces," Japanese J. Appl. Phys., vol. 50, Jul 2011.
72. F. Akyol, D. N. Nath, S. Krishnamoorthy, P. S. Park, and S. Rajan, "Suppression of electron overflow and efficiency droop in N-polar GaN green light emitting diodes," Appl. Phys. Lett., vol. 100, Mar 12 2012.
73. T. Kim, A. J. Danner, and K. D. Choquette, "Enhancement in external quantum efficiency of blue light-emitting diode by photonic crystal surface grating," *Electronics Letters,* vol. 41, pp. 1138-1139, Sep 29 2005.

74. J. J. Wierer, A. David, and M. M. Megens, "III-nitride photonic-crystal light-emitting diodes with high extraction efficiency," *Nature photonics,* vol. 3, pp. 163-169, Mar 2009.

75. J. K. Kim, S. Chhajed, M. F. Schubert, E. F. Schubert, A. J. Fischer, M. H. Crawford, J. Cho, H. Kim, and C. Sone, "Light-Extraction Enhancement of GaInN Light-Emitting Diodes by Graded-Refractive-Index Indium Tin Oxide Anti-Reflection Contact," *Advanced Materials,* vol. 20, pp. 801-804, 2008.

76. J. Q. Xi, M. F. Schubert, J. K. Kim, E. F. Schubert, M. F. Chen, S. Y. Lin, W. Liu, and J. A. Smart, "Optical thin-film materials with low refractive index for broadband elimination of Fresnel reflection," *Nature photonics,* vol. 1, pp. 176-179, Mar 2007.

77. Y. K. Ee, R. A. Arif, N. Tansu, P. Kumnorkaew, and J. F. Gilchrist, "Enhancement of light extraction efficiency of InGaN quantum wells light emitting diodes using SiO(2)/polystyrene microlens arrays," *Appl. Phys. Lett.,* vol. 91, Nov 26 2007.

78. Y. K. Ee, P. Kumnorkaew, R. A. Arif, H. Tong, H. P. Zhao, J. F. Gilchrist, and N. Tansu, "Optimization of Light Extraction Efficiency of III-Nitride LEDs With Self-Assembled Colloidal-Based Microlenses," *IEEE J. Sel. Top. Quantum Electron.,* vol. 15, pp. 1218-1225, Jul-Aug 2009.

79. Y. K. Ee, P. Kumnorkaew, R. A. Arif, H. Tong, J. F. Gilchrist, and N. Tansu, "Light extraction efficiency enhancement of InGaN quantum wells light-emitting diodes with polydimethylsiloxane concave microstructures," *Optics Express,* vol. 17, pp. 13747-13757, Aug 3 2009.

80. X. H. Li, R. B. Song, Y. K. Ee, P. Kumnorkaew, J. F. Gilchrist, and N. Tansu, "Light Extraction Efficiency and Radiation Patterns of III-Nitride Light-Emitting Diodes With Colloidal Microlens Arrays With Various Aspect Ratios," *IEEE Photonics Journal,* vol. 3, pp. 489-499, Jun 2011.

Chapter 3: Numerical Simulations and Analysis of InGaN QW LEDs with Carrier Transport Effect

The accurate modeling of the InGaN quantum well (QW) light-emitting diodes (LEDs) is an important parameter for understanding and optimizing the device characteristics. The internal quantum efficiency (IQE) for InGaN QW active regions can be simulated primarily by taking into considering the carrier-screening and valence band mixing in the active regions, as previously described in reference 1. However, the accurate simulation of the InGaN QW LEDs under operating bias condition requires further consideration in the drift-diffusion equations for taking into account the carrier transport effect. The use of drift-diffusion equation was included by using the Poisson's equation solver from the APSYS method, and the studies were performed for understanding the contribution of both intrinsic and extrinsic factors leading to efficiency droop in InGaN QW LEDs. The simulation results of conventional InGaN/GaN QW LEDs as an example will be analyzed after the discussion of the physical models and material parameters used in the simulations.

3.1 Introduction to the Numerical Methods – Drift Diffusion Equations

3.1.1 Flow Chart of Simulations

The numerical method developed employs the use of Poisson's equation solver by APSYS [2]. The development of the numerical simulation can be described by the flow chart shown in figure 3-1. The simulation starts by using 2D/3D finite-element method for developing the structures of the LED devices. The structures were presented in the form of mesh with varying dimensions for both the lateral and vertical directions. A representative of the LEDs layers in mesh structures is shown in figure 3-2. The material parameters including doping levels and other band parameters are also defined in the mesh structures in the layer development step. The use of Poisson equation solvers for drift-diffusion equation is included in the second step, where the physics based simulation with realistic parameters was carried out. The key aspect of the second step is the use of drift-diffusion equation for simulating the carrier transport effect, which was not

included in prior simulation works in reference 1. Thus, the simulation tool include the 2D/3D finite element analysis of electrical, optical and thermal properties of compound semiconductor devices, and the emphasis has been placed on band structure engineering and quantum mechanical effects in our studies. The data extraction for the numerical methods focused on the electrical, optical, and structure parameters of the step 2.

It is important to note that the numerical simulation in this study on InGaN QWs LEDs does not only focus on the solutions in the active region, but also take into consideration the carrier transport throughout the LED device structures. The devices are under electrical bias condition with voltage applied on or/and current injected through the ohmic metal contacts during the simulation of device performances. The modified drift-diffusion theory was employed accounting for the carrier transport effect, and the solutions are self-consistently coupled with the ***k·p*** based quantum mechanical solver for the calculation of band structures and spontaneous emission radiative recombination rates.

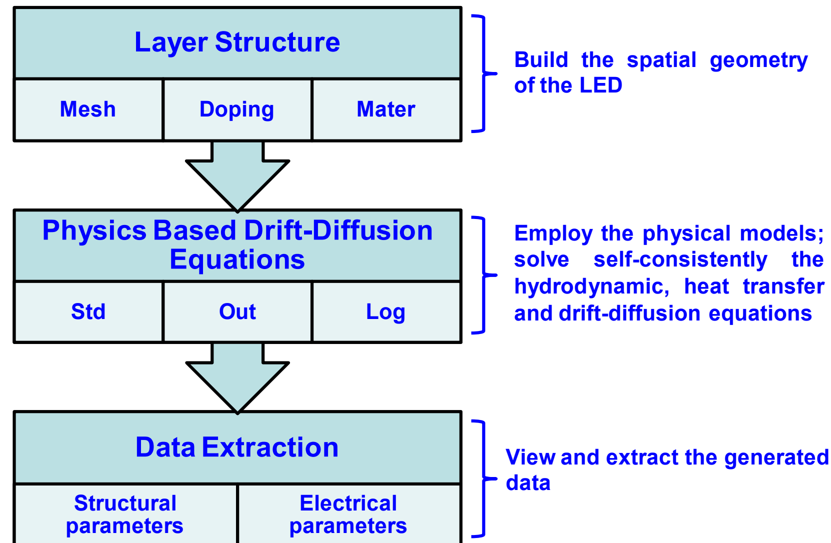

Figure 3-1 *The process flow of numerical simulation*

In the development of the simulations, the following classifications of files were indicated. The three basic classification input files were divided into to the layer definition (step 1, with .layer), physics based drift diffusion equations (step 2, with .sol), and the data extraction file for plotting purpose (step 3, with .plt). The full details of geometric structure and mesh allocation of the

investigated LEDs is defined in the .layer file. The processing the layer file will generate ".geo" file with the direct information of spatial geometry, ".doping" file with the doping information of each layer (p-type, n-type and undoped), and ".mater" file with the material choices and its corresponding material parameters of each layers. The ".mesh" file generated from .geo file contains the meshing information of each layer and each interface by using finite element method. Next, the physical models used in the simulation with various bias and drift-diffusion equations are defined in the ".sol" file. The ".sol" file incorporates the information provided by ".mesh", ".mater" and ".doping" files.

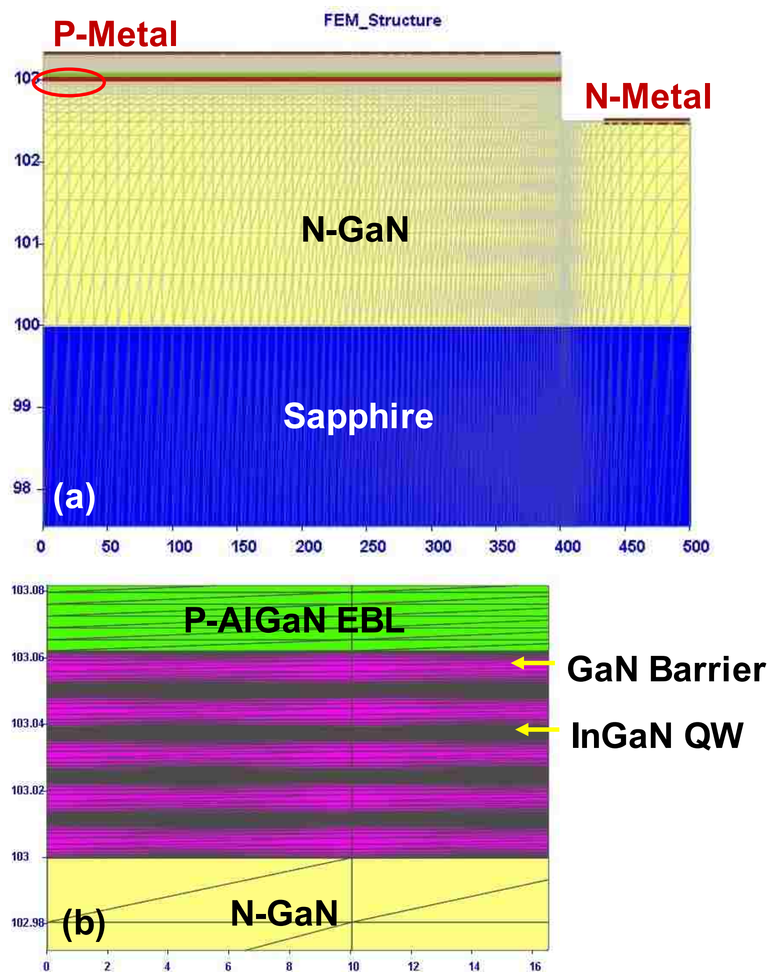

Figure 3-2 *(a) A representative schematic for the 2-D mesh structure for InGaN-based QW LEDs in lateral LED configuration, and (b) the enlarged mesh structures near the active regions of the LEDs.*

After self-consistently solving the hydrodynamic, heat transfer and drift-diffusion equations, three types of output files would be generated including ".std" file and ".out" file, and ".plt" file for

plotting and data extraction. The ".log" file was created for capturing all the simulation data of each iterations. All the structural and electrical properties can be plotted by from the data stored in ".plt" file.

Note that the use of this method will enable the improved simulation of the efficiency-droop issues in InGaN QW LEDs. The 3D mesh distribution is required for simulation of the 'extrinsic' efficiency droop, which depends strongly on the current crowding issue. However, the simulation of the 'intrinsic' efficiency droop in LEDs does not require the 3D mesh structures, instead a 2D mesh method is sufficient. Note that the use of 2D mesh structure reduces the computation time significant without reducing the accuracy for the analysis of the intrinsic efficiency droop in nitride-based LEDs.

3.1.2 Parameters and Equations Used in the Simulation

Band Structures

The energy bandgaps of III-Nitrides cover a wide range from 0.7eV (InN) to 6 eV (AlN) at room temperature. Thus, optical wavelengths of the material family can theoretically range from near-infrared to ultraviolet spectrum regime. Figure 3-3 plots the energy bandgaps of III-nitride alloys as a function of lattice constant with the indication of the lattice-matching condition to GaN. The temperature dependence of energy bandgaps is considered, as described by Varshni's empirical expression [3]

$$E_g(T) = E_g(0K) - \frac{\alpha \cdot T^2}{\beta + T} \qquad (3\text{-}1),$$

where E_g (0K), empirical parameters α and β are shown in the Table 3-1.

Table 3-1 lists the band structure parameters used in the simulation for wurtzite nitride binaries (GaN, AlN, InN) obtained from reference [4] and [5] and Table 3-2 lists important parameters used to calculate the properties of ternaries AlGaN, AlInN or InGaN as well as quaternaries AlInGaN. For the bandgap calculation of ternaries, the bowing formula is employed as follow:

$$E_g(A_xB_{1-x}N) = x \cdot E_g^{AN} + (1-x) \cdot E_g^{BN} - b_bowing \cdot E_g^{AN} \cdot E_g^{BN} \qquad (3\text{-}2),$$

where the bandgap bowing parameter, *b_bowing* can be found in Table 3-2. The bandgap of

quaternaries AlGaInN is calculated as follows [6]:

$$E_g(Al_xGa_zIn_yN)=\frac{E_g(Al_{1-u}In_uN)\cdot x\cdot y+E_g(Al_{xt}Ga_{1-xt}N)\cdot z\cdot x+E_g(In_{yt}Ga_{1-yt}N)\cdot y\cdot z}{z\cdot x+x\cdot y+y\cdot z} \quad \text{(3-3a)}$$

$$u\equiv(1-x+y)/2 \quad \text{(3-3b)}$$

$$xt\equiv(1+x-z)/2 \quad \text{(3-3c)}$$

$$yt\equiv(1+y-z)/2 \quad \text{(3-3d)}$$

$$z=1-x-y \quad \text{(3-3e).}$$

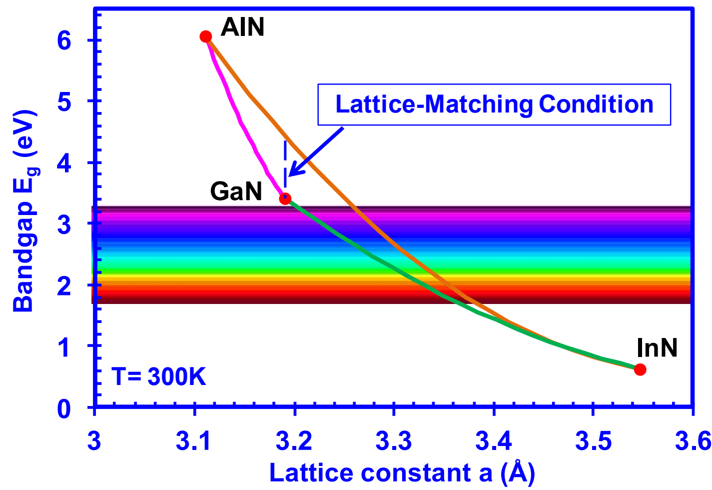

Figure 3-3 *Energy bandgap diagram of III-Nitride alloys*

The conduction band effective masses parallel ($mass_{//}$) or perpendicular to ($mass_{\perp}$) the growth z-direction are used in the parabolic conduction band approximation for wurtzite crystal. For the valence band, 6-band ***kp*** method developed by Chuang et al. [7-9] are utilized with the consideration of valence band coupling, carrier screening and strain effect.

The valence subband can be obtained by solving the eigenvalue equation (3-2) as follow:

$$\sum_{j'=1}^{6} H_{jj'}^{LK}\cdot a_{j'}\left(\vec{k}\right)=E\cdot a_j\left(\vec{k}\right) \quad \text{(3-4).}$$

The Lowding's perturbation method enabled the six-by-six Hamiltonian matrix for the valence bands be blockdiagonalized into the following upper and lower Hamiltonians:

$$H_{6\times6}^{v} = \begin{bmatrix} H_{3\times3}^{U} & 0 \\ 0 & H_{3\times3}^{L} \end{bmatrix} \tag{3-5a}$$

$$H_{3\times3}^{U} = \begin{bmatrix} F & K & -iH_t \\ K_t & G & \Delta - iH_t \\ iH_t & \Delta + iH_t & \lambda \end{bmatrix} \tag{3-5b}$$

$$H_{3\times3}^{L} = \begin{bmatrix} F & K & -iH_t \\ K_t & G & \Delta + iH_t \\ -iH_t & \Delta - iH_t & \lambda \end{bmatrix} \tag{3-5c}.$$

The matrix elements in the above matrix are defined as follows:

$$\begin{aligned}
&F = \Delta_1 + \Delta_2 + \lambda + \theta \\
&G = \Delta_1 - \Delta_2 + \lambda + \theta \\
&\lambda = \lambda_k + \lambda_\varepsilon \\
&\lambda_k = \frac{\hbar^2}{2 \cdot m_0}(A_1 k_z^2 + A_2 k_t^2) \\
&\lambda_\varepsilon = D_1 \varepsilon_{zz} + D_2(\varepsilon_{xx} + \varepsilon_{yy}) \\
&\theta = \theta_k + \theta_\varepsilon \\
&\theta_k = \frac{\hbar^2}{2 \cdot m_0}(A_1 k_z^2 + A_2 k_t^2) \\
&\theta_\varepsilon = D_1 \varepsilon_{zz} + D_2(\varepsilon_{xx} + \varepsilon_{yy}) \\
&K_t = \frac{\hbar^2}{2m_0} A_5 k_t^2 \\
&H_t = \frac{\hbar^2}{2m_0} A_6 k_t k_z \\
&\Delta = \sqrt{2}\Delta_3 \\
&k_t^2 = k_x^2 + k_y^2
\end{aligned} \tag{3-5d}.$$

The corresponding parameters used in Eq. (3-5d) can be found in Table 3-1. Specifically, the strain induced by the lattice mismatch between pseudomorphically grown epilayer and the bulk substrate greatly affects the band structures and thus the optical property of devices. The strain tensor for the epilayer grown on the substrate is calculated as:

$$\varepsilon_{xx} = \varepsilon_{yy} = \frac{a_0 - a}{a} \tag{3-6a}$$

$$\varepsilon_{zz} = -\frac{2 \cdot C_{13}}{C_{33}} \cdot \varepsilon_{xx} \quad (3\text{-}6b)$$

$$\varepsilon_{xy} = \varepsilon_{yz} = \varepsilon_{zx} = 0 \quad (3\text{-}6c),$$

where a_0 and a are lattice constants of the epilayer and GaN substrate, respectively. As shown in figure 3-4(a), when $a_0 > a$, the lattice structure of the the epilayer would endure compressive strain which would potentially lead to cracking in the sample. This phenomenon can usually be observed in AlGaN grown on GaN. On the other hand, as shown in figure 3-4(b), tensile strain would occur in the crystal when $a_0 < a$, which would potentially lead to clustering in the sample. InGaN grown on GaN, for instance, falls into this scenario.

Under the strain, the hydrostatic energy shift, P_{ce}, is introduced in conduction band edge, and the reference valence band edge is calculated as:

$$E_v^0 = E_c - (E_g + \Delta_1 + \Delta_2 + P_{ce}) \quad (3\text{-}7)$$

where $P_{ce} = a_{cz}\varepsilon_{zz} + a_{ct}\varepsilon_{xx} + \varepsilon_{yy}$.

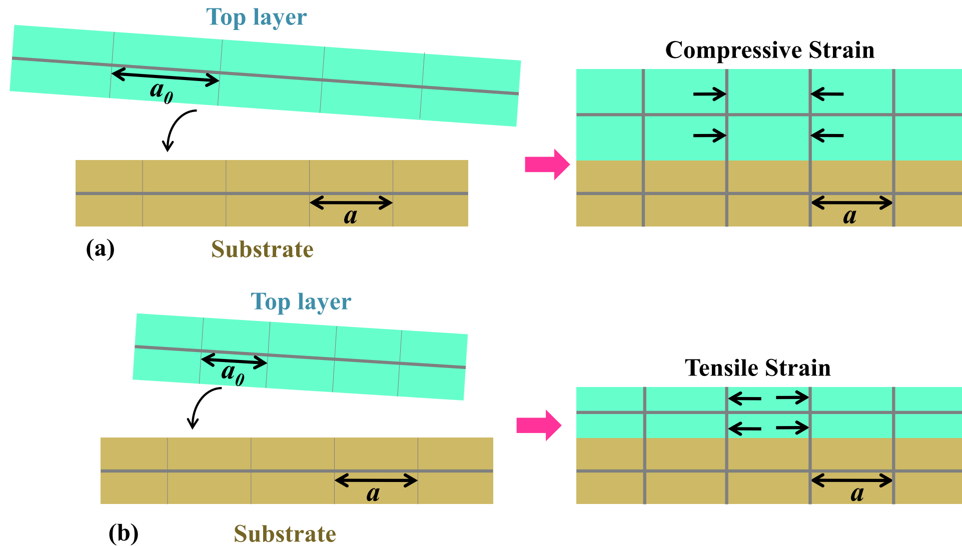

Figure 3-4 *Schematics of (a) compressive strain and (b) tensile strain induced by lattice mismatch between the substrate and the thin film on top.*

The polarization fields consisting of spontaneous and piezoelectric contributions in wurzite III-nitrides along c-plane orientation strongly affect the band structures. The spontaneous polarization field is a material parameter and the values for the binary alloys are listed in Table 3-

1. The bowing formula is employed for the spontaneous polarization for ternaries:

$$P_{sp}(A_xB_{1-x}N) = x \cdot P_{sp}^{AN} + (1-x)\cdot P_{sp}^{BN} - p_bowing \cdot P_{sp}^{AN} \cdot P_{sp}^{BN} \quad \text{(3-7),}$$

where the polarization bowing parameter, *p_bowing* can be found in Table 3-2. The spontaneous polarization of quaternaries AlGaInN is calculated as follows:

$$P_{sp}(Al_xGa_zIn_yN) = \frac{P_{sp}(Al_{1-u}In_uN)\cdot x\cdot y + P_{sp}(Al_{xt}Ga_{1-xt}N)\cdot z\cdot x + P_{sp}(In_{yt}Ga_{1-yt}N)\cdot y\cdot z}{z\cdot x + x\cdot y + y\cdot z} \quad \text{(3-8a)}$$

$$u \equiv (1-x+y)/2 \quad \text{(3-8b)}$$

$$xt \equiv (1+x-z)/2 \quad \text{(3-8c)}$$

$$yt \equiv (1+y-z)/2 \quad \text{(3-8d)}$$

$$z = 1-x-y \quad \text{(3-8e),}$$

where $xt \equiv (1+x-y)/2$ is used.

On the other hand, piezoelectric polarization field is related to the strain in the samples. For InN, the piezoelectric polarization follows:

$$P_{pz}^{InN} = -1.374\cdot\varepsilon_{xx} + 7.559\cdot{\varepsilon_{xx}}^2 \quad \text{(3-7a)}$$

for GaN,

$$P_{pz}^{GaN} = -0.918\cdot\varepsilon_{xx} + 9.541\cdot{\varepsilon_{xx}}^2 \quad \text{(3-7b)}$$

for AlN,

$$P_{pz}^{AlN} = -1.808\cdot\varepsilon_{xx} + 5.624\cdot{\varepsilon_{xx}}^2 \text{ for } \varepsilon_{xx} < 0 \quad \text{(3-7c)}$$

$$P_{pz}^{AlN} = -1.808\cdot\varepsilon_{xx} - 7.888\cdot{\varepsilon_{xx}}^2 \text{ for } \varepsilon_{xx} < 0 \quad \text{(3-7d)}$$

The piezoelectric polarizations for the ternaries and quaternaries are described by linear interpolation as follow:

$$P_{pz}(A_xB_yC_zN) = x\cdot P_{pz}^{AN} + y\cdot P_{pz}^{BN} + z\cdot P_{pz}^{CN} \quad \text{(3-8),}$$

where $z = 1-x-y$.

Radiative, Shockley-Read-Hall and Auger Recombinations

The Fermi's Golden rule is the governing equation to calculate the transition rate from an initial

eigenstate, |*i*> to a final eigenstate |*j*>, and the transition probability. In the quantum well (QW) system, the spontaneous recombination of electron in i^{th} level of conduction band and holes in j^{th} level of valence band is described by Fermi's Golden Rule, and the spontaneous emission rate is simulated using the following expression [10]:

$$r_{sp}^{qw}(E) = \sum_{i=j} (\frac{2\pi}{\hbar}) \cdot \left|H_{ij}\right|^2 \cdot f_j \cdot (1 - f_i) \cdot D(E) \cdot \rho_{ij} \qquad \text{(3-9)},$$

where optical mode density $D(E) = \frac{\bar{n}^3 E^2}{\pi^2 \hbar^3 c^3}$ is used.

The $\left|H_{ij}\right|^2$ is related to the momentum matrix elements M_{ij}:

$$\left|H_{ij}\right|^2 = \left(\frac{q}{m_0}\right)^2 \left(\frac{2\hbar\omega}{4\varepsilon_r \varepsilon_0 \omega^2}\right) \cdot M_{ij}^2 \qquad \text{(3-10)}.$$

The momentum matrix element M_{ij} is calculated by the:

$$\begin{aligned} M_{hh} &= A_{hh} \cdot \langle \phi_i | g_j \rangle \cdot M_b \\ M_{lh} &= A_{lh} \cdot \langle \phi_i | g_j \rangle \cdot M_b \\ M_{ch} &= A_{ch} \cdot \langle \phi_i | g_j \rangle \cdot M_b \end{aligned} \qquad \text{(3-11)},$$

where M_b is the averaging the bulk dipole moment with TE mode (M_b^{TE}) and TM mode (M_b^{TM}) as follows:

$$M_b^{TE} = \frac{m_0}{6} \cdot \left(\frac{1}{m_e^t} - 1\right) \cdot \frac{E_g \cdot \left[\left(E_g + \Delta_1 + \Delta_2\right) \cdot \left(E_g + 2\Delta_2\right)\right] - 2\Delta_3^2}{\left(E_g + \Delta_1 + \Delta_2\right) \cdot \left(E_g + \Delta_2\right) - \Delta_3^2} \qquad \text{(3-12a)}$$

and

$$M_b^{TM} = \frac{m_0}{6} \cdot \left(\frac{1}{m_e^z} - 1\right) \cdot \frac{\left(E_g + \Delta_1 + \Delta_2\right) \cdot \left(E_g + 2\Delta_2\right) - 2\Delta_3^2}{E_g + 2\Delta_2} \qquad \text{(3-12b)}.$$

The linear extrapolation is used to obtain m_e^t and m_e^t for binaries, ternaries and quaternaries. A_m (m=hh, lh, ch) is simplified dipole moment enhancement factors described as follows:

$$A_{hh} = 2/3$$
$$A_{lh} = \frac{3\cos^2(\theta_e)}{2} \qquad \text{for TE mode} \qquad \text{(3-13a)}$$
$$A_{ch} = 0$$

and

$$A_{hh} = 0$$
$$A_{lh} = 3 - 3\cos^2(\theta_e) \qquad \text{for TM mode} \qquad \text{(3-13b),}$$
$$A_{ch} = 3$$

where

$$\cos(\theta_e) \equiv \frac{E_j}{E_j + {m_r}/{m_e}\left(E - E_{ij}\right)} \qquad \text{for } E > E_{ij} \qquad \text{(3-14a)}$$

$$\cos(\theta_e) \equiv 1 \qquad \text{for } E \le E_{ij} \qquad \text{(3-14b),}$$

The E_j is the electron energy in the jth subband of conduction band, and the E_{ij} is the energy difference between holes in i^{th} level of valence band and electron in j^{th} level of conduction band. Spectrum Broadening induced by the intra-band scattering is considered, and Lorentzian shape function is introduced in the calculation of total spontaneous emission spectrum as follows:

$$R_{sp}^{qw} = \frac{1}{\pi}\int r_{sp}^{qw}(E)\frac{\Gamma}{\left(E_{ij} - E\right)^2 + \Gamma^2}dE \qquad \text{(3-15),}$$

where the $\Gamma = \hbar/\tau$ represents the half-width of the broadened energy level. τ is the intra-band scattering relaxation time and E_{ij} is the transition energy from i^{th} conduction band to j^{th} valence band.

In Eq. (3-16), Fermi statistics of carriers in the ith level and j^{th} level is described by f_i and f_j, respectively, as follows:

$$f_i = \frac{1}{1+\exp\left[\frac{E_i - \frac{m_{ij}}{m_i}\left(E - E_{ij}\right) - E_{fp}}{kT}\right]} \tag{3-16a}$$

$$f_j = \frac{1}{1+\exp\left[\frac{E_j - \frac{m_{ij}}{m_j}\left(E - E_{ij}\right) - E_{fn}}{kT}\right]} \tag{3-16b}$$

The m_i and m_j are the relative effective masses of the ith of valence band and the jth level of conduction band, respectively. The reduced effective mass between the ith and the jth level is defined by

$$\frac{1}{m_{ij}} = \frac{1}{m_i} + \frac{1}{m_j} \tag{3-17}$$

Shockley-Read-Hall (SRH) recombination is another recombination mechanism and one

$$R_n^{tj} = \frac{1}{\tau_n}\left(1 - f_{tj}\right)\cdot n - \frac{1}{\tau_n} f_{tj} \cdot n_{1j} \tag{3-18a}$$

$$R_p^{tj} = \frac{1}{\tau_p} f_{tj} \cdot n - \frac{1}{\tau_p}\left(1 - f_{tj}\right)\cdot p_{1j} \tag{3-18b}$$

where the minority carrier lifetime of electron τ_n and hole τ_p are defined in the simulation. The n_{1j} is the electron concentration when the electron quasi-Fermi level coincides with the energy level E_{tj} of the jth trap. A similar definition applies to p_{1j}. The f_{tj} is the trap occupancy under steady state conditions:

$$f_{tj} = \frac{c_{nj} n + c_{pj} p_{1j}}{c_{nj}(n + n_{1j}) + c_{pj}(p + p_{1j})} \tag{3-19}$$

The capture coefficients c_{nj} and c_{pj} for electrons and holes are related to the lifetime of the carrier due the jth recombination center and the trap density N_{tj}.

$$c_{nj} = \frac{1}{\tau_{nj} N_{tj}} \tag{3-20a}$$

$$c_{pj} = \frac{1}{\tau_{pj} N_{tj}} \quad (3\text{-}20b).$$

Lastly, the Auger recombination involving three carriers are calculated using Eq.(3-21)

$$R_{Auger} = \left(C_n n + C_p P\right) \cdot \left(np - n_i^2\right) \quad (3\text{-}21),$$

where the Auger coefficients of C_n and C_p are defined in the simulation.

Carrier Transport -- Drift and Diffusion Model

The electrical properties of the investigated semiconductor devices are governed by the Poisson Equation (Eq. 3-22) which indicates that the divergence of electric displacement field equates to the free carrier density in the volume [10]:

$$-\nabla \cdot \left(\frac{\varepsilon_0 \varepsilon_r}{q} \nabla V \right) = -n + p + N_D \left(1 - f_D\right) - N_A f_A + \sum_j N_{tj} \left(\delta_j - f_{tj}\right) \quad (3\text{-}22).$$

The last three terms in Eq. 3-22 represent the ionized donors, ionized acceptors and the fixed charges such as the surface charges, ionized deep trap or recombination centers. The occupancies f_D and f_A of the shallow impurities are described as follows:

$$f_D = \frac{1}{1 + \frac{1}{g_d} \exp\left[\frac{\left(E_D - E_{fn}\right)}{kT} \right]} \quad \text{for donors} \quad (3\text{-}23a)$$

$$f_A = \frac{1}{1 + g_a \exp\left[\frac{\left(E_A - E_{fp}\right)}{kT} \right]} \quad \text{for acceptors} \quad (3\text{-}23b).$$

The current continuity equations expresses the conservation of local charge:

$$\nabla \cdot J_n - \sum_j R_n^{tj} - R_{sp} - R_{st} - R_{Auger} + G_{opt}(t) = \frac{\partial n}{\partial t} + N_D \frac{\partial f_D}{\partial t} \quad \text{for electrons} \quad (3\text{-}24a)$$

$$\nabla \cdot J_p + \sum_j R_p^{tj} + R_{sp} + R_{st} + R_{Auger} - G_{opt}(t) = -\frac{\partial p}{\partial t} + N_A \frac{\partial f_A}{\partial t} \quad \text{for holes} \quad (3\text{-}24b).$$

The carrier flux density (or the current density divided by the charge of electron q) in Eq. (4-x) is defined as a function of carrier density (n or p), carrier mobility (μ_n or μ_p) and quasi-fermi level (E_{fn} or E_{fp}) as follows:

$$J_n = n\mu_n \nabla E_{fn} \quad (3\text{-}25a)$$

$$J_p = p\mu_p \nabla E_{fp} \quad (3\text{-}25b).$$

Following the hydrodynamic model developed by Azoff [11], the carrier current density can be expressed by:

$$J_n = \mu_n \left\{ -n\nabla[\varphi + \chi + \gamma_n] + \nabla(nkT_e) - \frac{3}{2} nkT_e \nabla \ln(m_e) \right\} \quad (3\text{-}26a)$$

$$J_p = \mu_p \left\{ -p\nabla[\varphi + \chi + \gamma_p] + \nabla(pkT_e) - \frac{3}{2} pkT_e \nabla \ln(m_h) \right\} \quad (3\text{-}26b),$$

where

$$\gamma_n \equiv \frac{N_c F\left[{(E_c - E_{fn})}/{kT_e} \right]}{\exp\left[-{(E_c - E_{fn})}/{kT_e} \right]} \quad (3\text{-}27a),$$

$$\gamma_p \equiv \frac{N_v F\left[{(E_{fp} - E_v)}/{kT_e} \right]}{\exp\left[-{(E_{fp} - E_v)}/{kT_e} \right]}$$

(3-27b),

The χ and φ are electron affinity and electrostatic potential, respectively.

The μ_n and μ_p in Eq. (3-26) represents the carrier mobility for electrons and holes, respectively. The field dependence of mobility is described as follows:

$$\mu_n \equiv \frac{\mu_{0n} + (v_{sn}/F_{0n})(F/F_{0n})^3}{1 + (F/F_{0n})^4} \quad (3\text{-}28),$$

where the F_{0n} is a threshold field beyond which the electron velocity saturates to a constant value of $v_{sn} = \mu_{0n}F_{0n}$. Similar expression also applies to the hole mobility. Besides, carrier mobility has strong dependency on the impurity level due to the impurity scattering. The Caughey-Thomas approximation is employed for the calculation of mobility as a function of impurity density

$$\mu_0(N) = \mu_{\min} + \frac{\mu_{\max} - \mu_{\min}}{1 + \left(\frac{N}{N_{ref}}\right)^{\alpha}} \quad \text{(3-29)},$$

where $N = N_A + N_D + \sum_j N_{tj}$.

In calculating the parameters of ternary compounds AlGaN, InGaN and AlInN, linearly interpolation formula is often used as follows:

$$P(A_x B_{1-x} C) = x \cdot P(AC) + (1-x) \cdot P(BC) \quad \text{(3-30)}.$$

Material Parameters

Parameters	GaN	AlN	InN
Lattice constant (Å)			
a	3.189	3.112	3.545
c	5.185	4.982	5.703
Energy parameters			
E_g (eV) at 0K	3.510	6.10	0.69
α (meV·K^{-1})	0.914	2.63	0.414
β (K)	825	2082	454
Δ_{so} (eV)			
$\Delta_1=\Delta_2=\Delta_3$ (=Δ_{cr}/3) (eV)	0.00567	0.012	0.00167
Conduction-band effective mass			
$mass_{//}$ *at T=300K*	0.21	0.32	0.07
$mass_{\perp}$ *at T=300K*	0.2	0.3	0.07
Valence-band effective mass			
A_1	-7.21	-3.86	-8.21
A_2	-0.44	-0.25	-0.68
A_3	6.68	3.58	7.57
A_4	-3.46	-1.32	5.23
A_5	-3.4	-1.47	-5.11
A_6	-4.9	-1.64	-5.96
Elastic stiffness constants			
C_{11} (GPa)	390	396	223
C_{12} (GPa)	145	137	115
C_{13} (GPa)	106	108	92
C_{33} (GPa)	398	373	224
Spontaneous polarization			
P_{sp} (C/m^2)	-0.034	-0.09	-0.042
Dielectric constants			

ε_r	9.5	8.5	15
Refractive index			
n	2.5067	2.0767	3.4167

Table 3-1 *Material parameters of binaries GaN, AlN and InN for band structure calculations.*

	InGaN	AlGaN	Al(Ga)InN
Band Parameters			
Bandgap bowing *b_bowing* (eV)	1.4	0.8	4.1
Band offset	0.7	0.7	0.7
Polarization bowing *p_bowing* (C/m^2)	-0.037	-0.019	-0.07
Mobility			
μ_{max0_n} ($cm^2/V\cdot s$)	684	306	684
μ_{min0_n} ($cm^2/V\cdot s$)	386	132	386
N_{rn} (cm^{-3})	10^{17}	10^{17}	10^{17}
β_{1n}	1.5	1.5	1.5
α_n	1.37	0.29	1.37
β_{2n}	1	1	1
v_{sn} (m/s)	10^5	$1.12\text{x}10^5$	10^5
μ_{max0_p} ($cm^2/V\cdot s$)	10	10	10
μ_{min0_p} ($cm^2/V\cdot s$)	10	10	10
N_{rp} (cm^{-3})	$2.75\text{x}10^{17}$	$2.75\text{x}10^{17}$	$2.75\text{x}10^{17}$
β_{1p}	1	1	1
α_p	0.395	0.395	0.395
β_{2p}	1	1	1
v_{sp} (m/s)	10^5	10^5	10^5
Thermal Conductivity			
κ (W/(m·K))	10	62	62
Recombination parameters			
τ_n (=1/A_n) (s)	10^{-6}	10^{-6}	10^{-6}
τ_p (=1/A_p) (s)	10^{-6}	10^{-6}	10^{-6}
B (cm^3/s)	$2\text{x}10^{-24}$	$2\text{x}10^{-24}$	10^{-6}
C_n (cm^6/s)	10^{-34}	10^{-34}	10^{-34}
C_p (cm^6/s)	10^{-34}	10^{-34}	10^{-34}

Table 3-2 *Parameters for the calculation of material properties of ternary InGaN, AlGaN and AlInN.*

3.2 Simulation and Related Issues of InGaN/GaN QW LEDs

3.2.1 Current Crowding Effect

In order to confirm the simulation model developed here, we implement the numerical model

for simulating conventional InGaN based QW LEDs. Here, we will investigate the various issues and limitation in InGaN/GaN QW LEDs, which lead to the efficiency droop issue in the current device technology. Figure 3-5 shows the schematics of InGaN/GaN MQW LEDs investigated. The devices were designed to have mesa geometry of 400 μm x 500 μm, and the corresponding coordinate is provided for clarity in the discussion of the structure. For LEDs with lateral configuration [figure 3-5(a)], both p-type and n-type ohmic contacts are placed on the top of the devices, and the light would be extracted out from either the top or the bottom of the devices depending on the transparency of the two ends. The mesa structure includes the four periods of multiple quantum wells (MQWs) region consisted of 3 nm $In_{0.25}Ga_{0.75}N$ QWs surrounded by 10 nm GaN barriers, the upper 50 nm $Al_{0.1}Ga_{0.9}N$ electron blocking layer (EBL) with Mg-doping of $3x10^{17}$ cm^{-3} and the 200 nm p-type GaN with Mg-doping of $1.2x10^{18}$ cm^{-3}. The whole mesa structure is grown on 3 μm n-type GaN template on 100 μm sapphire substrate. The n-type GaN has a doping level of $5x10^{18}$ cm^{-3} and the MQWs region are unintentionally doped with the background concentration of n = $5x10^{16}$ cm^{-3}. The forward bias is applied on the metal contacts and creates the current flowing through the active region.

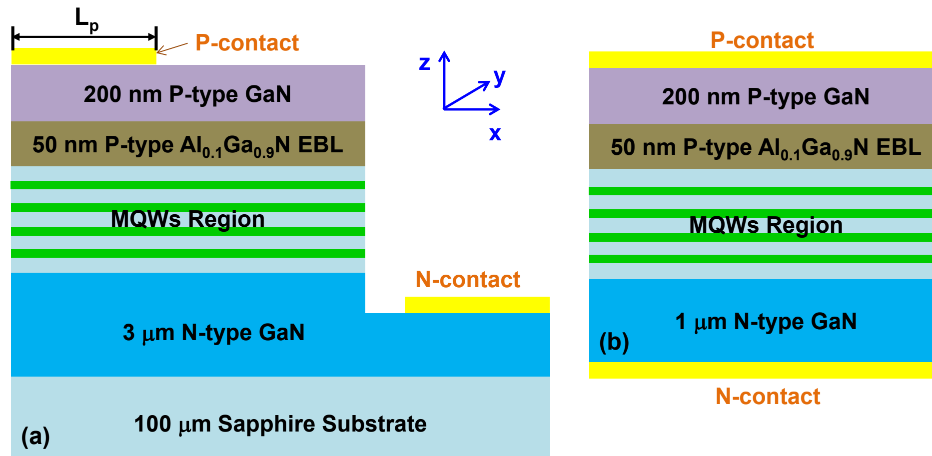

Figure 3-5 *Schematics of InGaN/GaN MQW LED with (a) lateral configuration and (b) vertical configurations.*

In contrast, the LED with vertical injection configuration shown in figure 3-5(b) has the p-type and n-type metal contact deposited on the top and bottom of the devices. One of the ohmic contacts can be transparent so that the light can be escape to free space. The device can be

realized by removing the sapphire substrate and part of the GaN template via laser lift-off or other processes to recycle the template/substrate for cost effective purpose [12, 13]. Besides, the vertical injection configuration would significantly suppress the current crowding effects in InGaN/GaN QW LEDs due to the use of insulating Al_2O_3 and the poor carrier transport in III-nitride materials [14-17].

Figure 3-6 plots the carrier concentration in the last QW region near the p-EBL of the lateral LEDs with different p-contact length (L_p) and of the vertical LED at current density J = 100 A/cm^2 as an illustration of current crowding effect. The total length of p-type GaN is 400 μm and the L_p varied from 100 μm to 400 μm in this study. Both the electron concentration [figure 3-6(a)] and the hole concentrate [figure 3-6(b)] peak at the position of the p-contact edges for all lateral LEDs, indicating the highest recombination rates occurring near the edge of the metal contact. Insufficient carrier concentration elsewhere, especially hole concentration away from p-contact, is observed, even from lateral InGaN LED with L_p = 400 μm. This finding is in good agreement with the literature [16]. This uniformed carrier distribution along the lateral direction of the LED devices will lead to current crowding effect. The radiative recombination rate will be limited to the edge of the p-contact, resulting in nonuniform light distribution from the LEDs. In addition, strong monomolecular recombination and Auger recombination will generate significant heat in a very small area, leading to detrimental effect to the device operation and lifetime. In contrast to lateral LEDs, the vertical LED provide very uniform carrier distribution across the whole device.

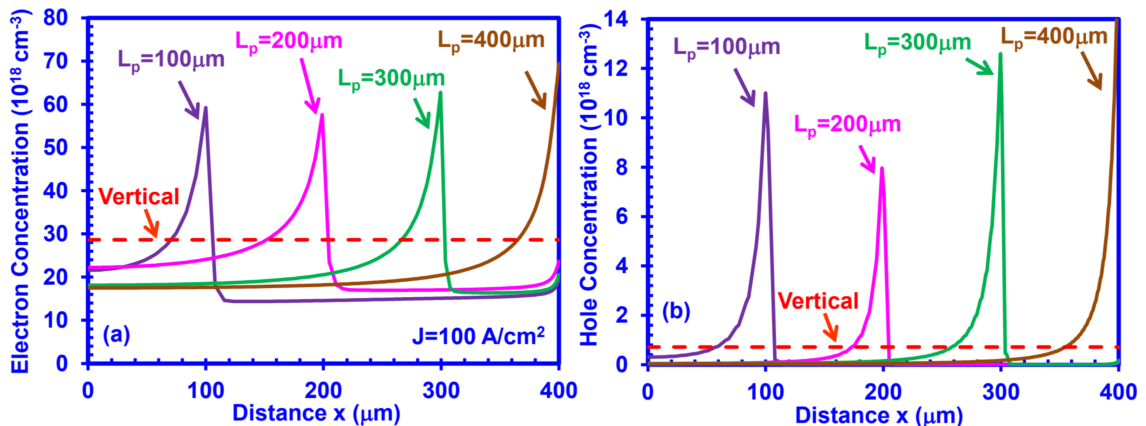

Figure 3-6 *(a) Electron concentration and (b) hole concentration in the last QW active region of the lateral LEDs and the vertical LED at J = 100 A/cm^2 along lateral direction (x-direction). The length of p-contact in lateral LEDs, L_p, varies from 100 μm to 400 μm.*

The lattice temperature will rise as a result of the generation of phonons, i.e. heat. The lattice temperature of three LEDs are compared in figure 3-7 at J = 100 A/cm^2. The lateral InGaN based MQW LED with L_p = 100 μm in figure 3-7(a) exhibits significant unevenness of temperature along the x-direction. The heat generated between p-contact on top of mesa and n-contact on top of exposed n-GaN template are coming from 1) the recombination processes and 2) the Joule heating from increased resistance. The highest lattice temperature inside the device can be as large as 368.9°C. In contrast, the lateral LED with L_p = 400 μm in figure 3-7(b) has the p-contact covering the whole active region and create a much uniform temperature gradient along x-direction. The highest lattice temperature of 305.4°C is near the edge of p-contacts as a result of the Joule heating from the lateral current flow. On the other hand, the temperature distribution of the vertical LED in figure 3-7(c) is very uniform as compared to the lateral LEDs. The slight increase of 0.037°C from operation temperature of 300°C in the p-AlGaN EBL and p-GaN region is due to the relatively low carried mobility and high resistivity of p-type III-nitrides. However, this increase of lattice temperature is very minimal.

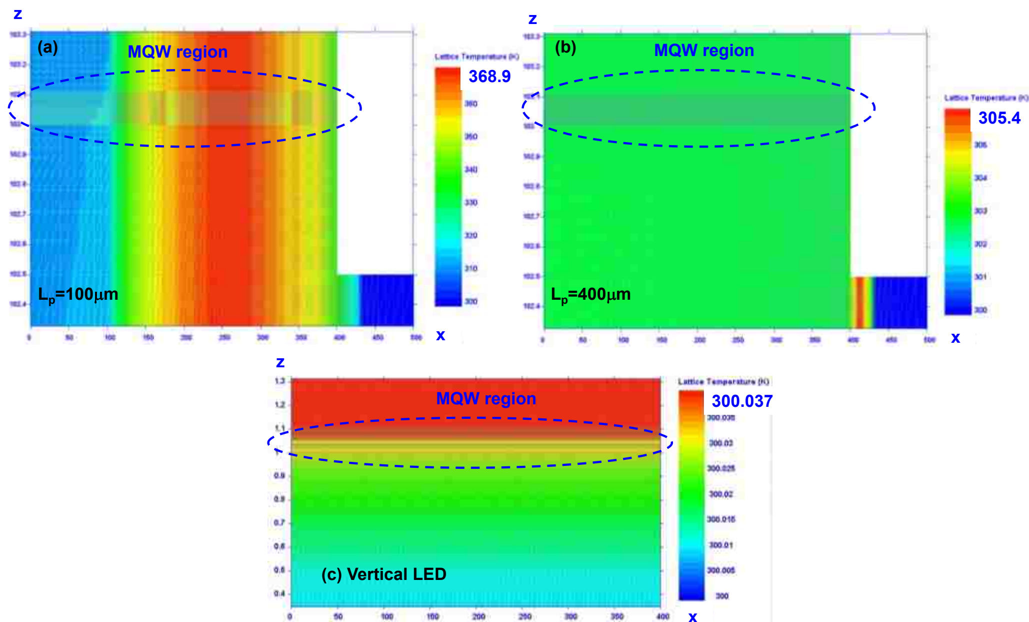

Figure 3-7 *Lattice temperature gradient map of (a) lateral LEDs wth L_p = 100 μm, (b) lateral LEDs wth L_p = 400 μm and (c) vertical LED at J = 100 A/cm^2.*

To further illustrate the effect of decreased resistance with increase L_p, we investigated the I-V characteristics of the four lateral LEDs and the vertical LED as shown in figure 3-8. The increased slop of the I-V curves after the turn-on of diodes indicate the decrease of resistance in the circuit as the length of top p-contact increases. The decreased length from the edge of p-contact to that of n-contact and the reduced heat generation attribute to the reduction of resistance. The best I-V characteristic is obtained from vertical LEDs due to the uniform injection of carriers and no lateral transport of carrier is required. Thus, the LEDs with vertical configuration is better for improved device performance. In order to exclude the effects of the temperature and resistance, we will employ the vertical LEDs in our following device simulations.

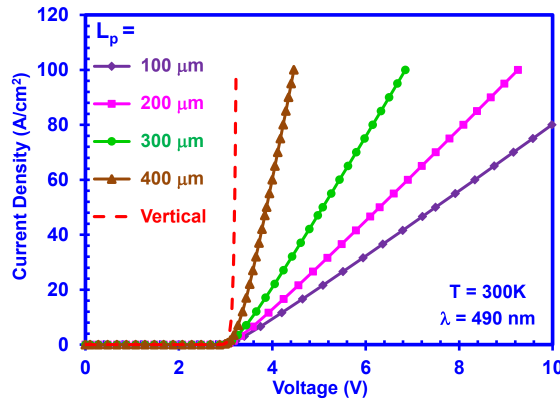

Figure 3-8 *I-V curves of the four lateral LEDs wth different L_p and lateral LEDs.*

3.2.2 Single QW versus Multiple QWs

In this study, we present the investigation on the effect of the number of InGaN/GaN QWs on device performance. The lateral LED configuration shown in figure 3-5(b) is employed in this study. Figure 3-9 plots (a) the conduction band structure and electron concentration and (b) the valence band structure and hole concentration across the n-GaN template, multiple QW (MQW) regions and AlGaN EBL of LED with 4 periods of InGaN QWs surrounded by GaN barriers under bias. The band lineups are tilled due to the strong polarization fields inside III-nitride materials. Here the band offset of 0.7 is used in the study. The electrical bias will first lead to the shifting of quasi-Fermi level for holes in the valence band due to the low mobility of holes. Due to the low mobility of holes. Please note that the electrons are injected from the left hand side and the holes are from the right hand side of the MQW regions. The distribution of both carriers are not uniform

in different QWs, and the carrier concentration peaks in the last QW region. Specifically, the electron concentration and hole concentration in the last QW are 6.3 times and 9.5 times higher than those in the first QW, respectively. Thus, the recombination rate will be dominant in the last QW region. Besides, the density of electrons is higher than that of holes in each QW, indicating the spontaneous emission rate will be limited by the number of available holes.

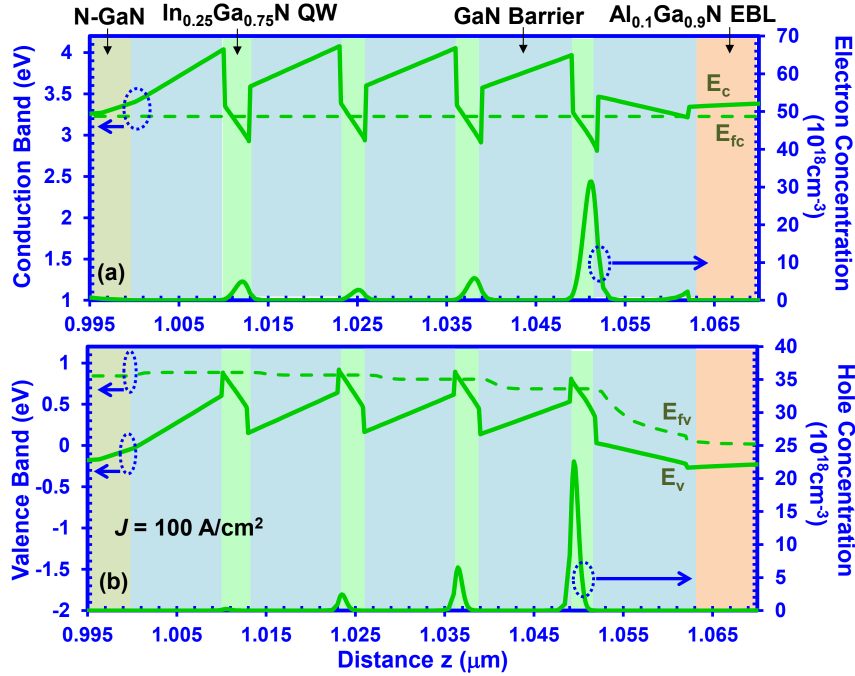

Figure 3-9 *Band lineups and carrier distributions of MQW LED with four periods of 3 nm $In_{0.25}Ga_{0.75}N$ QWs / 10 nm GaN barriers where (a) shows the conduction band structure and electron concentration and (b) shows the valence band structure and hole concentration at J = 100 A/cm²*.

In comparison, the band lineups and carrier concentration of a single QW (SQW) LED are shown in figure 3-10. Every other parameter of this SQW LED is the same with the MQW LED other than the number of QWs. The band lineups, the quasi-Fermi levels and the carrier concentration of SQW LEDs are very similar with that of the last QW of previous MQW LED. This finding indicate the sufficiency of growing single QW as the active region of LED devices.

Figure 3-11 plots the comparison of radiative recombination rate (R_{rad}) between (a) MQW LED and (b) SQW LED with the same emission wavelength of 490 nm under bias. As expected, the R_{rad} for MQW is much higher in the last QW region as compared to that in the other QWs. The peak values of R_{rad} are 0.007×10^{27} $cm^{-3}s^{-1}$, 0.036×10^{27} $cm^{-3}s^{-1}$, 0.203×10^{27} $cm^{-3}s^{-1}$ and 2.993×10^{27}

$cm^{-3}s^{-1}$ in the first, second, third and fourth QW region, respectively. On the other hand, the peak values of R_{rad} in the SQW LED is $3.147x10^{27}$ cm^3s^{-1} which is comparable with that of the last QW in MQW LED. The total radiative recombination rate of MQW LED, however, is slightly higher than that of the SQW LED.

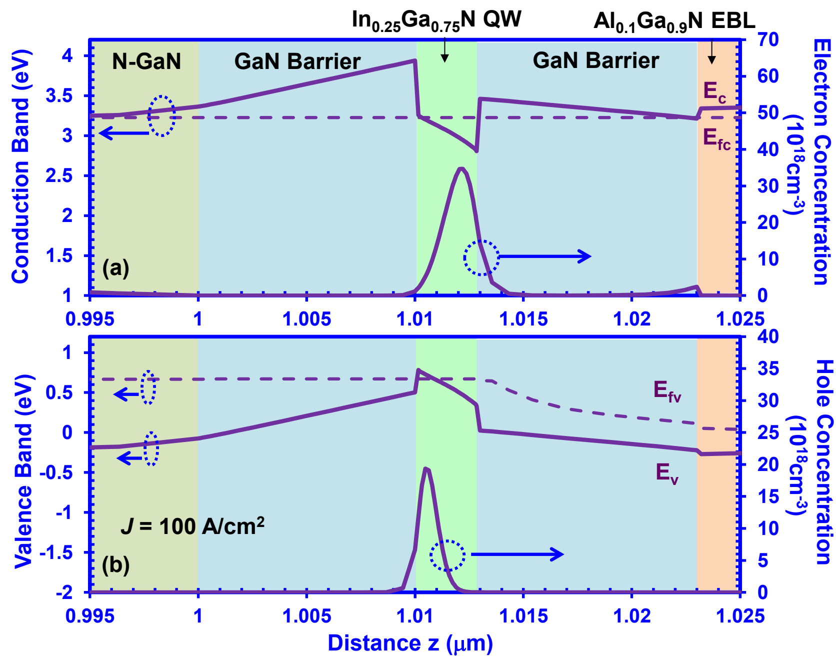

Figure 3-10 *Band lineups and carrier distributions of SQW LED with 3 nm $In_{0.25}Ga_{0.75}N$ single QW surrounded by 10 nm GaN barriers at $J = 100\ A/cm^2$.*

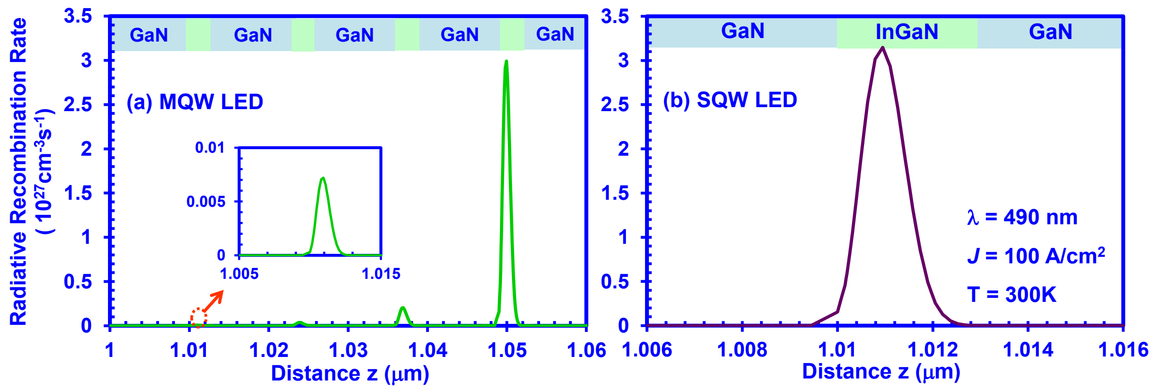

Figure 3-11 *Radiative recombination rates of (a) MQW LED and (b) SQW LED at $J = 100\ A/cm^2$. The emission wavelengths of both QWs are 490 nm*

Lastly, the light output powers of both LEDs are compared and the results are shown in figure 3-12. The light emission are comparable with the two investigated LEDs with a slight higher intensity from MQW LEDs. This is consistent with the previous results. The finding in this study is in good agreement with experimental observations [16]. Thus, the following studies will employ

the SQW as active region of InGaN based LEDs.

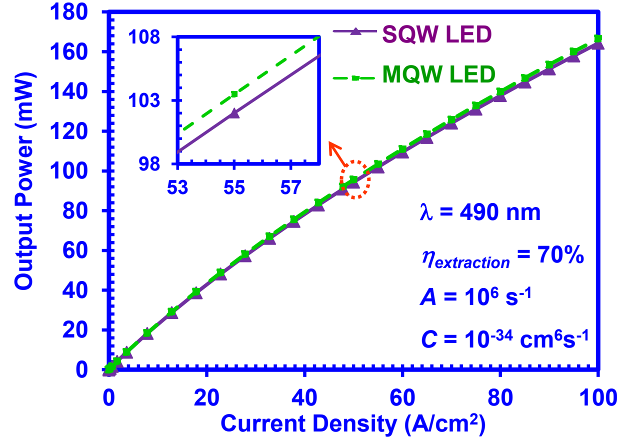

Figure 3-12 *Light output power as a function of current density for both SQW LED and MQW LED with the extraction efficiency of 70%, SRH recombination rate of* $10^6 s^{-1}$ *and Auger recombination rate of* 10^{-34} $cm^6 s^{-1}$.

3.2.3 Efficiency Droop

As discussed in Chapter 2, efficiency droop issue is a great obstacle limiting the development of high power LED for general illumination purpose. Here in this study, several important factors will be examined in influencing the efficiency behavior of conventional InGaN QW LEDs. Figure 3-13 shows the internal quantum efficiency (IQE) of the lateral and vertical LEDs emitting at 490 nm. All of the four LEDs exhibits reduction in IQE as the current density increases, which is referred as efficiency droop phenomenon. The vertical configuration of LEDs can significantly suppress the efficiency reduction as compared to the lateral device, and the active region of MQWs in vertical LED shows very similar efficiency behavior with that of the SQW vertical LEDs. Thus, the employment of vertical configuration is beneficial for enhancing the device performance at high current injection. However, this approach does not maintain high efficiency level to higher current density due to some other intrinsic issues in InGaN QW LEDs.

One of possible issues is Auger recombination. As mentioned earlier, strong Auger recombination in the InGaN LED would lead to increase of nonradiative recombination process. The total current density J is related to the recombination rates as follow:

$$\eta_{inj} \cdot J = J_{qw} = q \cdot d_{QW} \cdot R_{total} = q \cdot d_{QW} \cdot (R_{rad} + R_{nonrad}) \quad \text{(3-31).}$$

With the increasing nonradiative recombination, the radiative recombination process will be suppressed, leading to reduction of efficiency:

$$\eta_{IQE} = \eta_{inj} \cdot \eta_{rad} = \eta_{inj} \cdot \frac{R_{rad}}{(R_{rad} + R_{nonrad})} \quad (3\text{-}32).$$

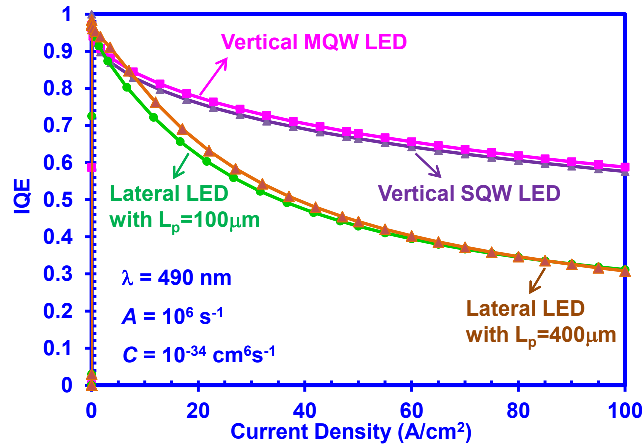

Figure 3-13 *Internal quantum efficiency (IQE) of four investigated LEDs emitting at 490 nm including lateral LEDs with L_p=100 μm and 400 μm, and vertical LEDs with MQW and SQW.*

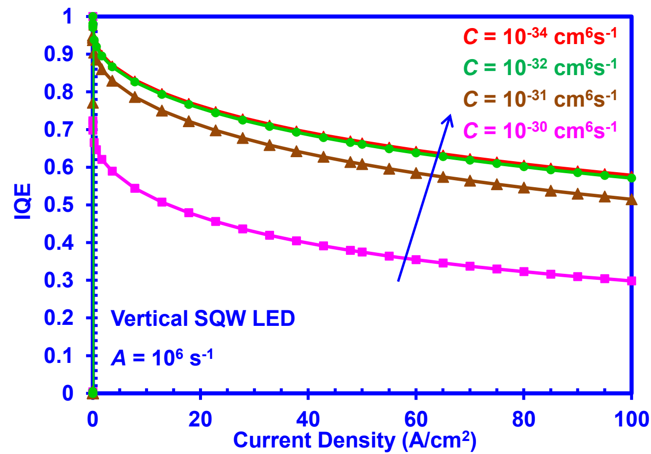

Figure 3-14 *IQE of vertical SQW LEDs emitting at 490 nm as a function of current density for different Auger recombination coefficient C. C varies from 10^{-34} cm^{6}s^{-1}, 10^{-32} cm^{6}s^{-1}, 10^{-31} cm^{6}s^{-1}, and 10^{-30} cm^{6}s^{-1}.*

To illustrate this, figure 3-14 shows the IQE of LEDs with different Auger recombination coefficients C ranging from 10^{-30} cm^{6}s^{-1} down to 10^{-34} cm^{6}s^{-1}. With decreasing Auger recombination, the efficiency of LED can be enhanced significantly at all current density.

However, even when the enhancement saturates with C < 10^{-32} cm^6s^{-1}, the efficiency still exhibits the droop phenomenon as current density increases. In addition, the Auger recombination coefficient of InGaN/GaN materials and heterostructures is still inconclusive now, so the role of Auger recombination is still under intensive investigation.

Another very important factor in efficiency calculation of Eq (3-32) is injection efficiency η_{inj}. The non-unity η_{inj} is the result of carrier leakage [19]. As shown in figure 3-8(a) and figure 3-9(a) where the electron concentrations were plotted for InGaN MQW LED and InGaN SQW LED, one can notice the small peak of electron density near the interface of last GaN barrier and AlGaN EBL. This result corresponds to the escaped electrons from the InGaN QW region to the GaN barrier region, which would lead to a reduction in the current injection efficiency. To suppress this carrier leakage process, novel barrier design to enhance the effective barrier height and carrier confinement is needed. The detailed study will be discussed in Chapter 4.

Reference for Chapter 3

1. H. P. Zhao, R. A. Arif, Y. K. Ee, and N. Tansu, "Self-Consistent Analysis of Strain-Compensated InGaN-AlGaN Quantum Wells for Lasers and Light Emitting Diodes," IEEE J. Quantum Electron., vol. 45(1-2), pp. 66-78, January-February 2009.
2. APSYS by Crosslight Software, Inc., Burnaby, Canada, http://www.crosslight.com
3. Y. P. Varshni, "Temperature Dependence of Energy Gap in Semiconductors," *Physica,* vol. 34, no. 1, pp. 149-&, 1967.
4. I. Vurgaftman and J. R. Meyer, Nitride Semiconductor Devices, J. Piprek, Ed. New York: Wiley, 2007, ch. 2.
5. I. Vurgaftman, and J. R. Meyer, "Band parameters for nitrogen-containing semiconductors," *J. Appl. Phys.,* vol. 94, no. 6, pp. 3675-3696, Sep 15, 2003.
6. I. Vurgaftman, J. R. Meyer, and L. R. Ram-Mohan, "Band parameters for III-V compound semiconductors and their alloys," *J. Appl. Phys.,* vol. 89, no. 11, pp. 5815-5875, Jun 1, 2001.
7. S. L. Chuang, and C. S. Chang, "k·p method for strained wurtzite semiconductors," *Physical Review B,* vol. 54, no. 4, pp. 2491-2504, 1996.
8. S. L. Chuang, and C. S. Chang, "A band-structure model of strained quantum-well wurtzite semiconductors," *Semiconductor Science and Technology,* vol. 12, no. 3, pp. 252-263, Mar, 1997.

9. S. L. Chuang, Physics of Optoelectronics Devices. New York: Wiley, 1995, ch. 4 and 9.
10. J. Singh, Electronics and Optoelectronics Properties of Semiconductor Structures, Cambridge (2003).
11. E. M. Azoff, “Energy transport numerical simulation of graded AlGaAs/GaAs heterojunction bipolar transistors,” *Electron Devices, IEEE Transactions on,* vol. 36, no. 4, pp. 609-616, 1989.
12. W. S. Wong, T. Sands, N. W. Cheung *et al.*, “Fabrication of thin-film InGaN light-emitting diode membranes by laser lift-off,” *Appl. Phys. Lett.,* vol. 75, no. 10, pp. 1360-1362, 1999.
13. S.-J. Wang, K.-M. Uang, S.-L. Chen *et al.*, “Use of patterned laser liftoff process and electroplating nickel layer for the fabrication of vertical-structured GaN-based light-emitting diodes,” *Appl. Phys. Lett.,* vol. 87, no. 1, pp. 011111, 2005.
14. X. Guo, and E. F. Schubert, “Current crowding in GaN/InGaN light emitting diodes on insulating substrates,” *J. Appl. Phys.,* vol. 90, no. 8, pp. 4191-4195, Oct 15, 2001.
15. V. K. Malyutenko, S. S. Bolgov, and A. D. Podoltsev, “Current crowding effect on the ideality factor and efficiency droop in blue lateral InGaN/GaN light emitting diodes,” *Appl. Phys. Lett.,* vol. 97, no. 25, Dec 20, 2010.
16. Y. Y. Kudryk, and A. V. Zinovchuk, “Efficiency droop in InGaN/GaN multiple quantum well light-emitting diodes with nonuniform current spreading,” *Semiconductor Science and Technology,* vol. 26, no. 9, Sep, 2011.
17. H. Y. Ryu, and J. I. Shim, “Effect of current spreading on the efficiency droop of InGaN light-emitting diodes,” *Optics Express,* vol. 19, no. 4, pp. 2886-2894, Feb 14, 2011.
18. A. David, M. J. Grundmann, J. F. Kaeding *et al.*, “Carrier distribution in (0001)InGaN/GaN multiple quantum well light-emitting diodes,” *Appl. Phys. Lett.,* vol. 92, no. 5, pp. 053502, 2008.
19. H. P. Zhao, G. Y. Liu, R. A. Arif *et al.*, “Current injection efficiency induced efficiency-droop in InGaN quantum well light-emitting diodes,” *Solid-State Electronics,* vol. 54, no. 10, pp. 1119-1124, Oct, 2010.

4: Novel Device Designs of InGaN QW LEDs for Efficiency Enhancement

The efficiency droop phenomenon and green gap issue lead to great limitation for the development of solid state lighting as stated in Chapter 2. In this chapter, the novel barrier design with the insertion of thin large bandgap barrier surrounding the InGaN QW for efficiency droop suppression will be discussed. The characteristics of InGaN QW LEDs with lattice-matched AlGaInN thin barriers will be investigated. In addition, the large overlap design of InGaN-delta-InN QW LEDs will be optimized for the IQE enhancement for green, yellow and red light emission.

4.1 Novel Barrier Designs for Efficiencies Droop Suppression

4.1.1 Concept of Efficiencies and Efficiency Droop Issue in InGaN QW LEDs

The external quantum efficiency of the light-emitting devices consists of the internal quantum efficiency (IQE) (η_{IQE}) and light extraction efficiency ($\eta_{Extraction}$), which can be expressed as follow:

$$\eta_{EQE} = \eta_{IQE} \cdot \eta_{Extraction} \qquad (4.1),$$

and the internal quantum efficiency (η_{IQE}) is the product of current injection efficiency ($\eta_{Injection}$) and radiative efficiency (η_{Rad}) as follow:

$$\eta_{IQE} = \eta_{Injection} \cdot \eta_{Radiative} \qquad (4.2).$$

After the current being injected into the device, the electron and holes would recombine in either the barrier region or the quantum well (QW) region. The ratio of injected current that recombined in the QW active region is defined as current injection efficiency ($\eta_{Injection}$), which can be expressed as follow:

$$\eta_{\text{Injection}} = \frac{I_{QW_total}}{I_{total}} = \frac{I_{QW_total}}{I_{QW_total} + I_{Barrier_total}} \qquad (4.3),$$

For analytical model of the current injection efficiency calculation, the formulation for quantum well lasers / LED devices follows the treatment in reference [1] where the current injection efficiency model for GaAs-based laser devices was developed. We extend the treatment of the model for GaN-based LED devices in this work, and the $\eta_{Injection}$ can be calculated as follow:

$$\eta_{\text{Injection}} \equiv \frac{1}{1 + \frac{\tau_{bw}}{\tau_B} \cdot \left(1 + \frac{\tau_{QW_total}}{\tau_e}\right)} \quad (4.4),$$

where τ_{BW} represents the total carrier transport and capture time from the barrier to QW, τ_{QW_total} is total carrier recombination lifetime in the QW region, τ_B is the total carrier recombination lifetime in the barrier regions and τ_e is the carrier thermionic emission escape time from the QW back to the barrier regions.

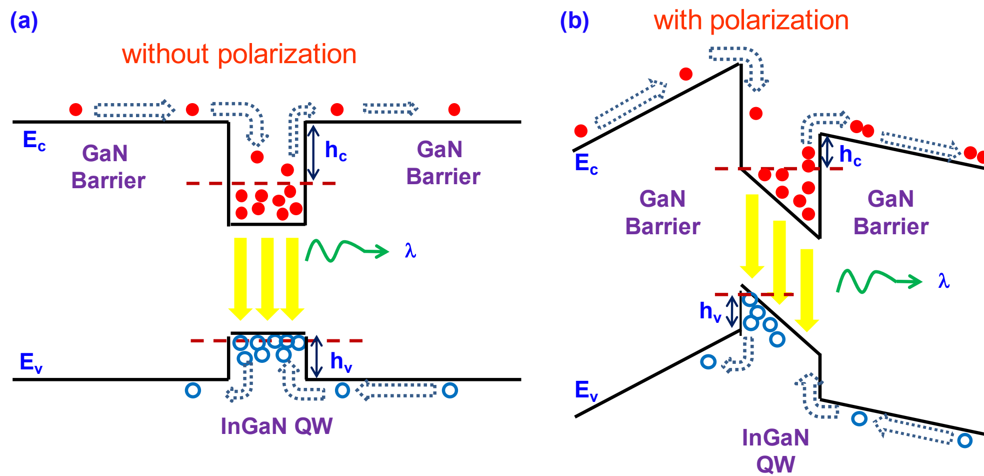

Figure 4-1 *Illustration of band structures and current/carrier flow of (a) nonpolar InGaN/GaN QW and (b) polar InGaN/GaN QW.*

For c-plane InGaN/GaN QW system, severe carrier leakage could attribute to the existence of efficiency droop phenomenon. Figure 4-1 shows the schematics of band structures and the carrier flow of (a) nonpolar InGaN/GaN QW and (b) polar InGaN/GaN QW, respectively. Although large conduction band offset and valence band offset can be achieved for nonpolar InGaN/GaN QW system in figure 4-1(a), the effective barrier heights for carriers in c-plane InGaN/GaN QWs are greatly reduced due to the severe band bending induced by the strong electrostatic field in the III-nitride material in figure 4-1(b). Thus, it is much easier for electrons and holes to escape from the QW region, especially at high carrier density. Furthermore, attributed to the existence of charge separation issue, the operation carrier density in InGaN based QW system are typically 50-100 times higher than that of the InGaAs based QW system. Thus, with the reduced QW size, the carrier leakage issue of InGaN based QW system could be much more severe than those of

the InGaAs based QW system. Note that the internal quantum efficiency (IQE) of InGaN QW LEDs is the product of the injection efficiency and radiative efficiency, where the injection efficiency is defined as the ratio of the current that recombined in the active region over the total injected current. The increasing current leakage would in turn lead to decrease of the injection efficiency and IQE of LEDs.

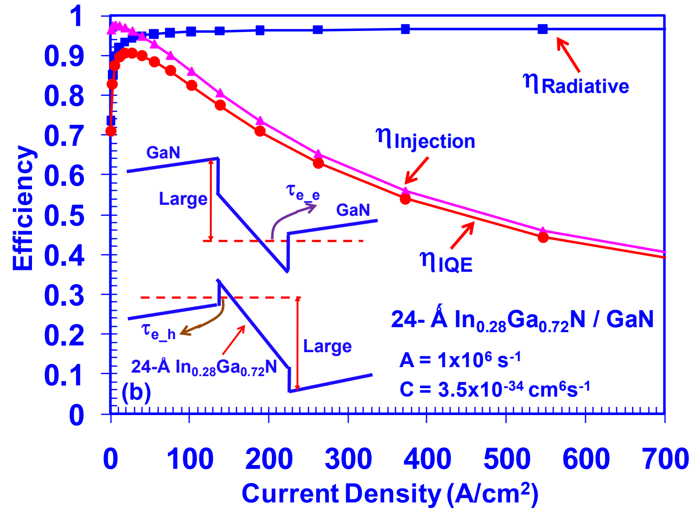

Figure 4-2 *Internal quantum efficiency (IQE) (η_{IQE}), radiative efficiency ($\eta_{Radiative}$) and current injection efficiency ($\eta_{Injection}$) of 24-Å $In_{0.28}Ga_{0.72}N$ QW surrounded by 10-nm GaN barrier (λ = 480 nm) at 300 K as a function of total current density [2].*

To illustrate this phenomenon quantitatively, an example of 24 Å $In_{0.28}Ga_{0.72}N$ QW surrounded by 10 nm GaN barrier is examined for the efficiency behavior using analytical model discussed earlier as shown in figure 4-2 [2]. The efficiencies of this QW system emitting at 480 nm was plotted as a function of current density at 300 K. The monomolecular recombination coefficient *A* of 1×10^{6} s^{-1} and Auger recombination coefficient *C* of 3.5×10^{-34} cm^{6}/s were used in the calculation. As shown in figure 4-2, the radiative efficiency (η_{Rad}) increases monotonically with increasing current density, and keeps relatively close to utility up to the current density in the range of 100-700 A/cm^2. On the other hand, the injection efficiency ($\eta_{Injection}$) decreases significantly with increasing current density due to the increasing current leakage in the QW system. As a result, the IQE of the QWs (η_{IQE}), which is the product of these two efficiencies, reaches its peak at current density around 10-20 A/cm^2 and starts to exhibit the droop phenomenon with further

increasing current density. This efficiency behavior predicted by our analytical model is in good agreement with the experimentally-reported efficiency-droop trends in InGaN QW LEDs [3, 4]. The thermionic carrier escape leads to severe degradation of both $\eta_{Injection}$ and η_{IQE}, which is also indicated by several recent works [5-9].

4.1.2 Analysis of Novel Barrier Design for Droop Suppression

To suppress the efficiency-droop as a result of the quenching of current injection efficiency, the novel barrier design to increase the effected barrier height is required to reduce the thermionic carrier leakage at high current density [2][10, 11]. The use of thin large bandgap material in the barrier region surrounding the InGaN QW region is proposed. Figure 4-3 depicts the band structure schematics of (a) conventional InGaN QW with GaN barrier only and (b) the novel InGaN QW with the insertion of large-bandgap thin barrier surrounding the active region. With the increasing effect barrier heights for electrons (h_c) and holes (h_v) owing to the insertion of the large bandgap thin barrier, the carriers are less likely to escape out of the active region. The large bandgap material could be AlGaN, AlInN, or quaternary AlGaInN. The growth condition of AlGaN alloy with high Al-content is too distinct from those of InGaN and GaN to be incorporated. The AlInN and AlGaInN alloys can be grown lattice matched to GaN, leading to the reduction of lattice strain and material dislocations. Thus, we would focus on the use of low Al-content AlGaN ($Al_{0.1}Ga_{0.9}N$) and lattice matched AlInN with In-content around 17%-18% and AlGaInN as the material candidates for the barrier integration.

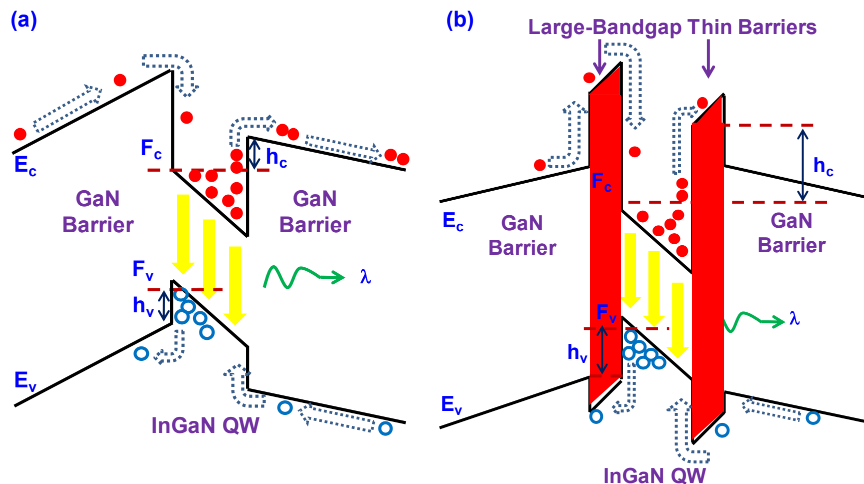

Figure 4-3 *Schematic of (a) conventional c-plane InGaN QW with GaN barrier and (b) InGaN QW structure inserted with large bandgap thin barriers.*

4.2 Characteristics of InGaN QW LEDs with Different Thin Barrier Designs

4.2.1 Analytical Simulations of InGaN QW LEDs with Large-Bandgap Thin Barrier

The analytical model derived from current continuity equation is used in this section for the calculation of injection efficiency, and the band structures are obtained by self-consistent 6 band ***k·p*** method [2]. Figure 4-4 shows the comparison of calculated current injection efficiency ($\eta_{Injection}$) as a function of current density for InGaN QW LEDs with the employment of three different barrier designs. The three novel structures studied here include 1) 24 Å $In_{0.28}Ga_{0.72}N$ QW with 10 nm GaN barriers as reference, 2) 24 Å $In_{0.28}Ga_{0.72}N$ QW with 1.5 nm $Al_{0.1}Ga_{0.9}N$ thin barrier and 10 nm GaN barrier layers, and 3) 24 Å $In_{0.28}Ga_{0.72}N$ QW with 1.5 nm $Al_{0.83}In_{0.17}N$ thin barrier and 10 nm GaN barrier layers. The use of thin $Al_{0.1}Ga_{0.9}N$ leads to the enhancement of injection efficiency as compared to conventional InGaN/GaN QWs due to the suppression of carrier leakage. Specially, the use of $Al_{0.83}In_{0.17}N$ thin barrier layers shows even better improvement in maintaining high injection efficiency level up to very high current density. Note that $Al_{0.83}In_{0.17}N$ is lattice-matched to GaN.

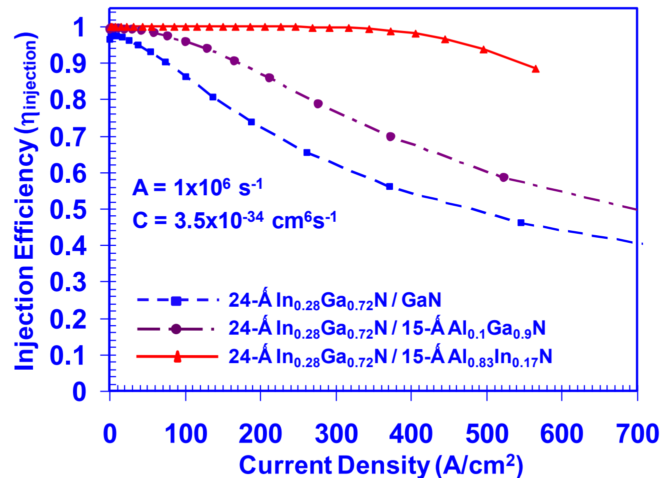

Figure 4-4 *Injection efficiency as a function of total current density for 24 Å $In_{0.28}Ga_{0.72}N$ / GaN QW, 24 Å $In_{0.28}Ga_{0.72}N$ / 15 Å $Al_{0.1}Ga_{0.9}N$ QW and 24 Å $In_{0.28}Ga_{0.72}N$ / 15 Å $Al_{0.83}In_{0.17}N$ QW [2].*

Figure 4-5 shows the comparison of calculated IQE (η_{IQE}) as a function of current density for the InGaN QW LEDs with three barrier design discussed above. The IQE of $In_{0.28}Ga_{0.72}N$ QW with

1.5 nm $Al_{0.1}Ga_{0.9}N$ thin barrier exhibits obvious reduction at J > 100 A/cm^2, while the use of AlInN barrier layer leads to higher IQE and minimum efficiency droop throughout a large current density range up to J > 450 A/cm^2. The analytical simulation results showed that the insertion of large bandgap thin barrier owns the potential of suppression of efficiency droop issue and enhancing the IQE of the devices at high current density. Besides, the use of lattice-matched AlInN thin barrier surround the InGaN QW in nitride LEDs is important for efficiency droop suppression.

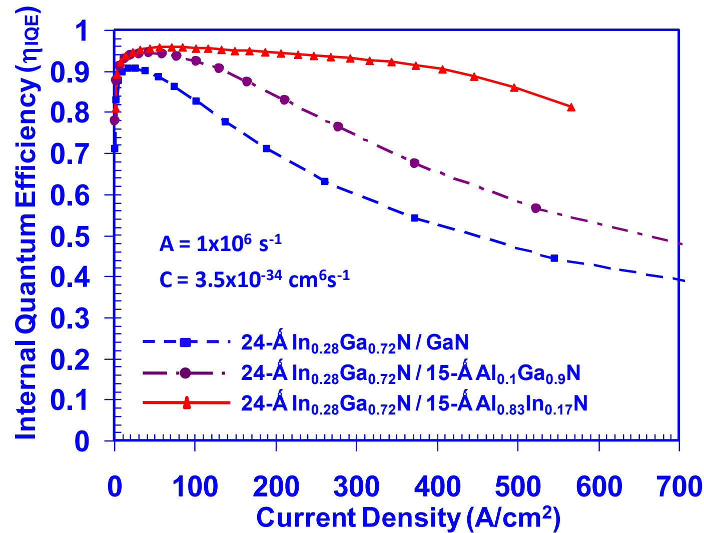

Figure 4-5 *IQE as a function of total current density for 24-Å $In_{0.28}Ga_{0.72}N$ / GaN QW, 24-Å $In_{0.28}Ga_{0.72}N$ / 15-Å $Al_{0.1}Ga_{0.9}N$ QW and 24-Å $In_{0.28}Ga_{0.72}N$ / 15-Å $Al_{0.83}In_{0.17}N$ QW [2].*

4.2.2 Numerical Simulations of InGaN QW LEDs with AlGaInN Thin Barrier

The numerical simulation is also carried out by using APSYS numerical tool [12] in device configurations with the consideration of carrier transport as discussed in Chapter 3 [11]. Figure 4-6 shows the schematics of LED device structures used in the simulation and the material choices for the thin large bandgap barrier layer. The devices were designed to have rectangular geometry of 400 μm x 500 μm with a vertical current injection configuration. The 1 μm thick GaN bulk with n-type doping level of 5x10^{18} cm^{-3} was employed as the template / substrate of the devices. The active region consisted of a 3-nm-thick $In_{0.28}Ga_{0.72}N$ QW sandwiched by AlGaInN thin barrier layers (~ 1 nm) followed by GaN barriers (~ 8 nm) for LED (B), (C), (D) and (E). The InGaN QW with GaN barrier (~ 9 nm) only, denoted as LED (A) was used as a reference. The GaN barriers, AlGaInN thin barriers and InGaN QW layers were unintentionally doped with the background

concentration of n = 5×10^{16} cm^{-3}. The upper 50-nm-thick $Al_{0.1}Ga_{0.9}N$ electron blocking layer (EBL) with Mg-doping of 3×10^{17} cm^{-3} was grown on top of the last GaN barrier, followed by 200-nm-thick p-type GaN with Mg-doping of 1.2×10^{18} cm^{-3} on top of the device. The p-contact and n-contact were deposited on top and at the bottom of the p-GaN and n-GaN layers, respectively. The emission wavelengths of investigated InGaN QW LEDs were designed around 480 nm – 490 nm, and the operation temperature was 300 K.

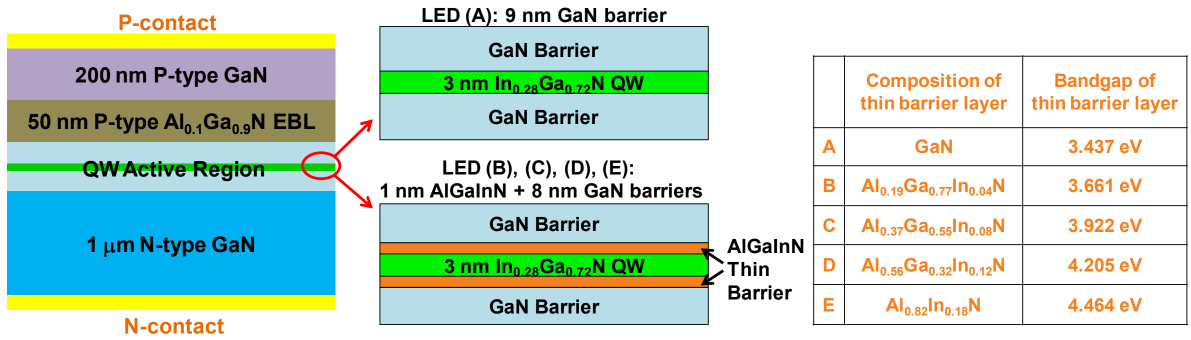

	Composition of thin barrier layer	Bandgap of thin barrier layer
A	GaN	3.437 eV
B	$Al_{0.19}Ga_{0.77}In_{0.04}N$	3.661 eV
C	$Al_{0.37}Ga_{0.55}In_{0.08}N$	3.922 eV
D	$Al_{0.56}Ga_{0.32}In_{0.12}N$	4.205 eV
E	$Al_{0.82}In_{0.18}N$	4.464 eV

***Figure 4-6** Schematics of five investigated InGaN QW LEDs. The inserted table summarizes the material composition and corresponding bandgaps of the thin AlGaInN barrier used in the study.*

The inserted table in figure 4-6 summarizes the compositions of AlGaInN alloys at the lattice-matching condition. The lattice constants of GaN, AlN and InN used in this study are 3.189, 3.112 and 3.545, respectively. The lattice matching condition is determined by the following relation (4-5):

$$a(Al_xGa_{1-x-y}In_yN) = x \cdot a(AlN) + (1-x-y) \cdot a(GaN) + y \cdot a(InN) = a(GaN) \quad (4\text{-}5).$$

Four different compositions of lattice-matched AlGaInN layers were employed with increasing energy bandgap, as presented in LED (B), (C), (D) and (E). The AlGaInN thin barriers included (B) $Al_{0.19}Ga_{0.77}In_{0.04}N$, (C) $Al_{0.37}Ga_{0.55}In_{0.08}N$, (D) $Al_{0.56}Ga_{0.32}In_{0.12}N$ and (E) $Al_{0.82}In_{0.18}N$. In another word, the In-content of thin AlGaInN barrier varied from 0%, 4%, 8%, 12% up to 18%. The bandgap bowing parameters of InGaN / AlGaN / AlInN ternaries of 1.4 eV / 0.8 eV / 4.1 eV were used [21], and the corresponding bandgaps of AlGaInN thin barriers were calculated as 3.661 eV, 3.922 eV, 4.205 eV and 4.464 eV at room temperature for LED (B), (C), (D) and (E), respectively. The increased bandgap was obtained with increasing Al-content in the alloy. Specifically, the

lattice-matched ternary $Al_{0.82}In_{0.18}N$ owns the great potential as the thin barrier material in LED (E) due to the largest bandgap available among the lattice-matching AlGaInN alloys and the integration feasibility with GaN.

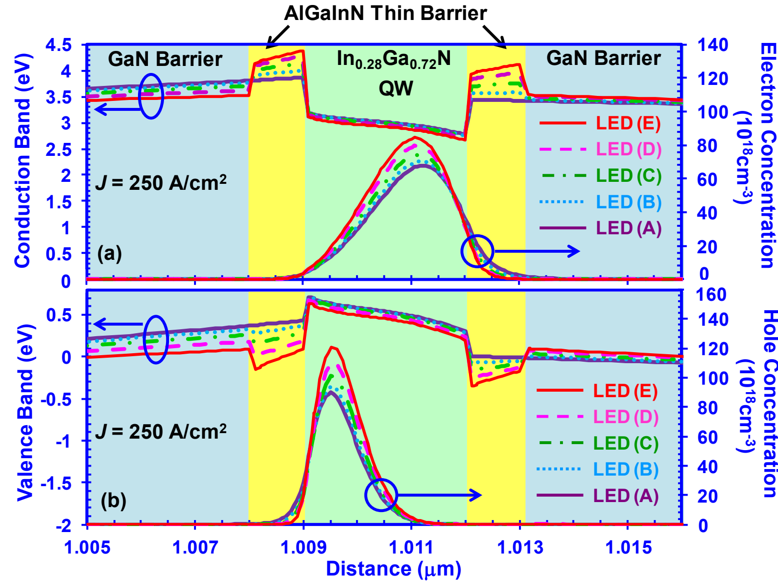

Figure 4-7 *(a) Conduction band structures and electron concentrations and (b) valence band structures and hole concentrations of 3 nm $In_{0.28}Ga_{0.72}N$ QW LEDs with five different barrier designs at J= 250 A/cm^2.*

The characteristics of the four InGaN QW LEDs at high current density (J) of 250 A/cm^2 were analyzed and compared. The screening caused by the defects was taken into account and the surface charge density was assumed to be 50% of the calculated values. The band offset ratio was set as 70%:30% for all layers. Figure 4-7 plots the band structures and carrier distributions in the layers of 3 nm $In_{0.28}Ga_{0.72}N$ QW, 1 nm AlGaInN (or GaN for LED (A)) thin barriers and 8 nm GaN thick barriers at J= 250 A/cm^2. Figure 4-7(a) focuses on the conduction bands and electron concentrations and figure 4-7(b) focuses on the valence bands and hole concentrations. The insertion of large-bandgap thin barriers lead to the increases of effective barrier heights of electrons (h_c) from 164 meV in LED (A) to 698 meV in LED (E), and effective barrier heights of holes (h_v) from 171 meV in LED (A) to 410 meV in LED (E), respectively. Thus, the carrier leakage would potentially be suppressed. With the increasing bandgap of AlGaInN thin barriers from device (A) to (E), the peak electron concentrations were increased from $6.8x10^{19}$ cm^{-3} to $8.4x10^{19}$ cm^{-3} and the peak hole concentrations were increased from $9x10^{19}$ cm^{-3} to $12.1x10^{19}$ cm^{-}

^{3}, respectively. In addition, the distributions of both carriers were observed to be aligned to the center of the quantum well region with the stronger quantum confinement from the use of large bandgap barrier, which would in turn lead to the enhancement of radiative recombination rate.

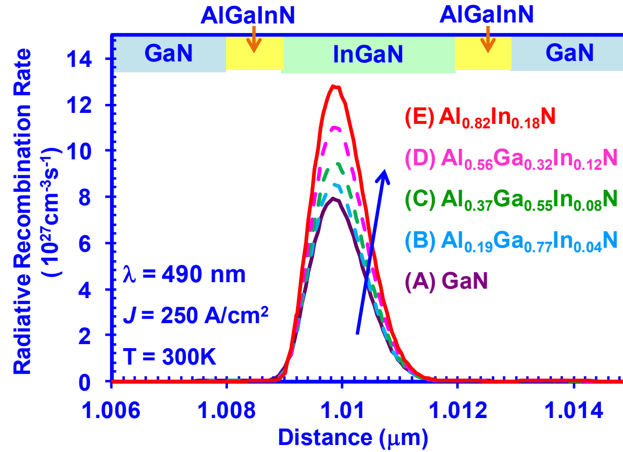

Figure 4-8 *Radiative recombination rates across the active regions of the five LEDs at J= 250 A/cm^2.*

Figure 4-8 shows the radiative recombination rates of the five investigated LED structures across the active regions. As the adjacent thin barrier changes from GaN in LED (A) to $Al_{0.82}In_{0.18}N$ in LED (E), the peak radiative recombination rates inside the InGaN QW were enhanced from 7.9x10^{27} cm^{-3}s^{-1} to 12.8x10^{27} cm^{-3}s^{-1}. The total radiative recombination rates were calculated as 9.2x10^{23} cm^{-2}s^{-1} of LED (A) with GaN barrier only and 14.6x10^{23} cm^{-2}s^{-1} of LED (E) with $Al_{0.82}In_{0.18}N$ thin barrier, which corresponds to an increase of 57.6%. This is attributed to higher carrier concentration and enhanced electron-hole distribution overlap.

Due to the much lighter effective mass of electrons as compared to that of the holes, the carrier leakages were mainly attributed to the electron leakage in nitrides. The thermionic electron carrier leakage from InGaN QWs to the p-type regions were observed to reduce as a result of the insertion of AlGaInN thin barriers. To examine the carrier/current leakage, figure 4-9 shows the comparison of (a) the electron concentration in the last GaN barriers and (b) electron and hole current density of the five LEDs at J = 250 A/cm^2. The peak electron concentrations were 3.9x10^{18} cm^{-3}, 3.4x10^{18} cm^{-3}, 2.4x10^{18} cm^{-3}, 1.3x10^{18} cm^{-3} and 0.4x10^{18} cm^{-3} for LED (A), (B), (C), (D) and (E), respectively. The electron escape from the active region was suppressed as a result of the increased barrier heights of AlGaInN thin barriers, leading to the significantly reduced

electron concentration in the last GaN barrier and AlGaN EBL.

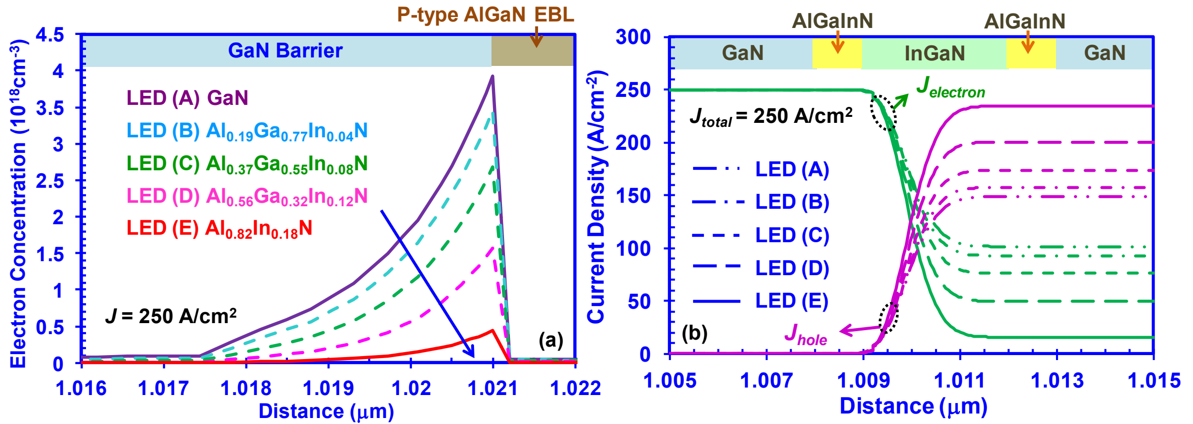

Figure 4-9 *(a) Electron concentrations in last GaN barriers and (b) the electron current densities ($J_{electron}$) and hole current densities (J_{hole}) across the active region of LED (A)-(E) at J = 250 A/cm^2.*

To further illustrate the successful suppression of current leakage by the thin AlGaInN barrier, the electron current densities ($J_{electron}$) and hole current densities (J_{hole}) across the active region at J = 250 A/cm^2 were plotted in figure 4-9(b). Note that the n-contacts were placed at the bottom of the devices (left-hand side in figure 4-9(b)), and the p-contacts were placed on the top of the devices (right-hand side in figure 4-9(b)). The hole currents were almost depleted after being transported through the active region, while the electron currents exhibited large leakage currents after the InGaN QW layers. The electron leakage current densities were 101 A/cm^2 for LED (A) with GaN barrier only, 90 A/cm^2 for LED (B) with $Al_{0.19}Ga_{0.77}In_{0.04}N$ thin barriers, 71 A/cm^2 for LED (C) with $Al_{0.37}Ga_{0.55}In_{0.08}N$ thin barriers, 42 A/cm^2 for LED (D) with $Al_{0.55}Ga_{0.33}In_{0.12}N$ thin barriers and 16 A/cm^2 for LED (E) with $Al_{0.82}In_{0.18}N$ thin barriers. The use of thin large-bandgap AlGaInN alloys in the GaN barrier regions led to reduction of electron leakage current density as high as 84.2% at J = 250 A/cm^2.

The light output power of 3-nm $In_{0.28}Ga_{0.72}N$ QW LEDs with five barrier designs of (A) GaN barriers, (B) $Al_{0.19}Ga_{0.77}In_{0.04}N$ thin barriers, (C) $Al_{0.37}Ga_{0.55}In_{0.08}N$ thin barriers, (D) $Al_{0.55}Ga_{0.33}In_{0.12}N$ thin barriers and (E) $Al_{0.82}In_{0.18}N$ thin barrier as a function of current density were plotted in figure 4-10. In this analysis, the extraction efficiency extraction extraction, monomolecular recombination coefficient A and Auger recombination coefficient C were assumed as 70%, 10^6 s^{-1} and 10^{-34} cm^{6}s^{-1}, respectively. The output power was observed as higher for

InGaN QW LEDs with AlGaInN thin barrier layers, as compared to that of reference sample, for all current density. The highest output power was from InGaN QW with the largest bandgap barrier $Al_{0.82}In_{0.18}N$ alloy. Specifically, the output power was increased from 428mW (A) to 687 mW (E), which corresponds to an increase of 60.3% at J = 250 A/cm^2.

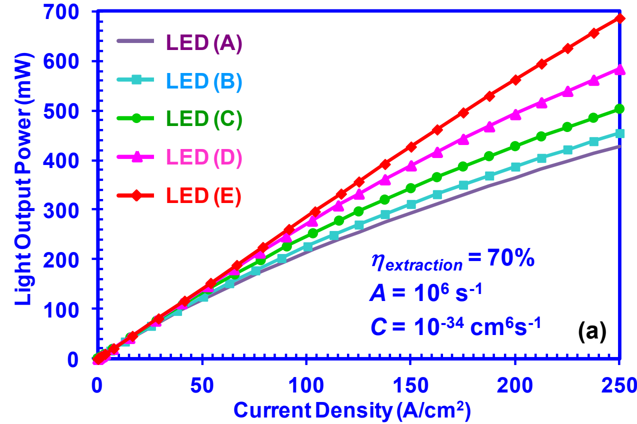

Figure 4-10 *Light output powers and (b) IQE (η_{IQE}) for 3 nm $In_{0.28}Ga_{0.72}N$ QW LEDs with five barrier designs of (A) GaN barriers, (B) $Al_{0.19}Ga_{0.77}In_{0.04}N$ thin barriers, (C) $Al_{0.37}Ga_{0.55}In_{0.08}N$ thin barriers, (D) $Al_{0.56}Ga_{0.32}In_{0.12}N$ thin barriers and (E) $Al_{0.82}In_{0.18}N$ thin barrier as a function of current density.*

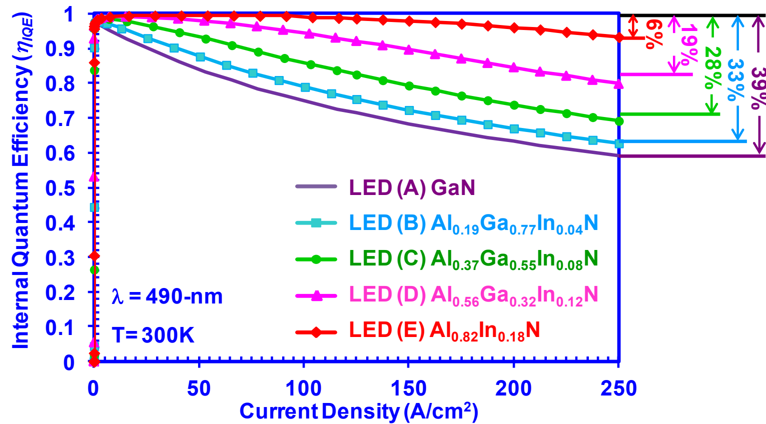

Figure 4-11 *IQE (η_{IQE}) for LED (A)-(E) as a function of current density.*

Figure 4-11 plots internal quantum efficiency (IQE) of the five investigated LED designs. It is obvious that the use of large bandgap AlGaInN thin barrier layers significantly improves the IQE of the devices at all current density. Furthermore, efficiency droop phenomenon was observed from all the five InGaN QW LEDs, but the efficiency of LED (A) with GaN barrier started to reduce at lower current density as compared to the other four LEDs with AlGaInN thin barriers. The IQE

of LED (A), (B), (C), (D) and (E) showed efficiency reduction of 39%, 33%, 26%, 16% and 6% at J = 250 A/cm^2, respectively, which confirms the suitability of this approach in suppressing efficiency droop in nitride LEDs. The InGaN QWs were designed to be the same for the five LEDs, and the radiative efficiency was assumed to be very similar among these four devices. Thus, the enhancement of the IQE can be mainly attributed to the increase of injection efficiency due to the success suppression of carrier leakage. In summary, the use of lattice-matched AlInN thin barrier shows the optimal enhancement in both output power and IQE of LEDs due to the largest bandgap available for lattice-matched AlGaInN alloys, which is consistent with our prediction.

4.2.3 Effect of Lattice-Matched AlInN Thin Barrier Thickness

To investigate the effect of the barrier thickness on the device performance, we further studied the LED (E) with lattice-matched $Al_{0.82}In_{0.18}N$ thin barrier of 1 nm (denoted as 'LED (E1)'), 1.5 nm (denoted as 'LED (E1.5)') and 2 nm (denoted as 'LED (E2)') sandwiched by 8 nm GaN thick barriers. Figure 4-12 plots (a) the conduction bands and electron concentrations and (b) the valence bands and hole concentrations of three InGaN QW LEDs. The band lineups and carrier distributions of LED (E1.5) and LED (E2) were spatially shifted so that the InGaN layers are aligned with that of LED (E1) for better comparison. At J= 250 A/cm^2, the electron concentrations in the InGaN QW layer show minimal improvement with the increased $Al_{0.82}In_{0.18}N$ barrier thickness. On the other hand, the peak hole concentration increase from 1.21x10^{20} cm^{-3} to 1.29x10^{20} cm^{-3} and 1.35x10^{20} cm^{-3} when the $Al_{0.82}In_{0.18}N$ barrier thickness increased from 1 nm to 1.5 nm and 2 nm, respectively. This finding indicates the existence of hole leakages in InGaN QW LEDs which can be further suppressed by slight increase of the thin barrier thickness.

Figure 4-13 shows the electron current densities ($J_{electron}$) and hole current densities (J_{hole}) across the active region of the three InGaN QW LEDs with 1 nm, 1.5 nm and 2 nm AlInN thin barriers at J = 250 A/cm^2. The reference LED (A) with 10 nm GaN barrier was included for comparison purpose. The electron current densities after the active region were about 15.6 A/cm^2, 0.9 A/cm^2, 0.05 A/cm^2 for LED (E1), (E1.5) and (E2), respectively, while that of LED (A) was as high as 107.6 A/cm^2. The results show that the electron leakage current has been substantially suppressed when dAlInN ~ 1.5 nm, and thick layer of large-bandgap barrier is not a

necessity for leakage current suppression.

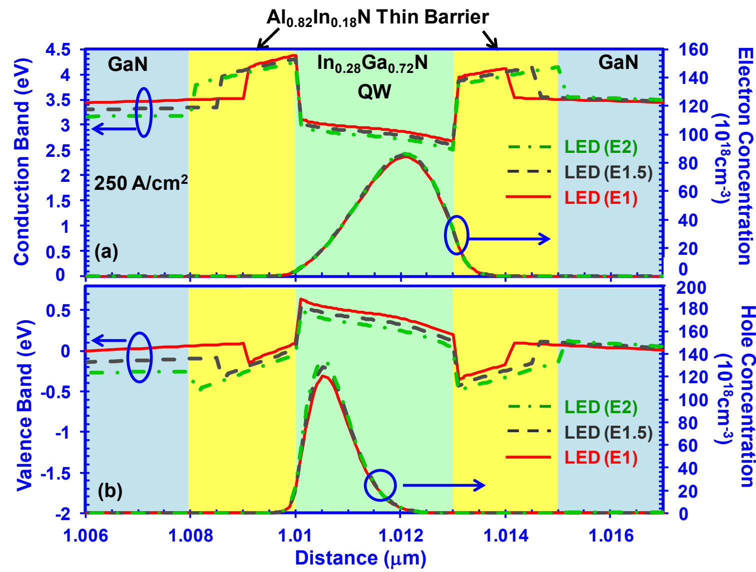

Figure 4-12 *(a) Conduction band structures and electron concentrations and (b) valence band structures and hole concentrations of 3 nm $In_{0.28}Ga_{0.72}N$ QW LEDs with 1 nm (E1), 1.5 nm (E1.5) and 2 nm (E2) $Al_{0.82}In_{0.18}N$ thin barriers at J= 250 A/cm^2.*

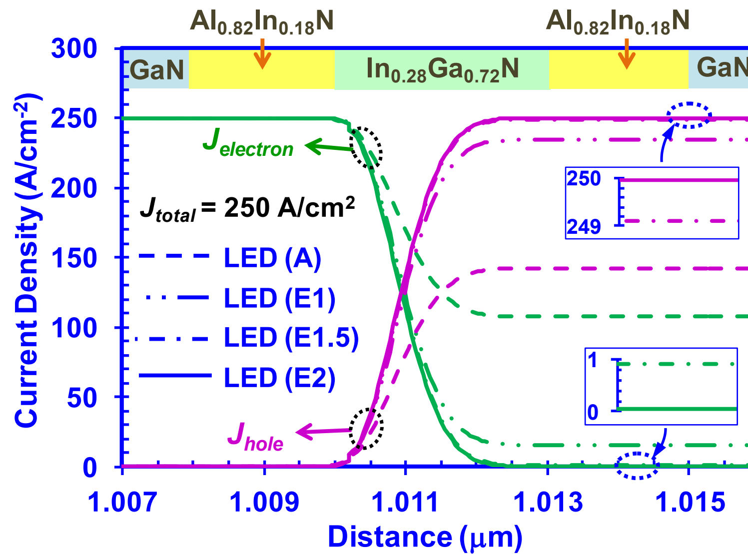

Figure 4-13 *The electron current densities ($J_{electron}$) and hole current densities (J_{hole}) across the active region of LED (A), (E1), (E1.5) and (E2) at J = 250 A/cm^2.*

The light output power and IQE of LED (A), (E1), (E1.5) and (E2) were plotted as a function of current density in figure 4-14(a) and 4-14(b), respectively. We extended the maximum current density form 250 A/cm^2 to 500 A/cm^2 for better understanding of the thickness effect on device performance. As shown in figure 7(a), the light output power was significantly enhanced with the

insertion of $Al_{0.82}In_{0.18}N$ thin barrier with various thicknesses. LED (E2) with 2 nm $Al_{0.82}In_{0.18}N$ thin barrier exhibited the highest output power among these four LEDs at all current density. Specifically, at J = 500 A/cm^2, the light output powers of LED (E1), (E1.5) and (E2) were 1140 mW, 1400 mW and 1481 mW, while that of LED (A) was only 661 mW. Note that the difference between LED (E1.5) with 1.5 nm $Al_{0.82}In_{0.18}N$ thin barrier and LED (E2) with 2-nm $Al_{0.82}In_{0.18}N$ thin barrier was minimal, which is in good agreement with previous findings.

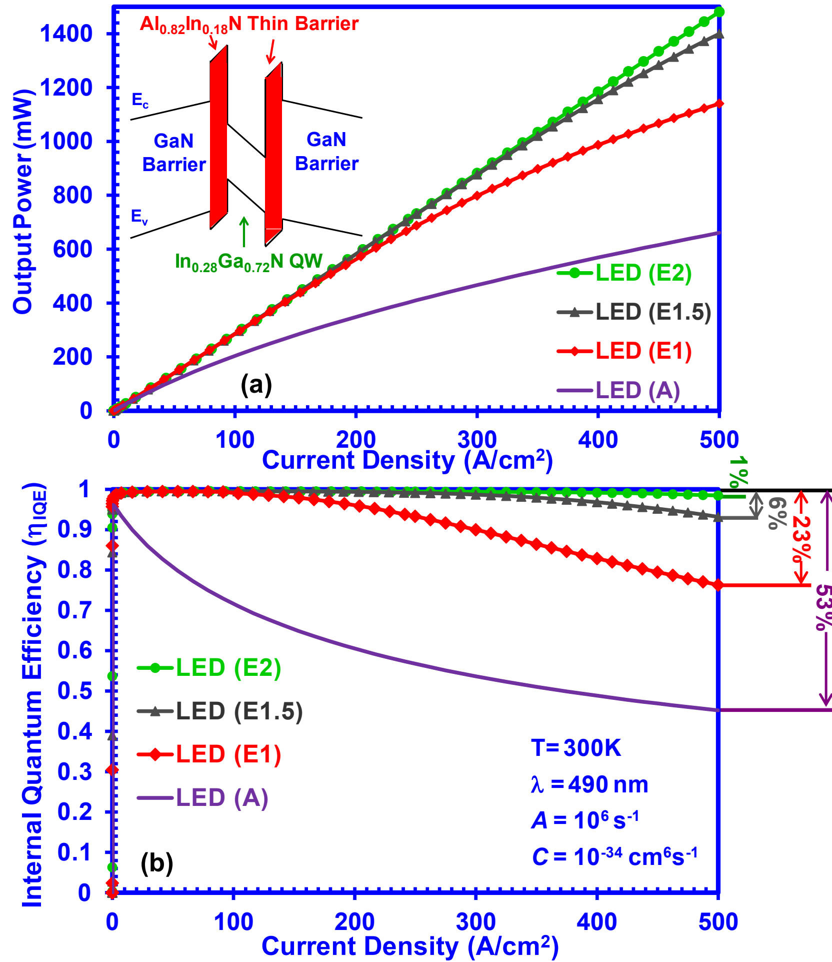

Figure 4-14 *(a) Light output powers and (b) IQE (η_{IQE}) for 3 nm $In_{0.28}Ga_{0.72}N$ QW LEDs with GaN barrier (A), 1 nm (E1), 1.5 nm (E1.5) and 2 nm (E2) $Al_{0.82}In_{0.18}N$ thin barriers as a function of current density. The insertion in (a) shows the schematic of InGaN QW LED with $Al_{0.82}In_{0.18}N$ thin barriers. The maximum current density is extended to 500 A/cm^2.*

The efficiency droop was significantly reduced by the insertion of lattice matched AlInN thin barriers surrounding the InGaN QW from the results of figure 7(b). The reduction of IQEs of LED (A), (E1), (E1.5) and (E2) were 53%, 23%, 6% and 1% at J = 500 A/cm^2, respectively. Both LED

(E1.5) with 1.5 nm $Al_{0.82}In_{0.18}N$ thin barrier and (E2) with 2-nm $Al_{0.82}In_{0.18}N$ thin barrier maintained the high IQE level (IQE > 90%) till very high current density (J > 500 A/cm2), while the conventional InGaN QW with GaN barrier (LED (A)) show droop phenomenon at very low current density (J < 10 A/cm^2). The findings confirmed that the use of a thin layer (< 2 nm) of large-bandgap barrier is sufficient in efficiency droop suppression.

4.2.4 Effect of Lattice-Matched AlInN Thin Barrier Positioning

To study the effect of the thin barrier position, we compared the performance of three types of InGaN QW LEDs with 1 nm $Al_{0.82}In_{0.18}N$ thin barrier at different positions. Figure 4-15 shows the band lineups and the corresponding quasi Fermi levels of LED (E), LED (ER) and LED (EL) at J= 250 A/cm^2. LED (E), as described in the earlier discussion and shown in figure 4-15(a), have lattice-matched $Al_{0.82}In_{0.18}N$ thin barrier on both sides of InGaN QW layer. In addition, LED (ER) in figure 4-15(b) have the $Al_{0.82}In_{0.18}N$ thin barrier on the right hand side of InGaN QW for electron leakage blocking, and LED (EL) in figure 4-15(c) have the $Al_{0.82}In_{0.18}N$ thin barrier on the left hand side of InGaN QW for hole leakage blocking. Note that the electrons were injected from the left hand side near the n-type GaN and the holes were injected from the right hand side near the p-type GaN. The quasi Fermi levels for electrons in conduction bands (F_c) remained stable with the change of $Al_{0.82}In_{0.18}N$ thin barrier position, while the quasi Fermi levels for holes in valence bands (F_v) showed slight increase at the layer of $Al_{0.82}In_{0.18}N$ thin barrier.

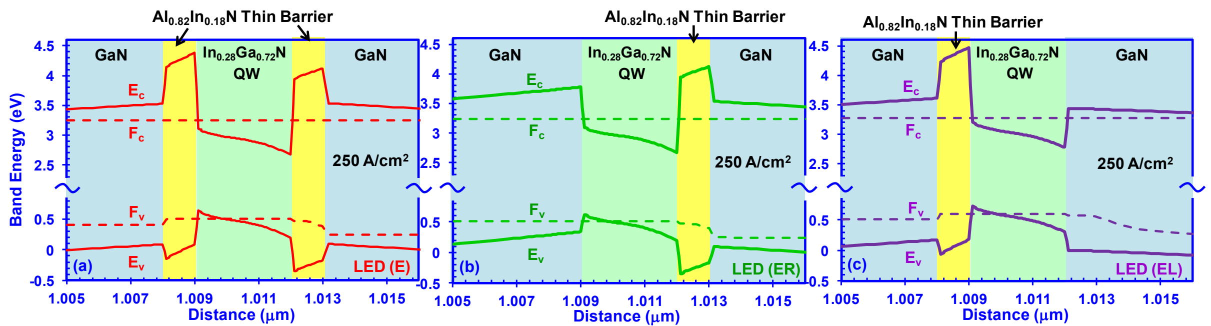

Figure 4-15 *Band Lineups and corresponding quasi Fermi levels of (a) LED (E) with 1 nm $Al_{0.82}In_{0.18}N$ thin barriers on both sides of 3 nm $In_{0.28}Ga_{0.72}N$ QW, (b) LED (ER) with 1 nm $Al_{0.82}In_{0.18}N$ thin barrier on the right-hand side of $In_{0.28}Ga_{0.72}N$ QW and (c) LED (EL) with 1 nm $Al_{0.82}In_{0.18}N$ thin barrier on the left-hand side of $In_{0.28}Ga_{0.72}N$ QW at J= 250 A/cm^2.*

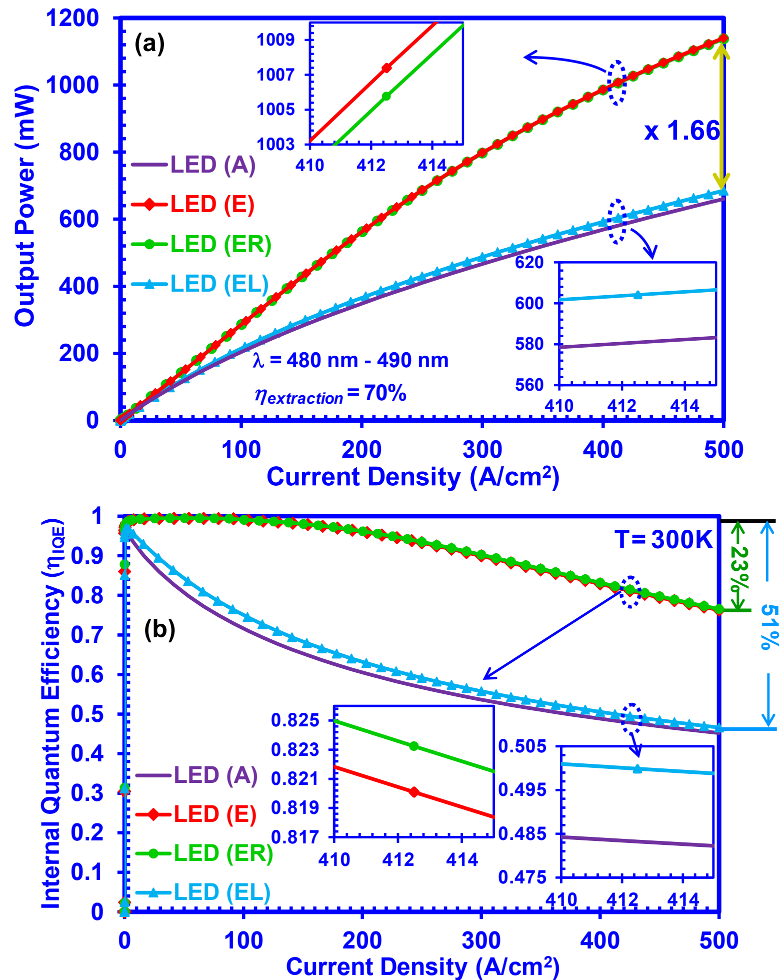

Figure 4-16 *(a) Light output power and (b) IQE (η_{IQE}) of LED (A) with GaN barrier, LED (E) with $Al_{0.82}In_{0.18}N$ thin barriers on both sides, LED (ER) with $Al_{0.82}In_{0.18}N$ thin barriers on the right-hand side and LED (EL) with $Al_{0.82}In_{0.18}N$ thin barriers on the left-hand side of 3 nm $In_{0.28}Ga_{0.72}N$ QW, respectively.*

Figure 4-16(a) and (b) show the light output power and IQE of LED (E), (ER), (EL) and (A) up till J = 500 A/cm^2 at room temperature, respectively. The emission wavelengths were around 480 nm-490 nm for all LED structures. The power and IQW of LED (EL) were similar to these of LED (A), and LED (ER) showed similar performance with LED (E). The inserts show the enlarged curves where the light output power of LED (ER) is slightly lower than that of LED (E) due to the hole leakages. Similarly, the power of light output power of LED (EL) is slightly higher than that of LED (A) due to the hole leakage suppression. The output power of LED (ER) were about 1.66 times higher than that of LED (EL) at J = 500 A/cm^2, which is about 1.72 times higher than that of

the reference LED (A), as shown in figure 4-16(a). In figure 4-16(b), the reduction of IQE at J = 500 A/cm^2 were 23.1%, 23.3%, 50.6% and 53% for LED (E), LED (ER), LED (EL) and LED (A), respectively. The results is in good agreement with the previous finding that the electron leakage is the dominate process of the carrier loss mechanisms which attributes to the existence of efficiency droop phenomenon. In additional to surrounding both sides of the InGaN QW with thin large bandgap barriers, the enhancement of injection efficiency and thus reduction of efficiency droop can also be realized by the insertion of a thin layer of large bandgap barrier on the path of electron leakage near the p-GaN side. The finding of this position study indicates the importance of electron leakage suppression in enhancing the efficiency of InGaN QW LEDs at high current, and it provides an alternative device structure for easier experimental implementation.

The simulation in this work was carried out using numerical method with the coupling of carrier transport and carrier recombination processes in all layers. From the simulation with the consideration of polarization field of III-nitrides, carrier screening effect and carrier transport, the InGaN QW LEDs with lattice-matched AlGaInN thin barriers exhibited better carrier confined, higher carrier concentration and larger radiative recombination rates in the active region with a decreased carrier leakage current outside the active region as compared to conventional InGaN QW LEDs with GaN barrier only, Thus, the light output power as well as the quantum efficiency was enhanced for all the LEDs with AlGaInN thin barriers at all current density, and the highest power with least efficiency droop was obtained from LED with the employment of lattice-matched ternary $Al_{0.82}In_{0.18}N$ thin barrier. The barrier thickness study indicates the sufficiency of thin barrier (~1-2 nm) in suppressing the carrier escape and thus efficiency droop. The barrier position study points out the importance of electron leakage in device performances and provides possible practical solutions for the efficiency droop suppression in high-power nitride LEDs.

4.3 Novel QW Designs of InGaN-Delta-InN QW LEDs for Green, Yellow and Red Emission

Previously, the use of InGaN-delta-InN QWs structures with emission wavelength in the yellow

and red spectral regimes were proposed and investigated using self-consistent 6 band $\boldsymbol{k \cdot p}$ methods [13]. In this section, the characteristics of InGaN QW with the insertion of several monolayers of InN as the active region of LEDs will be studied using numerical simulations with the hybrid operation of voltage bias at low current density and current bias at high current density. The carrier transport effect is taken into consideration in the device simulation with the device area of 400 μm x 500 μm. The $\boldsymbol{k \cdot p}$ based quantum mechanical solver is employed for quantum well solution, which is self-consistently coupled with the modified drift-diffusion theory for carrier transport.

4.3.1 InGaN-Delta-InN QW LEDs with Different InN Thickness

Figure 4-17 shows the calculated band lineups and wavefunctions of (a) conventional 30 Å $In_{0.25}Ga_{0.75}N$ QW LED as reference, (b) 15 Å $In_{0.25}Ga_{0.75}N$ / 3 Å InN / 15 Å $In_{0.25}Ga_{0.75}N$ QW LED and (c) 15 Å $In_{0.25}Ga_{0.75}N$ / 6 Å InN / 15 Å $In_{0.25}Ga_{0.75}N$ QW LED. As shown in the band structures, the insertion of delta-InN layer leads to the increase of quasi-Fermi levels for holes in the valence band, which in turn results in the extension of interband transition wavelengths. In addition, the shift of electron and hole wavefunctions towards the position of delta-InN layer is also observed. The wavefunction overlaps for InGaN QW with 3 Å InN and 6 Å InN are increased to 66.7% and 53.6%, respectively, while that of the CV InGaN QW is only 41.2%. As a result, the charge separation issue will be suppressed due to the introduction of the energy local minima by delta-InN layer.

The shift of electron and hole wavefunction by the introduction of delta-InN layer leads to the different carrier concentrations among the three QW LED designs. Figure 4-18 illustrates the carrier distribution across the barrier and QW regions at J = 100 A/cm^2. For electrons in the conduction band [figure 4-18(a)], the peak electron concentrations have increased from 4.06×10^{19} cm^{-3} for CV InGaN QW to 4.85×10^{19} cm^{-3} for InGaN QW with 3 Å delta-InN and 7.03×10^{19} cm^{-3} for InGaN QW with 6 Å delta-InN, respectively. Besides, the insertion of delta-InN layer leads to the shift of electron distribution towards the center of QW region, and thicker delta-InN layer results in stronger shift. It is more obvious in hole distribution [figure 4-18(b)] where the peak of hole concentration for CV InGaN QW is observed at the left hand side of the active

region, while that for InGaN QW with 6 Å delta-InN shifts the right hand side of the active region. The alignment of electron and hole distributions shows the suppression of the charge separation issue, leading to the enhancement of spontaneous emission rate.

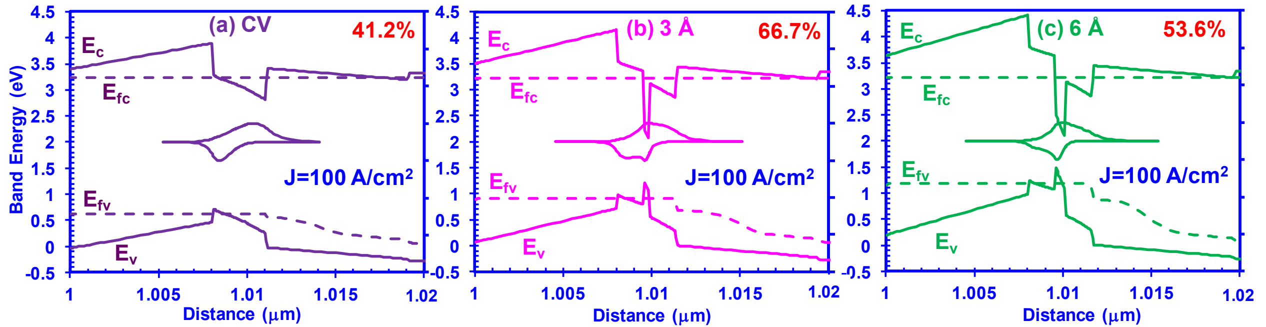

Figure 4-17 *Band lineups and corresponding wavefunctions of (a) conventional (CV) 30 Å $In_{0.25}Ga_{0.75}N$ QW LED, (b) 15 Å $In_{0.25}Ga_{0.75}N$ / 3 Å InN / 15 Å $In_{0.25}Ga_{0.75}N$ QW LED and (c) 15 Å $In_{0.25}Ga_{0.75}N$ / 6 Å InN / 15 Å $In_{0.25}Ga_{0.75}N$ QW LED at J = 100 A/cm^2.*

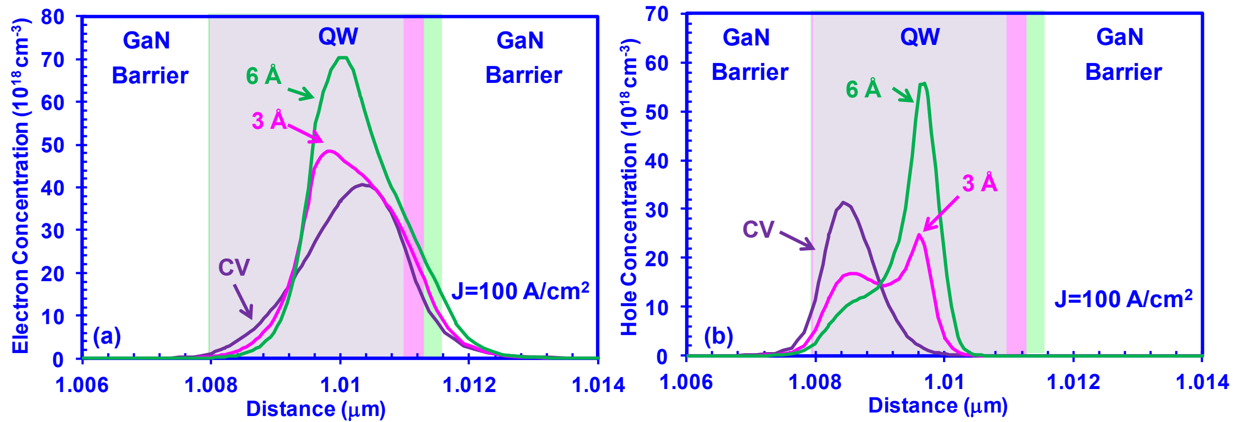

Figure 4-18 *(a) Electron concentration in conduction band and (b) hole concentration in valence band for CV InGaN QW LED, InGaN QW LED with 3 Å delta-InN layer and InGaN QW LED with 6 Å delta-InN layer at J = 100 A/cm^2.*

The spontaneous emission rates of the three LEDs at J= 50 A/cm^2 and 100 A/cm^2 were plotted in figure 4-19. The emission wavelengths for CV InGaN QW LED, InGaN QW LED with 3 Å delta-InN layer and InGaN QW LED with 6 Å delta-InN layer at J = 50 A/cm^2 are around 486 nm, 552 nm and 660 nm, respectively. The significant redshift in emission wavelength is achieved without any decrease in the radiative recombination rate. This is in contrast to the conventional approach where the extension of emission wavelength is always accompanied by the reduction of radiative recombination rates. The highest peak intensity is obtained from the QWs with larger electron-

hole wavefunction overlap, i.e. InGaN QW with 3 Å delta-InN layer. In addition, larger full width at half maximum (FWHM) of the emission spectrum is observed from the InGaN-delta-InN QW LEDs as compared to the conventional InGaN QW LEDs. It could be the result of spectrum broadening from the use of wider QW. In addition, larger full width at half maximum (FWHM) of the emission spectrum is observed from the InGaN-delta-InN QW LEDs as compared to the conventional InGaN QW LEDs. It could be the result of wider total QW thickness and carrier population of the excited states.

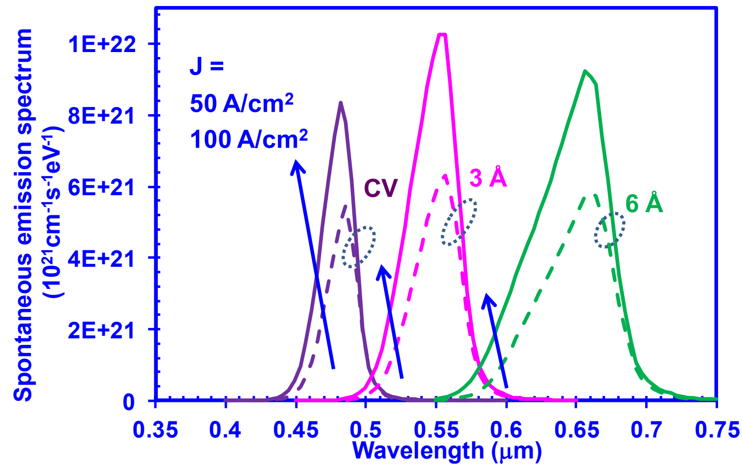

Figure 4-19 *Spontaneous emission spectrum of CV InGaN QW LED, InGaN QW LED with 3 Å delta-InN layer and InGaN QW LED with 6 Å delta-InN layer at J = 50 A/cm^2 and 100 A/cm^2.*

4.3.2 InGaN-Delta-InN QW LEDs with Different InN Positioning

The positioning of delta-InN layer inside the 30 Å $In_{0.25}Ga_{0.75}N$ QWs is also being investigated on the example of InGaN-delta-InN QW LEDs with delta-InN layer. Three QW designs in this study include a) 10 Å $In_{0.25}Ga_{0.75}N$ / 6 Å InN / 20 Å $In_{0.25}Ga_{0.75}N$ (denoted as LED N), (b) 15 Å $In_{0.25}Ga_{0.75}N$ / 6 Å InN / 15 Å $In_{0.25}Ga_{0.75}N$ (denoted as LED C) and (c) 20 Å $In_{0.25}Ga_{0.75}N$ / 6 Å InN / 10 Å $In_{0.25}Ga_{0.75}N$ (denoted as LED P), as shown in figure 4-20 where the band lineups and wavefunctions at J = 100 A/cm^2 are plotted. A slight decrease in emission wavelength is observed from the use of LED N [λ= 660 nm] to LED P [λ= 652 nm]. As indicated in figure 4-17(a), for conventional 30 Å $In_{0.25}Ga_{0.75}N$ QWs, the electron wavefunction and hole wavefunction are positioned at the right hand side and left hand of the active region, respectively. This spatial

separation is attributed to the existence of the III-Nitride materials. Placing the delta-InN layer on the left hand side of active region introduces energy local minima with stronger shift of electron wavefunctions [LED N in figure 4-20(a)]. Similarly, placing the delta-InN layer on the right hand side has stronger effect on hole wavefunctions [LED P in figure 4-20(c)]. The wavefunction overlaps at J = 100 A/cm^2 are calculated as 62.9%, 66.1% and 61.5% for LED designs with the delta-InN layer at the left, the center and the right of the QW active region as shown in figure 4-20 (a), (b) and (c), respectively. The result of the enhanced overlap with delta-InN layer placed near p-GaN region indicates the importance of shifting hole wavefunction in obtaining high overlap and thus high spontaneous emission rate.

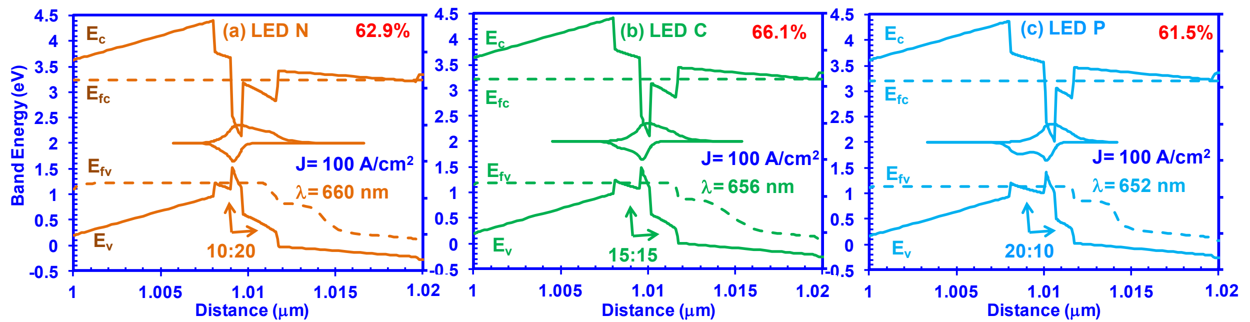

Figure 4-20 *Band lineups and corresponding wavefunctions of QW designs that consist of (a) 10 Å $In_{0.25}Ga_{0.75}N$ / 6 Å InN / 20 Å $In_{0.25}Ga_{0.75}N$ (denoted as LED N), (b) 15 Å $In_{0.25}Ga_{0.75}N$ / 6 Å InN / 15 Å $In_{0.25}Ga_{0.75}N$ (denoted as LED C) and (c) 20 Å $In_{0.25}Ga_{0.75}N$ / 6 Å InN / 10 Å $In_{0.25}Ga_{0.75}N$ (denoted as LED P) at J = 100 A/cm^2.*

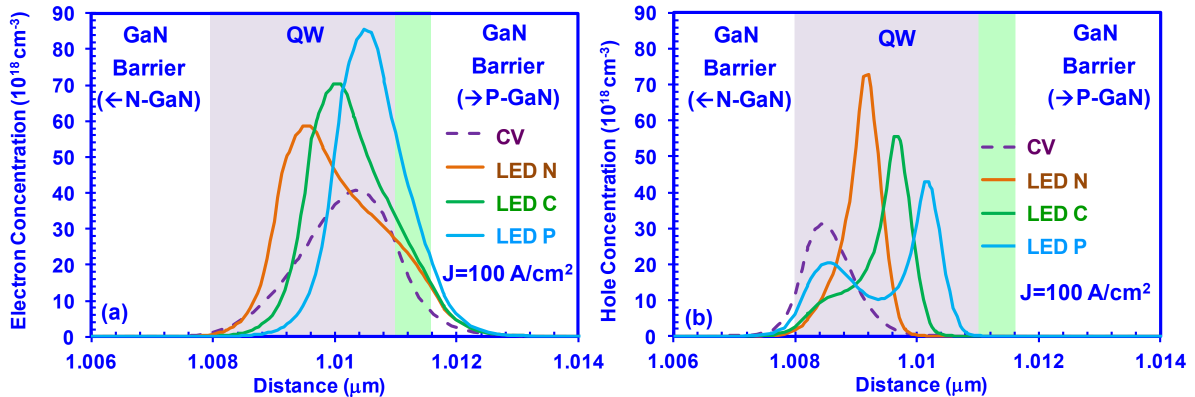

Figure 4-21 *(a) Electron concentration in conduction band and (b) hole concentration in valence band of CV InGaN QW LED and three InGaN QW LEDs with different positions of 6 Å delta-InN layer at J = 100 A/cm^2. InGaN QW LED is included as a reference.*

Figure 4-21 illustrates the carrier distributions across the QW and GaN barrier layers of the three LED structures under investigation. The electron and hole concentrations of conventional InGaN QW LEDs are included as a reference. As predicted in the previous analysis, the design of delta-InN on the left hand side of QW region (LED N) is effective in shifting the electrons to the center of the QW region, while the design of delta-InN on the right hand side of QW region (LED P) is effective in shifting the holes to the right. The mobility of electrons is higher than that of the holes, and the electrons are much lighter than that of the holes. Thus, it is easier to rearrange the electron distribution by novel QW structures in figure 6(a). In contrast, the shifts of holes are not as complete. The double peaks of the hole distribution are observed for LED P as a result of the double peaks in the hole wavefunction in figure 4-20(c). Although the peak hole concentration decreases as the peak position shifts towards the right hand side of QW region, the better alignment of carrier concentration can still be obtained from the use of LED P.

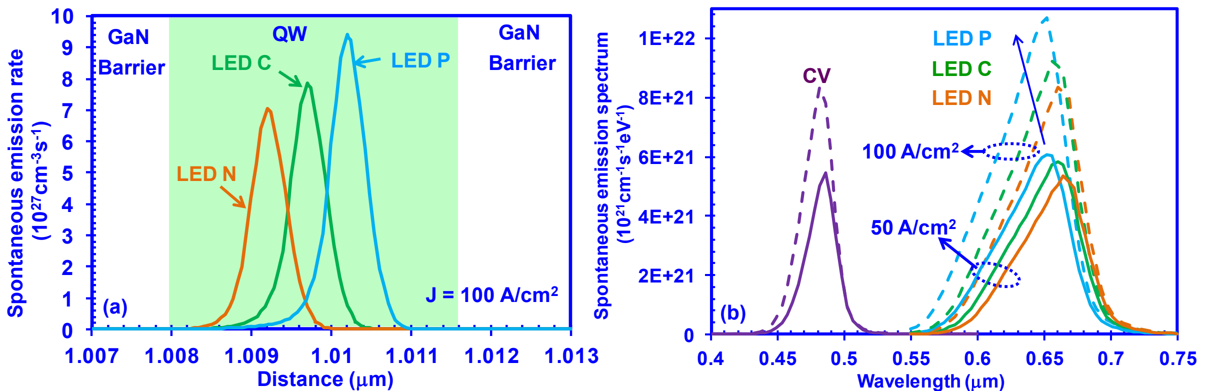

Figure 4-22 *Spontaneous emission spectrum of of CV InGaN QW LED and three InGaN QW LEDs with different positions of 6 Å delta-InN layer at J = 100 A/cm^2.*

Figure 4-22(a) plots the spontaneous emission rates across the QW region of the three InGaN QW LEDs with different positions of 6 Å delta-InN layer at J = 100 A/cm^2. LED P exhibits the highest spontaneous radiative recombination rate with the peak position near the p-GaN due to the better alignment of carrier concentrations. The spontaneous emission spectrum of LED N, LED C and LED P were plotted in figure 4-22(b). The highest spontaneous emission rate is obtained from LED P which gives the highest electron-hole wavefunction overlap among the three designs. All of the three InGaN-delta-InN QW LEDs with red light emission exhibits

comparable radiative recombination rate as compared to the CV InGaN QW LEDs with cyan light emission.

The light output power-current-voltage curves of the three InGaN-delta-InN QW LEDs were illustrated in figure 4-23(a) and 4-23(b), respectively. The monomolecular recombination coefficient A, Auger recombination coefficient C and extraction efficiency $\eta_{extraction}$ are assumed as 10^7 s^{-1}, 10^{-33} cm^6s^{-1} and 70%, respectively. The I-V characteristics of LED N, LED C and LED P are comparable with slight decrease in forward bias voltage from LED N to LED P. LED P with the delta-InN placed close to the p-GaN side shows the highest output power at all current density attributed to the enhanced spontaneous emission rates in the active region. Specifically, at J = 100 A/cm^2, the light output power of LED P is 20% and 40% higher than that of the LED C and LED N, respectively. This result is in good agreement with the previous discussion.

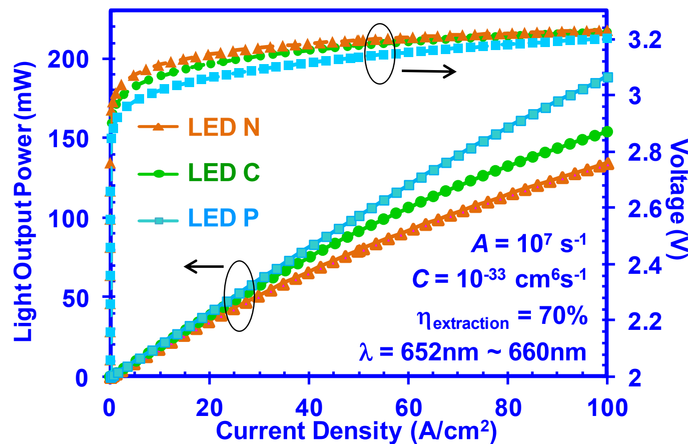

Figure 4-23 *Light output power as a function of current density for the three investigated LED designs in this study. The emission wavelength are around 652 nm to 660 nm.*

In summary, by taking into account the carrier transport, the device characteristics of the InGaN-delta-InN QW LEDs under electrical biasing condition were obtained. The use of delta layer active region resulted in significant red-shift in the emission wavelength with the increase in optical matrix element and electron-hole wavefunction overlap. Thus, the spontaneous emission rates were not compromised by the extension of emission wavelength, which indicated the successful suppression of charge separation issues. The position optimization study of the delta-InN layer showed increased spontaneous emission rate and internal quantum efficiency from the use of delta-InN layer on the right hand side of the active region. The results indicated the

importance of considering the position of delta-InN layer in the optimization of the device performance.

References for Chapter 4

1. N. Tansu, and L. J. Mawst, “Current injection efficiency of InGaAsN quantum-well lasers,” J. Appl. Phys., vol. 97, no. 5, pp. 054502, 2005.
2. H. P. Zhao, G. Y. Liu, R. A. Arif et al., “Current injection efficiency induced efficiency-droop in InGaN quantum well light-emitting diodes,” Solid-State Electronics, vol. 54, no. 10, pp. 1119-1124, Oct, 2010.
3. T. Mukai, M. Yamada, and S. Nakamura, “Characteristics of InGaN-based UV/blue/green/amber/red light-emitting diodes,” Japanese J. Appl. Phys. Part 1-Regular Papers Short Notes & Review Papers, vol. 38, no. 7A, pp. 3976-3981, Jul, 1999.
4. M. R. Krames, O. B. Shchekin, R. Mueller-Mach et al., “Status and future of high-power light-emitting diodes for solid-state lighting,” Journal of Display Technology, vol. 3, no. 2, pp. 160-175, Jun, 2007.
5. W. W. Chow, M. H. Crawford, J. Y. Tsao et al., “Internal efficiency of InGaN light-emitting diodes: Beyond a quasiequilibrium model,” Appl. Phys. Lett., vol. 97, no. 12, pp. 121105, 2010.
6. J. Hader, J. V. Moloney, and S. W. Koch, “Temperature-dependence of the internal efficiency droop in GaN-based diodes,” Appl. Phys. Lett., vol. 99, no. 18, Oct 31, 2011.
7. G.-B. Lin, D. Meyaard, J. Cho et al., “Analytic model for the efficiency droop in semiconductors with asymmetric carrier-transport properties based on drift-induced reduction of injection efficiency,” Appl. Phys. Lett., vol. 100, no. 16, pp. 161106, 2012.
8. I. E. Titkov, D. A. Sannikov, Y.-M. Park et al., “Blue light emitting diode internal and injection efficiency,” AIP Advances, vol. 2, no. 3, pp. 032117, 2012.
9. J. Wang, L. Wang, L. Wang et al., “An improved carrier rate model to evaluate internal quantum efficiency and analyze efficiency droop origin of InGaN based light-emitting diodes,” J. Appl. Phys., vol. 112, no. 2, pp. 023107, 2012.
10. H. P. Zhao, G. Y. Liu, J. Zhang, R. A. Arif, and N. Tansu, “Analysis of Internal Quantum Efficiency and Current Injection Efficiency in Nitride Light-Emitting Diodes”, Journal of Display Technology, vol. 9, no. 4, pp. 212-225, April 2013.
11. 61. G. Y. Liu, J. Zhang, C. K. Tan, and N. Tansu, “Efficiency-Droop Suppression by Using Large-Bandgap AlGaInN Thin Barrier Layers in InGaN Quantum Wells Light-Emitting Diodes”, IEEE Photonics Journal, vol. 5, no. 2, Art. 2201011, April 2013.
12. APSYS by Crosslight Software, Inc., Burnaby, Canada, http://www.crosslight.com.
13. H. P. Zhao, G. Y. Liu, and N. Tansu, “Analysis of InGaN-delta-InN quantum wells for light-emitting diodes,” Appl. Phys. Lett., vol. 97, no. 13, Sep 27, 2010.

Chapter 5: Metalorganic Chemical Vapor Phase Epitaxy of III-Nitride Materials and Fabrication of Light-Emitting Diodes

5.1 Introduction to MOVPE system

5.1.1 Configurations and Design of MOVPE P75 Reactor

The material and device growths in this report are carried out by using metalorganic vapor phase epitaxy (MOVPE) or metalorganic chemical vapor deposition (MOCVD). Two prevailing techniques in the epitaxy of III-V semiconductor compounds are molecular bean epitaxy (MBE) and MOVPE. In contrast to MBE where the physical deposition of evaporated sources takes place in a vacuum chamber with a growth rate typically smaller than 0.2-0.5 μm per hour, the growth of single crystalline material in MOVPE reactor is the result of chemical reaction at a certain chamber pressure. The growth rate for MOVPE process is typically a few micrometers per hours, the scalability for MOVPE reactor with multi-wafer capability is also more practical. In addition, the MOVPE growth is usually carried out at higher growth temperature, thus it is thermodynamically favourable growth process. The detailed process of III-nitrides growth will be discussed. The MOVPE reactor used in this work is the vertical type turbo-disc Veeco Pioneer-75 system.

Figure 5-1 shows the configuration of Veeco P-75 MOVPE reactor and the flow of the gases. The main components of the reactor consist of two chambers, growth chamber and loadlock (LL) chamber. These chambers are separated by the gate valve (GV). The LL chamber is used to load the wafers or substrates and take the processed wafers out of the system. It is connected with a Varian pump and N_2 supply used in pump and purge processes for cleaning purpose. The growth chamber is where the gases and the precursors of Group-III and Group-V come in and participate in the material epitaxy at high purity level. The wafer on the wafer carrier would be transferred into the growth chamber from LL chamber through a mechanical fork, thus the growth chamber would never be exposed to the outside ambient during normal operation.

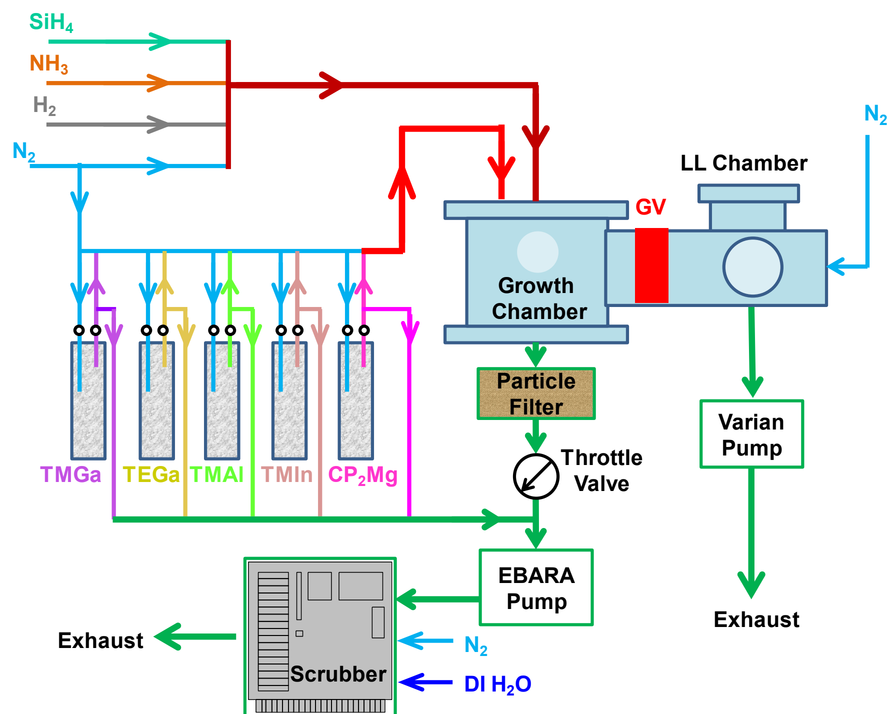

Figure 5-1 *Schematics of Veeco P75 MOVPE reactor system*

The purified gases of nitrogen (N_2), hydrogen (H_2), ammonia (NH_3), silane (SiH_4), would flow into the growth chamber through the top flow flange where an even distribution of gases would be delivered from the top shower head to the rotating wafer in the center of the chamber. Figure 5-2 shows the smoke patterning in the rotating disc system [1]. The speed of the rotation is optimized for different material growth in order to obtain the uniformity across the wafer. Purified N_2 as the carrier gas for metal-organic (MO) sources would flow into the source bubbler, pick up the vapor of the Alkyls and transport the vapor to the top flow flange. Five metalorganic (MO) bubblers are equipped in the reactor, and these sources include trimethylgallium (TMGa), triethylgallium (TEGa), trimethylaluminum (TMAl), trimethylindium (TMIn), and Bis(cyclopentadienyl)magnesium (Cp_2Mg). These MO sources are in the form of either liquid (TMGa, TEGa, TMAl and TMIn) or solid (Cp_2Mg).

The gases in the outlet of the growth chamber pass through a particle filter trap prior to being pumped out by the Ebara AA70W pump. The outlet of the Ebara pump is connected with a wet scrubber unit of Vector Ultra 3001 that provides abatement of toxic, corrosive, and water-reactive

gases from process equipment effluent. The throttle valve between the growth chamber and the Ebara pump is used to control the growth chamber pressure by tuning the opening from 0% to 100%. The other supporting facilities include heat exchanger for pumps and reactor cooling, process gas manifolds for gas flow controlling, constant temperature baths, gas purifiers for N_2, H_2, NH_3, etc.

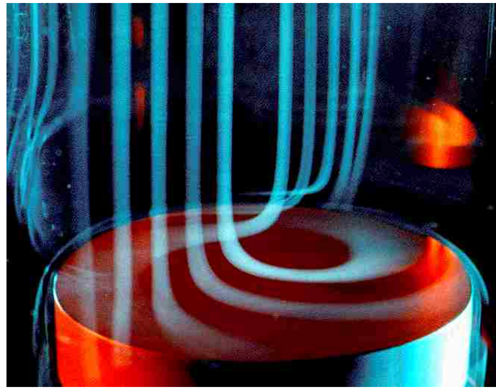

Figure 5-2 *Smoke flow patterning in rotation disc system [1]*

5.1.2 Growth Parameters in Epitaxy

There are several important parameters in the material growth, including V/III ratio growth, growth temperature, chamber pressure and rotation speed. These parameters optimizations are important for the development of materials, specifically in optimization of new materials used in the devices studied here.

i) V/III Ratio

One of the most important parameters in III-nitride growth, V/III ratio, is defined as the molar ratio of Group-V and Group-III. Group-V precursor in III-nitride growth is NH_3, and Group-III precursors include metal organic (MO) sources of TMGa, TEGa, TMIn and TMAl. Two types controlling configurations of molar flow rate have been used for MO bubblers; source bubblers of TMGa and TMAl use the double dilute configuration due to the high vapor pressure, however the TEGa and TMIn precursors do not consist of double dilution line. Figure 2-3 shows the schematic of the configuration without and with double dilution in (a) and (b), respectively. The stainless steel bubblers are soaked inside the temperature controlled bath to keep constant temperature of each bubbler.

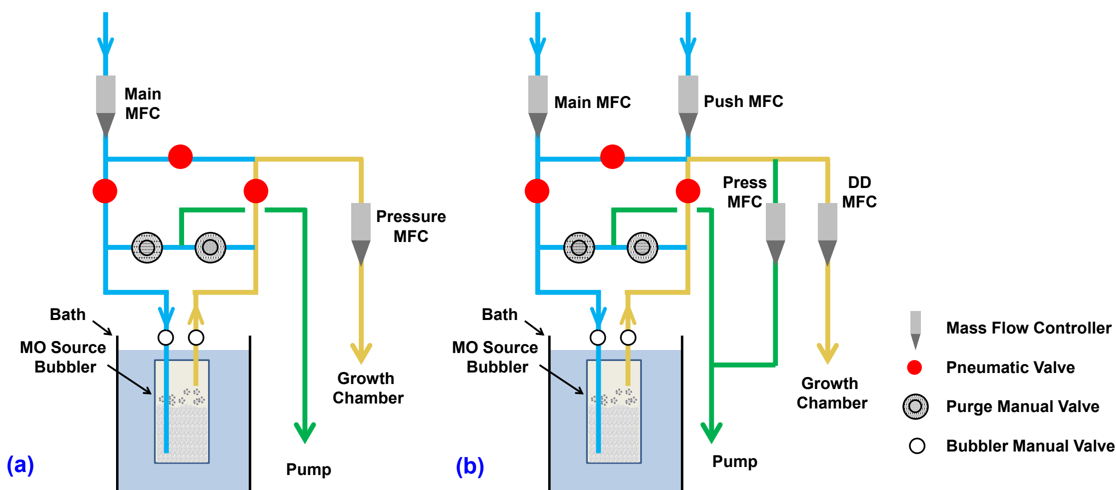

Figure 5-3 *Schematics of bubbler configuration (a) without and (b) with double dilution. TEGa and TMIn are using (a) and TMGa and TMAl are using (b).*

The vapor partial pressure of metal organic precursors inside the bubbler is a function of bubbler temperature *T* as follows:

$$P_{vapor} = 10^{(a-b/T)} \quad \text{(in Torr)} \quad (5.1a)$$

$$P_{vapor} = 10^{(a-b/T)} \cdot \frac{1013.25}{760} \quad \text{(in mbar)} \quad (5.1b),$$

where *a* and *b* are empirical parameters listed in Table 5-1.

	a	***B / K***	***T / K***	***P_{vapor} / Torr***	***P_{vapor} / mbar***	***$P_{bubbler}$ / Torr***
TMGa	8.07	1703	273.15	68.443	91.25	900
TEGa	8.083	2162	283.15	2.802	3.736	900
TMIn	10.98	3204	293.15	1.123	1.497	900
TMAl	8.224	2134.83	293.15	8.742	11.655	900

Table 5-1 *Parameter List of a, b, temperature T and corresponding P_{vapor} and $P_{bubbler}$ for MO sources.*

Group-III precursors of TEGa and TMIn are using bubbler configuration without double dilute, and the partial pressure of these two Group-III sources is calculated using following equation:

$$F_{III_partial} = F_{III_Main} \cdot \frac{P_{vapor}}{P_{bubbler} - P_{vapor}} \quad (5.2),$$

where F_{III_Main} and $P_{bubbler}$ are flow rate of N_2 carrier gas and bubbler pressure controlled by the main MFC and pressure MFC showing in figure 5-3(a), respectively. The values of $P_{bubbler}$ have been indicated in Table 5-1.

As observed from Table 5-1, the vapor pressures of TMGa and TMAl are much higher than those of TEGa and TMIn, thus double dilute arrangements are employed for TMGa and TMAl in order to reduce the flow so that the precursors will not precipitate and contaminate the gas line or the reaction chamber, and we can be more precise in controlling the flow. The partial pressure of these two Group-III sources is then calculated using following equation:

$$F_{III_partial} = F_{III_Main} \cdot \frac{F_{III_DD}}{F_{III_Main} + F_{III_Push}} \cdot \frac{P_{vapor}}{P_{bubbler} - P_{vapor}} \quad (5.3),$$

where F_{III_Main}, F_{III_Push}, and $F_{III\text{-}DD}$ are flow rates of pure N_2 carrier gas going through the bubbler, pure N_2 push gas, and double dilution of N_2 carrying MO source, respectively. They are controlled by the main MFC, Push MFC, Double Dilute MFC shown in figure 5-3(b) respectively.

The partial pressure of Group-V precursor can be obtained as follow:

$$P_{V_partial} = P_{GC_P} \cdot \frac{F_{NH_3}}{F_{NH_3} + F_{ambient_gas}} \quad (5.4),$$

where F_{NH3} + $F_{ambient_gas}$ = F_{total} represents the total gas flow into the growth chamber (GC). $F_{ambient_gas}$ is the flow rate of Group-V precursor NH_3 in standard cubic centimeters per minute (sccm) and $F_{ambient_gas}$ is the total flow rate of ambient gas of N_2 and H_2 flowing into the chamber during growth in sccm. P_{GC_P} is the growth chamber pressure in Torr which is defined by the growth recipe and controlled by both the total gas flow and the throttle valve underneath the chamber. Thus, the V/III molar ratio of the growth is defined as following:

$$V / III = \frac{P_{V_partial}}{F_{III_partial}} \quad (5.5),$$

b) Growth Temperature Control

The growth temperature is an essential factor in material epitaxy. Different sources have different pyrolysis temperatures and thus different temperatures would be used for different material growth. For instance, the gallium precursor of trimethylgallium (TMGa), $(C_2H_5)_3Ga$, has higher decomposition temperature than that of another gallium precursor triethylgallium (TEGa), $(CH_3)_3Ga$. As a result, the growth of GaN template using TMGa as gallium precursor owns higher growth temperature in order to sufficiently decompose the TMGa MO source. In contrast, the growth temperature of GaN barrier layer can be much lower due to the use of TEGa MO source. In addition, the incorporation of impurity is a temperature-sensitive process. Hence, the growth temperature significantly affects the material composition as well as the material quality.

The methods of temperature controlling in Veeco Pioneer 75 MOVPE Reactor include thermocouple (T/C) control mode and current control mode. Figure 5-4 illustrates the difference between the two types of the temperature control modes when the temperature is increased from ~ 516 °C to ~1015 °C within 7 mins. The temperature response of the T/C control mode is faster than current control mode, resulting in the higher temperature at a certain time. However, the thermocouple control feedback loop will cause the temperature overshoot (or undershoot) at the end of the course, while the current control mode gives very smooth temperature profile without oscillation at the end. The stability of temperature will greatly benefit the growth of InGaN QW due to the sensitivity of indium incorporation in the InGaN materials. Thus, we utilize the current control mode in the following experimental investigations for better controllability.

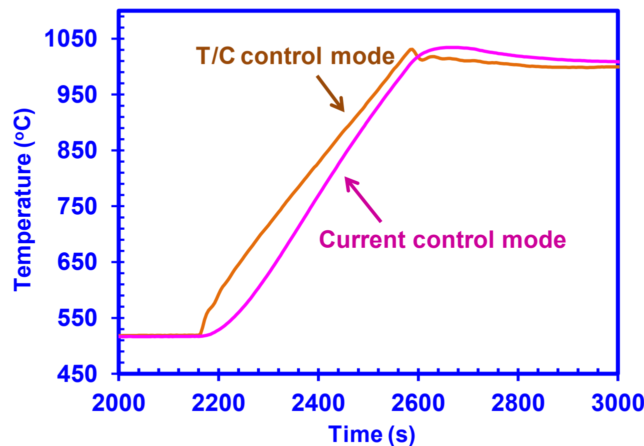

Figure 5-4 *Comparison of the temperature profile controlled by the thermocouple (T/C) and filament current.*

c) Other Important Parameters

Growth chamber pressure is another important parameter that influence the growth rate. It is controlled by the electronic feedback loop between the set point in the growth recipe, the real reading of the growth chamber pressure and the throttle valve before the Ebara pump. Typicak growth pressure for GaN template growth, InGaN / GaN QW growth and p-type GaN thin film are 500 Torr, 200 Torr and 100 Torr respectively. Beside, other important growth parameters are the rotation speed of the wafer carrier and the gas flow rates, all of which need to be checked carefully for a growth optimization experiments.

5.2 MOVPE of (In, Al)GaN on Sapphire Substrate

5.2.1 MOVPE Processes

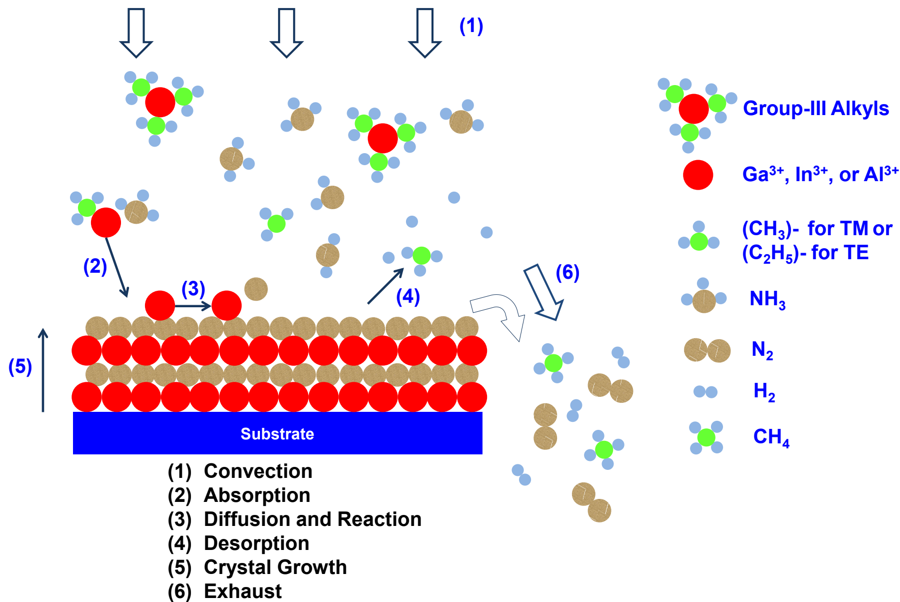

Figure 5-5 *Processes occurring during the metal-organic vaper phase deposition (MOVPE) of III-nitride material.*

MOVPE is the major method to obtain high quality, single crystalline III-nitrides. Figure 5-5 illustrates the processes occurring during the MOVPE of III-nitride material family including binary GaN, InN and AlN, ternary AlGaN, AlInN and AlGaN, and quaternary AlGaInN. The processes in MOVPE reactor includes: (1) convection of gases and sources, (2) absorption, (3) diffusion and

reaction, (4) desorption, (5) crystal growth and (6) exhaust. In our Veeco P75 MOVPE reactor system, as indicated earlier in this chapter, the group-V precursors of ammonia (NH_3), the process gas of N_2 carrying the group-III alkyls (TMGa, TEGa, TMAl, TMIn) and other process gases such as SiH_4, H_2 or pure N_2 are flowing into the chamber through the top shower head. The high temperature inside the growth chamber completely or partially pyrolyzes the ammonia and group-III precursors. The reaction of group-III and group-V will thus take place on the surface of the wafer, resulting in the epitaxy of single crystalline material. The by-products of N_2, H_2, CH_4, carbon and excess sources would be exhaust to the Ebara pump underneath the chamber.

5.2.2 Growth of GaN Template on Sapphire Substrate

For the majority of the experiments carried out in this report, the samples growth were carried out on a thick layer (~ 3 μm) of GaN bulk on sapphire substrates, which is referred as GaN templates. The growths of GaN artificial templates employ a growth of low-temperature (LT) GaN followed by the etch-back and recovery process for the circumvention of large dislocation density induced by the large lattice mismatch between GaN and Al_2O_3. The growth profile and the process flow of the GaN templates on sapphire substrates are shown in figure 5-6 and figure 5-7, respectively. The corresponding stages are labeled as (a)-(f) in both figures. After high temperature (HT) cleaning process in the H2 ambient at 1075 °C for couple minutes [step (a)], the temperature of the sample would be ramped down to 525 °C – 530 °C for the growth of 30-nm low temperature (LT) GaN buffer layer [stage (b)] with a high V/III ratio of 10,429. This amorphous GaN material is full of defects as shown in figure 5-7(b). The reflectivity of the in-situ growth would increase as a result of the material growth. The following etch back and recovery process includes stages (c)-(f). In stage (c), the temperature is ramped up to about 1010 °C and the flow of both TMGa source and NH_3 are increased. The islands of GaN material are grown on top of GaN buffer layer in three-dimensional (3D) growth direction, leading to the roughening of the surface which is reflected in the decrease of the reflectivity. As the 3D growth mode continues, the sizes of GaN islands increase with a increasing surface roughness leading to the lowest reflectivity in the growth [stage (d)]. During this process, the H_2 gas is constantly flowing into the chamber (~ 4000 sccm) and etches away part of the GaN material at high temperature, which

would greatly reduce the number of dislocations being extended from the GaN buffer layer.

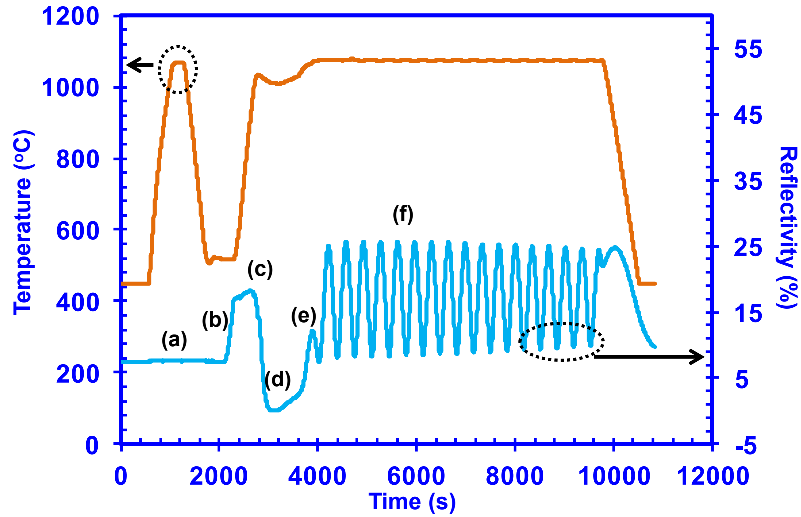

Figure 5-6 The growth profile of GaN template growth on sapphire substrates with different stages of (a)-(f).

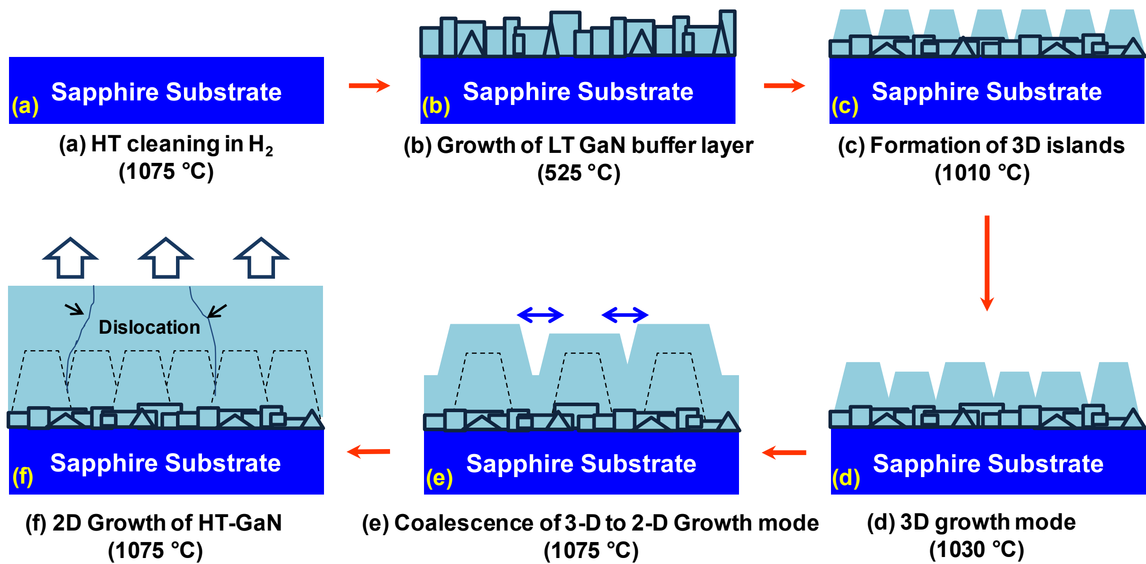

Figure 5-7 The process flow of (a) high temperature cleaning, (b) low temperature GaN growth, (c) formation of 3D islands, (d) 3D growth mode, (e) coalescence process and (f) high temperature GaN growth.

Subsequently, the growing islands start to coalescence with each other, and the growth mode is gradually changing from 3D to 2D. The reflectivity would gradually recover as a result of the smoother surface [stage (e)]. The V/III ratio is kept relatively high as 5406 in this etch back and

recovery process to enhance lateral growth. After the coalescence finishes, 2D growth of GaN thin films will take place at high temperature of 1075 °C [stage (f)]. The H_2 flow is reduced to 3000 sccm and the V/III ratio is further reduced to 3612 to encourage the vertical growth. Periodic oscillations of reflectivity are observed from thin film interference in stage (f), and the growth rate is calculated as ~ 1.8-1.9 μm/h. The dislocations and defects in GaN templates include point defects, threading edge dislocation, threading screw dislocation and mixed screw-edge dislocations.

5.3 Device Fabrication

5.3.1 Typical Device Structures

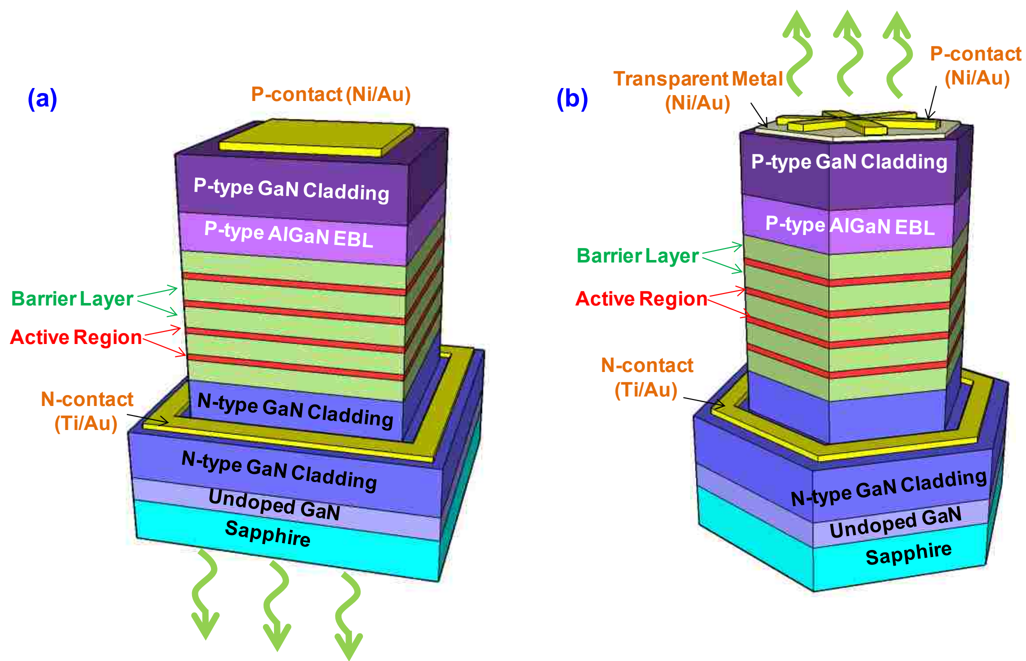

Figure 5-8 *Schematic of InGaN/GaN based MQW LEDs with (a) square-shaped bottom-emitting configuration and (b) hexagonal-shaped top-emitting configuration.*

The material growth and device fabrication processes of InGaN QW based LEDs are all completed in-house [2-5] using selective area epitaxy. Figure 5-8 shows the device structures of multiple quantum wells (MQWs) based InGaN LEDs with (a) square-shaped bottom-emitting configuration and (b) hexagonal-shaped top-emitting configuration. In our design, both square shape and hexagonal shape are used in top-emitting and bottom-emitting devices for comparison purpose. The epitaxial layers from the bottom to the top of the sample on either double-side-

polished sapphire substrate [figure 5-8 (a)] or single-side-polished sapphire substrate (figure 5-8 (b)) typically consist of 3 μm GaN template, 4-period of active regions sandwiched by barrier layers, 30 nm p-type AlGaN electron blocking layer (EBL) and 0.2 μm p-type doped GaN cladding layer.

The 3 μm thick GaN template growing on sapphire substrate consists of an 0.5 μm thick undoped GaN buffer layer followed by the 2.5 μm thick Si-doped GaN as n-type cladding layer. The n-type doping concentrate is typically ~ $5x10^{18}$ cm^{-3} for the n-type GaN bulk. The selective area epitaxy takes place after device fabrication in clean room. The device fabrication which will be discussed in detail in the following section. The periodic structure of barrier layer and active region as well as the upper cladding layers would be grown as mesa structure. The active region is usually 2~3 nm InGaN based quantum wells (QWs), and the barrier layer can be GaN, AlInN or other large bandgap III-nitrides with the total thickness around 10-15 nm. The large bandgap material of AlGaN layer with 10%-15% Al-content would be grown to on top of the last barrier layer to suppress the carrier leakage. It is followed by 0.2 μm magnesium (Mg) doped GaN with the typical carrier concentration of ~ $5x10^{17}$ cm^{-3}. Thus, the mesa structure is formed in well-defined area with the vertical channel for carriers to transport and recombine inside the active region. Lastly, the n-contact (cathod) and p-contact (anode) would be deposited on the top of n-GaN template and mesa, respectively, for electrical probe in electroluminescence measurements. For bottom-emitting device, the p-metal covers most part of the p-GaN top-layer for better current spreading. For top-emitting device, a thin layer of transparent metal consisted of 5 nm / 5 nm Ni/Au is deposited to cover p-GaN layer before the deposition of star-shape p-contact of 20 nm / 150 nm Ni/Au.

5.3.2 Photolithography Process in Device Fabrication

Photolithography is a method by which geometric patterns are transferred from a mask to the substrate (wafer) by changing the chemical structure of a photosensitive polymer under the exposure of high-energy light source. The organic polymer that allows the transferring of patterns is called “photoresist”. Two types of photoresists are widely used in experiments, positive-

photoresist where the material is soluble in developer solution after light exposure, and negative-photoresist where the material is insoluble in developer solution after light exposure.

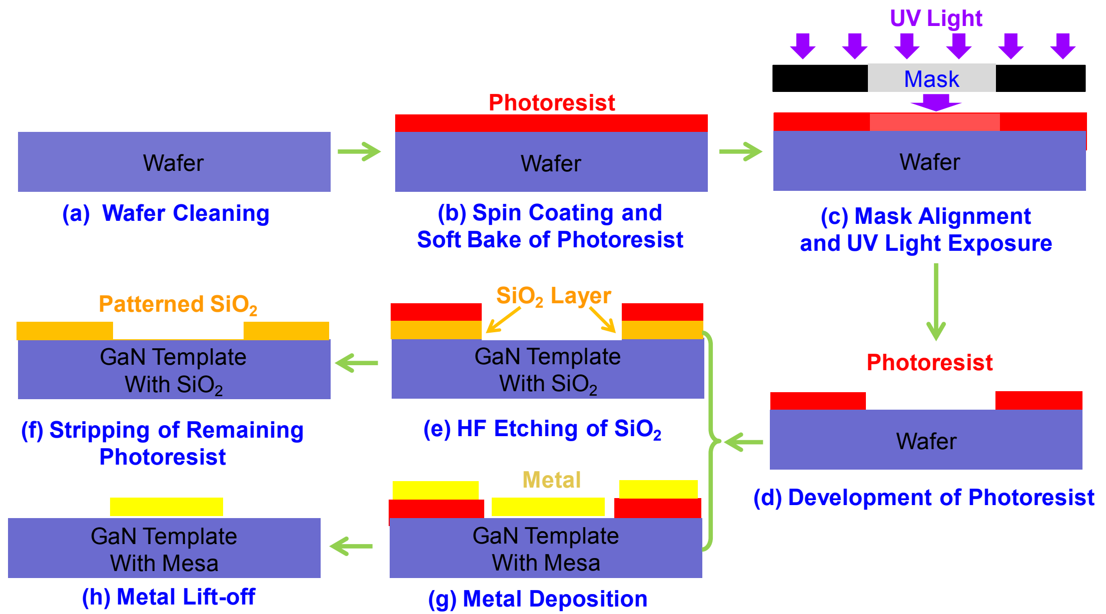

Figure 5-9 *Illustration of photolithography processes in cleanroom*

Figure 5-9 illustrates the photolithography process that uses the positive-photoresist S1813. After the wafer is prepared and cleaned [figure 5-9(a)], a uniform layer of photoresist would be spin-coated on the wafer [figure 5-9(b)] with the speed of 5000 revolutions per minute (rpm). The wafer can be GaN template with SiO_2 on top for mesa creation, or GaN template with grown mesa structure for metal pattern creation. The subsequently soft bake at 105^0C for 1 min would remove the residual solvent and increase the adhesion and hardness of the photoresist for later process. Next, the sample would be aligned under microscope with the mask, followed by the UV light exposure for 5.5 seconds [figure 5-9(c)]. The mask aligner used here is Karl Suss MA6 with UV lamp wavelength of 365 nm. The following step is the development of photoresist in developer of MF319 for ~1 minute [figure 5-9(d)], so that the exposed area of photoresist dissolved in developer. To create mesa pattern for regrowth purpose, the sample would then go through HE etching (HF:H_2O = 1:30 for ~1 minutes) to transfer the pattern from photoresist to SiO_2 layer that deposited earlier [figure 5-2(e)], and then the photoresist would be stripped away, leaving the patterned SiO_2 on top of GaN template [figure 5-9(f)]. To form metal contact, the deposition of

metal would be carried out by e-beam evaporator or sputtering [figure 5-9(g)], and after the metal lift-off in ultrasonic, the metal contact would be remain in the desired area [figure 5-9(h)].

The photolithography mask used in photolithography process [figure 5-9(c)] is designed using LayoutEditor.exe. Figure 5-10 illustrate the mask patterns of n-contact, mesa, p-contact and transparent metal for (a) square-shaped bottom-emitting devices, (b) hexagonal-shaped bottom-emitting devices, (c) square-shaped top-emitting devices and (d) hexagonal-shaped top-emitting devices. The edge lengths of mesa patterns range from 310 μm to 510 μm for square shape and from 156 μm to 256 μm for hexagonal shape, corresponding to the area of 0.096 mm^2 to 0.26 mm^2 for square shape and 0.063 mm^2 to 0.17 mm^2 for hexagonal shape. The design of different device shape, device area and electrode of p-contact is for comparison purpose.

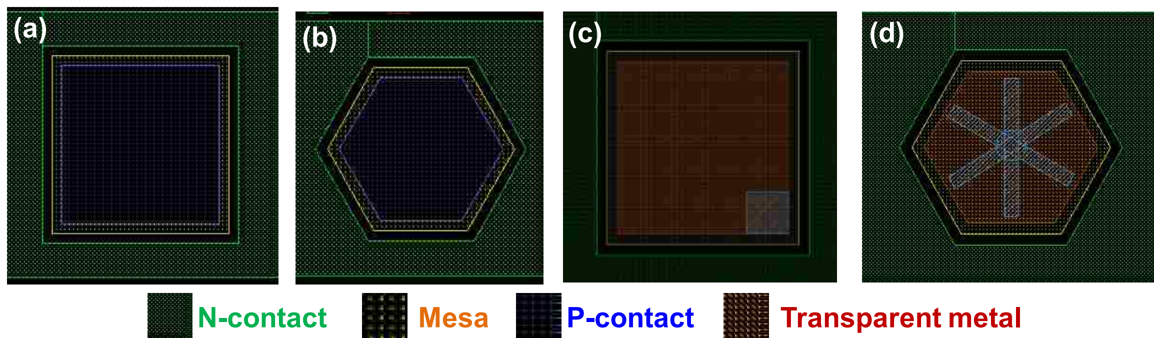

Figure 5-10 *Mask design of n-contact, mesa, p-contact and transparent metal for (a) square-shaped bottom-emitting devices, (b) hexagonal-shaped bottom-emitting devices, (c) square-shaped top-emitting devices and (d) hexagonal-shaped top-emitting devices.*

5.3.3 Device Fabrication Process Flow

The device fabrication processes include the clean room fabrication and material growth in MOVPE reactor. In this report, the selective area epitaxy method is employed for device fabrication. Figure 5-11 illustrates the process flow of the device fabrication for LEDs and solar cells. After the n-type GaN templates have been grown on sapphire substrate by employing MOVPE, the sample would be brought to clean room of class 100. A 400-nm SiO_2 layer would be deposited on top of GaN template by plasma-enhanced chemical vapor deposition (PECVD). The following photolithography process, similar to what described in figure 5-9 (a)-(f), would create patterns on SiO_2 layer which will be used as mask in the subsequent MOVPE regrowth of mesa

structure. As the III-nitride material would only grow on top of the exposed GaN surface, the selective area epitaxy (SAE) would take place and the vertical structure showing in figure 5-8 will be formed. This approach ease the issue of surface roughness associated with reactive ion etching (RIE) approach. Subsequently, photolithography would be carried out on sample with mesa structure of active region and p-type layers to create patterns for metal deposition with the processes analogous to that shown in figure 5-9 (a)-(d) followed by (g)-(h). After deposition and lift-off of both p-contact and n-contact, rapid thermal annealing of the metal contact would be carried out at 450 °C for 40 seconds to enhance the ohmic contact of the metal and semiconductors and the device is ready for electrical and optical characterizations.

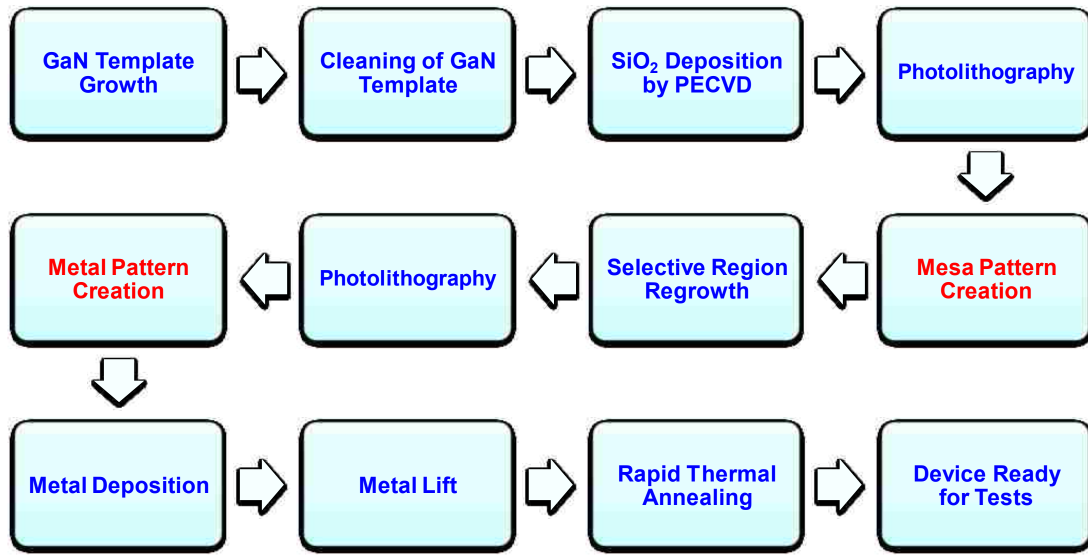

Figure 5-11 *Process flow of III-nitride device fabrication*

Reference for Chapter 5

1. http://www.wpi.edu/academics/che/HMTL/CFD_in_CRE_IV/Mitrovic.pdf

2. H. P. Zhao, G. Y. Liu, X. H. Li, G. S. Huang, J. D. Poplawsky, S. T. Penn, V. Dierolf, and N. Tansu, "Growths of staggered InGaN quantum wells light-emitting diodes emitting at 520-525 nm employing graded growth-temperature profile," *Appl. Phys. Lett.,* vol. 95, Aug 10 2009.

3. H. P. Zhao, G. Y. Liu, X. H. Li, R. A. Arif, G. S. Huang, J. D. Poplawsky, S. T. Penn, V. Dierolf, and N. Tansu, "Design and characteristics of staggered InGaN quantum-well light-emitting diodes in the green spectral regime," *IET Optoelectronics,* vol. 3, pp. 283-295, Dec

2009.

4. H. P. Zhao, J. Zhang, G. Y. Liu, and N. Tansu, "Surface plasmon dispersion engineering via double-metallic Au/Ag layers for III-nitride based light-emitting diodes," *Appl. Phys. Lett.,* vol. 98, Apr 11 2011.

5. H. P. Zhao, G. Y. Liu, J. Zhang, J. D. Poplawsky, V. Dierolf, and N. Tansu, "Approaches for high internal quantum efficiency green InGaN light-emitting diodes with large overlap quantum wells," *Optics Express,* vol. 19, pp. A991-A1007, Jul 4 2011.

Chapter 6: Metalorganic Vapor Phase Epitaxy of Lattice-Matched AlInN Compounds and InN Alloy

6.1 Applications and Growth Challenges of AlInN Alloys

6.1.1 Applications of AlInN Alloys

In designing structures in nitride-based devices for photonics and electronics applications, the most-widely studied heterostructures have been primarily limited to AlGaN / GaN and InGaN / GaN configurations. The use of ternary AlInN alloy has attracted significant interest as an alternative to InGaN and AlGaN in III-Nitride based applications for light-emitting diodes (LEDs) and laser diode (LD) [1-9], solar-blind photodetector [10], short wavelength Distributed Bragg Reflector (DBR) [11, 12] and near-infrared optoelectronic devices based on intersubband transition [13]. The use of AlInN alloy has also been explored for high electronic mobility transistor as the alternative to AlGaN attributing to its larger band offset and reduced lattice mismatch strain. Prior works related to the first theoretical and experimental demonstration of high channel conductivity of AlInN based FETs had also been reported [14-19]. In addition, recent works have demonstrated the suitability of AlInN alloy as a strong material candidate for solid state cooling applications, with the thermoelectric figure of merit (Z*T) value of nearly lattice-matched AlInN obtained as high as 0.532 at room temperature (T=300K) [20-22]. The potential of employing large bandgap AlInN barrier materials to suppress the carrier leakage process in the InGaN QW LEDs has also been reported recently, and the suppression of efficiency droop in nitride LEDs can be realized by the use of AlInN thin barrier [1],. The use of lattice-matched (In-content ~ 17%) or slightly-tensile-strained (In-content ~ 10% up to 16%) AlInN alloys are of great interest for integrating as barrier materials in InGaN QW LEDs.

The availability of large bandgap lattice-matched AlInN material is of great importance for energy-efficiency device technologies including optoelectronic, power electronic and thermoelectric applications. Specifically, AlInN material with In-content ~17% - 18% is of great interest for achieving lattice matching condition to GaN substrate / template, which in turn leads to elimination of lattice-mismatch strain. The lattice-matching condition of AlInN can also potentially

lead to a reduction in threading dislocation and cracking, as well as the elimination of strain-driven piezoelectric polarization field in the material.

6.1.2 Challenges of AlInN Alloy Epitaxy

In comparison to the studies performed for AlGaN and InGaN alloys, the metalorganic vapor phase epitaxy (MOVPE) optimization studies of the AlInN alloy are still relatively lacking. The challenges in the growth of high quality AlInN by MOVPE can be attributed to the large contrast of the optimized growth conditions for AlN and InN alloys. The large immiscibility and differences in the thermal stability between AlN and InN lead to phase separation and composition inhomogeneity. The optimized growth temperatures of AlN (~1100 ^{o}C) and InN (~550 ^{o}C) are very distinct for these two binary materials grown by MOVPE, which leads to further challenges in achieving optimized growth conditions for AlInN alloy.

Up to today, the growths of AlInN thin films have been carried out by reactive radio-frequency (RF) magnetron sputtering [23, 24], molecular beam epitaxy (MBE) [25-27] and MOVPE [28-34] on c-plane sapphire substrates. In addition, recent works by MOVPE has also been reported for the growth of AlInN on GaN template on Si substrate [35]. However, comprehensive studies on the effect of the growth conditions for MOVPE of lattice-matched AlInN thin film have not been performed. In addition, the detailed comparison of the properties of AlInN thin films grown on GaN / sapphire templates and on free-standing GaN substrates has not been extensively studied and compared yet. The understanding on the growths and optical properties of AlInN alloy will have important impact on the development of the nitride-based devices including such layers.

6.2 AlInN Alloys with Various Indium Content on GaN / Sapphire Virtual Templates

6.2.1 MOCVD Growth of AlInN Allloys on GaN Templates

The growths of $Al_{1-x}In_xN$ materials with indium-contents (x) ranging from x = 0.38% to x = 25.3% were carried out by employing MOVPE in reference [34]. Two different types of templates were employed, as follow: 1) MOVPE-grown 3-μm-thick unintentionally-doped GaN (u-GaN) templates

grown on (0001) sapphire substrates with a dislocation density in the order of ~ 1×10^9 cm^{-2}, and 2) 470 μm free-standing GaN native substrates grown by hydride vapor phase epitaxy (HVPE) with a typical defect density in the order of 10^6 cm^{-2} (provided by Kyma Technologies) [36]. The growth temperature, reactor pressure and V/III ratio were optimized with the goal of obtaining lattice-matched AlInN on GaN templates / substrates. All the AlInN thin films studied here were grown using a vertical-type Veeco P-75 MOVPE reactor. Trimethylindium (TMIn) and trimethylaluminum (TMAl) were used as the Group-III precursors, and ammonia (NH_3) was employed as the group V precursor. Purified N_2 was used as carrier gas in the growth of AlInN alloy. In the growth of the AlInN film, the rotation speed of the sample was 1500 rpm.

The AlInN films were grown on top of GaN / sapphire template. The u-GaN / sapphire template and the AlInN thin film growths were carried out separately. For the growth of 3 μm thick GaN templates on the c-plane sapphire substrates, the etch-back and recovery process with 30 nm low temperature buffer layer was employed, and the growths of high-temperature u-GaN layers were carried out at a growth temperature of 1075 °C. For the AlInN thin film growth, an additional 210-nm-thick high-temperature u-GaN layer was grown to remove any surface defects prior to the AlInN material growth. To control the In/Al ratio of the AlInN thin film for achieving lattice-matching condition, the growth temperature was decreased from 860 °C to 750 °C resulting in increased In-content in the film, and independently the molar ratio [TMIn] / [TMIn + TMAl] was varied from 0.34 up to 0.64 to further enhance the indium incorporation in the film. After obtaining the growth condition for the AlInN alloy with various compositions, the optimization of the growth conditions for the nearly-lattice-matched alloy was carried out.

6.2.2 Characterizations of AlInN Alloys With Various In-contents on GaN Templates

Various characterizations were carried out for AlInN alloys grown on GaN virtual template including X-ray diffraction (XRD), scanning electron microscopy (SEM), and atomic force microscopy (AFM). The crystal quality and In-content of the AlInN epilayers were analyzed by using high-resolution X-ray diffraction (HRXRD) using a Philips triple axis diffractometer. The measurements were performed in a triple axis geometry giving a resolution of 36 arcsec at (2θ =

30-40 deg). The rocking curve scans were performed under ω-2θ (omega - 2theta) method around the (002) reflection of the GaN. The use of scanning electron microscope (SEM) [Hitachi 4300] was employed to analyze the surface morphology of the samples, and atomic force microscopy (AFM) [Veeco Dimension 3000] was employed for analyzing the surface roughness of the grown film. The root mean square (RMS) surface roughness was measured over a scanning area of 1 μm x 1 μm.

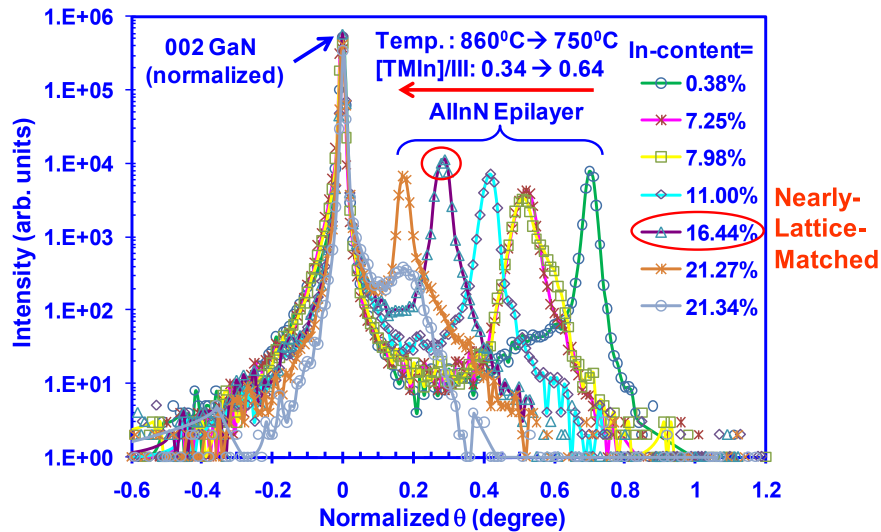

Figure 6-1 *Normalized XRD ω-2θ scans of AlInN epilayers on GaN/sapphire templates with the indication of nearly-lattice-matched condition.*

Figure 6-1 shows the XRD rocking curves [(0002) direction] of the AlInN alloy grown on GaN / sapphire templates at a growth pressure of 20 Torr for various growth temperatures and [TMIn] / [III] molar ratios. From our studies, by reducing the growth temperature and increasing the [TMIn] / [III] molar ratio, the In-contents in AlInN thin film could be increased from 0.38% up to 21.4%. As shown in figure 6-1, the peaks of the XRD plots for AlInN epitaxial layers with increasing In-content were observed to approach that of GaN. The full width at half maximum (FWHM) of the ω-scan rocking curves for GaN layers were estimated be in the range of 31 - 49 arcsec. The nearly-lattice-matched layer was found for growth temperature of 780 °C, [TMIn] / [III] ratio of 0.64, and growth rate of 0.15 μm/hr. The angle separation (Δθ) of the AlInN epilayer and GaN peaks of 1044 arcsec was determined for the nearly-lattice-matched layer, which corresponded to In-content of ~ 16.44%.

The XRD peak intensity and the corresponding FWHM data for the investigated AlInN layers are listed in Table 6-1. The AlInN thin films with In-content below ~ 8% were grown with thicknesses exceeding the critical thickness, and the strain would have been released by the formation of dislocations the material. The determination of the In-contents on cracked films (In-content < 8%) may be less accurate due to the partial relaxation in the films. The cracks in the low In-content AlInN films may result in less accurate compositional measurements in the samples specifically with In-contents of ~ 0.38% up to ~ 8%. In contrast, the thicknesses of AlInN films with In-contents ~ 11% - 21 % are well maintained below the corresponding critical thicknesses [35], which result in minimal error in the determination of the lattice parameters. The narrow FWHM in the range of ~ 110 - 140 arcsec from the optimized pseudomorphically-grown AlInN films indicated the high quality of the AlInN epilayer. The strongest AlInN XRD peak intensity was obtained from that of the nearly-lattice-matched layer with the narrow FWHM of 134 arcsec.

In-content (x) of $Al_{1-x}In_xN$	Thickness of $Al_{1-x}In_xN$ (μm)	Peak Intensity (arb. units)	FWHM (arcsec)
0.0038	0.36	7958	81.8
0.0725	0.21	4198	199
0.0798	0.2	3291	191
0.11	0.19	7191	137
0.1644	0.2	11357	134
0.2127	0.2	6677	108
0.2134	0.2	377	360

Table 6-1 *XRD rocking curve FWHM and intensity for AlInN thin films on GaN / sapphire templates.*

Figure 6-2 shows the lattice mismatch ratio of AlInN grown on GaN templates along c-axis and a-axis with all the In-contents studied here. The lattice-matching condition corresponds to In-content of 17% in AlInN alloy on GaN, thus our growths of AlInN alloys with In-content ~ 16.44%

on GaN template resulted in nearly-lattice-matched thin film. Note that the XRD rocking curves were obtained by Bragg diffraction along (0002) direction, which was measured along the growth direction of c-axis in wurzite structure. The lattice constant along c-axis (*c*) was calculated from the rocking curve based on the following relation [37]:

$$\frac{c_{GaN} - c_{AlInN}}{c_{GaN}} = -\Delta\theta \cot(\theta_{GaN}) \quad (6\text{-}1).$$

After the parameter *c* was obtained, the In-content and lattice constant along a-axis (*a*) could be described by the linear interpretation as follow:

$$c_{Al_{1-x}In_xN} = x \cdot c_{InN} + (1-x) \cdot c_{AlN} \quad (6\text{-}2a)$$

$$a_{Al_{1-x}In_xN} = x \cdot a_{InN} + (1-x) \cdot a_{AlN} \quad (6\text{-}2b).$$

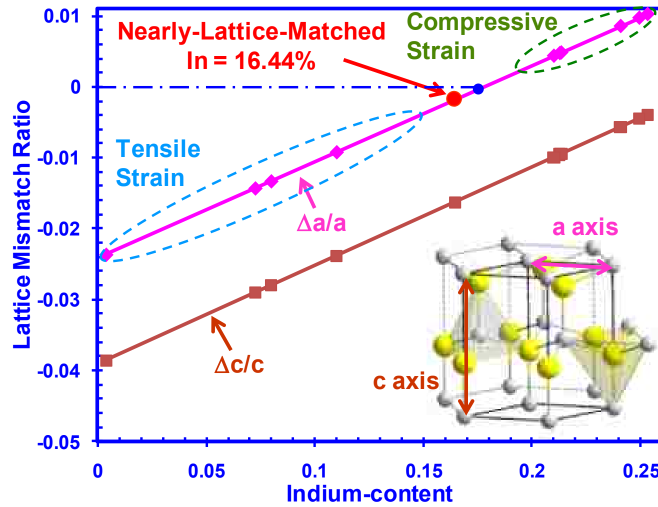

Figure 6-2 *Lattice mismatch ratio of AlInN grown on GaN templates along c-axis and a-axis as a function of the In-contents. The insert shows the wurtzite crystal structure of nitride material system.*

Note that lattice constant (*a*) corresponds to the lattice parameter that determines the lattice matching condition in the growth of c-plane wurtzite semiconductors, specifically AlInN on c-plane GaN template. The strain field between $Al_{1-x}In_xN$ and GaN varied from tensile (x = 0.38%) to compressive (x = 25.32%) with lattice-matched condition obtained at $\Delta a/a$ = -0.18%, which corresponded to a nearly-lattice-matched condition (x = 16.44%).

To further illustrate the effect of strain field in AlInN alloy on the sample surface morphology, the microscope images of the tensile and nearly-lattice-matched AlInN alloys grown on GaN / sapphire templates were compared in figures 6-3(a) and (b). As shown in figure 3(a), the surface morphology of the tensile-strained AlInN with In-content of ~0.38%, which was grown at 860 ^{o}C with the thickness of 0.36 μm, is full of cracks from the tensile strain driven strain relaxation. In contrast, as shown in figure 6-3(b), the nearly-lattice-matched AlInN alloy with thickness of 0.2 μm shows crack-free layer.

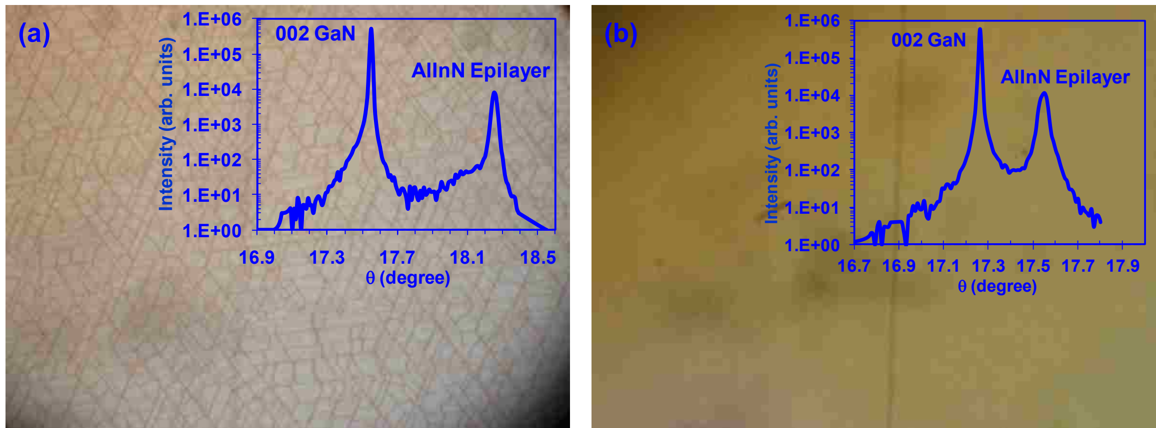

Figure 6-3 *Microscope image comparison of two AlInN samples on GaN/sapphire templates with (a) In-content=0.38% and (b) In-content=16.44%. The insets show the XRD* ω*-2*θ *scans of corresponding AlInN alloys on GaN / sapphire templates.*

6.3 Growth Optimizations of Nearly-Lattice-Matched AlInN on GaN / Sapphire Templates

The growth condition optimization for the lattice-matched AlInN thin film was investigated for samples grown on GaN / sapphire template. Specifically, the effects of various growth parameters on the surface morphology of the nearly-lattice-matched AlInN samples were investigated. In our studies, the growth parameters investigated include growth pressure, V/III ratio, and growth rate. The growth pressure was decreased from 100 Torr down to 20 Torr, while maintaining the V/III ratio of 9314. The V/III ratio was increased afterwards from 5205 up to 9314 with a constant growth pressure of 20 Torr.

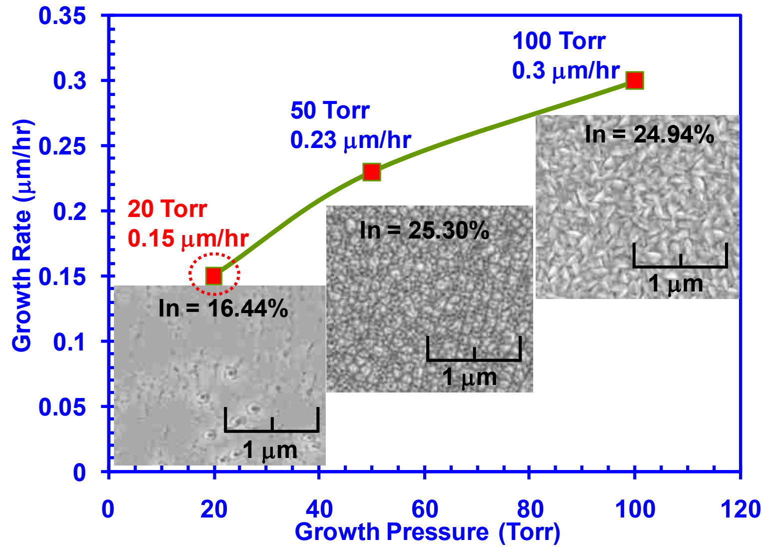

Figure 6-4 *Growth rate and indium content of nearly-lattice-matched AlInN alloys versus the growth pressure for AlInN alloys grown on GaN / sapphire template. The insets show SEM images of the sample surface morphology for the different growth pressures.*

Figure 6-4 shows the effect of the growth pressure on the growth rate and indium incorporation of the AlInN alloys. In this study, the total flow rate was kept the same for the AlInN thin film growths under different growth pressures. The corresponding surface morphology of the AlInN thin film was characterized by SEM measurements, as shown in the insets of figure 6-4. By increasing the growth pressure in the reactor from 20 Torr to 100 Torr, the growth rate of the films was increased from 0.15 μm/hr to 0.3 μm/hr. The use of higher growth pressure and growth rate also led to a higher indium incorporation in the AlInN thin film. Our results indicated that the indium content in the thin films increases from 16.44% to 25% by increasing the growth pressure from 20 Torr up to 100 Torr. The SEM image of the nearly-lattice-matched AlInN with In-content = 16.44%, which was grown at 20 Torr, showed the smoothest surface morphology. In contrast, the growth of AlInN with In-content = 25% performed at higher growth pressure exhibited a grain-like surface profile.

To further confirm the growth pressure effect, atomic force microscopy (AFM) was carried out to measure the AlInN surface roughness, as shown in figure 6-5. The thicknesses of AlInN thin films studied ranged from 0.2 μm up to 0.26 μm over a scanning area of 1 μm x 1 μm. As the

growth pressure was reduced from 100 Torr (50 Torr) to 20 Torr, the root mean square (RMS) surface roughness of AlInN alloys grown on GaN/ sapphire template varied from ~ 5.61 nm (~ 6.84 nm) to ~ 1.01 nm. Thus, both AFM and SEM measurement results confirm that the use of low growth pressure leads to a reduction in the surface roughness of the AlInN film.

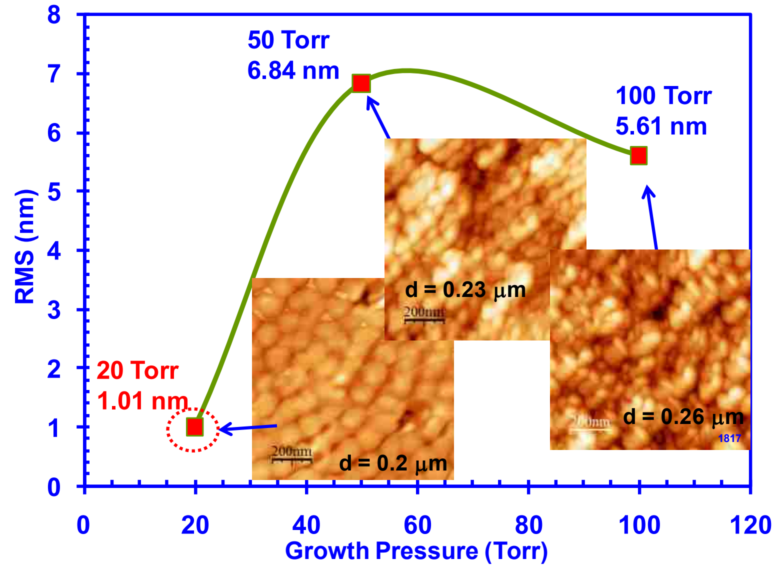

Figure 6-5 *Surface roughness versus growth pressure for AlInN alloys grown on GaN / sapphire template. The inserts show AFM images of the surface morphology of AlInN grown with the different growth pressures.*

Figure 6-6 shows the effect of V/III ratio on the growth rate and surface morphology of the AlInN thin films. In this particular study, the AlInN layers were grown at 780 °C with constant growth pressure of 20 Torr, and the V/III ratio of the epitaxy was increased from 5205 to 9314. The insets in figure 6-6 show the corresponding SEM images of the surface morphologies for the AlInN thin films. By increasing the V/III ratios from 5209 to 9314, the growth rate of the films was decreased from 0.28 μm/hr to 0.15 μm/hr. While the use of higher growth pressure and growth rate was found to lead to a higher indium incorporation in the AlInN thin film, this study showed that the indium content in the AlInN thin films decreased as the V/III ratio increased. The smoothest surface morphology was also observed for the nearly-lattice-matched AlInN film with In-content of 16.44%, which was grown with V/III ratio of 9314, as compared to those measured for AlInN films grown with lower V/III ratios.

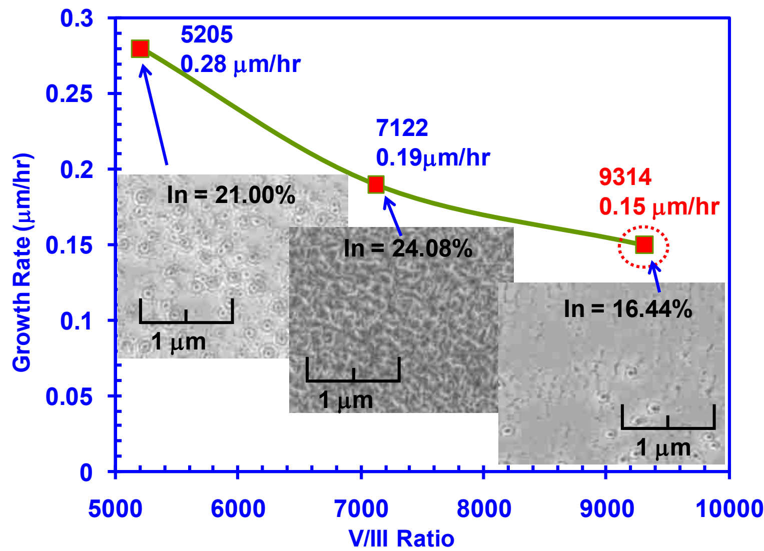

Figure 6-6 *Growth rate and indium content of nearly-lattice-matched AlInN alloys as a function of V/III ratio for AlInN alloys grown on GaN / sapphire template. The insets show the corresponding SEM images for the respective V/III ratio.*

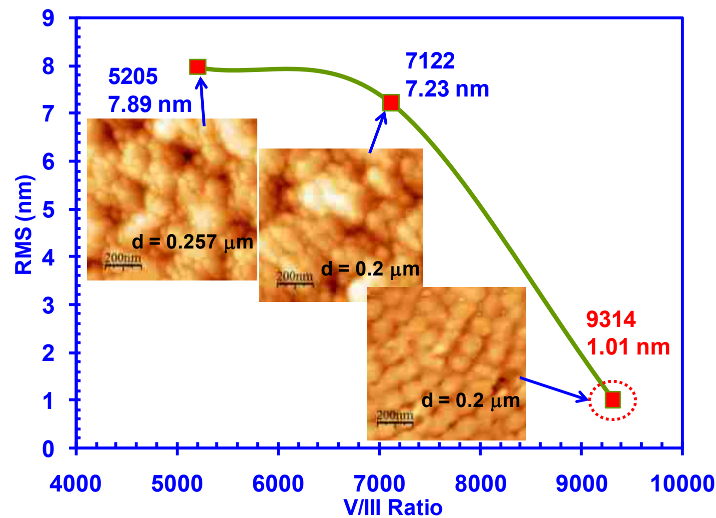

Figure 6-7 *Surface roughness of AlInN grown on GaN/ sapphire template versus the V/III ratio. The insets show the corresponding AFM images for the respective growth pressures and V/III ratio.*

Figure 6-7 shows the AFM measurement results for nearly-lattice-matched AlInN thin film grown at different V/III ratios. The thicknesses of AlInN thin films studied ranged from 0.2 μm up to 0.26 μm with a scanning area of 1 μm x 1 μm. As the V/III ratio was increased from 5205 (7122) to 9314, the root mean square (RMS) surface roughness of AlInN alloys grown on GaN/ sapphire template varied from ~ 7.89 nm (~ 7.23 nm) to ~ 1.01 nm. Thus, the use of high V/III ratio and low

growth pressure in the epitaxy of AlInN thin film lead to a reduction in the surface roughness of the grown film.

6.4 Electrical Characteristics of AlInN on GaN Templates

The electrical characteristics, including sheet resistivity, electron mobility and carrier concentration of $Al_{1-x}In_xN$ alloys on GaN templates on sapphire substrates were characterized by employing Van der Pauw Hall method [22]. Table 6-2 shows the summary of the Hall measurement data of four AlInN thin films with various indium contents. As shown in Table 6-2, the sheet resistivity of the AlInN film decreases from ~ 7×10^4 Ω/cm^2 to 341 Ω/cm^2, as the In-content was increased from 0.4% to 21%.

In-content (x) of $Al_{1-x}In_xN$	Thickness of $Al_{1-x}In_xN$ (μm)	Sheet Resistivity (Ω/cm^2)	Hall Mobility ($cm^2/(V*s)$)	Bulk Concentration (cm^{-3})
0.00399	0.36	69658	18	-1.4E+17
0.11	0.23	937	269	-1.1E+18
0.17	0.207	412	462	-1.6E+18
0.21	0.208	341	400	-2.2E+18

Table 6-2 *Hall measurement results of $Al_{1-x}In_xN$ alloy on GaN / sapphire templates.*

In our finding, the electron mobilities for the AlInN films show increasing trend for higher In-content films. However, the nearly-lattice-matched AlInN alloy with In-content of 17% exhibits the highest electron mobility among all measured samples, presumably attributed to the improved material quality leading to a reduction in scattering processes in the film. The bulk n-type concentrations are measured in the range of ~ 10^{18} cm^{-3} for AlInN with In-contents in the range of 11% - 21%, while the n-type background concentration of ~ 10^{17} cm^{-3} was measured for the AlInN film with In-content of 0.4%. Further improvement of the material quality is still required in order to

achieve higher carrier mobility and lower background carrier concentration. Note that the low In-content $Al_{1-x}In_xN$ thin film has cracks resulting from strain relaxation. Specifically, the Hall measurements are less reliable for the $Al_{1-x}In_xN$ with x = 0.399% since conduction paths within the film are broken.

6.5 Growth of Nearly-Lattice-Matched AlInN Alloy on GaN Native Substrate

6.5.1 Growth of Nearly-Lattice-Matched AlInN Alloy on GaN Native Substrate

The growth optimization studies were also carried out of nearly-lattice-matched AlInN alloys on GaN free-standing substrate (Kyma Technologies) for comparison purpose. Figure 8 shows the effect of growth pressure and V/III ratio on the material quality of AlInN thin film on GaN native substrates. In figure 6-8(a), the growth pressure was reduced from 100 Torr (50 Torr) to 20 Torr, which is analogous to the studies discussed in figures 6-4 and 6-5. The surface roughness of AlInN alloys on GaN substrates decreased from 5.93 nm (6.36 nm) to only 0.89 nm. The insets exhibit the sample surface morphology characterized by SEM measurements. The comparison of the SEM images indicates that the use of low growth pressure leads to a smoother surface of the AlInN thin film as compared to those grown under higher growth pressure, which is in good agreement with the finding from the growths on GaN / sapphire template.

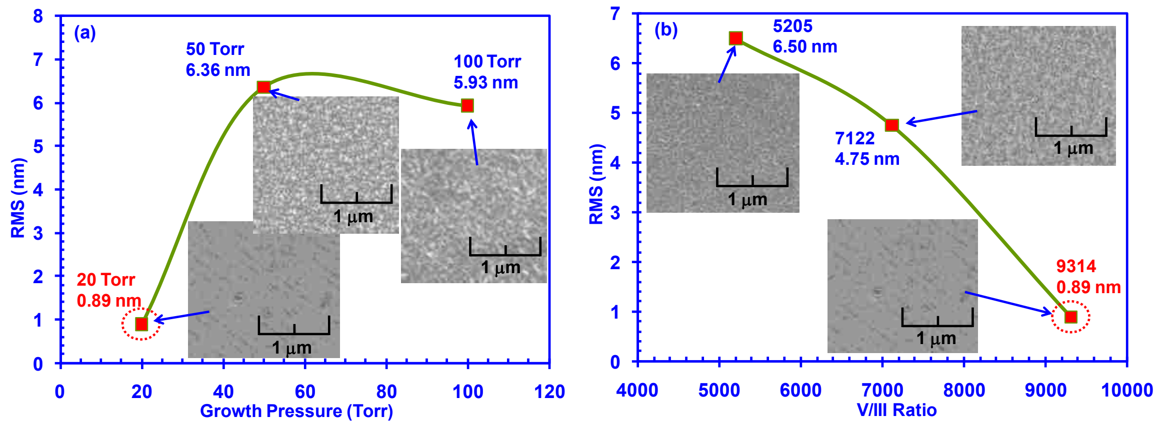

Figure 6-8 *Surface roughness as a function of: (a) growth pressure and (b) V/III ratio for AlInN grown on free-standing GaN substrate on sample surface roughness with the insets show the corresponding SEM images for the respective growth pressures and V/III ratio.*

Figure 6-8(b) shows the AFM RMS roughness and SEM images as a function of V/III ratio to illustrate the surface morphology of the AlInN layers grown on GaN native substrate. As the V/III ratio increased from 5205 (7122) to 9314, the roughness for AlInN alloys on GaN substrates decreased from 6.5 nm (4.75 nm) and 0.89 nm. Both the AFM and SEM results indicate that the use of higher V/III ratio resulted in improved surface morphology of the AlInN grown on GaN native substrate, which is in good agreement with the finding for the material grown on GaN / sapphire template.

6.5.2 Morphology Comparison of AlInN on GaN Substrates and GaN / Sapphire Virtual Templates

Figure 6-9 shows the comparison of the SEM images of 0.2 μm thick nearly-lattice-matched AlInN thin film grown on GaN template on sapphire substrate (sample 1804) and on GaN native substrate (sample #1805) under the identical optimized growth conditions with growth temperature of 780 ^{o}C, growth pressure of 20 Torr, and V/III ratio of 9314. The SEM images exhibited very similar surface morphology for both AlInN samples, marked by the existence of V-defects on the film similar to the finding reported in the literatures [38-40]. The V-defect densities were estimated as ~ $4x10^{8}$ cm^{-2} and ~ $3x10^{8}$ cm^{-2} on sample #1804 (on GaN / sapphire template) and sample #1805 (on GaN native substrate), respectively. The AFM measurements indicated a slightly smaller RMS roughness of about 0.89 nm on the nearly-lattice-matched AlInN grown on GaN substrate (#1805), in comparison to the RMS roughness of 1.01 nm for the sample grown on GaN / sapphire template (#1804). Thus, both AFM and SEM measurements showed that the use of GaN native substrate led to the growths of AlInN thin film with improved surface morphology. The surface morphologies of the AlInN thin films are very similar to those reported in the literatures [35, 40]. The RMS roughness from 0.2 μm thick nearly-lattice-matched AlInN films grown on both GaN / sapphire template and GaN substrate are in good agreement with the reported data in the literature for MOVPE-grown AlInN [32, 33, 35, 40-43].

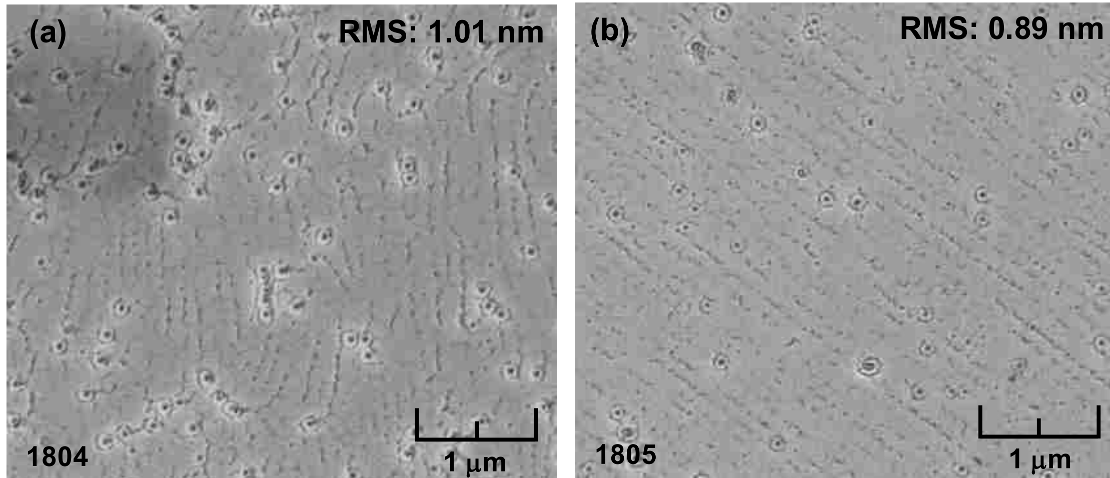

Figure 6-9 *SEM images of surface morphology of 0.2-μm-thick nearly-lattice-matched AlInN thin film grown on: (a) GaN / sapphire template (#1804) and (b) GaN free-standing substrate (#1805).*

Figure 6-10 shows the XRD rocking curves for samples #1804 and #1805 around the (002) reflection. The angle separations of AlInN epilayer and GaN peaks were 1044 arcsec and 900 arcsec for sample #1804 and #1805, which corresponded to In-contents of 16.44% and 18.05%, respectively. The discrepancy in the In-content for the two samples grown under the same growth conditions could be attributed to the different thermal conductivity and wafer thicknesses of these two substrates (GaN / sapphire template and GaN native substrate). The GaN native substrate has higher thermal conductivity and thicker substrate thickness ($d_{GaN_substrate}$ = 470 μm) in comparison to those of sapphire ($d_{sapphire}$ = 430 μm), which could lead to a slightly different surface temperature during the epitaxy of the AlInN film. As shown in the figure 6-10, the FWHMs of the GaN XRD rocking curves (ω-2θ scans) around (002) reflection of GaN for samples #1804 and #1805 are 31.2 arcsec and 25.6 arcsec, respectively. The FWHMs of the AlInN XRD rocking curves (ω-2θ scans) for samples #1804 and #1805 are 134 arcsec and 91 arcsec, respectively, which are among the best results reported in literature [65, 66, 69]. This finding indicates that the use of free-standing GaN substrate led to the growths of AlInN alloy with improved crystal quality. Note that differences in In-contents of AlInN on sample #1804 and #1805 is considerably small enough (~1.61%) to assume that the FWHMs would not be affected by the different In-contents in the film.

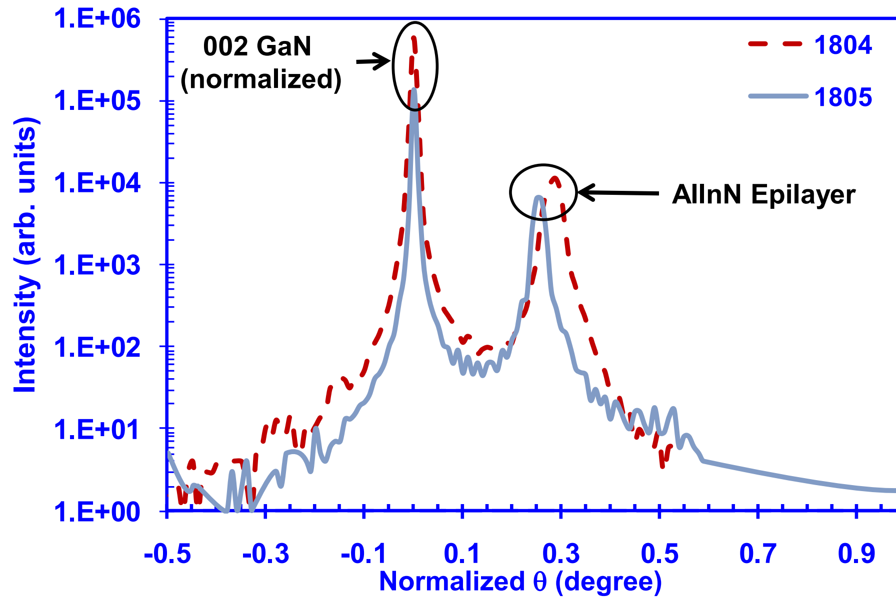

Figure 6-10 *XRD ω-2θ scans for nearly-lattice-matched AlInN on GaN / sapphire template (#1804) and on GaN free-standing substrate (#1805).*

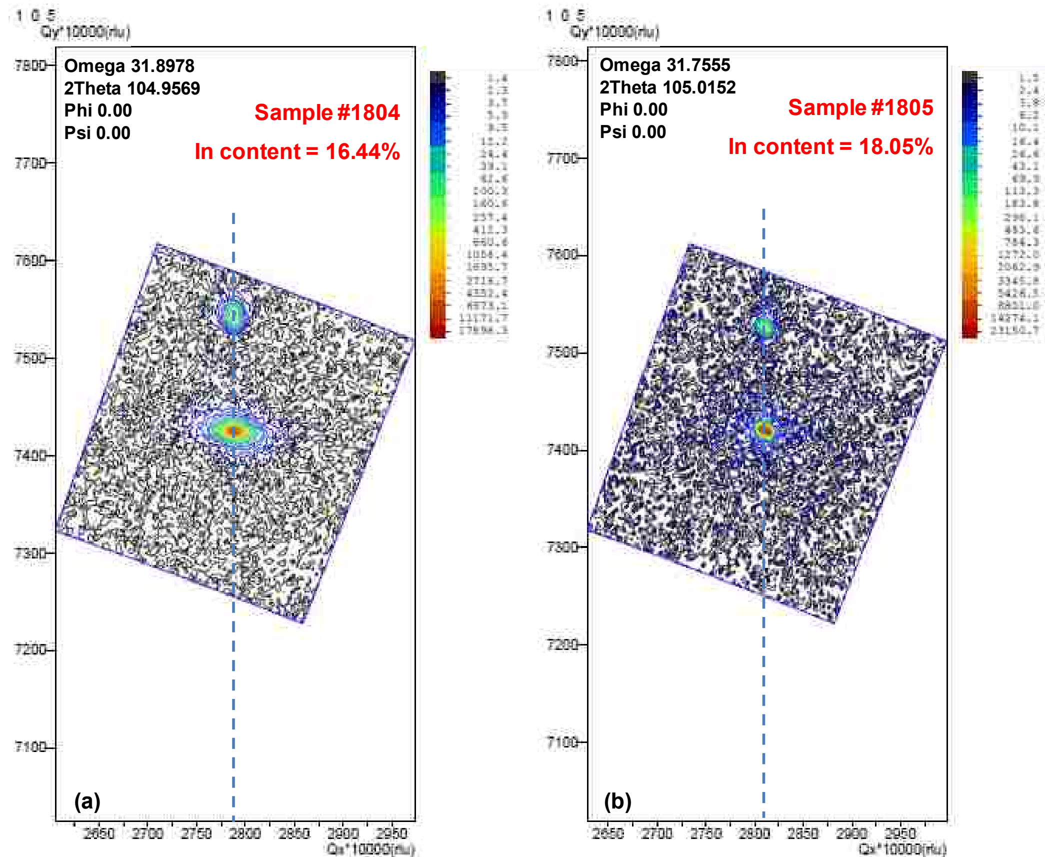

Figure 6-11 *Reciprocal space map around the (105) reflection of the nearly-lattice-matched AlInN on (a) GaN /sapphire template (#1804) and (b) GaN free-standing substrate.*

Figure 6-11 shows the reciprocal space map around the (105) reflection of the nearly-lattice-matched AlInN on (a) GaN/ sapphire template (#1804) with In content = 16.44% and (b) GaN free-standing substrate (#1805) with In content = 18.05%. As shown in figures 6-11(a) and 6-11(b), the Bragg reflections of the AlInN thin film and GaN are vertically aligned with respect to each other at the same in-plane Q_x values. The finding in figures 6-11(a) and 6-11(b) show that the nearly-lattice-matched AlInN epitaxial layers as grown pseudomorphically on both GaN / sapphire template and GaN free-standing substrate, respectively.

6.6 Photoluminescence Measurements of AlInN / GaN Heterostructures

The photoluminescence (PL) measurement has been carried out on the 0.2-μm-thick nearly-lattice-matched AlInN alloy layers grown on GaN/sapphire template (sample 1804) and on GaN native substrate (sample 1805) at the same growth condition. By frequency-quadrupling the output of the Ti:sapphire oscillator at 840 nm, a pump beam with the photon energy of 5.904 eV (210 nm) was focused on each AlInN epilayer at an average pump intensity of 505 W/cm2. The sample was mounted inside a cryostat with the temperature being varied in the range of 4.5 K - 300 K. The PL signals were collected by a pair of the lenses, sent through a spectrometer, and measured by a PMT.

Figure 6-12 shows the PL spectra of sample 1804 and sample 1805 recorded at 4.5 K and at 300 K in (a) and (b), respectively. The peak wavelengths in the low-temperature spectra [figure 6-8(a)] appear at 336 nm for sample #1804 and at 344 nm for sample #1805 which corresponds to the peak photon energy of 3.806 eV for sample #1804 and 3.69 eV for sample #1805, respectively. The energy difference of 16 meV can be attributed to the difference in the In-content and thus different bandgaps. The peak intensity of sample #1805 is approximately 75% higher than that of sample #1804 most likely due to the improved material quality of the AlInN alloy on GaN substrate. The PL linewidths were determined to be about 28.8 nm for sample #1804 and about 31.2 nm for sample #1805 at 4.5 K, respectively. The sharp peaks at about 360 nm were coming from the photon emission from the GaN template / bulk underneath the AlInN epilayer. The room temperature PL spectra [figure 6-12(b)] show broad emission bands at wavelength of

331 nm for sample #1804 and 347.4 nm for sample #1805, representing the peak photon energy of 3.746 eV and 3.596 eV, respectively. The red-shift of 60 meV from sample #1804 and 94 meV from sample #1805 is due to the increase of the AlInN bandgap from low temperature (4.5 K) to room temperature (300 K). At 300 K, the peak intensity is about 8% higher and the total PL intensity is about 24% higher from the sample grown on bulk GaN with respect to these from the sample grown on GaN template. The PL linewidths were measured as about 30 nm and 32.8 nm for the two samples at 300K, respectively.

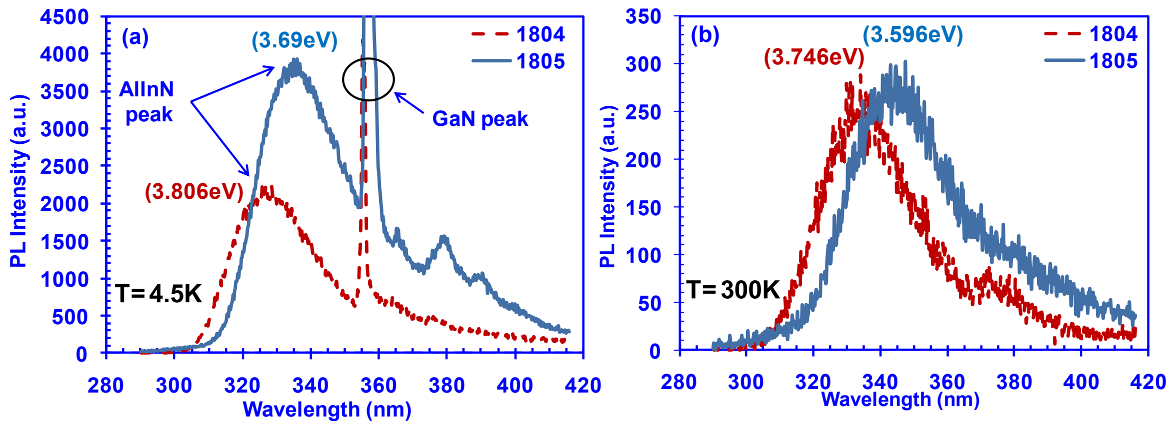

Figure 6-12 *PL spectra measured for lattice-matched AlInN on GaN/ sapphire template and GaN substrate at T = (a) 4.5 K and (b) 300 K.*

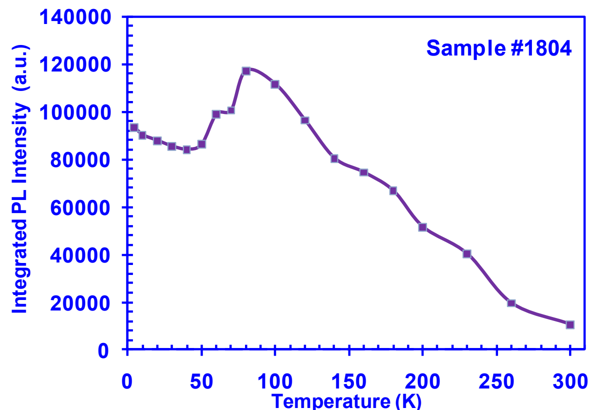

Figure 6-13 *The integrated PL intensities as a function of the temperature for AlInN alloy grown on GaN / sapphire substrate.*

The integrated PL intensity for the lattice matched AlInN alloy on GaN/ sapphire template (sample 1804) as a function of ambience temperature was plotted in figure 6-13. At low temperature, T < 40 K, a significant fraction of the photon-generated carriers was trapped into the

defects, and eventually recombined nonradiatively at the defects, leading to the reduction of PL intensity with increasing temperature. For T = 40 K- 80 K, the PL intensity increased with increasing temperature due to the release of carriers from the defects that then radiatively recombined in the bulk with higher thermal energy. The reduction of the PL intensity with further temperature increase from 80 K to 300 K is due to the increase of the nonradiative process as a result of thermal excitation.

6.6 MOVPE of InN Alloy by Pulsed Growth Mode

High quality InN alloy is of great importance for optoelectronics and photovoltaic applications. Specifically, in this report, the realization of InGaN-delta-InN QW LEDs requires the growth of couple monolayer InN with high quality. InN thin films have been prepared using MOVPE [44-47] or MBE techniques [48-50]. Previously, pulsing growth mode were employed for high quality InN bulk growth in MOVPE chamber [44-46]. Figure 6-14 shows the TMIn and NH_3 flow rate profile using the growth of InN bulk [45]. The TMIn source flow is turned on and off periodically while the NH_3 flow can be kept constant. The InN material would be formed with droplets during the ON period (36 s) and the droplet will be etched away by H_2 from the decomposition of NH_3 during the OFF period (18 s). Thus, the high quality InN with smooth surface can be formed.

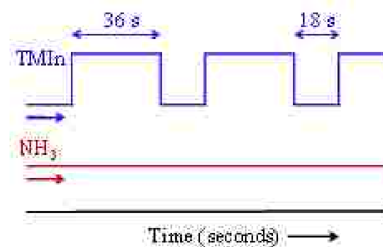

Figure 6-14 *TMIn and NH_3 profile of InN pulse growth mode with ON:OFF = 36s:18s [45].*

Figure 6-15 illustrates the SEM images of InN with and without In-droplet when the growth condition varies [44]. The growth condition of ON/OFF times, the V/III, the growth temperatures and so on can be optimized for the integration of InN delta layer inside the InGaN QW for the radiative recombination rate enhancement.

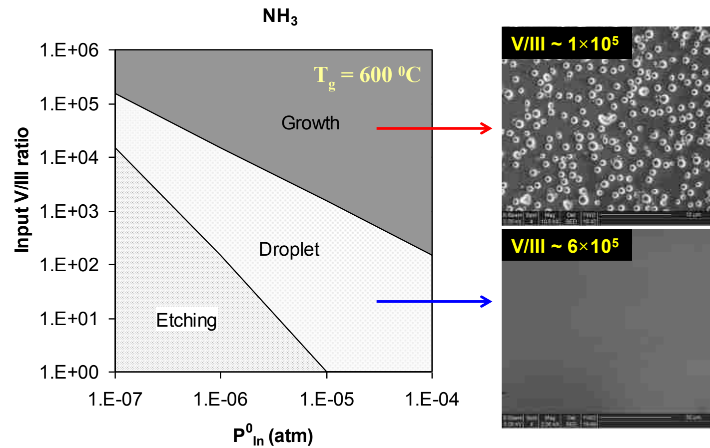

Figure 6-15 *The effect of growth condition on the surface morphology of InN thin film on GaN template [44].*

References of Chapter 6:

1. H. P. Zhao, G. Y. Liu, R. A. Arif, and N. Tansu, "Current injection efficiency induced efficiency-droop in InGaN quantum well light-emitting diodes," *Solid-State Electronics,* vol. 54, pp. 1119-1124, Oct 2010.
2. H. P. Zhao, G. Y. Liu, J. Zhang, J. D. Poplawsky, V. Dierolf, and N. Tansu, "Approaches for high internal quantum efficiency green InGaN light-emitting diodes with large overlap quantum wells," *Optics Express,* vol. 19, pp. A991-A1007, Jul 4 2011.
3. H. P. Zhao, G. Y. Liu, and N. Tansu, "Analysis of InGaN-delta-InN quantum wells for light-emitting diodes," *Appl. Phys. Lett.,* vol. 97, Sep 27 2010.
4. H. P. Zhao and N. Tansu, "Optical gain characteristics of staggered InGaN quantum wells lasers," *J. Appl. Phys.,* vol. 107, Jun 1 2010.
5. J. Zhang, H. P. Zhao, and N. Tansu, "Large optical gain AlGaN-delta-GaN quantum wells laser active regions in mid-and deep-ultraviolet spectral regimes," *Appl. Phys. Lett.,* vol. 98, Apr 25 2011.
6. G. Y. Liu, H. P. Zhao, J. Zhang, J. H. Park, L. J. Mawst, and N. Tansu, "Selective area epitaxy of ultra-high density InGaN quantum dots by diblock copolymer lithography," *Nanoscale Res. Lett.,* vol. 6, Apr 15 2011.
7. X. H. Li, R. B. Song, Y. K. Ee, P. Kumnorkaew, J. F. Gilchrist, and N. Tansu, "Light Extraction Efficiency and Radiation Patterns of III-Nitride Light-Emitting Diodes With Colloidal Microlens Arrays With Various Aspect Ratios," *IEEE Photonics Journal,* vol. 3, pp. 489-499, Jun 2011.
8. H. J. Kim, S. Choi, S. S. Kim, J. H. Ryou, P. D. Yoder, R. D. Dupuis, A. M. Fischer, K. W. Sun, and F. A. Ponce, "Improvement of quantum efficiency by employing active-layer-friendly lattice-matched InAlN electron blocking layer in green light-emitting diodes," *Appl. Phys. Lett.,* vol. 96, Mar 8 2010.

9. S. Choi, H. J. Kim, S. S. Kim, J. Liu, J. Kim, J. H. Ryou, R. D. Dupuis, A. M. Fischer, and F. A. Ponce, "Improvement of peak quantum efficiency and efficiency droop in III-nitride visible light-emitting diodes with an InAlN electron-blocking layer," *Appl. Phys. Lett.,* vol. 96, May 31 2010.

10. Z. T. Chen, S. X. Tan, Y. Sakai, and T. Egawa, "Improved performance of InAlN-based Schottky solar-blind photodiodes," *Appl. Phys. Lett.,* vol. 94, p. 213504, 2009.

11. J. Dorsaz, J.-F. Carlin, S. Gradecak, and M. Ilegems, "Progress in AlInN--GaN Bragg reflectors: Application to a microcavity light emitting diode," *J. Appl. Phys.,* vol. 97, p. 084505, 2005.

12. G. Cosendey, J. F. Carlin, N. A. K. Kaufmann, R. Butte, and N. Grandjean, "Strain compensation in AlInN/GaN multilayers on GaN substrates: Application to the realization of defect-free Bragg reflectors," *Appl. Phys. Lett.,* vol. 98, May 2 2011.

13. S. Nicolay, J.-F. Carlin, E. Feltin, R. Butte, M. Mosca, N. Grandjean, M. Ilegems, M. Tchernycheva, L. Nevou, and F. H. Julien, "Midinfrared intersubband absorption in lattice-matched AlInN/GaN multiple quantum wells," *Appl. Phys. Lett.,* vol. 87, p. 111106, 2005.

14. M. Gonschorek, J. F. Carlin, E. Feltin, M. A. Py, and N. Grandjean, "High electron mobility lattice-matched AlInN/GaN field-effect transistor heterostructures," *Appl. Phys. Lett.,* vol. 89, p. 062106, Aug 7 2006.

15. J. Xie, X. Ni, M. Wu, J. H. Leach, U. Ozgur, and H. Morkoc, "High electron mobility in nearly lattice-matched AlInN/AlN/GaN heterostructure field effect transistors," *Appl. Phys. Lett.,* vol. 91, p. 132116, 2007.

16. A. Dadgar, F. Schulze, J. Blasing, A. Diez, A. Krost, M. Neuburger, E. Kohn, I. Daumiller, and M. Kunze, "High-sheet-charge-carrier-density AlInN/GaN field-effect transistors on Si(111)," *Appl. Phys. Lett.,* vol. 85, pp. 5400-5402, Nov 29 2004.

17. M. Higashiwaki and T. Matsui, "InAlN/GaN heterostructure field-effect transistors grown by plasma-assisted molecular-beam epitaxy," *Japanese J. Appl. Phys. Part 2-Letters & Express Letters,* vol. 43, pp. L768-L770, Jun 15 2004.

18. M. Higashiwaki, T. Mimura, and T. Matsui, "High-performance short-gate InAlN/GaN heterostructure field-effect transistors," *Japanese J. Appl. Phys. Part 2-Letters & Express Letters,* vol. 45, pp. L843-L845, Aug 2006.

19. J. Kuzmik, "InAlN/(In)GaN high electron mobility transistors: some aspects of the quantum well heterostructure proposal," *Semiconductor Science and Technology,* vol. 17, pp. 540-544, Jun 2002.

20. H. Tong, J. Zhang, G. Y. Liu, J. A. Herbsommer, G. S. Huang, and N. Tansu, "Thermoelectric properties of lattice-matched AlInN alloy grown by metal organic chemical vapor deposition," *Appl. Phys. Lett.,* vol. 97, p. 112105, Sep 13 2010.

21. J. Zhang, S. Kutlu, G. Y. Liu, and N. Tansu, "High-temperature characteristics of Seebeck coefficients for AlInN alloys grown by metalorganic vapor phase epitaxy," *J. Appl. Phys.,* vol. 110, Aug 15 2011.

22. J. Zhang, H. Tong, G. Y. Liu, J. A. Herbsommer, G. S. Huang, and N. Tansu, "Characterizations of Seebeck coefficients and thermoelectric figures of merit for AlInN alloys

with various In-contents," *J. Appl. Phys.,* vol. 109, Mar 1 2011.

23. L. F. Jiang, W. Z. Shen, and Q. X. Guo, "Temperature dependence of the optical properties of AlInN," *J. Appl. Phys.,* vol. 106, pp. 013515-8, 2009.
24. S. Yamaguchi, R. Izaki, Y. Iwamura, and A. Yamamoto, "Thermoelectric and thermal properties of AlInN thin films prepared by reactive radio-frequency sputtering," *physica status solidi (a),* vol. 201, pp. 225-228, 2004.
25. R. E. Jones, R. Broesler, K. M. Yu, J. W. Ager, III, E. E. Haller, W. Walukiewicz, X. Chen, and W. J. Schaff, "Band gap bowing parameter of $In_{1-x}Al_xN$," *J. Appl. Phys.,* vol. 104, p. 123501, 2008.
26. S. Iwata, Y. Nanjo, T. Okuno, S. Kurai, and T. Taguchi, "Growth and luminescence properties of subsequently grown AlInN layers on AlN homoepitaxial layers by ammonia gas source molecular beam epitaxy," *Japanese J. Appl. Phys. Part 1-Regular Papers Brief Communications & Review Papers,* vol. 46, pp. 3394-3396, Jun 2007.
27. Z. GaCevic, S. Fernandez-Garrido, J. M. Rebled, S. Estrade, F. Peiro, and E. Calleja, "High quality InAlN single layers lattice-matched to GaN grown by molecular beam epitaxy," *Appl. Phys. Lett.,* vol. 99, p. 031103, 2011.
28. Z. L. Miao, T. J. Yu, F. J. Xu, J. Song, C. C. Huang, X. Q. Wang, Z. J. Yang, G. Y. Zhang, X. P. Zhang, D. P. Yu, and B. Shen, "The origin and evolution of V-defects in In(x)Al(1-x)N epilayers grown by metalorganic chemical vapor deposition," *Appl. Phys. Lett.,* vol. 95, Dec 7 2009.
29. H. P. D. Schenk, M. Nemoz, M. Korytov, P. Vennegues, A. D. Drager, and A. Hangleiter, "Indium incorporation dynamics into AlInN ternary alloys for laser structures lattice matched to GaN," *Appl. Phys. Lett.,* vol. 93, Aug 25 2008.
30. H. Kim-Chauveau, P. de Mierry, J. M. Chauveau, and J. Y. Duboz, "The influence of various MOCVD parameters on the growth of Al(1-x)In(x)N ternary alloy on GaN templates," *J. Crys. Growth,* vol. 316, pp. 30-36, Feb 1 2011.
31. D. F. Brown, S. Keller, T. E. Mates, J. S. Speck, S. P. DenBaars, and U. K. Mishra, "Growth and characterization of In-polar and N-polar InAlN by metal organic chemical vapor deposition," *J. Appl. Phys.,* vol. 107, Feb 2010.
32. R. B. Chung, F. Wu, R. Shivaraman, S. Keller, S. P. DenBaars, J. S. Speck, and S. Nakamura, "Growth study and impurity characterization of Al(x)In(1-x)N grown by metal organic chemical vapor deposition," *J. Crys. Growth,* vol. 324, pp. 163-167, Jun 1 2011.
33. T. C. Sadler, M. J. Kappers, and R. A. Oliver, "The impact of hydrogen on indium incorporation and surface accumulation in InAlN epitaxy," *J. Crys. Growth,* vol. 331, pp. 4-7, Sep 15 2011.
34. G. Liu, J. Zhang, X.-H. Li, G. S. Huang, T. Paskova, K. R. Evans, H. Zhao, and N. Tansu, "Metalorganic vapor phase epitaxy and characterizations of nearly-lattice-matched AlInN alloys on GaN/sapphire templates and free-standing GaN substrates," *J. Crys. Growth,* vol. 340, pp. 66-73, 2012.
35. C. Hums, A. Gadanecz, A. Dadgar, J. Bläsing, H. Witte, T. Hempel, A. Dietz, P. Lorenz, S. Krischok, and J. A. Schaefer, "MOVPE growth and characterization of AlInN FET structures

on Si (111)," *Advances in GaN, GaAs, SiC and related alloys on silicon substrates,* vol. 1068, 2008.

36. T. Paskova and K. R. Evans, "GaN Substrates—Progress, Status, and Prospects," *IEEE J. Sel. Top. Quantum Electron.,* vol. 15, pp. 1041-1052, 2009.
37. X. Zhang, P. Li, D. Parent, G. Zhao, J. Ayers, and F. Jain, "Comparison of X-ray diffraction methods for determination of the critical layer thickness for dislocation multiplication," *Journal of Electronic Materials,* vol. 28, pp. 553-558, 1999.
38. Z. L. Miao, T. J. Yu, F. J. Xu, J. Song, C. C. Huang, X. Q. Wang, Z. J. Yang, G. Y. Zhang, X. P. Zhang, D. P. Yu, and B. Shen, "The origin and evolution of V-defects in InxAl1-xN epilayers grown by metalorganic chemical vapor deposition," *Appl. Phys. Lett.,* vol. 95, Dec 7 2009.
39. R. B. Chung, F. Wu, R. Shivaraman, S. Keller, S. P. DenBaars, J. S. Speck, and S. Nakamura, "Growth study and impurity characterization of AlxIn1-xN grown by metal organic chemical vapor deposition," *J. Crys. Growth,* vol. 324, pp. 163-167, Jun 1 2011.
40. H. Kim-Chauveau, P. de Mierry, J. M. Chauveau, and J. Y. Duboz, "The influence of various MOCVD parameters on the growth of Al1-xInxN ternary alloy on GaN templates," *J. Crys. Growth,* vol. 316, pp. 30-36, Feb 1 2011.
41. K. Bejtka, R. W. Martin, I. M. Watson, S. Ndiaye, and M. Leroux, "Growth and optical and structural characterizations of GaN on freestanding GaN substrates with an (Al,In)N insertion layer," *Appl. Phys. Lett.,* vol. 89, Nov 6 2006.
42. D. F. Brown, S. Keller, T. E. Mates, J. S. Speck, S. P. DenBaars, and U. K. Mishra, "Growth and characterization of In-polar and N-polar InAlN by metal organic chemical vapor deposition," *J. Appl. Phys.,* vol. 107, p. 033509, 2010.
43. G. Cosendey, J.-F. Carlin, N. A. K. Kaufmann, R. Butte, and N. Grandjean, "Strain compensation in AlInN/GaN multilayers on GaN substrates: Application to the realization of defect-free Bragg reflectors," *Appl. Phys. Lett.,* vol. 98, p. 181111, 2011.
44. M. Jamil, R. A. Arif, Y. K. Ee, H. Tong, J. B. Higgins, and N. Tansu, "MOVPE of InN films on GaN templates grown on sapphire and silicon (111) substrates," *Physica Status Solidi a-Applications and Materials Science,* vol. 205, pp. 1619-1624, Jul 2008.
45. M. Jamil, H. P. Zhao, J. B. Higgins, and N. Tansu, "MOVPE and photoluminescence of narrow band gap (0.77 eV) InN on GaN/sapphire by pulsed growth mode," *Physica Status Solidi a-Applications and Materials Science,* vol. 205, pp. 2886-2891, Dec 2008.
46. M. Jamil, H. P. Zhao, J. B. Higgins, and N. Tansu, "Influence of growth temperature and V/III ratio on the optical characteristics of narrow band gap (0.77 eV) InN grown on GaN/sapphire using pulsed MOVPE," *J. Crys. Growth,* vol. 310, pp. 4947-4953, Nov 15 2008.
47. N. Khan, A. Sedhain, J. Li, J. Y. Lin, and H. X. Jiang, "High mobility InN epilayers grown on AlN epilayer templates," *Appl. Phys. Lett.,* vol. 92, p. 172101, 2008.
48. J. Wu, W. Walukiewicz, K. M. Yu, W. Shan, J. W. A. III, E. E. Haller, H. Lu, W. J. Schaff, W. K. Metzger, and S. Kurtz, "Superior radiation resistance of In[sub 1 - x]Ga[sub x]N alloys: Full-solar-spectrum photovoltaic material system," *J. Appl. Phys.,* vol. 94, pp. 6477-6482, 2003.

49. G. Koblmuller, C. S. Gallinat, S. Bernardis, J. S. Speck, G. D. Chern, E. D. Readinger, H. Shen, and M. Wraback, "Optimization of the surface and structural quality of N-face InN grown by molecular beam epitaxy," *Appl. Phys. Lett.,* vol. 89, p. 071902, 2006.

50. X. Wang, S. Liu, D. Ma, X. Zheng, G. Chen, F. Xu, N. Tang, B. Shen, P. Zhang, X. Cao, B. Wang, S. Huang, K. J. Chen, S. Zhou, and A. Yoshikawa, "Fe-doped InN layers grown by molecular beam epitaxy," *Appl. Phys. Lett.,* vol. 101, p. 171905, 2012.

Chapter 7: Device Characterizations of InGaN-AlInN QWs LEDs for Efficiency Droop Suppression and LEDs with Large-Overlap Design for Green LEDs

7.1 Fabrication of InGaN QW LEDs with AlInN Thin Barrier

The experimental realization of InGaN QW LEDs with the insertion of AlInN thin barrier was carried out after the optimized lattice-matched AlInN alloy was obtained in Chapter 6. Figure 7-1 shows the schematics of same 2.88 nm InGaN QW with three different barrier designs. They includes 1) 10 nm GaN barriers (sample #1 of conventional InGaN QWs LEDs), 2) 1 nm direct AlInN thin barrier layer followed by 10 nm GaN barrier layers (sample #2 of InGaN-AlInN QWs LEDs) and 3) 0.5 nm GaN spacer layer between the region of InGaN QW and the AlInN thin barrier (sample #3 of InGaN-GaN-AlInN QWs LEDs). Four periods of the three types of active regions were grown and fabricated into bottom-emitting devices.

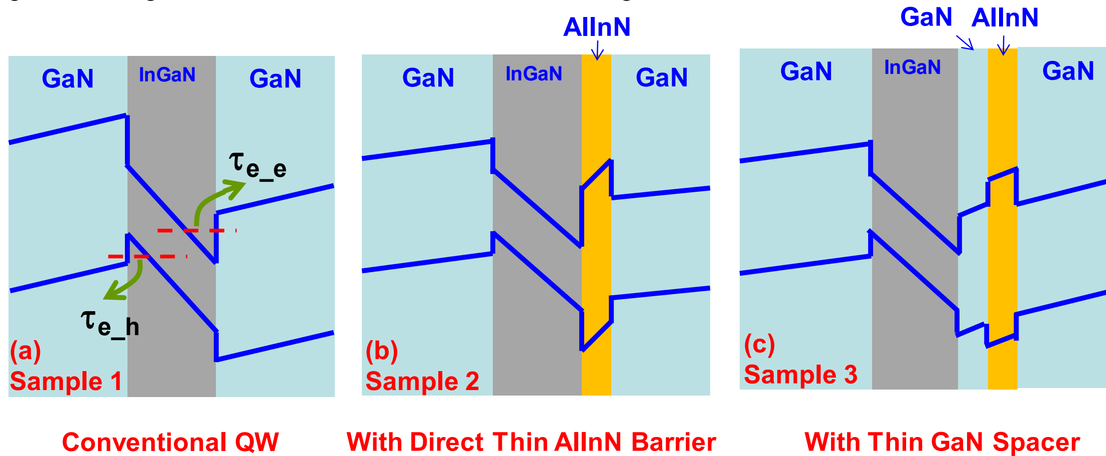

Figure 7-1 *Schematics of fabricated InGaN QWs LEDs with three different barrier designs of a) 10 nm GaN barrier (sample #1 of conventional InGaN QWs LEDs), b) direct 1 nm AlInN thin barrier followed by 10 nm GaN barrier (sample #2 of InGaN-AlInN QWs LEDs) and c) 0.5 nm GaN spacer followed 1 nm AlInN thin barrier and 10 nm GaN barrier (sample #3 of InGaN-GaN-AlInN QWs LEDs).*

Figure 7-2 shows the real growth temperature profile of InGaN QW with the insertion of AlInN alloy in the barrier. The InGaN QWs region and the majority of GaN barriers were grown at the temperature of 733 °C and the chamber pressure of 200 Torr with the growth rates of 1.6 nm/min and 1.5 nm/min, respectively. The growth of AlInN thin barrier is carried out at growth pressure of 20 Torr and growth temperature of 739 °C to 748 °C with a growth rate of 2.5 nm/min. For sample

#2 (InGaN-AlInN LEDs), the insertion of the AlInN thin barrier layer on top of InGaN QW layer were performed after the 48-second transition period, as the growth pressure reduced from 200 Torr to 20 Torr and the growth temperature increased from 733 °C to 740 °C. For sample #3 (InGaN-GaN-AlInN LEDs), the growth of 0.5 nm GaN spacer layer was carried out during the 48-sec period of pressure and temperature grading.

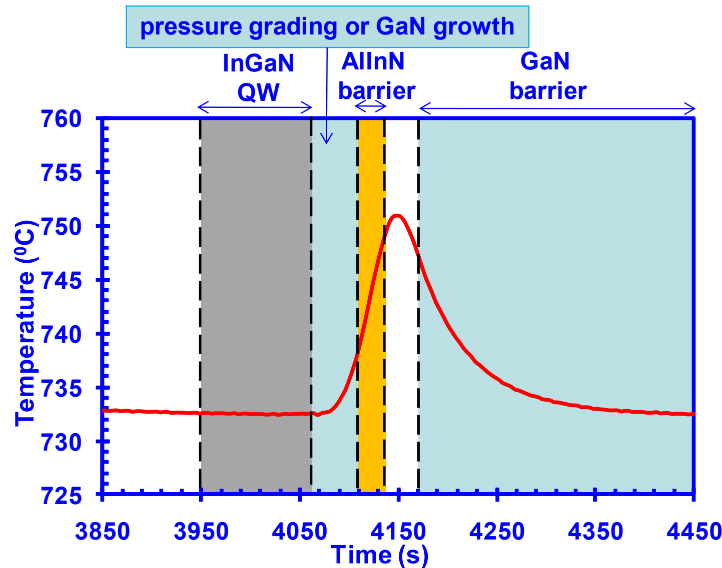

Figure 7-2 *Real growth temperature profile of InGaN-AlInN QWs LEDs with 48 sec pressure grading and InGaN-GaN-AlInN QWs LEDs with the growth of 0.5 nm GaN spacer layer.*

7.2 Characterizations of InGaN-AlInN QW LEDs

7.2.1 Power-Dependent Cathodoluminescence Measurement

The luminescence characteristics of InGaN QW LEDs with AlInN thin barrier were carried out by power-dependent cathodoluminescence (CL) measurements at T=300K, as shown in figure 7-3, with a 10 keV electron beam in spot mode (area = 2.0×10^{-9} cm^2). The various excitation power densities were introduced by varying the electron beam current (with constant accelerating voltage of 10 kV) from 200 nA up to 1000 nA. Figure 7-3 shows (a) the measured CL spectra and (b) the CL total intensity plotted against CL pump current of the InGaN-AlInN QWs (sample #2) and InGaN-GaN-AlInN QWs (sample #3). Strong cathodoluminescence was observed from both samples and that the CL intensity was observed to increase monotonically without any indication of droop. Sample #2 with the direct insertion of AlInN thin barrier shows longer emission

wavelength with relatively higher intensity under CL measurement as compared with sample #3 with GaN spacer layer.

Figure 7-4 shows (a) the measured CL spectra and (b) the CL total intensity plotted as a function of CL pump current of the InGaN-AlInN QWs (sample #2) and conventional (CV) InGaN QWs (sample #1). In comparison to the CV InGaN QWs, the InGaN-AlInN QWs shows longer CL wavelength. The observed lower CL intensity at higher CL current from InGaN-AlInN QWs could possibly be due to the defects introduced by InGaN/AlInN interface. Further growth optimization for enhancing the luminescence from the InGaN-AlInN is required.

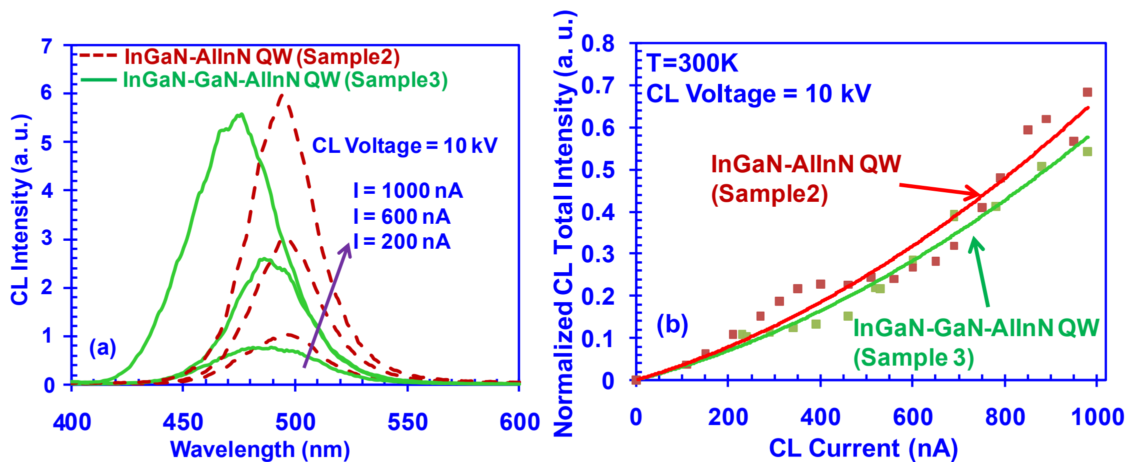

Figure 7-3 *Comparison of CL measurements results of InGaN-AlInN QWs (sample #2) and conventional InGaN/GaN QWs (sample #3) at T=300K: (a) the CL spectra at different current CL current and (b) normalized CL intensity for both samples.*

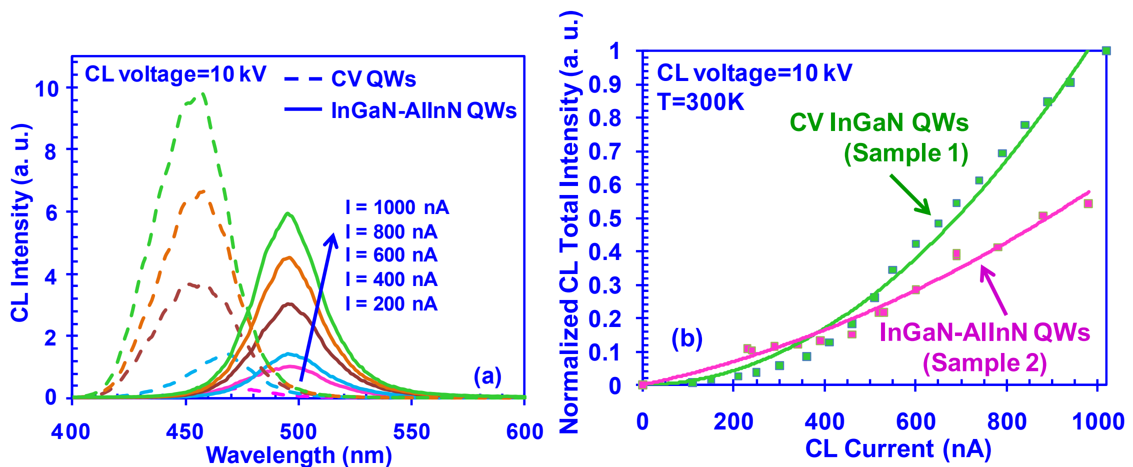

Figure 7-4 *Comparison of CL measurements results of InGaN-AlInN QWs (sample #2) and conventional InGaN/GaN QWs (sample #1) at T=300K: (a) the CL spectra at different current CL current; (b) normalized CL intensity for both samples.*

7.2.2 Electroluminescence Measurement

Electroluminescence (EL) measurements were carried out under continuous wave (CW) operation at room temperature. Figure 7-5 shows the EL spectra of InGaN-AlInN QWs LEDs (sample #2) and conventional InGaN QWs LEDs (sample #1) with the device size of 510 μm x 510 μm under various current injections. InGaN-AlInN QWs LEDs and conventional InGaN QWs LEDs exhibited the peak emission wavelengths around 500 nm and 440 nm, respectively. The difference in emission wavelength could be attributed to the effect of pressure grading or the modification of band lineup with the insertion of AlInN thin barrier. In addition, lower EL intensity from InGaN-AlInN LEDs was observed, which could be due to the defects raised from the interface of InGaN/AlInN or as a result of the more sever charge separation issue existing in the QWs emitting at longer wavelength regime.

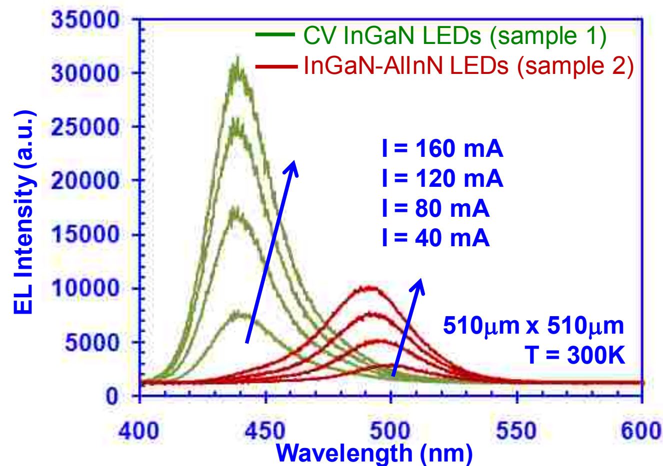

Figure 7-5 *Comparison of EL spectra of InGaN-AlInN LEDs (sample #2) and conventional InGaN LEDs (sample #1) under CW operation at T= 300K with various current injection. The device area is 510 μm x 510 μm.*

Figure 7-6 plots the light output power versus current density (*J*) from conventional InGaN QWs LEDs and InGaN-AlInN QWs LEDs. The slope of the output power curve represents the external and internal quantum efficiency of LEDs. The efficiency droop was observed from conventional InGaN QWs LEDs at the $J > 40 A/cm^2$ while the efficiency droop was not observed for InGaN-AlInN QWs LEDs up to $J = 80 A/cm^2$. The reduced efficiency droop could be attributed to the lower efficiency of InGaN-AlInN QWs LEDs as a result of defects or charge separation

issue, or due to the successful suppression of carrier leakage and hence efficiency droop. Further characterizations are required for the investigation of this origin.

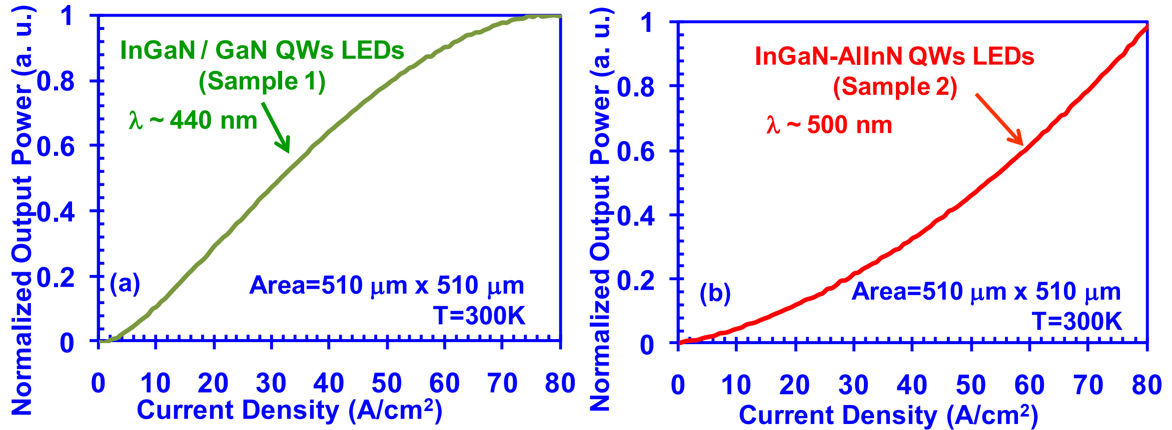

Figure 7-6 *Normalized output power as a function of current density plotted for InGaN-AlInN LEDs (sample #2) and conventional InGaN LEDs (sample #1) with emission wavelength round 500 nm and 440 nm, respectively.*

7.3 Fabrication of InGaN MQWs LEDs with Large-overlap Designs

7.3.1 Growth of Staggered InGaN MQWs LED

The concept of staggered InGaN QW have been introduced in Chapter 2, and this active region can be incorporated as active regions in typical nitride-based LED devices [1-7] using the growth and fabrication techniques presented in Chapter 5. The 2-layer and three-layer staggered InGaN QW LEDs were grown and fabricated into bottom-emitting devices by employing graded temperature techniques. Due to the growth temperature sensitivity of indium incorporation of InGaN alloy, the three-layer structure of high In-content InGaN sub-layer sandwiched by two low In-content InGaN sub-layers could be realized by changing the growth temperature. Figure 7-1 plots (a) the schematics, (b) graded growth temperature profile, (c) constant TMIn flow rate and (d) staggered In-content structure of the novel QW design. As the growth temperature decrease from T_1 of layer #1 to T_2 of layer #2, the In-content will increase accordingly from x of layer #1 to y of layer #2 with constant TMIn source flow. Then, the layer #3 with In-content of x can be grown with growth temperature increase from T_2 back to T_1. Another technique to realize three-layer staggered InGaN QW structure is graded TMIn profile [3].

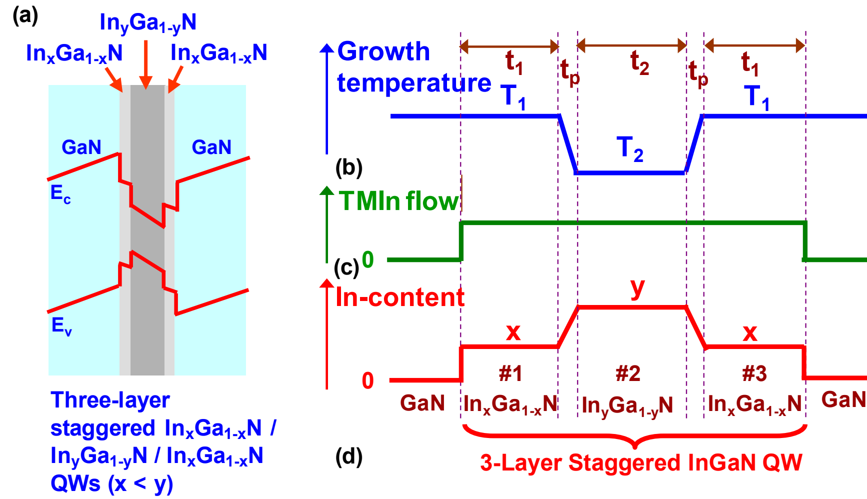

Figure 7-7 *(a) The schematic and (b)-(d) the growth profile of three-layer staggered InGaN QWs. The graded growth temperature profile, constant TMIn flow rate and staggered In-content structure are shown in (b), (c) and (d), respectively.*

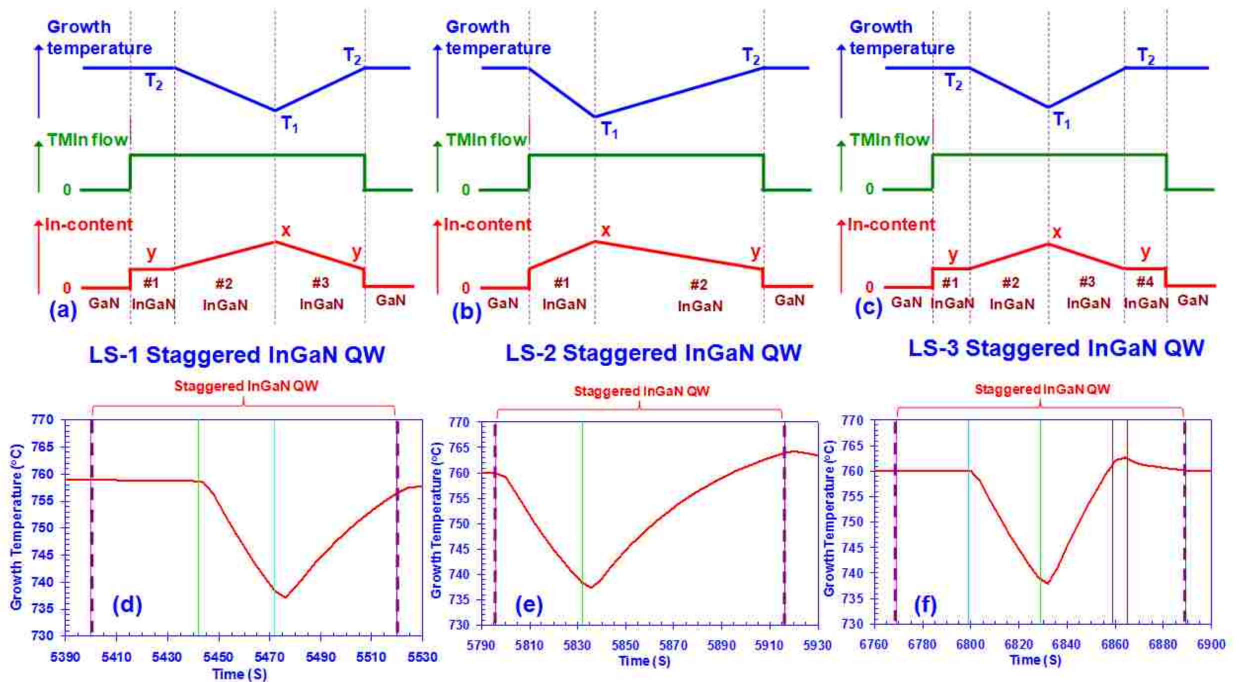

Figure 7-8 *Schematics of the growth temperature, TMIn-flow rate, and In-content for the linearly-shaped staggered InGaN QW [(a), (b), (c)] and the corresponding real growth temperature profiles [(d), (e), (f)].*

Similar to the concept of three-layer staggered InGaN QW with shape interface between InGaN sub-layers, linearly-shaped InGaN staggered QWs designed with energy local minima near the center will result in the shift of both electron and hole wavefunction toward the center of the QW region which leads to significant enhancement in the electron-hole wavefunction overlap (Γ_{e_hh}) and spontaneous emission rate [7]. Figure 7-8 shows the designed growth profile of linearly-shaped InGaN QW [figure 7-8(a), (b), (c)] and the real growth temperature profile [figure 7-8(d), (e), (f)]. The energy local minima is designed on the left side, on the right side or in the middle of the QW region for LS-1 staggered InGaN QW [figure 7-8(a), (d)], LS-2 staggered InGaN QW [figure 7-8(b), (e)], and LS-3 staggered InGaN QW [(c), (f)], respectively. By linearly changing the growth temperature from high T_2 level to low T_1 and then back to high T_2, the In-content of the InGaN QW region can be tuned linearly and various In-content profile can be obtained. The good matching between the real growth temperature profile and design temperature profile indicate that this approach as promising for manufacturing implementation.

7.3.2 Discussion of InGaN-Delta-InN QW LEDs Growth

The theoretical analysis in Chapter 4 has provided strong motivation of the novel InGaN QW design with the insertion of narrow-bandgap delta-layer for extension of emission wavelength with large optical matrix element and large radiative recombination rate. Experimentally, the pulsed growth mode of InN bulk on GaN template has been introduced in Chapter 6. The growth of InGaN-delta-InN QW LEDs, however, still needs optimization due to the different growth conditions InN and InGaN material in the QWs. The InGaN QWs typically are grown at 725 °C to 750 °C depending on the required wavelength, while the optimized growth temperature for InN thin films are around 575 °C. Thus, the temperature profile of the integration needs to be carefully designed. To carry out the growth of delta-InN with the thickness less than 1 nm, the control of growth rate is crucial. Hence, the gas flow rate and the V/III ratio have to be optimized to achieve precise control in the thin layer growth.

7.4 Characterizations of InGaN MQWs LEDs with Large-overlap Designs

7.4.1 Electroluminescence at Room Temperature

The electroluminescence (EL) studies of both conventional InGaN QW LEDs and staggered InGaN QW LEDs emitting at 520 nm-525 nm was carried out under continuous wave (CW) operation at room temperature [5, 6]. The details of these measurements had also been presented in reference 7. Figure 7-9 shows the EL measurement results of three-layer staggered InGaN QW LEDs where figure 7-9(a) represents the EL spectra and figure 7-9(b) represents the total output power for conventional InGaN QW LEDs and three-layer staggered InGaN QW LEDs. The EL spectra for both LEDs show peak wavelengths at 520-525 nm, as injection current density varied from 30mA up to 200mA at room temperature. The three-layer staggered InGaN LED shows ~ 1.8 times (1.3 times) enhancement in the peak EL intensity as compared to the conventional LED at I = 100 mA (I = 200 mA). The broader spectrum with larger full width at half maximum (FWHM) is also observed from staggered InGaN QW LED due to the less abrupt interface between InGaN sub-layers. The output power of the three-layer staggered InGaN QW LED plotted in figure 7-9(b) was measured as ~2.0 times higher in comparison to that measured from conventional LEDs at high current density. The EL measurement results confirmed the successful enhancement of spontaneous emission rate (i.e., the radiative recombination rate) by the three-layer staggered InGaN QW design, which is consistent with our theoretical prediction.

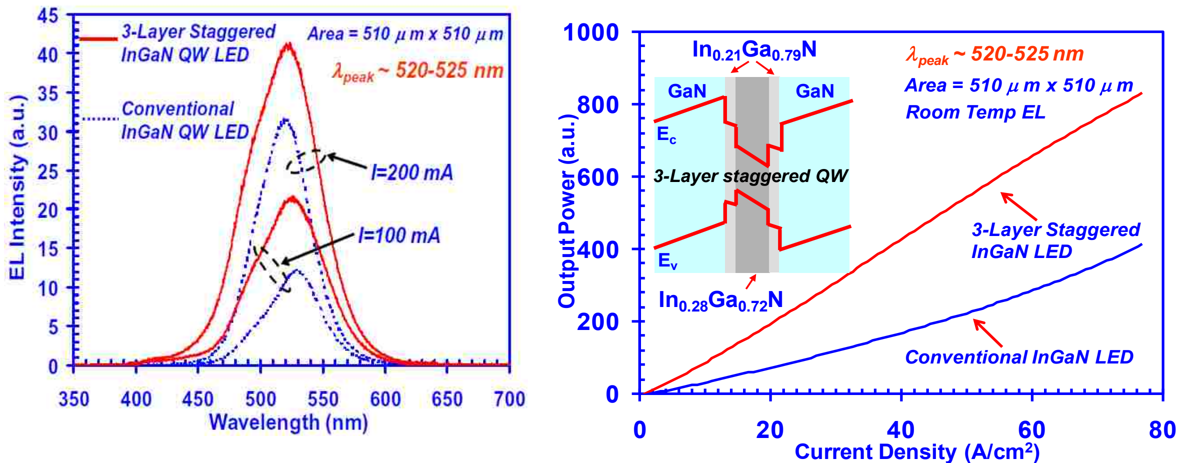

Figure 7-9 *(a) EL spectra and (b) the EL output power as a function of current density for conventional InGaN QW and three-layer staggered InGaN QW LEDs emitting at 520-525 nm with the device size of 510 μm x 510 μm [5].*

The luminescence characteristics of linearly-shaped staggered InGaN QWs samples were studied by power-density-dependent cathodoluminescence (CL) measurements performed at T = 300K [7]. A 10 keV electron beam in spot size of $2x10^{-9}$ cm^2 was used to excite the InGaN QWs active region and the electron beam current was varied from 20 nA up to 800 nA in the measurement. The emission wavelength for both conventional InGaN QWs and linearly-shaped staggered InGaN QWs are around 460 nm to 480 nm depending on the excitation power density. As shown in figure 7-10, the CL intensity for the linearly-shaped staggered InGaN QWs exhibited increase in output power by approximately 2-3 times over large CL current range in comparison to the conventional InGaN QWs emitting at the similar wavelength. The total CL intensities of LS-1, LS-2 and LS-3 staggered InGaN QW are comparable with each other. Further characterizations are required to investigate the performance of electrical injection devices and optimize the structure of linearly-shaped staggered InGaN QW LEDs.

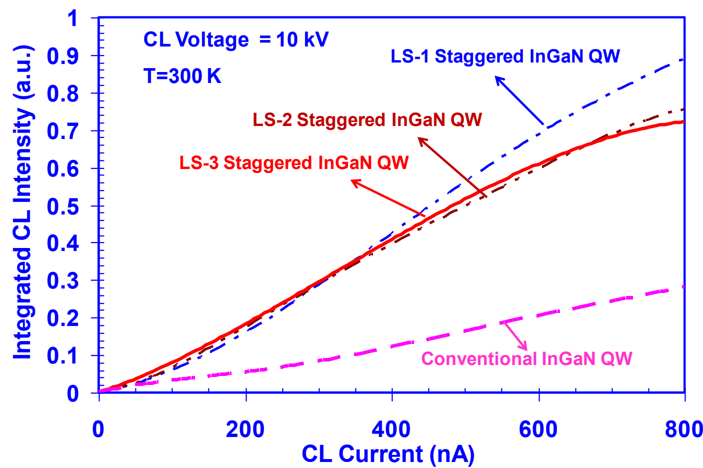

Figure 7-10 *Integrated CL intensity of conventional, LS-1 staggered, LS-2 staggered, and LS-3 staggered InGaN QW versus CL excitation currents at T = 300K.*

From our finding, we conclude that the key for enhancing the electron-hole wavefunction overlap for the suppression of charge-separation issue is the introduction of energy local minima near the center of active region that can be accomplished by various designs. Recently, O'Donnell and coworker studied various staggered InGaN QWs with different QW profiles for large overlap design [8]. Their results show that all the staggered InGaN QWs exhibits higher IQE

as compared to the conventional rectangular InGaN QWs, which is in very good agreement with our finding of staggered InGaN QWs concept.

7.4.2 Time-Resolved Photoluminescence for Carrier Lifetime

The time-resolved photoluminescence (TRPL) measurements were carried out to measure the total carrier recombination lifetime in the active region. The results would provide important evidence to confirm the improvement observed in staggered InGaN QW LEDs is due to the increase in radiative recombination rate [7]. The TRPL measurements were performed at room temperature using the excitation laser wavelength of 430 nm. Figure 7-11 shows the TRPL measurement results where the total carrier lifetimes of 18.9 ns and 12.3 ns were measured for conventional InGaN QW and three-layer staggered InGaN QW, respectively. Assuming that the material quality of both QWs are similar and the nonraditive recombination process are the same in both QW system, the 35% reduction in total carrier lifetime for staggered InGaN QW can be attributed to the increased radiative recombination rate of staggered InGaN QW as compared to the conventional QW based on the following relation:

$$\frac{1}{\tau_{total}} = \frac{1}{\tau_{Non_Rad}} + \frac{1}{\tau_{Rad}} \qquad (7.1).$$

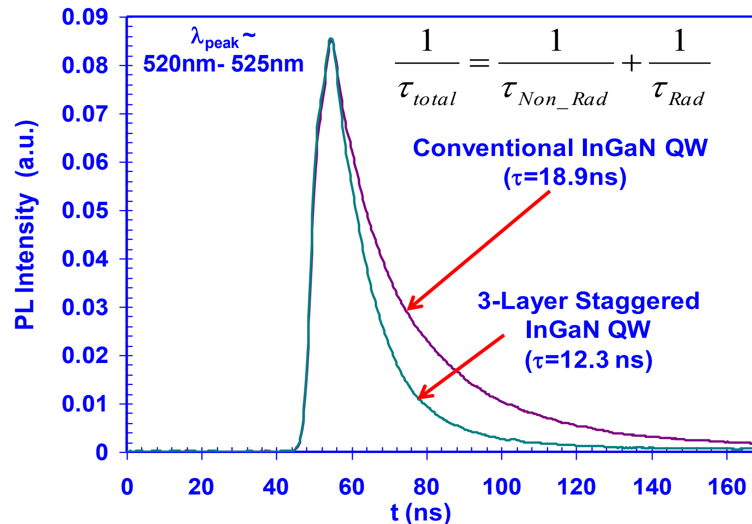

Figure 7-11 *The total carrier life time measurement for conventional InGaN QWs and three-layer staggered InGaN QWs emitting at 520-525 nm at T = 300 K [7].*

The carrier density in the QW active region during the TRPL measurement was estimated to be mid 10^9 cm^{-3} by analyzing the following experimental parameters : 1) the 430 nm excitation laser power (30 μJ/pulse), (2) the laser beam diameter (~300 μm), (3) the absorption coefficient for InGaN material (α_{QW} ~ 2×10^3 cm^{-1}) [29], and (4) the total thickness of four periods of 3 nm InGaN QWs active region (12 nm). The number of generated photon per pulse is calculated as:

$$n_{\text{gp}} = \frac{E_{\text{total_laser}}}{E_{\text{singlephoton}}} = \frac{30\mu J}{hc/\lambda} \quad (7.2).$$

Then the number of absorbed photon per pulse with the consideration of material absorption is:

$$n_{\text{ap}} = n_{\text{gp}} \cdot (1 - e^{-\alpha_{QW} \cdot d_{QW}}) \quad (7.3).$$

Assuming the number of generated electron-hole pairs are the same with the absorbed photon number, the carrier density can be obtained by dividing total carrier number with the volume of the QW regions. Thus, the carrier density is estimated to be mid 10^9 cm^{-3}. In another word, from our finding, the total carrier life time is 12.3 ns for staggered InGaN QW and 18.9 ns for conventional QW, respectively at the carrier density of 5×10^9 cm^{-3}.

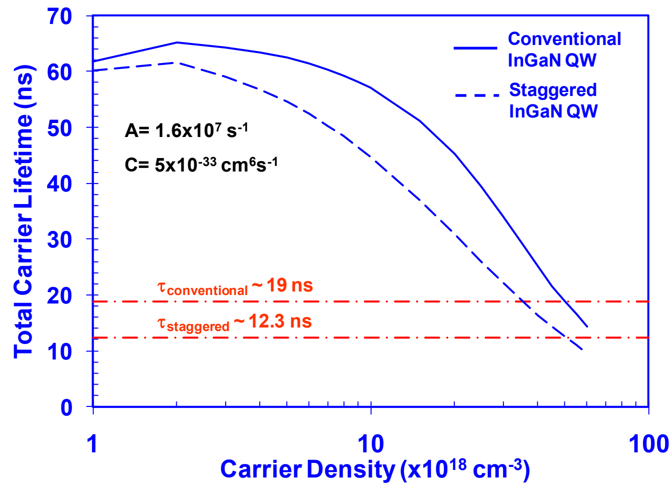

Figure 7-12 *The total carrier lifetime as a function of carrier density for conventional InGaN QW and staggered InGaN QW at monomolecular coefficient A =* 1.6×10^7 s^{-1} *and Auger coefficient C =* 5×10^{-33} cm^6s^{-1}.

Figure 7-12 shows the calculated total carrier lifetimes for both conventional InGaN QW and three-layer staggered InGaN QW emitting at ~525 nm at different carrier density. By fitting the

relation, the monomolecular recombination coefficient A is estimated as $1.6x10^7$ s^{-1}, and the Auger recombination coefficient C is estimated as $5x10^{-33}$ cm^6s^{-1}. Based on the estimated monomolecular coefficient and Auger coefficient, the radiative carrier lifetimes (τ_{rad}) for both three-layer staggered InGaN QWs and conventional InGaN QWs emitting at λ ~520 nm - 525 nm can be estimated as ~18.58 ns and ~39.35 ns, respectively, for carrier density n ~$5x10^{19}$ cm^{-3}. The finding indicates that the use of three-layer staggered InGaN QWs leads to ~2.12 times increase in radiative recombination rate, in comparison to that measured for conventional InGaN QWs.

7.4.3 Temperature Dependent Electroluminescence

The temperature-dependent / power-dependent EL measurements was carried out in a modified scanning electron microscopy (SEM) system with the integration of EL measurements capability. The schematic of the experimental setup is shown in figure 7-13. The external current source of either continuous wave (CW) mode or pulse mode was applied to the devices in a vacuum chamber via probes. The sample is fixed on a stage which temperature is controlled by both the liquid Helium flow and the heater of the temperature controller in the vacuum chamber. The luminescence signal was picked up by the parabolic mirror, and analyzed after going through the spectrometer and photomultiplier (PMT).

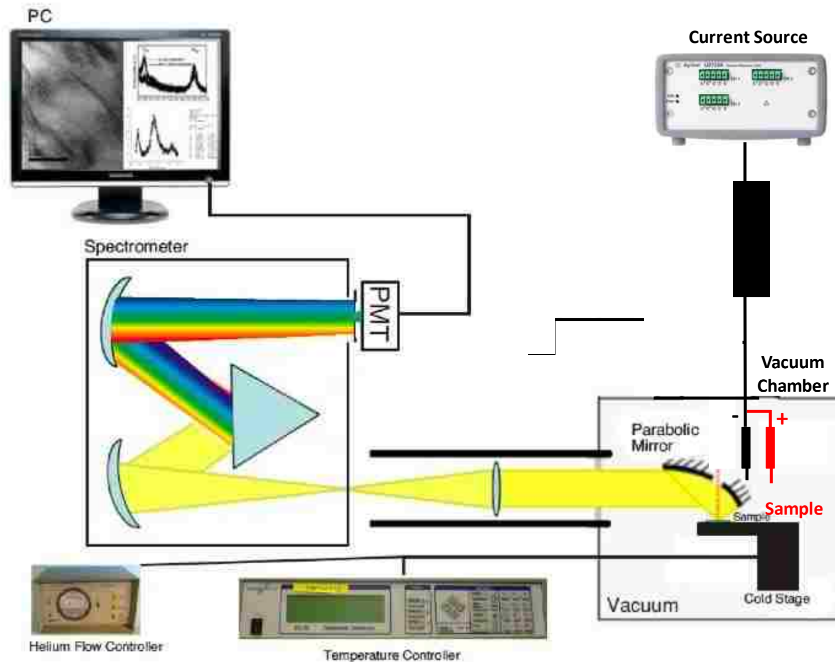

***Figure 7-13** Schematic of the setup of temperature-dependent / power-dependent EL measurement.*

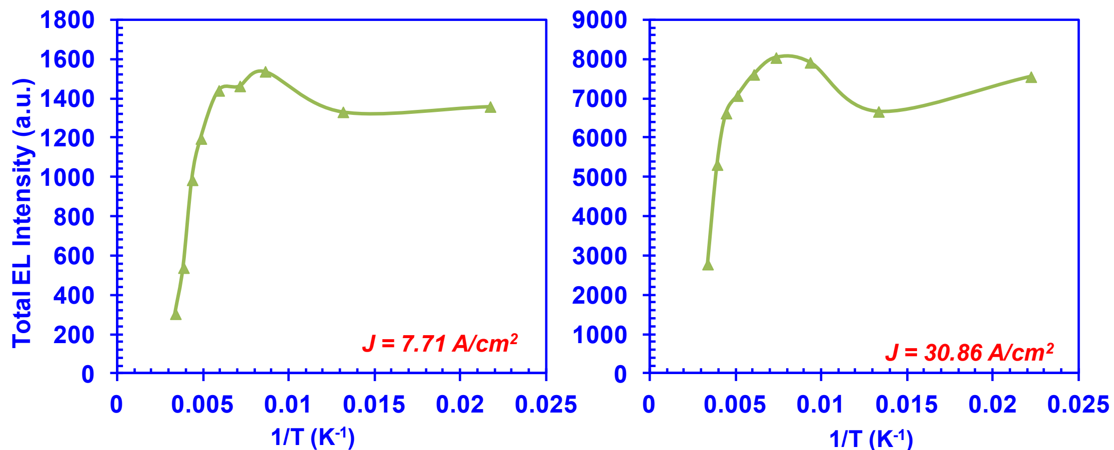

Figure 7-14 *Integrated EL intensity of three-layer staggered InGaN QW LEDs emitting at 500 nm as a function of the inverse of temperature at (a) J=7.71 A/cm^2 and (b) J= 30.86 A/cm^2 under CW operation.*

The electrically-injected luminescence measurement of three-layer staggered QW LEDs was carried out with the temperature range of 40K to 300K under CW operation. Figure 7-14 plots the integrated intensity in the range of 465 nm to 600 nm as a function of the inverse of temperature at (a) J= 7.71 A/cm^2 and (b) J= 30.86 A/cm^2. By taking the ratio of integrated EL intensity at room temperature (T=300K) divided by that at low temperature (T=40K), the IQE is estimated around 22.4% at J= 7.71 A/cm^2 and 36.7% at J= 30.86 A/cm^2. Note that the peak of IQE occurs at higher current density, which indicates the defect is still an issue in the green-emission InGaN QW LEDs. Further improvement in TDEL characterizations would include the optimization of the electrical contact of the devices in order to achieve improved device stability at low temperature measurements.

Reference for Chapter 7

1. R. A. Arif, Y. K. Ee, and N. Tansu, "Polarization engineering via staggered InGaN quantum wells for radiative efficiency enhancement of light emitting diodes," *Appl. Phys. Lett.,* vol. 91, Aug 27 2007.
2. R. A. Arif, Y. K. Ee, and N. Tansu, "Nanostructure engineering of staggered InGaN quantum Wells light emitting diodes emitting at 420-510 nm," *Physica Status Solidi a-Applications and Materials Science,* vol. 205, pp. 96-100, Jan 2008.
3. R. A. Arif, H. P. Zhao, Y. K. Ee, and N. Tansu, "Spontaneous emission and characteristics of

staggered InGaN quantum-well light-emitting diodes," *IEEE J. Sel. Top. Quantum Electron.,* vol. 44, pp. 573-580, May-Jun 2008.

4. H. Zhao, G. Liu, X. H. Li, G. Huang, J. D. Poplawsky, S. T. Penn, V. Dierolf, and N. Tansu, "Growths of staggered InGaN quantum wells light-emitting diodes emitting at 520–525 nm employing graded growth-temperature profile," *Appl. Phys. Lett.,* vol. 95, p. 061104, 2009.
5. H. P. Zhao, G. Y. Liu, X. H. Li, G. S. Huang, J. D. Poplawsky, S. T. Penn, V. Dierolf, and N. Tansu, "Growths of staggered InGaN quantum wells light-emitting diodes emitting at 520-525 nm employing graded growth-temperature profile," *Appl. Phys. Lett.,* vol. 95, Aug 10 2009.
6. H. P. Zhao, G. Y. Liu, X. H. Li, R. A. Arif, G. S. Huang, J. D. Poplawsky, S. T. Penn, V. Dierolf, and N. Tansu, "Design and characteristics of staggered InGaN quantum-well light-emitting diodes in the green spectral regime," *IET Optoelectronics,* vol. 3, pp. 283-295, Dec 2009.
7. H. P. Zhao, G. Y. Liu, J. Zhang, J. D. Poplawsky, V. Dierolf, and N. Tansu, "Approaches for high internal quantum efficiency green InGaN light-emitting diodes with large overlap quantum wells," *Optics Express,* vol. 19, pp. A991-A1007, Jul 4 2011.
8. K. P. O'Donnell, M. A. D. Maur, A. Di Carlo, K. Lorenz, and S. Consortium, "It's not easy being green: Strategies for all-nitrides, all-colour solid state lighting," *Physica Status Solidi-Rapid Research Letters,* vol. 6, pp. 49-52, Feb 2012.

Chapter 8 Analysis of InGaN QW LEDs with Different Polarity

8.1 Introduction of Polarity of InGaN QW LEDs

III-nitride semiconductors have strong polarization fields that have strong influence on device performance. The wurzite crystal structure leads to the existence of spontaneous polarization component, and the lattice mismatch between each layer results in the existence of piezoelectric polarization field. Both fields are highly oriented. In other words, the direction of the polarization fields or the polarity of the III-nitrides depends on the dipole moment along the crystal orientation.

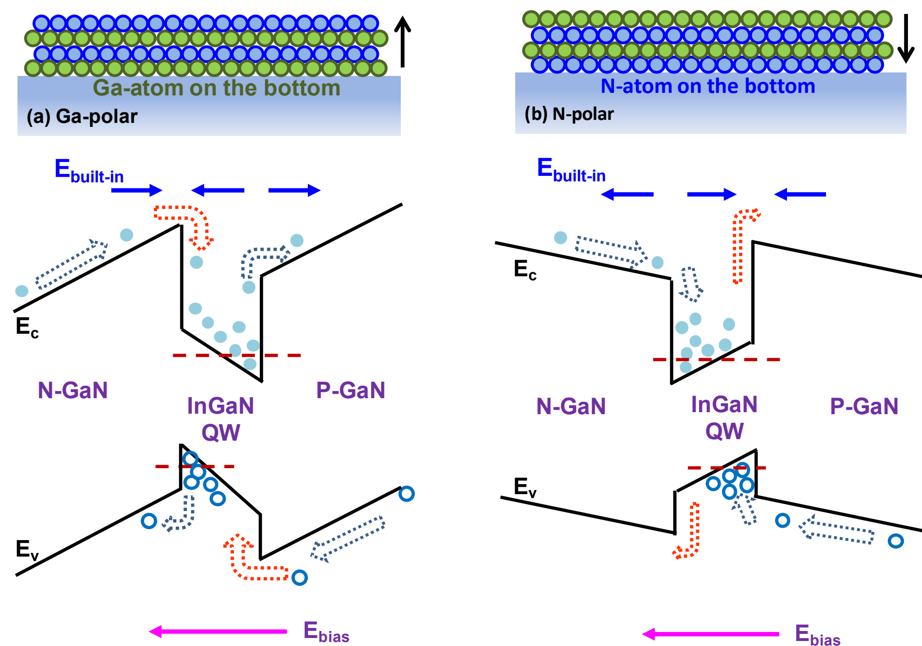

Figure 8-1 *Schematics and band structures of (a) Ga-polar GaN based InGaN QW LEDs and (b) Ga-polar GaN based InGaN QW LEDs under bias.*

III-nitrides can be grown with two types of polarity, gallium polar (Ga-polar) and nitrogen-polar (N-polar). Figure 8-1 shows the schematics of (a) Ga-polar GaN growth and (b) N-polar GaN growth with the corresponding InGaN QW band structures. For Ga-polar GaN which is the conventional polarity, a layer of Ga-atoms will be deposited first on the substrate followed by the N-atoms. The crystal direction of 001 is along the growth direction. The band tilting of InGaN QW grown on Ga-polar GaN is shown underneath the schematics. For N-polar GaN, a layer of N-atoms will be the firstly deposited and the Ga-atoms will be deposited later. The crystal direction of 001 is along the reverse of the growth direction. Thus, the band tilting is the opposite of that of

the Ga-polar. The investigation of optical properties of InGaN QW with different polarity is of great interests, and the analysis requires the full consideration of carrier diffusion and drift processes as a result of the change of build-in electric field and the applied electric field under device operation. Thus, it would be important to employ the numerical simulation with carrier transport effect. Previously, the polarity studies have been carried out in AlGaN / GaN [1-5] and InGaN / GaN [6-10] heterostructures for HEMT and LED devices. Efforts have been carried out to optimize the growth of N-polar III-nitrides by molecular beam epitaxy (MBE) [8, 10-12] and metal-organic chemical vapor deposition (MOCVD) [2, 13-15]. The advantages of employing N-polar III-nitride semiconductor in optoelectronic and electronic devices include easier realization of Ohmic contact, feasibility for high frequency operation, and the potential in enhancing injection efficiency and suppression of efficiency droop in LED devices.

8.2 Analysis of Ga-polar and N-polar InGaN QW LEDs

In this chapter, the InGaN based QW LEDs with different polarity will be compared in detail, and the use of N-polar InGaN QW as an alternative active region of LEDs for efficiency droop suppression will be presented. The device structure is similar to LED (A) showed in figure 4-6. The active region in this study consists of 3 nm $In_{0.25}Ga_{0.75}N$ QW sandwiched by 10 nm GaN barriers grown on top of n-GaN template. The 50 nm p-AlGaN electron blocking layer (EBL) and 200 nm p-GaN capping layer are grown on top of the active region. Then, the metal contacts are deposited on the top (p-contact) and at the bottom (n-contact) of the LED device to create the uniform vertical current injection channel. For Ga-polar conventional InGaN based LEDs, the parameters of the calculation of spontaneous and piezoelectric polarization fields are listed in Table 3-1. On the other hand, the calculated polarization fields in N-polar InGaN based LEDs have the opposite sign with the same absolute value. The carrier transport effect is taken into considerations and the screening ratio of the interface charge is assumed to be 50% of the calculated value.

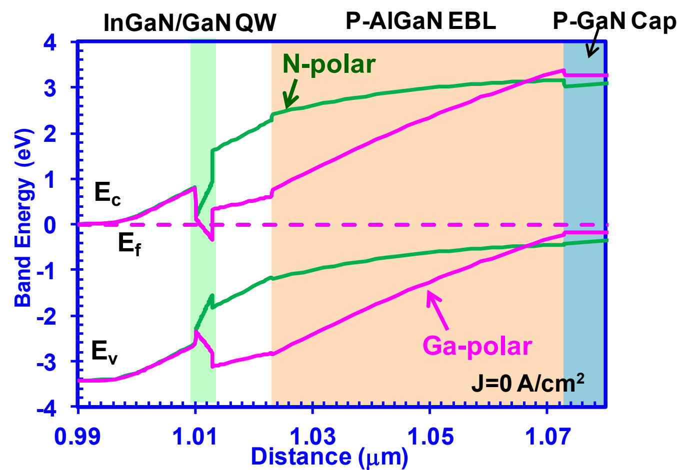

Figure 8-2 *Band structures and Fermi levels of Ga-polar and N-polar InGaN single quantum well (SQW) LEDs at equilibrium.*

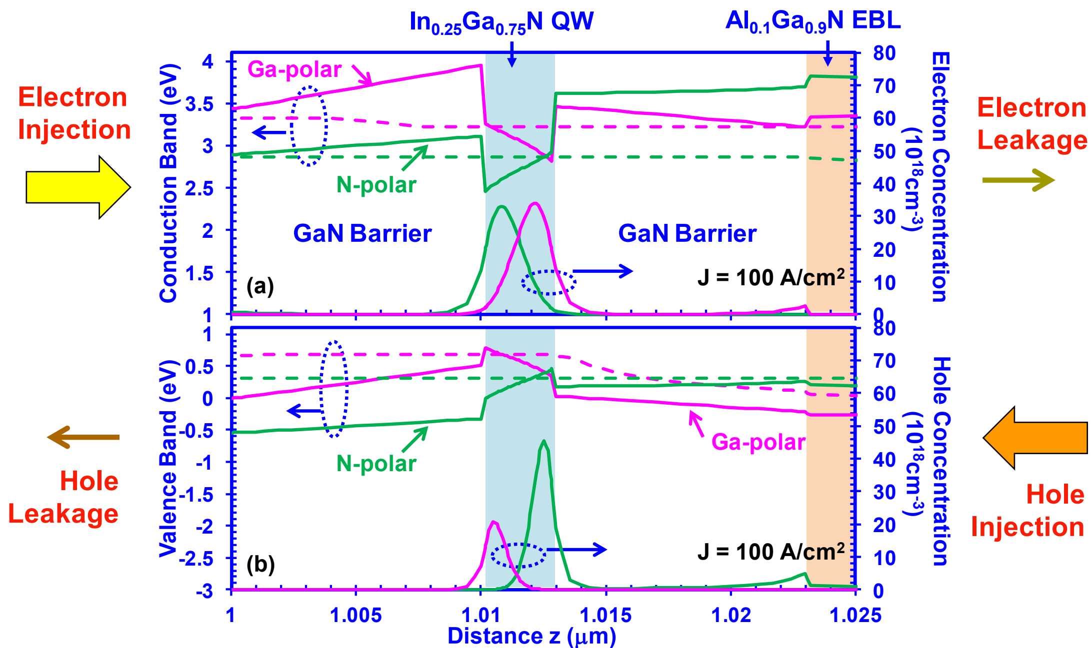

Figure 8-3 *(a) Conduction bands, quasi-Fermi level for electrons and electron concentrations, and (b) valence bands, quasi-Fermi level for holes and hole concentrations of Ga-polar and N-polar InGaN QW LEDs at J = 100 A/cm^2.*

The band structure comparisons of Ga-polar and N-polar InGaN single quantum well (SQW) LEDs at equilibrium condition and under forward bias are shown in figure 8-2 and figure 8-3, respectively. At equilibrium, as illustrated in figure 8-2, the Fermi levels are aligned for both QW system and the bands are overlapping in both the n-GaN template and p-GaN capping layer.

However, due to the different orientation of built-in electrostatic fields, the titling of the bands for InGaN QW, GaN barriers, p-AlGaN electron blocking layer (EBL) and part of p-GaN layers have different direction and strength.

When the current source is applied to the LED devices, the p-n junction is bias at a particular forward voltage. At J=100 A/cm^2, as shown in figure 8-3, the forward voltages are 3.32V and 2.87V for Ga-polar and N-polar InGaN QW LEDs, respectively. The ~0.45V reduced voltage on the p-n junction is reflected by the smaller separation of quasi-Fermi levels in N-polar InGaN QW LEDs in the green dash line in figure 8-3. In addition, as indicated in the reduced separation of quasi-Fermi-level and band edges, the use of N-polar InGaN QW leads to the lower barriers for injection of electrons on the left [figure 8-3(a)] and holes on the right [figure 8-3(b)]. This advantage results in the significant increase in hole carrier concentration shown in figure 8-3(b). Besides, the effective barrier heights for suppression of electrons [figure 8-3(a)] and holes [figure 8-3(b)] has been increased significantly by the use of N-polar InGaN QW. Specifically, the effective barriers heights for dominate electron escape increases from 0.23eV of Ga-polar InGaN QW to 0.69eV for N-polar InGaN QW. Thus, in the N-polar InGaN QW LED, the leakage electrons in the last GaN barrier are much lower.

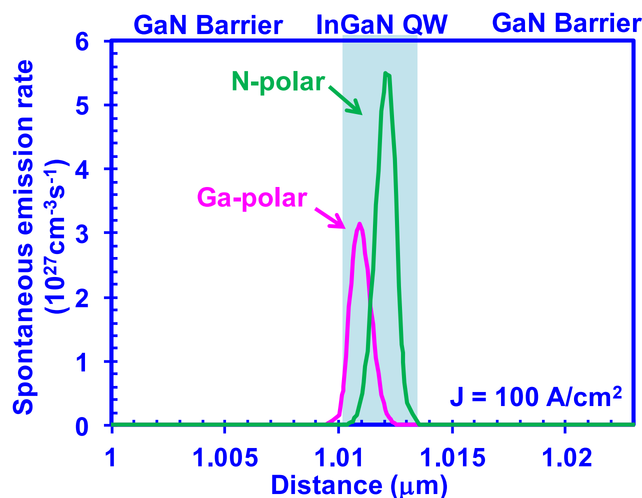

Figure 8-4 *Spontaneous emission rate of (a) Ga-polar GaN based InGaN QW LEDs and (b) Ga-polar GaN based InGaN QW LEDs under bias.*

Figure 8-4 shows the spontaneous emission rate at J=100A/cm^2 for LEDs with both polarity.

The increase in the spontaneous emission rate in the N-polar InGaN QW is attributed to the increase in the hole concentration and the reduction in electron leakage, which has been discussed in figure 8-3. The reduced carrier escape is also reflected in the electron current density across the whole active region in figure 8-5. The leakage current density is around 42.3 A/cm^2 after the recombination process in the QW region for Ga-polar QW LEDs, while that for the N-polar InGaN QW LEDs is close to zero. Thus, the thermionic carrier escape has been significantly suppressed by the increase effective barrier height from the use of N-polar InGaN/GaN heterostructure.

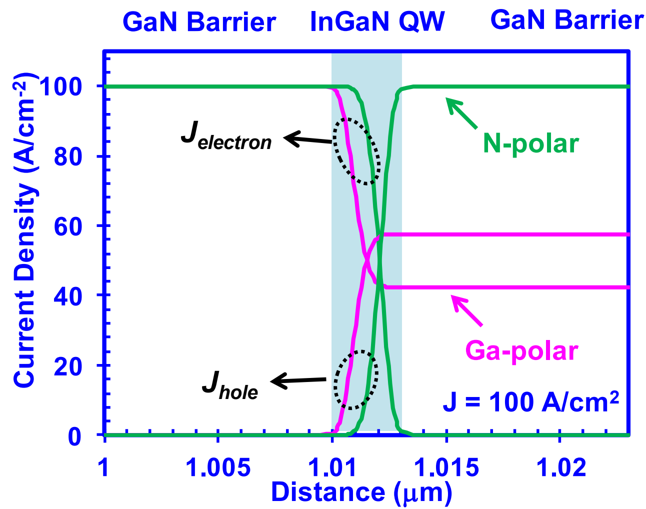

Figure 8-5 *Electron and hole current densities across the active region of N-polar and Ga-polar InGaN QW LEDs.*

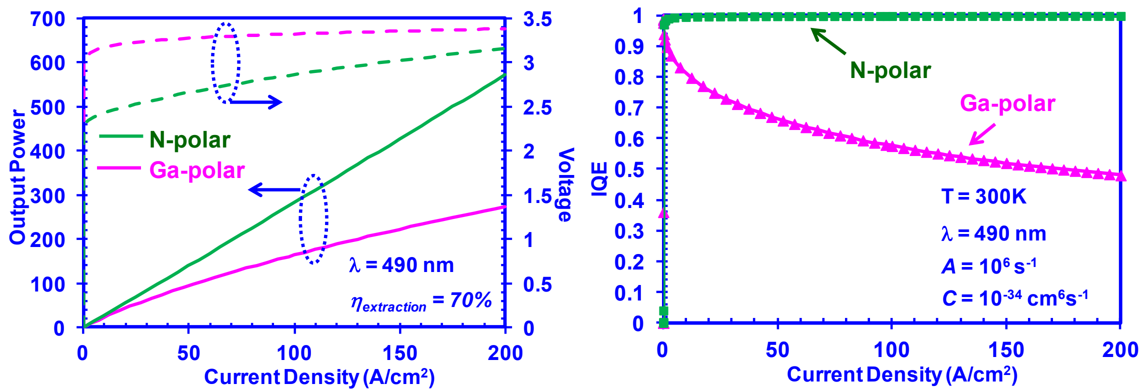

Figure 8-6 *Devices characteristics of Ga-polar InGaN SQW LEDs at different current density. (a) shows the light output power and voltage and (b) shows the IQE.*

The device characteristics of light output power, I-V curves and the IQE are plot in figure 8-6. The ~0.7V reduction in the turn on voltage from the use of N-polar InGaN QW in figure 8-6(b) can be attributed to the reduced barrier for carrier injection. The forward voltage also reduced accordingly. As predicted, the light output power and IQE have been increase significantly. Specifically, the light power shows 2.08 time increase and the IQE shows 2.09 times increase at J=200A/cm^2 by the use of N-polar InGaN QW LEDs. Furthermore, the efficiency of N-polar InGaN QW LED does not show droop phenomenon due to the successful suppression of carrier leakage. The device characteristics indicate the great potential of N-polar InGaN QW as the active region for high efficiency optoelectronics with the suppression of efficiency droop issues.

References for Chapter 8

1. O. Ambacher, J. Smart, J. R. Shealy, N. G. Weimann, K. Chu, M. Murphy, W. J. Schaff, L. F. Eastman, R. Dimitrov, L. Wittmer, M. Stutzmann, W. Rieger, and J. Hilsenbeck, "Two-dimensional electron gases induced by spontaneous and piezoelectric polarization charges in N- and Ga-face AlGaN/GaN heterostructures," *J. Appl. Phys.,* vol. 85, pp. 3222-3233, 1999.
2. S. Keller, N. Pfaff, S. P. DenBaars, and U. K. Mishra, "Polarization spectroscopy of N-polar AlGaN/GaN multi quantum wells grown on vicinal (000(1)over-bar) GaN," *Appl. Phys. Lett.,* vol. 101, Oct 29 2012.
3. B. Mazumder, M. H. Wong, C. A. Hurni, J. Y. Zhang, U. K. Mishra, and J. S. Speck, "Asymmetric interfacial abruptness in N-polar and Ga-polar GaN/AlN/GaN heterostructures (vol 101, 091601, 2012)," *Appl. Phys. Lett.,* vol. 101, Nov 26 2012.
4. B. Mazumder, M. H. Wong, C. A. Hurni, J. Y. Zhang, U. K. Mishra, and J. S. Speck, "Asymmetric interfacial abruptness in N-polar and Ga-polar GaN/AlN/GaN heterostructures," *Appl. Phys. Lett.,* vol. 101, Aug 27 2012.
5. L. Zhou, D. F. Storm, D. S. Katzer, D. J. Meyer, and D. J. Smith, "Comparison of microstructure of N-polar GaN/AlGaN/GaN heterostructures grown on different substrates," *J. Crys. Growth,* vol. 357, pp. 25-29, Oct 15 2012.
6. S. H. Park, D. Ahn, J. Park, and Y. T. Lee, "Optical Properties of Staggered InGaN/InGaN/GaN Quantum-Well Structures with Ga- and N-Faces," *Japanese J. Appl. Phys.,* vol. 50, Jul 2011.
7. A. Konar, A. Verma, T. Fang, P. Zhao, R. Jana, and D. Jena, "Charge transport in non-

polar and semi-polar III-V nitride heterostructures," *Semiconductor Science and Technology,* vol. 27, Feb 2012.

8. F. Akyol, D. N. Nath, E. Gur, P. S. Park, and S. Rajan, "N-Polar III-Nitride Green (540 nm) Light Emitting Diode," *Japanese J. Appl. Phys.,* vol. 50, May 2011.
9. J. Verma, J. Simon, V. Protasenko, T. Kosel, H. G. Xing, and D. Jena, "N-polar III-nitride quantum well light-emitting diodes with polarization-induced doping," *Appl. Phys. Lett.,* vol. 99, Oct 24 2011.
10. F. Akyol, D. N. Nath, S. Krishnamoorthy, P. S. Park, and S. Rajan, "Suppression of electron overflow and efficiency droop in N-polar GaN green light emitting diodes," *Appl. Phys. Lett.,* vol. 100, 111118, Mar 12 2012.
11. S. Dasgupta, Nidhi, F. Wu, J. S. Speck, and U. K. Mishra, "Growth and Characterization of N-Polar GaN Films on Si(111) by Plasma Assisted Molecular Beam Epitaxy," *Japanese J. Appl. Phys.,* vol. 51, Nov 2012.
12. J. W. Jeon, T. Y. Seong, and G. Namgoong, "Electrical Characteristics of Ti/Al Ohmic Contacts to Molecular Beam Epitaxy-Grown N-polar n-type GaN for Vertical-Structure Light-Emitting Diodes," *Journal of Electronic Materials,* vol. 41, pp. 2145-2150, Aug 2012.
13. H. Kim, Z. L. Guan, Q. A. Sun, A. Kahn, J. Han, and A. Nurmikko, "Surface and interface states of gallium-polar versus nitrogen-polar GaN: Impact of thin organic semiconductor overlayers," *J. Appl. Phys.,* vol. 107, Jun 1 2010.
14. P. S. Park, D. N. Nath, and S. Rajan, "Quantum Capacitance in N-Polar GaN/AlGaN/GaN Heterostructures," *IEEE Electron Device Letters,* vol. 33, pp. 991-993, Jul 2012.
15. Q. Sun, Y. S. Cho, I. H. Lee, J. Han, B. H. Kong, and H. K. Cho, "Nitrogen-polar GaN growth evolution on c-plane sapphire," *Appl. Phys. Lett.,* vol. 93, Sep 29 2008.

Chapter 9 Sensitivity of Dopant Activation in P-type III-Nitrides on LED Device Characteristics

9.1 Motivation of Sensitivity Study for Industrial Production

The yield of the production is crucial for commercial applications, and the variation in device performances can be detrimental for the mass production line. Sensitivity of each fabrication parameter needs to be taken into consideration for achieving high yield [1]. The p-type III-nitride materials is crucial for LED operation, as the small hole mobility and low hole carrier concentration is the attributing factor to many challenges including poor hole injection efficiency [2] and current crowding induced efficiency reduction [3-5] of InGaN based QW LEDs. For III-nitride based LEDs, the only-known dopant of p-type layers, magnesium, owns higher activation energy of ~200 meV as compared to ~29 meV of n-type dopant, silicon [6]. In addition, the acceptor-hydrogen complexes Mg-H formed in the NH_3-rich growth environment are electrically inactive [7-12]. Thus, post-growth rapid thermal annealing at around 800°C - 900°C is required to dissociate the Mg–H complexes and activate the Mg acceptor dopant. In the industrial production, the temperature inside the annealing chamber with multiple wafers will have variations across the radius distance [13-15]. Thus, the annealing temperature in the center of the furnace or chamber will be different from that at the edge. Typically, the temperature is higher in the center region than at the edge region, and the difference will be larger with higher temperature setting [14].

The low activation rate in the p-type dopants of III-nitrides is a great obstacle in delivering higher light output power and efficiency from the III-nitride based LEDs. Only a certain percentage of magnesium will be activated as acceptors in the semiconductor [7, 9, 12]. The hole concentration thus does not only depend on the concentration of magnesium, but also the annealing temperature. Typically, higher annealing temperature leads to higher activation level of the magnesium, thus it results in higher hole concentration in the material. However, the issues associated with the heavily doped p-type GaN, including lower hole mobility and deteriorative material quality limits the device performance [12].

Nevertheless, the non-uniformity of annealing temperature across the whole wafer area leads

to the different activation levels of acceptors in the p-type AlGaN EBL, p-GaN and heavily doped GaN capping layers. Here we present the study on the effect of p-type doping level profiles on the device characteristics of the InGaN-based MQW LEDs using the structures of commercial LEDs. The effects of doping level of each layer as well as the activation levels of the device as a whole will be investigated. The sensitivity study will provide guidance for industrial application to optimize the doping levels of p-type each layer and the annealing conditions to achieve higher yield and uniformity in device performance.

9.2 Effect of LEDs with Different P-type Doping Levels in Each Layer

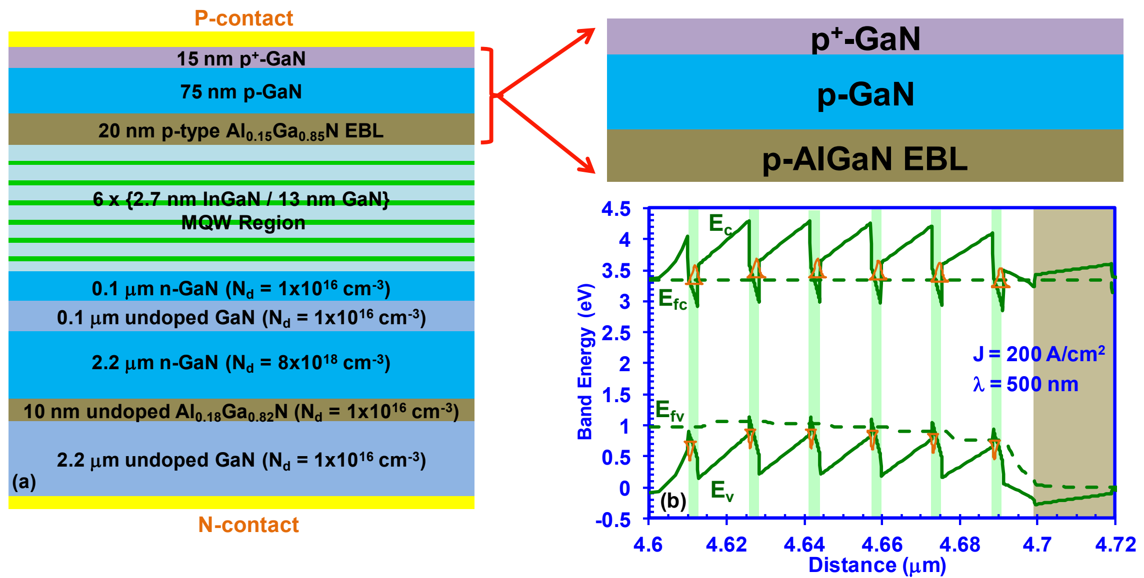

Figure 9-1 *(a) Schematics of the device structure and doping levels in the simulation, and (b) band structures of InGaN QW LEDs at J = 200 A/cm^2.*

Figure 9-1(a) shows the device structures and doping levels of each layer that are used in the study. The 2.2 mm undoped GaN with the background concentration of 10^{16} cm^{-3} followed by the 2.2 mm n-type doped GaN with the doping level of $8\text{x}10^{18}$ cm^{-3} serve as the substrate for the device structure. The multiple quantum well (MQW) active region consist of 6 periods of 2.7 nm $In_{0.25}Ga_{0.75}N$ QW sandwiched by 13 nm GaN barrier. The insert shows the enlarged illustration of the top three p-type layers of interest in this chapter. The reference doping levels of 20 nm p-type $Al_{0.15}Ga_{0.85}N$ electron blocking layer (EBL), 75 nm p-GaN and 15 nm p+-GaN contact layer are

$3x10^{17}$ cm^{-3}, $3x10^{17}$ cm^{-3}, $3x10^{18}$ cm^{-3}, respectively. The p-metal and n-metal contacts are deposited on top and at the bottom of the devices to create the vertical current injection device configurations, and the carrier transport effect have been taken into account. Figure 9-1(b) is the band structure, the quasi-Fermi level and corresponding wavefunctions in each QW for the reference sample at J= 200A/cm^2. The screening ratio of the interface charges is assumed to be 70% of the calculated value. The emission wavelength is calculated as ~500 nm.

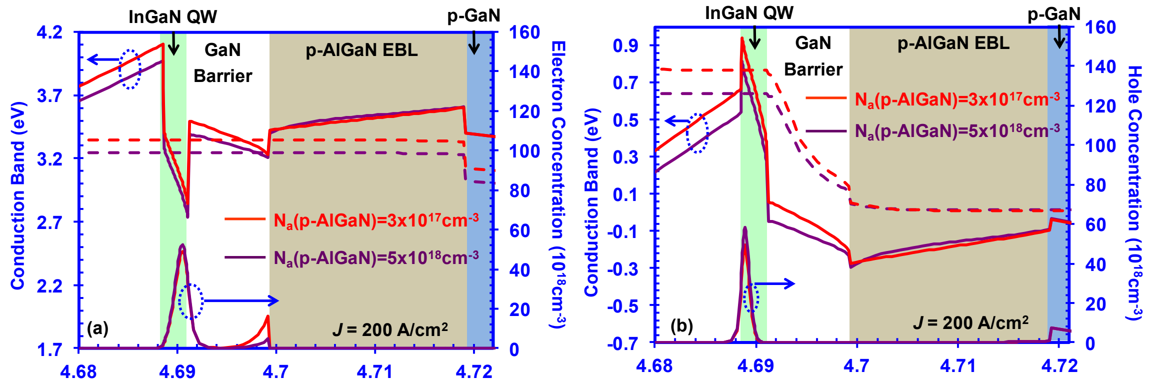

Figure 9-2 *(a) Conduction band and electron concentration and (b) valence band and hole concentration of the last QW of LEDs with p-AlGaN doping level of* $3x10^{17}$ cm^{-3} *and* $5x10^{18}$ cm^{-3} *at J= 200A/*cm^2.

The effect of the doping levels of p-AlGaN EBL will be firstly investigated, and the doping levels for p-GaN and p+-GaN are fixed at $3x10^{17}$ cm^{-3} and $3x10^{18}$ cm^{-3}, respectively. Figure 9-2 shows the (a) conduction band and quasi-Fermi level for electrons, and (b) valence band and quasi-Fermi level for holes of the last QW of LEDs with p-AlGaN doping level [N_a(p-AlGaN)] of $3x10^{17}$ cm^{-3} and $5x10^{18}$ cm^{-3} at J= 200A/cm^2, respectively. The quasi-Fermi levels for holes are aligned in pGaN layer for both LEDs, while the quasi-Fermi levels for electrons is reduced for LED with larger N_a(p-AlGaN). The separation of quasi-Fermi levels is thus smaller for LED with larger N_a(p-AlGaN), which indicate the reduced forward voltage. In fact, the voltage is around 3.44V for LED with N_a(p-AlGaN)= $3x10^{17}$ cm^{-3} and 3.21V for LED with N_a(p-AlGaN)= $5x10^{18}$ cm^{-3}, respectively. As a result, the band bending is less severe in LED with larger N_a(p-AlGaN), especially in the last GaN barrier region. Therefore, the escaped electron concentration is smaller in LEDs with higher p-AlGaN doping level in figure 9-2(a). In addition, the hole concentrations are slightly enhanced by the use of higher N_a(p-AlGaN) as shown in figure 9-2(b).

Figure 9-3 plots the device characteristics of InGaN QW LEDs with three different p-AlGaN doping levels, 5×10^{16} cm^{-3}, 3×10^{17} cm^{-3}, 3×10^{18} cm^{-3}. The extraction efficiency is assumed as 70% in calculating the light output power. The Shockely-Read-Hall recombination coefficient *A* and auger recombination coefficient *C* are set as 10^7 /s and 10^{-32} cm^6/s in calculating the IQE, respectively. As expected, the device performance will be enhanced by the increased p-AlGaN doping level, showing in the higher light output power, lower forward voltage and higher internal quantum efficiency (IQE). In addition, the efficiency droop issue is suppressed by the use of higher p-AlGaN doping. From these results, we can conclude that the doping level of p-AlGaN EBL has strong influence on the LED performance, and thus the doping sensitivity of the device characteristics becomes important for the high yields of the products.

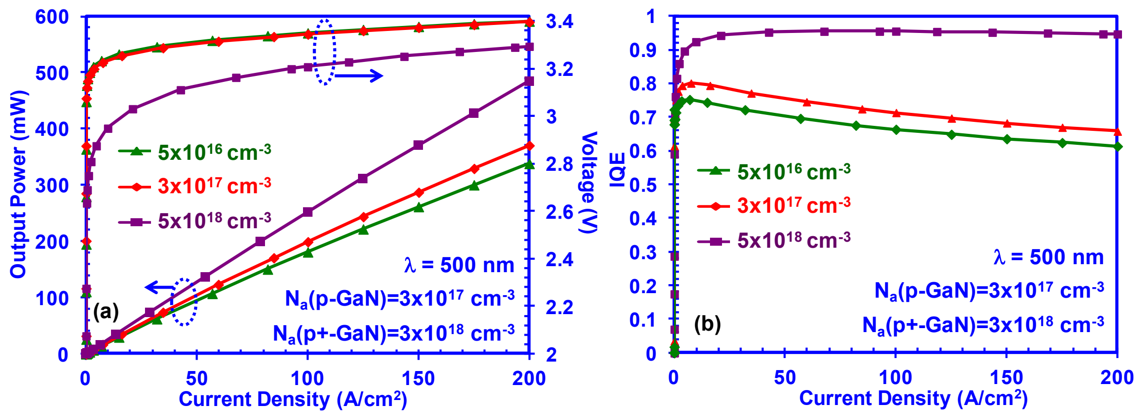

Figure 9-3 *(a) Light output power-current density-voltage characteristics and (b) internal quantum efficiency (IQE) of LEDs with different p-AlGaN doping levels.*

Figure 9-4(a) shows the light output power at J= 100A/cm^2 and 200A/cm^2 as a function of p-AlGaN doping level, N_a(p-AlGaN). The output power at J= 100A/cm^2 and 200A/cm^2 increases 34.4% and 44.8%, respectively, when N_a(p-AlGaN) increases from 3×10^{17} cm^{-3} to 5×10^{18} cm^{-3}. The parameter, doping sensitivity of output power (D-P sensitivity) is defined as follows. The reference p-AlGaN doping level (N_{a0}) is set as 3×10^{17} cm^{-3}, and the corresponding light output power (P_0) at J=100A/cm^2 and 200A/cm^2 are 710.9mW and 1323.1mW, respectively. The ratio of the change of the light output power with respective to the reference power $\Delta P_1/P_0$ to the change of doping level with respective to the reference doping level $\Delta N_a/N_{a0}$ is defined as the doping

sensitivity of power. Thus, the parameter D-P sensitivity represents how quick the power changes as the doping level varies due to the annealing temperature differences. It can be calculated as:

$$\text{D-P Sensitivity} = \frac{\frac{\Delta P_1}{P_0}}{\frac{\Delta N_{a1}}{N_{a0}}} = \frac{(P_1 - P_0)\cdot N_{a0}}{(N_{a1} - N_{a0})\cdot P_0} \qquad (9.1)$$

The D-P sensitivity is plotted in figure 9-4(b). It decreases from 0.109 to 0.022 at J= 100A/cm^2, and 0.105 to 0.029 at J= 200A/cm^2, respectively, as N_a(p-AlGaN) changes from low 5x10^{16} cm^{-3} to 5x10^{18} cm^{-3}. Higher current operation will slightly increase the sensitivity. Besides, the higher doping level will lead to smaller doping sensitivity of light output power.

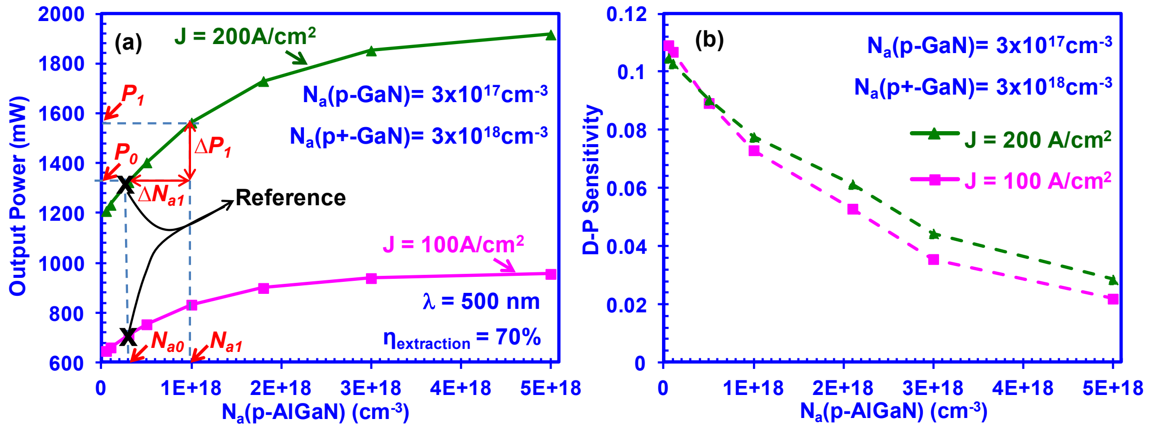

Figure 9-4 *(a) Light output power at J= 100A/cm^2 and 200A/cm^2 as a function of p-AlGaN doping level, N_a(p-AlGaN). The calculation of doping sensitivity of output power (D-P sensitivity) is illustrated. (b) P-AlGaN D-P sensitivity at J= 100A/cm^2 and 200A/cm^2.*

Similarly, the variation of IQE as p-AlGaN doping level changes is investigated in figure 9-5. The IQE and doping sensitivity of IQE (D-IQE sensitivity) IQE at J = 100 A/cm^2 and 200A/cm^2 are plotted in figure 9-5(a) and 9-5(b). Specifically, the IQE at J = 100 A/cm^2 and J = 200 A/cm^2 show 33.9% and 43.9% increase, respectively, as N_a(p-AlGaN) increases from reference 3x10^{17} cm^{-3} to 5x10^{18} cm^{-3}. Besides, the efficiency droop issue reflected by the difference in the two curves at J=100 A/cm^2 and 200 A/cm^2 is less sever at high doping level regime, which is in good agreement with the results in figure 9-3(b). The D-IQE sensitivity is defined as the ratio of the change of IQE with respect to the reference IQE, $\Delta IQE/IQE_0$ to the change of doping level with respective to the reference doping level $\Delta N_a/N_{a0}$, which is analogous to the definition of D-P

sensitivity. Figure 9-5(b) plots the D-IQE sensitivity as a function of p-AlGaN doping level. It decreases from 0.107 to 0.022 at J= 100A/cm^2, and 0.103 to 0.028 at J= 200A/cm^2, respectively, as N_a(p-AlGaN) changes from low 5x10^{16} cm^{-3} to 5x10^{18} cm^{-3}. The values of D-IQE sensitivity are comparable with those of D-P sensitivity, which indicates the similar effect of the doping level on device performance. In addition, similar to what has been observed from D-P sensitivity, the lower injection operation and higher doping level will help in reducing the sensitivity.

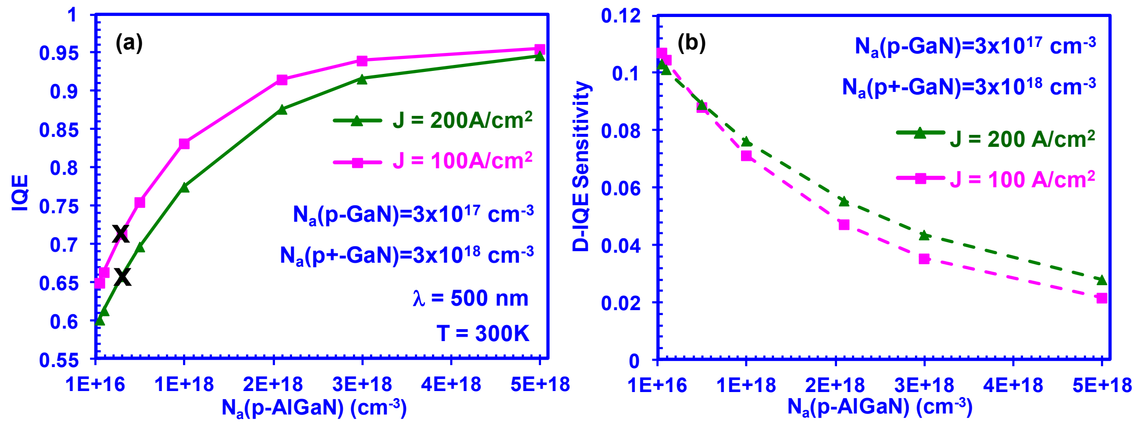

Figure 9-5 *(a) IQE at J= 100A/cm^2 and 200A/cm^2 as a function of p-AlGaN doping level, N_a(p-AlGaN). The calculation of doping sensitivity of IQE (D-IQE sensitivity) is illustrated. (b) P-AlGaN D-IQE sensitivity at J= 100A/cm^2 and 200A/cm^2.*

The effect of the doping level of p-GaN cap layer and p+-GaN contact layer is also investigated, and the changes of the light output power and IQE at J=200 A/cm^2 are shown in figure 9-6. As compared to the effect of N_a(p-AlGaN), the device performance is much less sensitive to the changes of N_a(p-GaN) and N_a(p+-GaN). Specifically, in figure 9-6(a), the light output power shows 0.47% and 0.002% increase with N_a(p-GaN) varying from the reference 3x10^{17} cm^{-3} to 5x10^{18}cm^{-3} and N_a(p-GaN) varying from the reference 3x10^{18} cm^{-3} to 8x10^{18} cm^{-3}, respectively. The results indicate that the influence of the doping levels of p-GaN and p+-GaN is much weaker as compared to that of p-AlGaN. Similarly, in figure 9-6(b), the IQE only shows 0.65% and 0.002% increase with increasing N_a(p-GaN) and N_a(p+-GaN), respectively. The doping sensitivities of power and IQE are also plotted in figure 9-6(c) and (d), respectively. The values in figure 9-6 (c) and (d) are much smaller in comparison with those in figure 9-4 (b) and 9-5 (b), indicating that the further the layer is away from the active region, the less the sensitivity will

become. Specifically, the D-P sensitivity decrease from 7.79×10^{-4} to 4.20×10^{-4} as N_a(p-GaN) increases, and from 3.34×10^{-5} to 4.18×10^{-6} as N_a(p+-GaN) increases. Besides, the D-IQE sensitivity decrease from 7.70×10^{-4} to 4.14×10^{-4} as N_a(p-GaN) increases, and from 6.64×10^{-5} to 1.44×10^{-5} as N_a(p+-GaN) increases. The nearly four orders of magnitude reduction in p+-GaN doping sensitivity as compared to p-AlGaN doping sensitivity suggests that the much reduced contribution of the p+-GaN doping level variation to the change of device performance. Thus, the p-type layer of great interests will be p-AlGaN EBL that is closest to the QW active region.

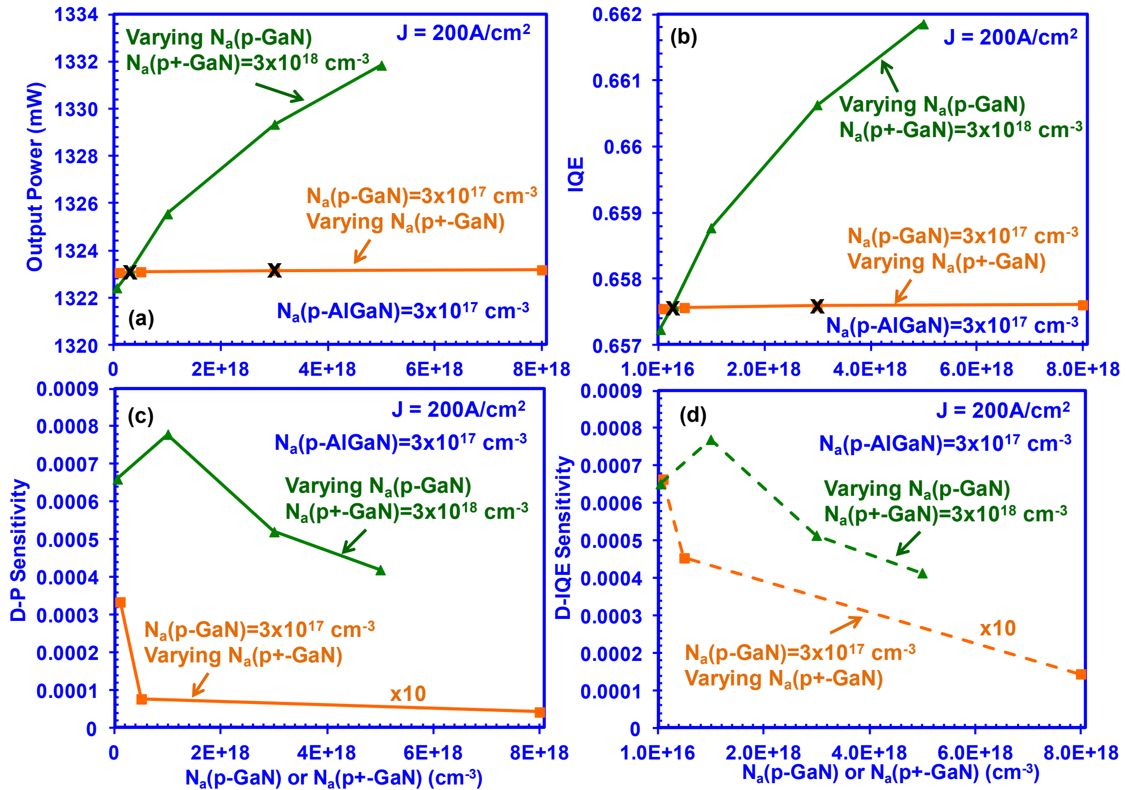

Figure 9-6 *(a) The light output power, (b) D-P sensitivity, (c) IQE and (d) D-P sensitivity at J= 200A/cm^2 as the doping levels of p-GaN (green line) and p+-GaN doping level (orange line) changes.*

9.3 Effect of LEDs with Activation Level

The LED devices grown on the wafer will be annealed as a whole in the annealing process. Thus, the activation condition will be the same for all layers. In this section, we are going to look into the effect of the InGaN MQW LEDs with different activation levels. Figure 9-7 shows the

device characteristics of InGaN QW LEDs with different activation levels with respective to the reference LED ["x1" in figure 9-7] with p-AlGaN, p-GaN and p+-GaN doping levels of $3x10^{17}$ cm^{-3}, $3x10^{17}$ cm^{-3}, 3 $x10^{18}$ cm^{-3}, respectively. 60% less activated LED sample with lower annealing temperature is denoted as "x0.4". In another word, the N_a(p-AlGaN), N_a(p-GaN) and N_a(p+-GaN) are $1.2x10^{17}$ cm^{-3}, $1.2x10^{17}$ cm^{-3}, $1.2x10^{18}$ cm^{-3}, respectively. 60% more activated sample with higher annealing temperature is denoted as "x1.6", which refers to the condition of N_a(p-AlGaN)= $4.8x10^{17}$ cm^{-3}, N_a(p-GaN)= $4.8x10^{17}$ cm^{-3} and N_a(p+-GaN)= $4.8x10^{18}$ cm^{-3}, respectively. As shown in the figure 9-7, higher activation level leads to smaller forward voltage, higher light output power and higher efficiency at all current density.

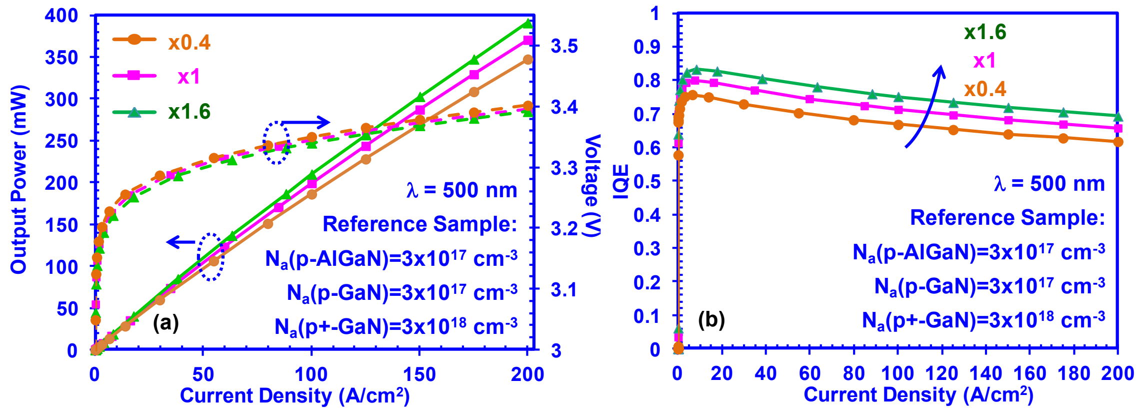

Figure 9-7 *(a) Light output power-voltage-current density characteristics and (b) IQE of LEDs with different activation levels.*

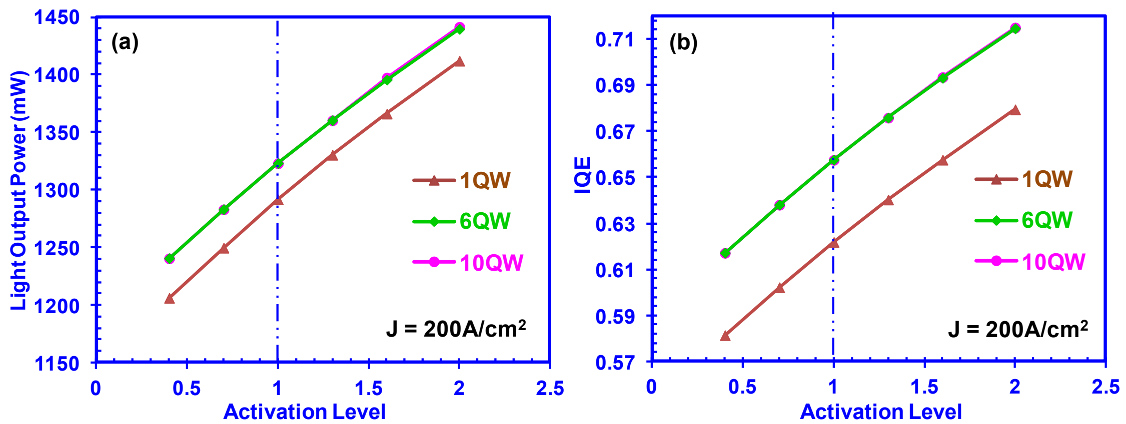

Figure 9-8 *(a) Light output power and (b) IQE at J=200A/cm^2 as a function of p-layer activation levels from LEDs with different QW numbers.*

Figure 9-8 shows the (a) light output power and (b) IQE at J=200A/cm^2 as a function of p-layer

activation levels with different QW numbers. For the case of LEDs with six periods of InGaN/GaN MQWs employed in the previous study, the increase in both light output power and IQE is observed as the activation level increases. Specifically, as compared to the reference LED, 60% smaller p-type doping level (x0.4) leads to 6.23% reduction in light output power and 6.95% reduction in IQE, and 60% larger p-type doping level (x1.6) results in 5.48% enhancement in light output power and 5.75% enhancement in IQE. The change of the slope is minimal, but slight reduction as activation level increase can still be observed, indicating the slight decrease of the sensitivity as the hole carrier concentrations reach a higher level.

Furthermore, the figure 9-8 also compared the sensitivity of the LEDs with different QW number. The use of larger QW period helps in enhancing device performance and reduction of the sensitivity. For instance, the variations of light output power at J = 200A/cm^2 are -6.62% to +5.76% as the activation level varies from 0.4 to 1.6 from LED with one period of InGaN/GaN QW. However, the enhancement by increasing QW number will saturate as shown in the LED with ten periods of QW. The device characteristics between LEDs with 6QWs and LEDs with 10QWs are very comparable with minimal enhancement.

In conclusion, the dopant activation is crucial for III-nitride based LED device operation and the high yield from commercial production line is of great interests for industrial application. The analysis on the p-type doping sensitivity of device performance has provided guidance in evaluating the yield of the fabrication process. The variation in annealing temperature in the chamber leads to uniform doping level of the devices across the radius distance. From the investigation of each layer doping, we found that the device performance is most sensitive to the change of p-AlGaN EBL doping level, and less related to the p-GaN above p-AlGaN layer and p-+GaN contact layer on top. From the study of activation variation of the device as a whole, we concluded that the higher activation level leads to better device performance and reduced sensitivity, and the increase of p-type doping level will be limited by the fabrication process and the detrimental effect of highly doped semiconductors.

References for Chapter 9

1. J. Piprek and Z. M. S. Li, "Sensitivity analysis of electron leakage in III-nitride light-emitting diodes," *Appl. Phys. Lett.,* vol. 102, p. 131103, 2013.
2. V. K. Malyutenko, S. S. Bolgov, and A. D. Podoltsev, "Current crowding effect on the ideality factor and efficiency droop in blue lateral InGaN/GaN light emitting diodes," *Appl. Phys. Lett.*, vol. 97, Dec 20 2010.
3. Y. Y. Kudryk and A. V. Zinovchuk, "Efficiency droop in InGaN/GaN multiple quantum well light-emitting diodes with nonuniform current spreading," Semiconductor Science and Technology, vol. 26, Sep 2011.
4. H. Y. Ryu and J. I. Shim, "Effect of current spreading on the efficiency droop of InGaN light-emitting diodes," Optics Express, vol. 19, pp. 2886-2894, Feb 14 2011.
5. A. David, M. J. Grundmann, J. F. Kaeding, N. F. Gardner, T. G. Mihopoulos, and M. R. Krames, “Carrier distribution in (0001) InGaN/GaN multiple quantum well light-emitting diodes”, Appl. Phys. Lett., vol. 92, no. 5, pp. 053502-1–053502-3, Feb. 2008.
6. Y. J. Wang, R. Kaplan, H. K. Ng, K. Doverspike, D. K. Gaskill, T. Ikedo, I. Akasaki, and H. Amono, “Magneto-optical studies of GaN and GaN/$Al_xGa_{1-x}N$: Donor Zeeman spectroscopy and two dimensional electron gas cyclotron resonance”, J. Appl. Phys. 79, 8007, 1996.
7. S. Nakamura, N. Iwasa, M. Senoh, and T. Mukai, "Hole Compensation Mechanism of P-Type Gan Films," *Japanese J. Appl. Phys. Part 1-Regular Papers Short Notes & Review Papers,* vol. 31, pp. 1258-1266, May 1992.
8. T. Tanaka, A. Watanabe, H. Amano, Y. Kobayashi, I. Akasaki, S. Yamazaki, and M. Koike, "p-type conduction in Mg-doped GaN and $Al_{0.08}Ga_{0.92}N$ grown by metalorganic vapor phase epitaxy," *Appl. Phys. Lett.,* vol. 65, pp. 593-594, 1994.
9. W. Gotz, N. M. Johnson, J. Walker, D. P. Bour, and R. A. Street, "Activation of acceptors in Mg-doped GaN grown by metalorganic chemical vapor deposition," *Appl. Phys. Lett.,* vol. 68, pp. 667-669, Jan 29 1996.
10. M. G. Cheong, K. S. Kim, C. S. Kim, R. J. Choi, H. S. Yoon, N. W. Namgung, E. K. Suh, and H. J. Lee, "Strong acceptor density and temperature dependences of thermal activation energy of acceptors in a Mg-doped GaN epilayer grown by metalorganic chemical-vapor deposition," *Appl. Phys. Lett.,* vol. 80, pp. 1001-1003, Feb 11 2002.
11. J. L. Lyons, A. Janotti, and C. G. Van de Walle, "Shallow versus Deep Nature of Mg Acceptors in Nitride Semiconductors," *Phys. Rev. Lett.,* vol. 108, p. 156403, 2012.
12. P. Kozodoy, H. Xing, S. P. DenBaars, U. K. Mishra, A. Saxler, R. Perrin, S. Elhamri, and W. C. Mitchel, "Heavy doping effects in Mg-doped GaN," *J. Appl. Phys.,* vol. 87, pp. 1832-1835, 2000.
13. H. A. Lord, "Thermal and Stress-Analysis of Semiconductor Wafers in a Rapid Thermal-Processing Oven," *IEEE Transactions on Semiconductor Manufacturing,* vol. 1, pp. 105-

114, Aug 1988.

14. R. S. Gyurcsik, T. J. Riley, and F. Y. Sorrell, "A Model for Rapid Thermal-Processing - Achieving Uniformity through Lamp Control," *IEEE Transactions on Semiconductor Manufacturing,* vol. 4, pp. 9-13, Feb 1991.

15. C. K. Chao, S. Y. Hung, and C. C. Yu, "Thermal stress analysis for rapid thermal processor," *IEEE Transactions on Semiconductor Manufacturing,* vol. 16, pp. 335-341, May 2003.

Chapter 10: Fabrications and Characterizations of InGaN Quantum Dots Using Selective Area Epitaxy

10.1 Introduction of InGaN based Quantum Dots

10.1.1 Motivations for the Pursuit of Quantum Dots Nanostructure

III-nitride based InGaN quantum wells (QW) are typically employed as active regions in energy-efficient and reliable light-emitting diodes (LEDs) for solid state lighting. However, the large spontaneous and piezoelectric polarization fields in III-Nitride material lead to a significant charge separation effect, which in turn result in low internal quantum efficiency of green-emitting nitride-based LEDs and high threshold current density in nitride lasers. Several approaches of QW structure modification have been proposed to improve the internal quantum efficiency (IQE) of LEDs including the employment of nonpolar substrates (a-plane or m-plane) or semipolar substrates as well as novel InGaN QWs with improved electron-hole wavefunction overlaps designs on polar substrates (c-plane), which has been extensively studied in the previous chapters.

In addition to the previously discussed approaches, the InGaN quantum dot (QD) based active regions have shown great potential for optoelectronic applications [1-6]. The three dimensional potential boundaries deeply localize carriers and thus electron-hole wavefunctions overlap is greatly enhanced [7-10]. For instance, the radiative lifetime of QW structure is much larger than the calculated radiative lifetime of QD structure where the lifetime is found to be in the order of ~1 nanosecond due to the stronger quantum effects [9]. The release of lattice mismatch, reduced internal electric field and smaller quantum confined Stark effect (QCSE) are beneficial properties of QD nanostructures in suppressing wavelength shift, efficiency droop and threshold current density. Besides, the non-radiative recombination centers and defects of materials can be significantly reduced. Futhermore, quantum dot design enables high In-content InGaN epitaxy, which enlarges the coverage of emission spectrum and enriches the design of QD based active region.

10.1.2 Fabrication Methods of InGaN based Quantum Dots

Various approaches have been proposed to fabricate InGaN based quantum dot nanostructures. They can be summarized into two categories: a) bottom-up approaches where the internal anisotropic strain is utilized to induce the surface instability of the thin films and thus form the dot shape, for instant, Stranski-Krastanow growth mode; b) top-down approach where nanopatterns would be created on the substrate first so that the nanoscaled selective area epitaxy would occur.

(i) Self-Assembled Stranski–Krastanow Growth Mode

The prevailing method of obtaining InGaN based QD structure is by employing Stranski–Krastanow (SK) growth mode, which was first noted by Ivan Stranski and Lyubomir Krastanov in 1938. It has been employed by both molecular beam epitaxy (MBE) and metal-organic chemical vapor deposition (MOCVD) technique for the epitaxy of nitride-based QDs [11-14] and arsenide-based QDs [15, 16]. The process step of SK growth is illustrated in figure 10-1, where both two-dimensional and three-dimensional epitaxial mode is observed in the "layer-plus-island" growth fashion. Initially, 2D thin film growth would take place on the surface of the substrate due to the strong interaction between atoms and surface [figure 10-1(a)]. This "layer-by-layer" mode would continue up to the thickness of several monolayers with the material strains accumulating in the epilayer [figure 10-1(b)]. Then, the growth mode would turn into 3D island formation with stronger adatom-adatom interaction as a result of the release of strain and a sign reversal in the chemical potential [figure 10-1(c)]. The thickness h_c where the growth transits from coalescence to nucleation is defined as critical thickness which is determined by the chemical and physical properties of both substrate and thin film on top. The 2D thin layer is referred as wetting layer. Hence, the nanostructure of quantum dots would be formed on top of wetting layer and the dots are in a random distribution of sizes and locations with local orders [figure 10-1(d)].

MOCVD growth of self-assembled InGaN QDs emitting in the 510–520 nm region has been carried out previously [14]. Figure 10-2 shows the dot morphology characterized by atomic force microscope (AFM). The use of self-assembled growth technique of InGaN QDs led to quantum dots with circular base diameter of 40 nm and an average height of 4 nm, and the QDs density

was measured as 4 x 10^9 cm^{-2}. The S-K growth mode of InGaN QDs resulted in relatively low density (mid 10^9 up to high 10^9 cm^{-2}), nonuniformity in QD distribution, and the existence of wetting layer. In contrast to InGaN-based QDs, S-K growths of In(Ga)As / GaAs QDs have led to high performance lasers with high QD density (high 10^{10} cm^{-2}) and uniform QD distribution.

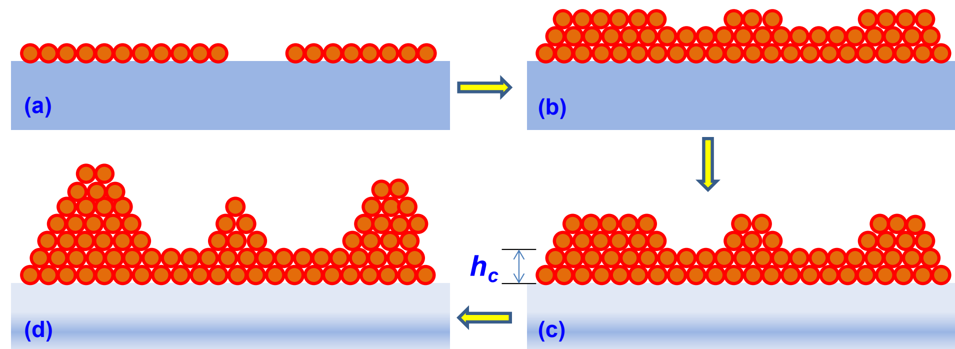

Figure 10-1 *Schematics of material growth evolution of Stranski-Krastanow growth mode*

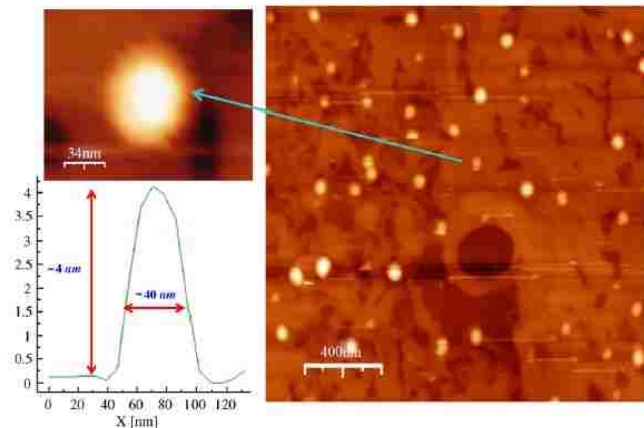

Figure 10-2 *AFM measurements of MOCVD-grown self-assembled InGaN QDs by employing the Stranski-Krastanow growth mode [14].*

Another important obstacle to fully explore the radiative and gain properties of QD structure from S-K growth mode is the inherent presence of the wetting layer. Several recent works have shown that the strain fields in the wetting layer from the S-K grown QDs reduces the envelop function overlap and recombination rate in QDs active region [7-9]. The wetting layer also serves as a carrier leakage path due to the coupling of wetting-layer states with localized QD states,

which leads to increase of threshold current in laser devices [17]. Figure 10-3 shows the detrimental effect of the wetting layer on the optical properties of QD devices. Here an example of $In_{0.2}Ga_{0.8}N$ quantum dot with hexagonal pyramid shape was employed. The electron-hole envelop function overlap reduced significantly with the increase wetting layer thickness, which would leads to the reduction of optical gain and radiative recombination rate in device operation. Thus, another technique to obtain high density and high uniform InGaN based QD without the wetting layer is required for the optimal device performance from QD structures.

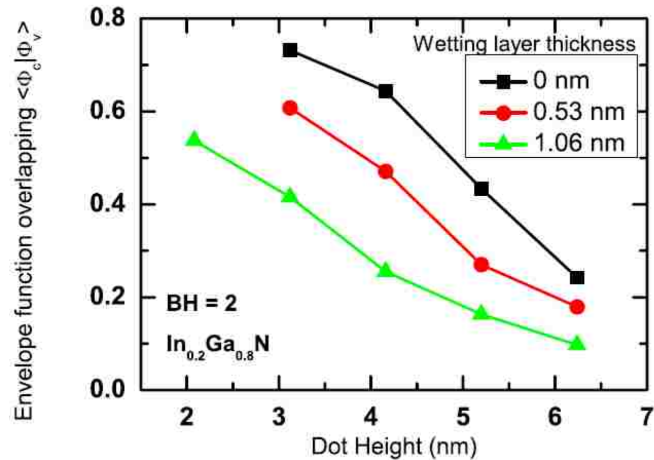

Figure 10-3 *The electron-hole envelop function overlap in the* $In_{0.2}Ga_{0.8}N$ *quantum dot device with different wetting layer thicknesses [9].*

(ii) Selective Area Epitaxy

The most straightforward way to obtain the three-dimensional quantum dot nanostructure is by etching the two-dimensional quantum well using mask. However, this approach introduces significant nonradiative defects and suffers from several surface recombination rates due to the imperfections on the surface. In addition, it is very costly to create patterns or structure in nanometer scale. Thus, it is not suitable to fabricate QD based devices for optoelectronic applications.

To eliminate of the detrimental wetting layer induced by S-K growth mode as well as fully control the formation of QDs, an alternative to grow ultra-high density QDs has been explored for arsenide-based QDs devices by utilizing selective area epitaxy [18-24]. The ideal QDs obtained

by this approach, in particular realized by employing diblock copolymer lithography, have comparable QD density to that of S-K growth mode, but potentially have better device performance due to the removal of the wetting layer and better carrier confinement. Previous studies on the selective area epitaxy of InGaN QDs have been pursued by using electron-beam lithography [25-27], and anodized aluminum oxide (AAO) template [28].

10.2 Fabrication of Ultra-high density and Highly Uniformed InGaN QDs

10.2.1 Selective Area Epitaxy of InGaN QDs by Diblock Copolymer Lithography

In this work, we present the selective area epitaxy (SAE) of ultra-high density and highly uniform InGaN-based quantum dots on the nano-patterned GaN template realized by diblock copolymer lithography [3]. The diblock copolymer lithography is ideal for device applications due to the adaptability to full wafer scale nanopatterning. All growths were performed by employing metalorganic chemical vapor deposition (MOCVD) on GaN templates grown on c-plane sapphire substrates. The distribution and size of QDs are well controlled, and the presence of the wetting layer is eliminated. Note that the use of SAE approach on dielectric nanopatterns defined by diblock copolymer process resulted in the growths of InGaN QDs without wetting layer, which potentially leads to the increase in optical matrix element. In addition to the improved matrix element in the QD, the use of dielectric layers can also serve as current confinement layer resulting in efficient carrier injection directly into the InGaN QDs arrays. The diblock copolymer lithography approach also leads to very high density patterning with excellent uniformity and low cost. In contrast, the use of AAO template leads to relatively non-uniform patterning, while the use of e-beam lithography leads to high cost approach.

10.2.2 Procedure of Selective-Area Epitaxy of InGaN Quantum Dots

The fabrication process consists of nano-template preparation by diblock copolymer lithography and selective area epitaxy by MOCVD. Figures 10-4(a)-(f) show the fabrication process flow schematics for the SAE-QDs defined by diblock copolymer approach. The growth of 3 μm GaN template on the c-plane sapphire substrate was carried out by employing MOCVD, which has been discussed in Chapter 5. Subsequently [figure 10-4(a)], 10 nm SiN_x was deposited

on the sample by plasma-enhanced chemical vapor deposition (PECVD) and followed by NH_3 annealing at a temperature of 800 ^{o}C for 20 mins to increase the adhesion of SiN_x on GaN template. The sample was then pretreated with PS-r-PMMA brush material followed by the deposition of cylinder forming diblock copolymer PS-b-PMMA [figure 10-4(b)]. The brush material is made of random copolymer that would lead to non-preferential affinity to the both blocks of the self-organizing PS-b-PMMA copolymer, which enabled the formation of the cylindrical morphology on the diblock copolymer layer during the thermal annealing as a result of the microphase separation. After the UV exposure (λ = 254 nm) and chemical etching by acetic acid, the PMMA block was removed, leaving the PS block to form the patterned copolymer that was used as the polymer stencil [figure 10-4(c)]. Subsequently, the sample went through the reactive ion etching (RIE) by CF_4 plasma and the nanopatterns were transferred from the copolymer layer to the underneath SiN_x layer [figure 10-4(d)]. After the removal the copolymer by O_2 plasma and wet etching, the SiN_x layer with the nanopatterns could serve as the mask in the following MOCVD process [figure 10-4(e)]. The details of the diblock copolymer processing steps [figures 10-4(b)-(e)] are described in references 55 [29] and 56. The opening region where GaN template was exposed to the metal-organic source would enable the QD growth [figure 10-4(f)]. The remaining SiN_x layer can also serve as an insulator between QDs within the active region of a device.

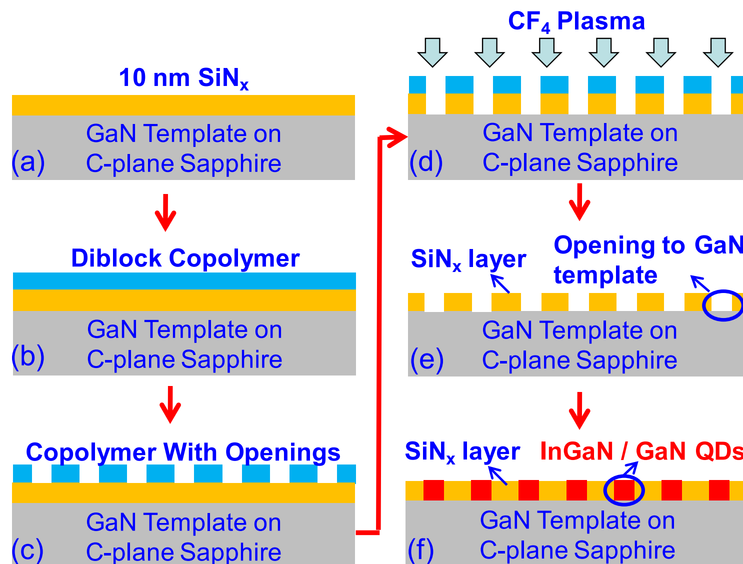

Figure 10-4 *MOCVD process flow of InGaN/GaN QDs SAE with dielectric patterns defined by the self-assembled diblock copolymer.*

The growths of the InGaN QD active region and GaN barrier layers employed triethylgallium (TEGa), trimethylindium (TMIn), and ammonia (NH_3) as gallium, indium and nitrogen precursors, respectively. The growth rates for InGaN active layer and GaN barrier layer in planar region were 3 nm/min and 2.4 nm/min, respectively. The growth temperature and growth pressure for the InGaN QDs and GaN barrier layers were kept at 735 °C and 200 Torr, respectively. The top GaN barrier layer also serves as the cap layer for the sample, and its similar growth temperature with that of the InGaN QDs leads to minimal dissolution of the In during the barrier layer growth. The V/III molar ratios employed for the growths of the GaN templates, GaN barrier, and InGaN active layers were 3900, 34500, and 18500, respectively. Based on growth calibration using XRD measurements, the In-content of the InGaN layer employed in the studies was calibrated as 15 %. In our experiments, two sets of structures were investigated as shown in figure 10-5, as follow: 1) Sample A consists of 1.5 nm InGaN sandwiched by 1 nm GaN barrier layers in the opening region with a total thickness designed to be 3.5 nm; and 2) Sample B consists of 3 nm InGaN layer sandwiched by 2 nm GaN barrier layers with the total thickness of 7 nm.

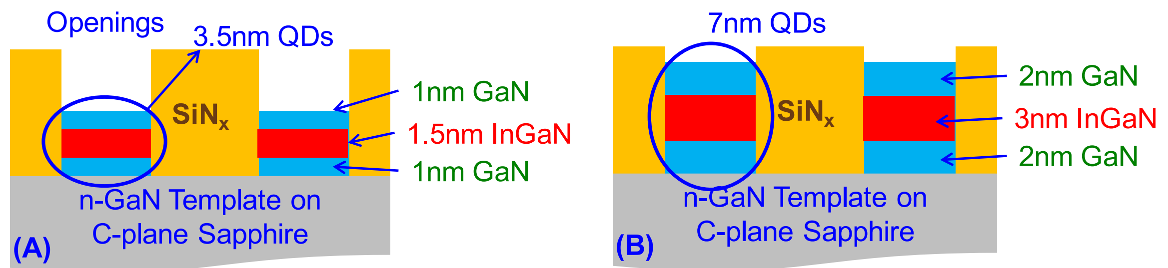

Figure 10-5 *Schematic of two groups of QD samples with the structures of: (A) 1.5-nm InGaN sandwiched between 1 GaN layers (Sample A); (B) 3 nm InGaN sandwiched between 2-nm GaN layers (Sample B).*

10.3 Structural and Morphology Characterizations

The measurements of scanning electron microscope (SEM) [Hitachi 4300] and atomic force microscopy (AFM) [Dimension 3000 and Agilent 5500] were performed to investigate the surface topographies and quantum dot morphologies. Figure 10-6 shows the SEM image of the copolymer deposited on SiN_x layer after undergoing the UV radiation which would result in

nanopore openings, prior to any active region growth. The SEM images shown in figure 10-6 is similar to the processing step described in figure 10-4(c). The diameter of the holes in the copolymer was measured as approximately 20-25 nm, and the arrangement of the copolymer shows 2-D hexagonal closed packed structure, although without long range order between grain boundaries.

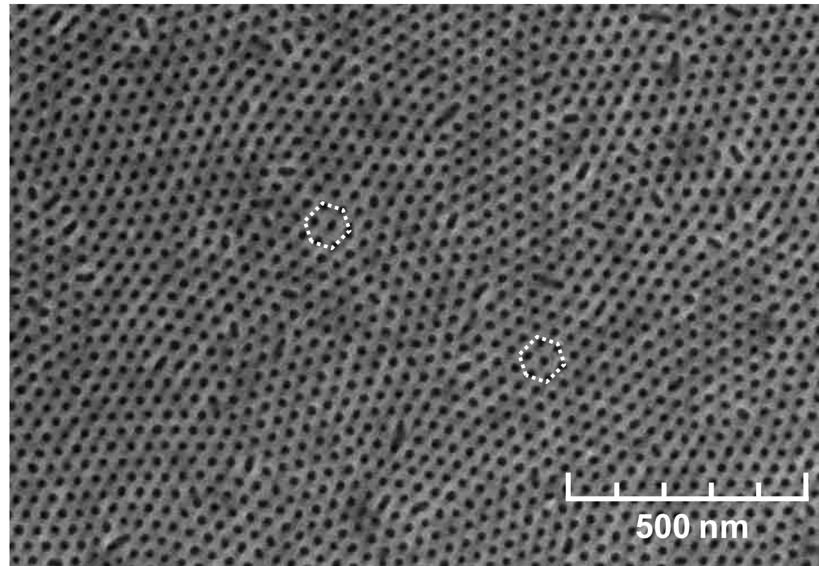

Figure 10-6 *SEM image of diblock copolymer nanopatterns on SiNx with the hexagonal array of openings after the UV exposure.*

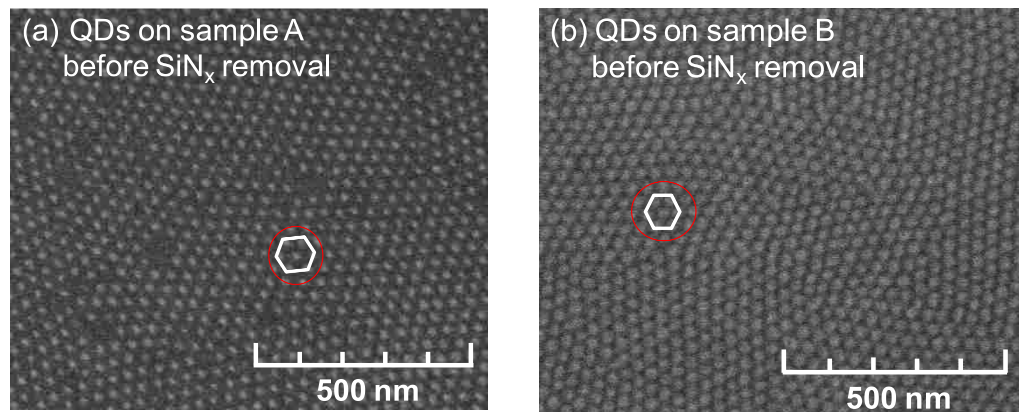

Figure 10-7 *SEM images of SAE-grown InGaN/GaN QDs with SiN_x layer for both samples investigated: (a) sample A; (b) sample B.*

Figures 10-7 show the SEM images of (a) sample A and (b) sample B with InGaN / GaN QDs surrounded by the SiN_x dielectric layer. The SEM measurements demonstrate the successful growth of InGaN/GaN QDs by selective area epitaxy with the elimination of wetting layer. The hexagonal arrangement of QD arrays on both samples is in good agreement with the arrangement of the openings on copolymer layer as shown in figure 10-6.

The SEM images of the samples A and B after the removal of SiN_x layer by HF wet etching were shown in figures 10-8(a) and (b), respectively. The SEM measurements indicate that the QDs on both samples were comparable in both size and distribution with QDs prior to the elimination of the SiN_x layer. The QD diameters were estimated to be about 22 nm and 25 nm on sample A and sample B, respectively. The QD densities for sample A and sample B were measured as $7x10^{10}$ cm^{-2} and $8x10^{10}$ cm^{-2}, respectively, which represent among the highest reported QD density for InGaN material systems.

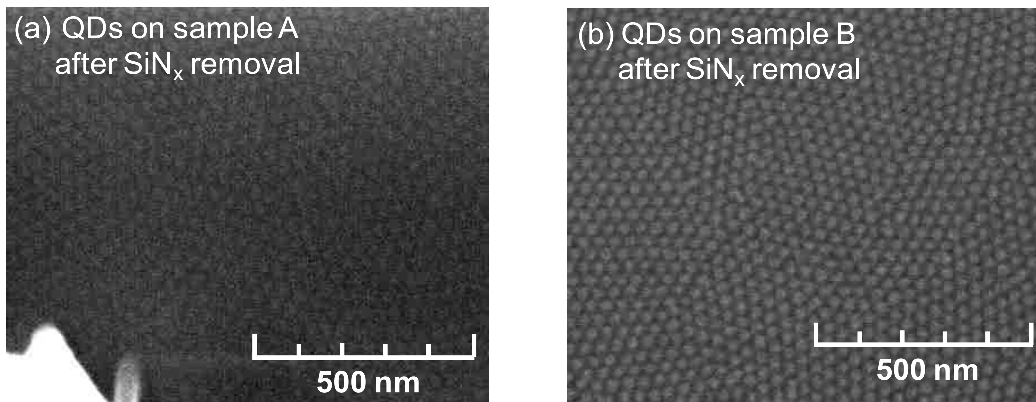

Figure 10-8 *SEM images of SAE-grown InGaN/GaN QDs after removal of SiN_x layer for both samples investigated: (a) sample A; (b) sample B.*

Compare to previously reported work on high density nitride based QDs [30, 31], our approach has several advantages. In reference 30, Krestnikov and co-workers reported the quantum-dot-like behavior in InGaN QW resulted from the In-clustering effect, and the density of the In-rich nanoislands within the QW layer was estimated in the range of 10^{11}-10^{12} cm^{-2}. The QD-like behavior in InGaN QW from the In-clustering effect resulted in relatively shallow QD / barrier systems. In reference 31, Tu and co-workers reported the growth of InGaN QDs by employing

GaN templates with SiN_x treatment which resulted in template roughening, and this process leads to dot density of near $3x10^{11}$ cm^{-2}. However, the use of roughening approach leads to QD distribution with relatively non-uniform size distributions. Thus, the use of SAE approach in growing InGaN QDs led to the capability to grow highly-uniform QDs with deep QD / barrier systems (ie. with GaN or other larger bandgap barrier materials) and very high QD density (~$8x10^{10}$ cm^{-2}).

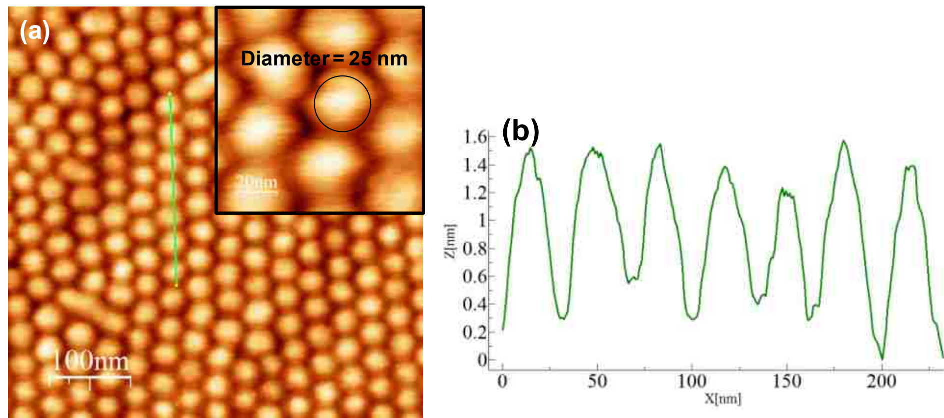

Figure 10-9 *AFM measurement using Dimension 3000 for SAE-grown InGaN/GaN QDs arrays on sample A after removal of SiN_x: (a) AFM scan with the scale of 0.5 μm x 0.5 μm; (b) the corresponding height and size of the cross-sectional profiles.*

Atomic force microscopy (AFM) measurements on InGaN / GaN QDs samples were carried out after the removal of SiN_x layer to provide with direct measurements of quantum dots morphology. The AFM measurements of the InGaN / GaN (Sample A) were carried out by using Dimension 3000, as shown in figures 10-9(a) and (b). Figure 10-9(a) shows the InGaN / GaN QDs arrays with the scale of 0.5 μm x 0.5 μm, and figure 10-9(b) refers to the height and lateral profile of the cross section indicated in figure 10-9(a). The highly uniform QDs were observed from AFM measurements. The dot density was estimated to be $7.5x10^{10}$ cm^{-2} with the average height of 1.84 nm and dot diameter of about 25 nm, and these results are in good agreement with those of the nanopatterns employed in the studies. The height and size profile of the cross-section in figure 10-9(b) indicates that the growth of the dots was well controlled and the sample

exhibits much less variations in dot size, shapes and distributions compared to those of SK growth mode.

For comparison purpose, separate AFM measurements were carried out on sample A by employing Agilent 5500 which consists of higher resolution tip, as shown in figures 10-10(a) and 10-10(b). Figure 10-10(a) shows the AFM image for InGaN / GaN QDs arrays (sample A) with the scale of 0.6 μm x 0.6 μm, and figure 10-10(b) shows the corresponding height and spacing profile for the sample. The QDs were shown to have cylindrical shape, and the quantum dots density was measured as 7.92 x 10^{10} cm^{-2} with average height of 2.5 nm and dot diameter of about 25 nm. The dip-like profile in the QDs could be attributed to different growth rate in the center and outer regions of the QDs, which require further studies to confirm this finding.

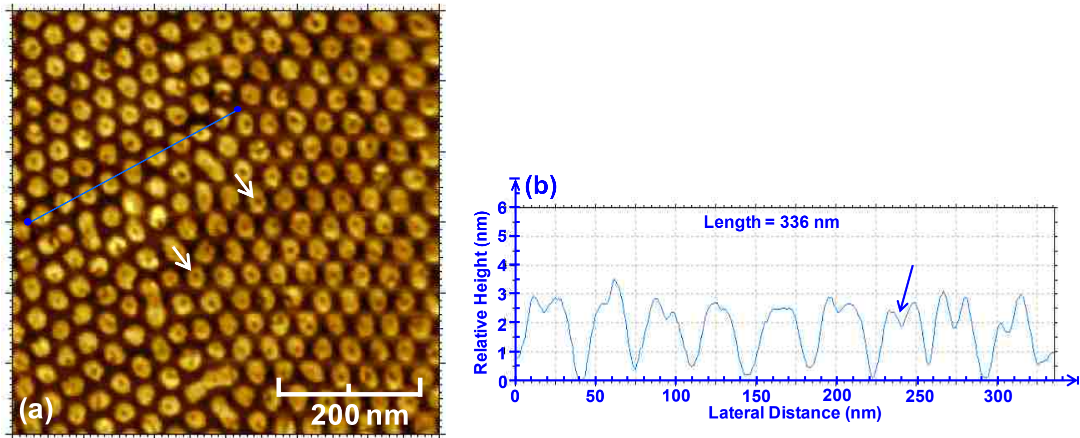

Figure 10-10 *AFM measurement using Agilent 5500 for SAE-grown InGaN/GaN QDs arrays on sample A after removal of* SiN_x*: (a) AFM scan with the scale of 0.6 μm x 0.6 μm; (b) the corresponding height and size of the cross-sectional profiles.*

The AFM image of the InGaN QDs grown on sample B is also shown in figure 10-11 with a scale of 1 μm x 1 μm (Dimension 3000). The density of dots on sample B is measured as 8×10^{10} cm^{-2} with the dot diameter of 25 nm and average height of 4.1 nm. Note that the larger heights in the AFM measurements of the QDs measured in sample B is in agreement with the thicker growths for sample B. The diameter of the quantum dots in our experiments was measured in the range of 22-25 nm, which is considered as relatively large QDs. The focus of the current studies is to investigate the various optimizations in the growth and annealing conditions for the

development of the SAE technique for InGaN QDs with diblock copolymer lithography and the current studies are focused on the dimension of 20-25 nm diameter QDs. In order to obtain stronger quantum effects in the 3-D carrier confinement, the QDs are preferably realized with smaller diameters (10-18 nm) [9]. However, the 3-D quantum effect in the carrier confinement still exists in the 20-25 nm QD diameter as discussed in the theoretical works in reference 36. Future optimization works on the investigation of SAE InGaN QDs with smaller QDs diameter are of importance for achieving nanostructures with stronger 3-D carrier confinement, and the optimization of this approach is required to achieve active regions with high optical quality for device applications.

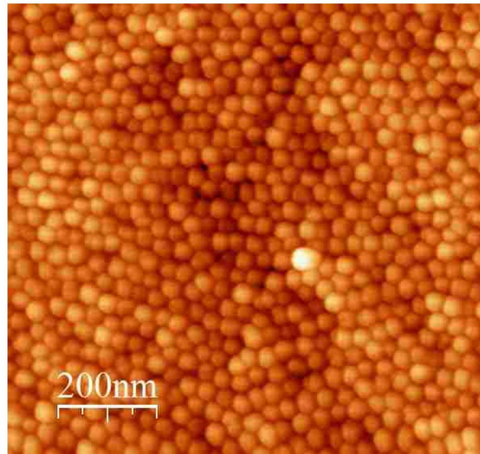

Figure 10-11 *AFM image of SAE-grown InGaN/GaN QDs on samples B measured by Dimension 3000 after removal of* SiN_x *on 1 μm x 1 μm area.*

10.4 Photoluminescence Studies and Discussion

The selective area epitaxy approach enabled the growth of ultrahigh density InGaN QDs, however, the strong photoluminescence (PL) was not observed from the InGaN / GaN QD samples. All the photoluminescence (PL) measurements were carried out by utilizing of He-Cd laser with wavelength at 325 nm as the excitation source at room temperature. From our studies, we found that the surface treatment during the SiN_x deposition could be the cause leading to defect formation in the GaN surface that results inpoor luminescence from SAE-grown QD samples. The surface treatment processes for the epitaxy of the QDs include SiN_x deposition,

and HF etching or CF_4 plasma etching. A series of photoluminescence studies on the SAE-grown InGaN QDs were performed to identify and further understand the effect of various treatments on the photoluminescence of the samples, which will provide guidance in addressing these issues.

To understand the impact of HF etching on the luminescence properties, the PL spectra comparison of InGaN single-QW samples grown on three different types of GaN template are shown in figure 10-12. The active regions in all these samples consists of similar structure; 6 nm GaN barrier followed by 2.5 nm InGaN and then 10 nm GaN cap layer. The comparison samples include the InGaN single-QW grown on three templates as follow: 1) GaN template with no surface treatment (as reference sample), 2) GaN template with HF etching only, and 3) GaN template with SiN_x deposition and HF wet etching. The data indicate that the HF etching does not lead to any detrimental effect on the InGaN QW grown afterward, while the SiN_x deposition process leads to significant detrimental effect on the InGaN QW grown on top of the GaN template as indicated from the significant reduction in the PL intensity.

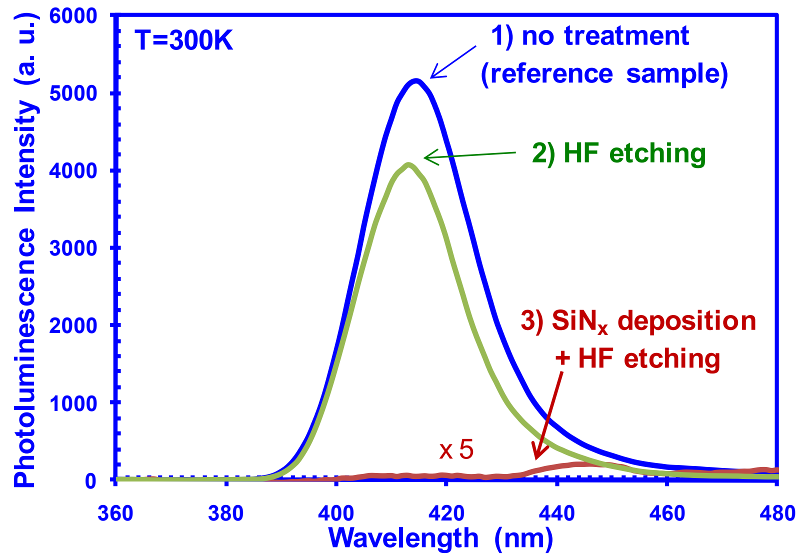

Figure 10-12 *PL comparison of planar SQW grown on (1) GaN with no surface treatment, (2) GaN with HF wet etching, and (3) GaN with SiN_x deposition and HF etching.*

To confirm the effect of SiN_x deposition on the GaN template surface, PL studies were conducted on two additional types of samples as shown in figure 10-13, as follows: 1) InGaN QDs grown on nanopatterned GaN template, and 2) planar InGaN QW with the same InGaN and GaN

thickness grown on the GaN templates that had been treated with SiN_x deposition and HF wet etching, i.e. the same process used to form the dielectric mask for selective QD growth. The spectra for both samples were compared to that of the InGaN QW grown on the GaN template with no surface treatment (reference sample), and very poor PL spectra were observed for both samples grown on the templates that had been treated with SiN_x deposition and HF wet etching, indicating that the surface modification from the SiN_x deposition on GaN template surface is responsible for the poor luminescence.

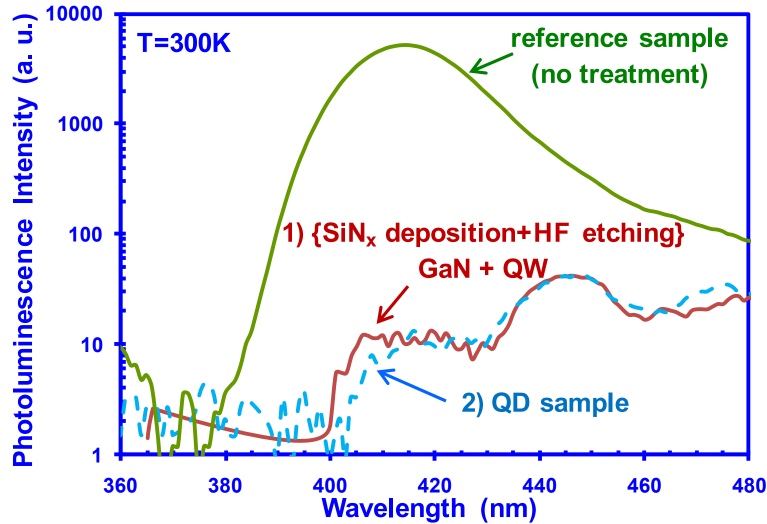

Figure 10-13 *PL comparison of (1) planar InGaN QW on GaN template that has been treated with SiNx deposition and HF etching, and (2) InGaN QD sample with the same InGaN and GaN layer thickness.*

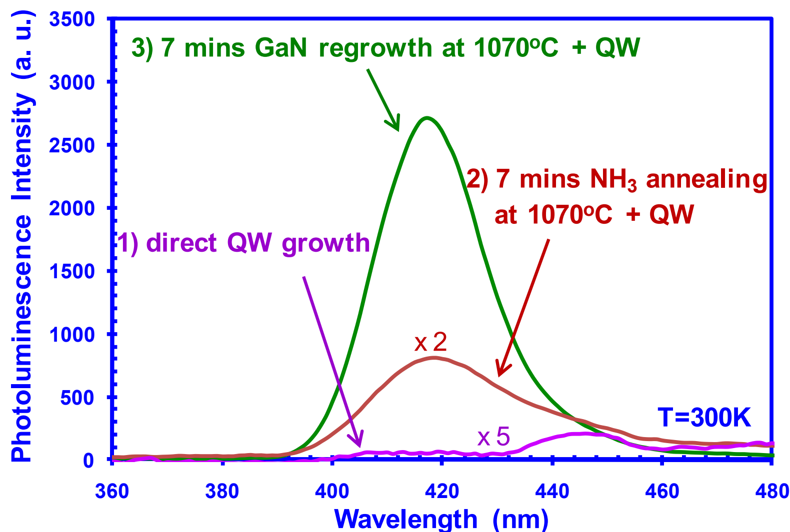

Figure 10-14 *PL enhancement study of SQW with different growth condition treatments.*

Experiments were carried out to identify possible approaches to address the SiN_x surface treatment issue, as illustrated in figure 10-14. Different growth conditions were applied to the GaN templates that have been treated with SiN_x deposition and HF etching, and the same InGaN quantum wells (6 nm GaN / 2.5 nm InGaN / 10 nm GaN) were grown afterwards. The PL spectrum from InGaN QW directly grown on GaN template undergoing SiN_x deposition and HF etching, without any additional growth treatment were shown in figure 10-14 (Direct QW Growth). By annealing the GaN template under NH_3 environment at 1070 ^oC for 7 minutes, the single QW grown on the second sample has almost 40 times enhancement in the peak intensity at 420 nm emission. The third sample consisted of a 7 minute GaN regrowth at 1070^oC prior to the single QW growth, and this sample exhibited additional ~7-times improvement in peak intensity as compared to that of the second sample. The series of PL studies indicate that the GaN regrowth and NH_3 annealing condition prior to the QD / QW active region growth could potentially lead to solutions for addressing the defect generated from the SiN_x deposition on GaN templates. Future studies will involve the application of these procedures to the selective QD growth. Our photoluminescence studies of different template treatment and different growth condition confirm the effect of SiN_x deposition on the GaN template surface, as well as provide possible solutions to enhance luminescence from the QD samples.

References for Chapter 10

1. Y.-R. Wu, Y.-Y. Lin, H.-H. Huang, and J. Singh, "Electronic and optical properties of InGaN quantum dot based light emitters for solid state lighting," *J. Appl. Phys.,* vol. 105, p. 013117, 2009.

2. M. Zhang, P. Bhattacharya, and W. Guo, "InGaN/GaN self-organized quantum dot green light emitting diodes with reduced efficiency droop," *Appl. Phys. Lett.,* vol. 97, Jul 5 2010.

3. G. Y. Liu, H. P. Zhao, J. Zhang, J. H. Park, L. J. Mawst, and N. Tansu, "Selective area epitaxy of ultra-high density InGaN quantum dots by diblock copolymer lithography," *Nanoscale Research Letters,* vol. 6, Apr 15 2011.

4. M. Zhang, A. Banerjee, C.-S. Lee, J. M. Hinckley, and P. Bhattacharya, "A InGaN/GaN quantum dot green (lambda = 524 nm) laser," *Appl. Phys. Lett.,* vol. 98, p. 221104, 2011.

5. J. Brault, B. Damilano, A. Kahouli, S. Chenot, M. Leroux, B. Vinter, and J. Massies, "Ultra-Violet GaN/Al0.5Ga0.5N Quantum Dot Based, Light Emitting Diodes," *J. Crys. Growth,* 2012.

6. A. Banerjee, T. Frost, E. Stark, and P. Bhattacharya, "Continuous-wave operation and differential gain of InGaN/GaN quantum dot ridge waveguide lasers (lambda = 420 nm) on c-plane GaN substrate," *Appl. Phys. Lett.,* vol. 101, p. 041108, 2012.

7. M. Winkelnkemper, A. Schliwa, and D. Bimberg, "Interrelation of structural and electronic properties in In(x)Ga(1-x)N/GaN quantum dots using an eight-band k center dot p model," *Physical Review B,* vol. 74, Oct 2006.

8. D. P. Williams, S. Schulz, A. D. Andreev, and E. P. O'Reilly, "Theory of GaN Quantum Dots for Optical Applications," *IEEE J. Sel. Top. Quantum Electron.,* vol. 15, pp. 1092-1103, Jul-Aug 2009.

9. Y. R. Wu, Y. Y. Lin, H. H. Huang, and J. Singh, "Electronic and optical properties of InGaN quantum dot based light emitters for solid state lighting," *J. Appl. Phys.,* vol. 105, Jan 1 2009.

10. S. Schulz and E. P. O'Reilly, "Theory of reduced built-in polarization field in nitride-based quantum dots," *Physical Review B,* vol. 82, p. 033411, 2010.

11. K. Tachibana, T. Someya, and Y. Arakawa, "Nanometer-scale InGaN self-assembled quantum dots grown by metalorganic chemical vapor deposition," *Appl. Phys. Lett.,* vol. 74, pp. 383-385, 1999.

12. S. Ruffenach, B. Maleyre, O. Briot, and B. Gil, "Growth of InN quantum dots by MOVPE," *physica status solidi (c),* vol. 2, pp. 826-832, 2005.

13. D. Simeonov, E. Feltin, J.-F. Carlin, R. Butte, M. Ilegems, and N. Grandjean, "Stranski-Krastanov GaN/AlN quantum dots grown by metal organic vapor phase epitaxy," *J. Appl. Phys.,* vol. 99, p. 083509, 2006.

14. Y. K. Ee, H. P. Zhao, R. A. Arif, M. Jamil, and N. Tansu, "Self-assembled InGaN quantum dots on GaN emitting at 520 nm grown by metalorganic vapor-phase epitaxy," *J. Crys. Growth,* vol. 310, pp. 2320-2325, Apr 2008.

15. R. L. Sellin, C. Ribbat, M. Grundmann, N. N. Ledentsov, and D. Bimberg, "Close-to-ideal device characteristics of high-power InGaAs/GaAs quantum dot lasers," *Appl. Phys. Lett.,* vol. 78, pp. 1207-1209, 2001.

16. H. Y. Liu, S. L. Liew, T. Badcock, D. J. Mowbray, M. S. Skolnick, S. K. Ray, T. L. Choi, K. M. Groom, B. Stevens, F. Hasbullah, C. Y. Jin, M. Hopkinson, and R. A. Hogg, "p-doped 1.3 mu m InAs/GaAs quantum-dot laser with a low threshold current density and high differential efficiency," *Appl. Phys. Lett.,* vol. 89, p. 073113, 2006.

17. D. R. Matthews, H. D. Summers, P. M. Smowton, and M. Hopkinson, "Experimental investigation of the effect of wetting-layer states on the gain--current characteristic of quantum-dot lasers," *Appl. Phys. Lett.,* vol. 81, pp. 4904-4906, 2002.

18. R. R. Li, P. D. Dapkus, M. E. Thompson, W. G. Jeong, C. Harrison, P. M. Chaikin, R. A. Register, and D. H. Adamson, "Dense arrays of ordered GaAs nanostructures by selective area growth on substrates patterned by block copolymer lithography," *Appl. Phys. Lett.,* vol. 76, pp. 1689-1691, 2000.

19. K. Tachibana, T. Someya, S. Ishida, and Y. Arakawa, "Selective growth of InGaN quantum

dot structures and their microphotoluminescence at room temperature," *Appl. Phys. Lett.,* vol. 76, pp. 3212-3214, 2000.

20. T. S. Yeoh, R. B. Swint, A. Gaur, V. C. Elarde, and J. J. Coleman, "Selective growth of InAs quantum dots by metalorganic chemical vapor deposition," *IEEE J. Sel. Top. Quantum Electron.,* vol. 8, pp. 833-838, 2002.

21. J. H. Park, A. A. Khandekar, S. M. Park, L. J. Mawst, T. F. Kuech, and P. F. Nealey, "Selective MOCVD growth of single-crystal dense GaAs quantum dot array using cylinder-forming diblock copolymers," *J. Crys. Growth,* vol. 297, pp. 283-288, 2006.

22. J. H. Park, J. Kirch, L. J. Mawst, C.-C. Liu, P. F. Nealey, and T. F. Kuech, "Controlled growth of InGaAs/InGaAsP quantum dots on InP substrates employing diblock copolymer lithography," *Appl. Phys. Lett.,* vol. 95, p. 113111, 2009.

23. T. F. Kuech and L. J. Mawst, "Nanofabrication of III-V semiconductors employing diblock copolymer lithography," *Journal of Physics D-Applied Physics,* vol. 43, May 12 2010.

24. L. J. Mawst and T. F. Kuech, "Patterned InGaAs/InGaAsP/InP quantum dot active lasers using diblock copolymer lithography and selective area MOCVD growth," in *IEEE Photonics Society, 2010 23rd Annual Meeting of the*, 2010, pp. 359-360.

25. V. Perez-Solorzano, A. Groning, M. Jetter, T. Riemann, and J. Christen, "Near-red emission from site-controlled pyramidal InGaN quantum dots," *Appl. Phys. Lett.,* vol. 87, p. 163121, 2005.

26. A. Chen, S. J. Chua, P. Chen, X. Y. Chen, and L. K. Jian, "Fabrication of sub-100 nm patterns in SiO2 templates by electron-beam lithography for the growth of periodic III-V semiconductor nanostructures," *Nanotechnology,* vol. 17, pp. 3903-3908, Aug 14 2006.

27. P. Chen, A. Chen, S. J. Chua, and J. N. Tan, "Growth and Optical Properties of Highly Uniform and Periodic InGaN Nanostructures," *Advanced Materials,* vol. 19, pp. 1707-1710, 2007.

28. P. Chen, S. J. Chua, Y. D. Wang, M. D. Sander, and C. G. Fonstad, "InGaN nanorings and nanodots by selective area epitaxy," *Appl. Phys. Lett.,* vol. 87, p. 143111, 2005.

29. J. Singh, K. K. Bajaj, and S. Chaudhuri, "Theory of Photoluminescence Line-Shape Due to Interfacial Quality in Quantum Well Structures," *Appl. Phys. Lett.,* vol. 44, pp. 805-807, 1984.

30. I. L. Krestnikov, N. N. Ledentsov, A. Hoffmann, D. Bimberg, A. V. Sakharov, W. V. Lundin, A. F. Tsatsul'nikov, A. S. Usikov, Z. I. Alferov, Y. G. Musikhin, and D. Gerthsen, "Quantum dot origin of luminescence in InGaN-GaN structures," *Physical Review B,* vol. 66, Oct 15 2002.

31. R. C. Tu, C. J. Tun, C. C. Chuo, B. C. Lee, C. E. Tsai, T. C. Wang, J. Chi, C. P. Lee, and G. C. Chi, "Ultra-high-density InGaN quantum dots grown by metalorganic chemical vapor deposition," *Japanese J. Appl. Phys. Part 2-Letters,* vol. 43, pp. L264-L266, Feb 15 2004.

Chapter 11: Summary and Future Outlook

11.1 Summary

This dissertation mainly focused on the device engineering for high power high efficiency III-nitride based optoelectronics. The original contributions of this report include 1) the study of InGaN-AlGaInN quantum well (QW) light-emitting diodes (LEDs) with different barrier heights, different barrier thickness and different barrier positions using numerical methods, 2) InGaN-delta-InN QW LEDs with different delta-InN thickness and delta-InN positions under electrical bias with consideration of carrier transport, 3) the material growth of AlInN alloys, 4) device fabrications of InGaN-AlInN QW LEDs, 5) the characterizations of LEDs with novel barrier designs, 6) N-polar InGaN QW LED as alternative approach for efficiency droop suppression , 7) the sensitivity of p-type III-nitrides doping levels on LED device characteristics, and 8) the fabrication of high density InGaN based QDs by selective area epitaxy. The detailed summary is as follows.

11.1.1 Novel Barrier Design for Efficiency-Droop Suppression in Nitride LEDs

Efficiency droop issue is a great limitation for cost competitiveness of solid state lighting and the development of high power optoelectronics. The thermionic carrier escape is identified as the the mechanism accounting for the current leakage that contributes to the existence of droop issue. The novel barrier design of inserting large bandgap thin barrier, specifically, lattice-matched AlGaInN thin barriers to increase effective barrier height for carrier leakage suppression has shown to be a promising approach for improved carrier confinement and reduction in efficiency droop.

The large-bandgap AlInN barrier layers have been designed with the goal of minimizing the layer thickness down to ~1–2 nm, in order to ensure practical experimental implementation with minimal impact of the material quality. In addition, we have also found that the use of barrier to the right side of the QW (for blocking the electron escape process) played the most important role in maintaining high injection efficiency in the QW.

The metal organic chemical vapor phase epitaxy (MOVPE) and the characterizations of AlInN alloys grown on both GaN/sapphire templates and free-standing GaN substrates were performed and discussed. The optimization of epitaxial conditions of lattice-matched AlInN material has been carried out with the investigation of effects of growth pressure, growth temperature, and V/III ratio. The optimized growth condition of nearly-lattice-matched AlInN with the In-contents around 16%-18% is compatible with that of InGaN QW and the GaN barrier, which enables the incorporation of AlInN thin barrier in InGaN/GaN QW LEDs. The device characterizations of cathodoluminescence and electroluminescence showed the great potential of this InGaN-AlInN design in addressing the efficiency enhancement at high current density.

Besides the novel barrier design, the use of N-polar InGaN QW as the alternative of the conventional Ga-polar InGaN QW has been shown to increase the barrier for carrier leakage as well. Thus, the N-polar InGaN QW LEDs can serve as the active region for LEDs with reduced efficiency droop.

11.1.2 Novel Active Region Design for Radiative Efficiency Enhancement

Another challenge of solid state lighting for general illumination is the 'green gap' issue due to the material related challenges and fundamental physical limitation of charge separation issue. The staggered InGaN QWs with step-function-like and linearly-shaped In-content profiles have been studied for the enhancement of radiative efficiency for high efficiency green light emission devices. In addition, the InGaN-delta-InN novel active region design showed great potential in maintaining high efficiency and high spontaneous emission rates with the significant extension of wavelength from blue to green and red spectrum regime.

The graded temperature techniques have been employed in realizing two-layer, three-layer and linearly shaped staggered InGaN QW active region during MOVPE growth. The device characterizations of cathodoluminescence, time-resolve photoluminescence and electroluminescence have shown the improved device performance due to the increase of radiative efficiency as predicted in the theory. The high quality, droplet-free InN alloy on GaN template can be realized by pulsed-growth mode of MOVPE techniques, and it provide the possible solutions in realization of InGaN-delta-InN QW LEDs.

11.1.3 Investigation of Dopant Activation In P-type III-Nitrides on LED Device Characteristics

Due to the uniform temperature distribution across the radius distance during the thermal activation process, the p-type III-nitride semiconductors have different doping level even though the concentration of acceptor, magnesium may be the same. Thus, the sensitivity of the deice performance on the dopant activation becomes important for industrial applications which set high standard and yield for the commercial product. Out analysis on the doping level of each p-AlGaN electron-blocking layer (EBL), p-GaN cap layer and p+-GaN contact layer shows that the effect of p-AlGaN doping level is strongest, and the p+-GaN is the weakest. In addition, the study on the activation levels of the device as a whole pointed out the changes in light output power and IQE of the LED devices as the activation level has variation of different degree. The employment of larger QWs helps in reducing the sensitivity of the doping levels, but there exists an optimal number of QWs.

11.1.4 Fabrication of Ultra-High Density and Highly Uniform InGaN Quantum Dots for High-Efficiency LEDs

The growths of ultra-high density and highly uniform InGaN quantum dots (QDs) on GaN/ sapphire template have been carried out by selective area epitaxy. It would be beneficial for high-efficiency LEDs, ultra-low threshold visible diode lasers and intermediate-band solar cells due to its three-dimensional quantum confinements. As compared to the prevailing method of Stranski–Krastanow (S-K) growth mode which would lead to uniformity in dot morphology and low dot density, the use of selective area approach on nanopatterned GaN template fabricated by diblock copolymer lithography resulted in well-defined QD density in the range of $8x10^{10}$ cm^{-2}, which corresponds to almost 20 times increase compared to conventional nitride QDs. In addition, this approach also eliminates the detrimental wetting layer. The availability of highly-uniform and ultra-high density InGaN QDs formed by this approach has significant and transformational impacts.

11.2 Future Outlook

III-nitride based solid state lighting will be the next revolution for the illumination infrastructure. The high efficiency and long life time semiconductor based light source, light-emitting diodes is the topic of today's solid state lighting technology. The challenges including efficiency droop, green gap and low light extraction efficiency needs to be resolve in order to further develop the solid state lighting technologyies. Here in this report, we have proposed novel approaches to provide possible solutions to those limitations. The strong motivation of the pursuit of novel barrier design for efficiency droop suppression has been provided by both the analytical and the numerical simulation results. The fabrication of InGaN QW LEDs with the insertion of AlInN thin barrier has been carried out, and the device characterizations showed the great potential of this InGaN-AlInN design in addressing the efficiency enhancement at high current density. However, the luminescence from the LEDs with novel barrier was still weak compared to the conventional InGaN/GaN QW LEDs, which could be the results of unoptimized incorporation of AlInN thin barrier in the device growth. The growth parameters of growth temperature, gas flow, chamber pressure would be investigated to further enhance the EL from the devices. In addition, the interface design between layers of AlInN, GaN and InGaN will be optimized in order to improve the surface quality of each layer in the active region. The future works of this study also include further characterizations of InGaN-AlInN QW LEDs to confirm the successful suppression of efficiency droop by the use of novel barrier design. Characterizations under different temperatures will be very useful in providing insights of the efficiency behavior of LEDs.

The InGaN based QW LEDs with large overlap design has exhibited strong potential in enhancing the electron-hole wavefunction overlaps and thus the optical gain and radiative recombination rate for green LEDs. The experimental results of the two-layer and three-layer staggered InGaN QW LEDs are in good agreement with the theoretical prediction. The linearly-shaped staggered InGaN QW LEDs as well as InGaN-delta-InN QW LEDs are promising approaches for resolving green gap issues, and the device realization and characterizations experimentally will be of great interest in the future.

In Chapter 10, the fabrication of highly-uniformed InGaN QD with ultra-high density has been reported. The strong quantum confinement in those highly packed InGaN QDs would be applicable for optoelectronic and photovoltaic devices due to the availability of high density and highly uniform III-nitride based QDs. The preliminary PL measurement suggested possible approaches to reduce the interface defects and thus the increase in luminescence from SiN_x treated samples. The approaches would be implemented in the QD samples in the future. Besides, the application of III-niride QDs in intermediate solar cells and laser diodes will be of great interests as well.

Curriculum Vitae
(Ms.) GUANGYU LIU

Education

July 2008 – May 2013, Lehigh University (Bethlehem, Pennsylvania, USA)
Ph.D. Candidate in Electrical Engineering, Department of Electrical and Computer Engineering

- Research Assistant, PhD Advisor: Prof. Nelson Tansu (ECE, Lehigh)
- Dissertation Title: "Device Engineering for Internal Quantum Efficiency Enhancement and Efficiency Droop Issue in III-Nitride Light-Emitting Diodes"
- Research Areas: physics of III-Nitride semiconductor optoelectronics materials and devices, physics of III-Nitride semiconductor nanostructures for sustainable energy applications.

Sep. 2004 – Jul. 2008, Huazhong University of Science and Technology (Wuhan, China)
Bachelor of Science (B.S.) in Electronic Science and Technology

- Thesis: "Fabrication of Nano-Magnetic Films and Influence of Film Microstructure to Microwave Properties"
- Award: "Best Graduation Thesis"

Professional Experiences

July 2008 – present, Lehigh University (Bethlehem, PA, USA)
Ph.D. Candidate and Research Assistant
Department of Electrical and Computer Engineering (ECE)
P. C. Rossin College of Engineering and Applied Science
Center for Optical Technologies (COT)
Ph.D. Advisor: Prof. Nelson Tansu

Research Interests

My research interests are related to III-Nitride semiconductor nanostructures and optoelectronics devices for sustainable energy applications, covering the theoretical / computational analysis, metalorganic chemical vapor deposition (MOCVD) growth, and device fabrication and characterization technology. The research topics include the pursuit of high performance green light-emitting diodes (LEDs), novel quantum structures for high power III-Nitride LEDs with low cost, and the growths of III-Nitride quantum dots (QDs) devices for solid state lighting and solar cells.

Awards & Honors Received

- ***2013 Rossin Doctoral Fellowship***, Lehigh University
- ***SPIE Scholarship in Optics and Photonics*** (2012), SPIE
- ***Sherman-Fairchild Fellowship for Solid State Studies*** (2012-2013), Lehigh University
- ***Sherman-Fairchild Fellowship for Solid State Studies*** (2009-2010), Lehigh University
- ***Lehigh University Research Assistantship*** (July. 2008- present), Lehigh University
- ***Lehigh University Dean's Scholarship*** (July. 2008- July 2009), Lehigh University
- ***Best Graduation Thesis*** (June, 2008), Huazhong University of Science and Technology
- ***Award of Excellent Student of HUST*** (2004-2007), Huazhong University of Science and Technology
- ***Scholarships for Excellence in Study*** (2004-2007), Huazhong University of Science and Technology

Professional Affiliations

- 2008 – present, Member, Institute of Electrical and Electronics Engineers (IEEE)
- 2008 – present, Member, IEEE Photonics Society
- 2008 – present, Member, International Society for Optical Engineering (SPIE)
- 2008 – present, Member, Optical Society of America (OSA)

Refereed Journal and Conference Publications

Publication Name Search in ISI Web of Knowledge: (Liu GY and Tansu)

Total Refereed Journal Publications: 23; Total First Authorship Refereed Publications: 13

1. **(Invited Conference Paper)** N. Tansu, H. P. Zhao, R. A. Arif, Y. K. Ee, **G. Y. Liu**, X. H. Li, and G. S. Huang, "Polarization Engineering of InGaN-Based Nanostructures for Low-Threshold Diode Lasers and High-Efficiency Light Emitting Diodes," in *Proc. of the IEEE Photonics Global 2008, Nanophotonics Symposium*, Singapore, Republic of Singapore, December 2008
2. H. P. Zhao, **G. Y. Liu**, X. Li, G. Huang, S. Tafon Penn, V. Dierolf and N. Tansu, "Growths of Staggered InGaN Quantum Wells Light-Emitting Diodes Emitting at 520-525 nm Employing Graded-Temperature Profile," in *Proc. of SPIE Photonic West 2009*, vol. 7231, Art. 72310E, San Jose, CA, January 2009.
3. H. P. Zhao, M. Jamil, **G. Y. Liu**, G. S. Huang, H. Tong, G. Xu, Y. J. Ding, N. Tansu, "Pulsed Metalorganic Vapor Phase Epitaxy of In-Polar and N-Polar InN Semiconductors on GaN / Sapphire Templates for Terahertz Emitters," *Proc. IEEE/OSA Conference on Lasers and Electro-Optics (CLEO) 2009*, Baltimore, MD, May 2009.
4. H. P. Zhao, **G. Y. Liu**, X. Li, G. S. Huang, S. Tafon Penn, V. Dierolf, and N. Tansu, "Staggered InGaN Quantum Wells Light-Emitting Diodes at 520-nm Employing Graded Temperature Growths," in *Proc. of the IEEE/OSA Conference on Lasers and Electro-Optics (CLEO) 2009*, Baltimore, MD, May 2009.
5. G. Sun, S. K. Tripathy, Y. J. Ding, **G. Y. Liu**, G. S. Huang, H. P. Zhao, N. Tansu, and J. B. Khurgin, "Stark Effect Induced by Photogenerated Carriers in Multiple GaN/AlN Asymmetric Coupled Quantum Wells," in *Proc. of the IEEE/OSA Conference on Lasers and Electro-Optics (CLEO) 2009*, Baltimore, MD, May 2009
6. H. P. Zhao, G. S. Huang, **G. Y. Liu**, X. H. Li, J. D. Poplawsky, S. Tafon Penn, V. Dierolf, and N. Tansu, "Characteristics of Staggered InGaN Quantum Wells Light-Emitting Diodes Emitting at 480-525 nm," in *Proc. of the 67th IEEE Device Research Conference (DRC) 2009*, University Park, PA, June 2009.
7. H. P. Zhao, **G. Y. Liu**, X. H. Li, G. S. Huang, J. D. Poplawsky, S. Tafon Penn, V. Dierolf, and N. Tansu, "Growths of Staggered InGaN Quantum Wells Light-Emitting Diodes Emitting at 520-525 nm Employing Graded Growth-Temperature Profile," *Appl. Phys. Lett.*, vol. 95(6), Art. 061104, August 2009
8. H. P. Zhao, **G. Y. Liu**, R. A. Arif, and N. Tansu, "Effect of Current Injection Efficiency on Efficiency-Droop in InGaN Quantum Well Light-Emitting Diodes," in *Proc. of the IEEE International Semiconductor Device Research Symposium (ISDRS) 2009*, College Park, MD, Nov 2009.
9. **(Invited Journal Paper)** H. P. Zhao, **G. Y. Liu**, X. H. Li, R. A. Arif, G. S. Huang, J. D. Poplawsky, S. Tafon Penn, V. Dierolf, and N. Tansu, "Design and Characteristics of Staggered InGaN Quantum Well Light-Emitting Diodes in the Green Spectral Regimes," *IET Optoelectronics,* vol. 3(6), pp. 283-295, December 2009.
10. **(Invited Conference Paper)** N. Tansu, H. P. Zhao, R. A. Arif, Y. K. Ee, **G. Y. Liu**, X. H. Li, H. Tong, and G. S. Huang, "Novel Approaches for Efficiency Enhancement in InGaN-Based Light-Emitting Diodes," in *Proc. of the 2nd International Conference on White LEDs and Solid State Lighting 2009*, Taipei, Taiwan, December 2009
11. **(Invited Conference Paper)** N. Tansu, H. P. Zhao, Y. K. Ee, **G. Y. Liu**, X. H. Li, and G. S. Huang, "Novel Device Concept for High-Efficiency InGaN Quantum Wells Light-Emitting Diodes," in *Proc. of the SPIE Photonics West 2010*, Gallium Nitride Materials and Devices V, San Francisco, CA, Jan 2010

12. **G. Y. Liu**, H. Zhao, and N. Tansu, "Electron-Phonon and Electron-Photon Intersubband Scattering Rates in Asymmetric AlN / GaN Coupled Quantum Wells," in *Proc. of the SPIE Photonics West 2010*, Physics and Simulation of Optoelectronics Devices XVIII, San Francisco, CA, Jan 2010.
13. H. Tong, J. A. Herbsommer, V. A. Handara, H. Zhao, **G. Y. Liu**, and N. Tansu, "Thermal Conductivity Measurement of Pulsed-MOVPE InN Alloy Grown on GaN / Sapphire by 3ω Method," in *Proc. of the SPIE Photonics West 2010*, Gallium Nitride Materials and Devices V, San Francisco, CA, Jan 2010.
14. G. Xu, Y. J. Ding, H. P. Zhao, M. Jamil, **G. Y. Liu**, N. Tansu, I. B. Zotova, C. E. Stutz, D. E. Diggs, N. Fernelius, F. K. Hopkins, C. S. Gallinat, G. Koblmüller, and J. S. Speck, "THz Generation from InN Films due to Destructive Interference between Optical Rectification and Photocurrent Surge," *Semiconductor Science and Technology,* vol. 25 (1), Art. 015004, January 2010.
15. **G. Y. Liu**, H. P. Zhao, J. Zhang, G. S. Huang, and N. Tansu, "Growths of Lattice-Matched AlInN Alloys on GaN," in *Proc. of the American Physical Society (APS) Annual March Meeting 2010*, Portland, Oregon, March 2010.
16. J. Zhang, H. Tong, **G. Y. Liu**, J. A. Herbsommer, G. S. Huang, and N. Tansu, "Thermoelectric Properties of MOVPE Grown AlInN Lattice-Matched to GaN," in *Proc. of the American Physical Society (APS) Annual March Meeting 2010*, Portland, Oregon, March 2010.
17. X. H. Li, Y. K. Ee, **G. Y. Liu**, P. Kumnorkaew, J. F. Gilchrist, and N. Tansu, "MOCVD Epitaxy of GaN by Employing SiO_2 Colloidal Microsphere Templates," in *Proc. of the American Physical Society (APS) Annual March Meeting 2010*, Portland, Oregon, March 2010.
18. **(Invited Conference Paper)** H. P. Zhao, **G. Y. Liu**, X. H. Li, Y. K. Ee, H. Tong, J. Zhang, G. S. Huang, and N. Tansu, "Novel Growth and Device Concepts for High-Efficiency InGaN Quantum Wells Light-Emitting Diodes," in *Proc. of the IEEE/OSA Conference on Lasers and Electro-Optics (CLEO) 2010*, San Jose, CA, May 2010.
19. **G. Y. Liu**, H. P. Zhao, J. H. Park, L. J. Mawst, and N. Tansu, "Growths of Ultra High Density InGaN-Based Quantum Dots on Self-Assembled Diblock Copolymer Nanopatterns," in *Proc. of the IEEE/OSA Conference on Lasers and Electro-Optics (CLEO) 2010*, San Jose, CA, May 2010.
20. G. Sun, S. K. Tripathy, Y. J. Ding, **G. Y. Liu**, G. S. Huang, H. P. Zhao, N. Tansu, and J. B. Khurgin, "Photoluminescence Emission in Deep Ultraviolet Region from GaN/AlN Asymmetric-Coupled Quantum Wells," in *Proc. of the IEEE/OSA Conference on Lasers and Electro-Optics (CLEO) 2010*, San Jose, CA, May 2010.
21. G. Sun, S. K. Tripathy, Y. J. Ding, **G. Y. Liu**, H. P. Zhao, G. S. Huang, N. Tansu, and J. B. Khurgin, "Photoluminescence Quenching Due to Relocation of Electrons in GaN/AlN Asymmetric-Coupled Quantum Wells," *Proc. IEEE/OSA Quantum Electronics and Laser Science Conference 2010*, San Jose, CA, May 2010.
22. **(Invited Review Article)** N. Tansu, H. P. Zhao, **G. Y. Liu**, X. H. Li, J. Zhang, H. Tong, and Y. K. Ee, "III-Nitride Photonics", *IEEE Photonics Journal*, vol. 2 (2), pp. 241-248, April 2010.
23. **(Invited Conference Paper)** H. P. Zhao, J. Zhang, **G. Y. Liu**, X. H. Li, Y. K. Ee, H. Tong, T. Toma, G. S. Huang, and N. Tansu, "Approaches for High-Efficiency InGaN Quantum Wells Light-Emitting Diodes-Device Physics and Epitaxy Engineering", *Proc. of American Vacuum Society (AVS) Meeting 2010*, Ann-Arbor, MI, May 2010.
24. **(Invited Conference Paper)** N. Tansu, H. P. Zhao, J. Zhang, **G. Y. Liu**, X. H. Li, H. Tong, T. Toma, G. S. Huang, and Y. K. Ee, "Device Physics and Epitaxy Engineering for High-Efficiency III-Nitride Light-Emitting Diodes," *Proc. of the International Union of Materials Research Societies - International Conference on Electronic Materials (IUMRS-ICEM) 2010*, Seoul, Korea, August 2010.
25. G. Sun, Y. J. Ding, **G. Y. Liu**, G. S. Huang, H. P. Zhao, N. Tansu, and J. B. Khurgin, "Photoluminescence Emission in Deep Ultraviolet Region from GaN/AlN Asymmetric-Coupled Quantum Wells", *Appl. Phys. Lett.*, vol. 97(2), Art. 021904, July 2010.
26. H. Tong, J. Zhang, **G. Y. Liu**, J. A. Herbsommer, G. S. Huang, and N. Tansu, "Thermoelectric Properties of Lattice-Matched AlInN Alloy Grown by Metalorganic Chemical Vapor Deposition", *Appl. Phys. Lett.*, vol. 97, Art. 112105, September 2010.

27. H. P. Zhao, **G. Y. Liu**, and N. Tansu, “Analysis of InGaN-delta-InN quantum wells for light-emitting diodes,” *Appl. Phys. Lett.*, vol. 97, Art. 131114, September 2010.

28. H. P. Zhao, **G. Y. Liu**, R. A. Arif, and N. Tansu, “Current Injection Efficiency Quenching Leading to Efficiency Droop in InGaN Quantum Well Light-Emitting Diodes,” *Solid State Electronics.*, vol. 54 (10), pp. 1119-1124, October 2010.

29. **G. Y. Liu**, H. P. Zhao, J. Zhang, H. Tong, G. S. Huang, and N. Tansu, “Growths and Characterization of Lattice-Matched AlInN Alloys”, in Proc. of *23rd Annual Meeting of the IEEE Photonics Society*, Denver, CO, Nov 2010.

30. H. P. Zhao, J. Zhang, T. Toma, **G. Y. Liu**, J. D. Poplawsky, V. Dierolf, and N. Tansu, “Cathodoluminescence Characteristics of Linearly-Shaped Staggered InGaN Quantum Wells Light-Emitting Diodes”, in Proc. of the *23rd Annual Meeting of the IEEE Photonics Society*, Denver, CO, November 2010.

31. J. Zhang, H. Tong, **G. Y. Liu**, J. A. Herbsommer, G. S. Huang, and N. Tansu, “Thermoelectric Properties of MOCVD-Grown AlInN Alloys with Various Compositions”, in Proc. of the *23rd Annual Meeting of the IEEE Photonics Society*, Denver, CO, November 2010.

32. **G. Y. Liu**, H. P. Zhao, J.-H. Park, L. J. Mawst, N. Tansu, “Selective Area Epitaxy of Ultra High Density InGaN Based Quantum Dots”, in Proc. *of the IEEE Photonics Society-Winter Topicals*, January 2011.

33. **(Invited Conference Paper)** N. Tansu, H. P. Zhao, J. Zhang, **G. Y. Liu**, X. H. Li, Y. K. Ee, R. B. Song, T. Toma, L. Zhao, and G. S. Huang, “Novel Approaches for High-Efficiency InGaN Quantum Wells Light-Emitting Diodes – Device Physics and Epitaxy Engineering,” in Proc. of the *SPIE Photonics West 2011*, *LEDs: Materials, Devices, and Applications for Solid State Lighting XV*, Paper 7954-42, San Francisco, CA, Jan 2011.

34. H. P. Zhao, J. Zhang, T. Toma, **G. Y. Liu**, J. D. Poplawsky, V. Dierolf, and N. Tansu, “MOCVD Growths of Linearly-Shaped Staggered InGaN Quantum Wells Light-Emitting Diodes at Green Spectral Regime,” Proc. *SPIE Photonics West 2011*, *GaN Materials and Devices VI*, Paper 7939-4, San Francisco, CA, Jan 2011.

35. J. Zhang, H. Tong, **G. Y. Liu**, J. A. Herbsommer, G. S. Huang, and N. Tansu, “Thermoelectric Properties of MOCVD-Grown AlInN Alloys with Various Compositions,” in Proc. of the *SPIE Photonics West 2011*, *Gallium Nitride Materials and Devices VI*, Paper 7939-37, San Francisco, CA, Jan 2011.

36. G. Sun, G. Xu, Y. J. Ding, H. P. Zhao, **G. Y. Liu**, J. Zhang, and N. Tansu, "Efficient Terahertz Generation from Multiple InGaN / GaN Quantum Wells", *IEEE J. Sel. Top. Quantum Electron.*, vol. 17, pp. 48-53, Jan-Feb 2011.

37. J. Zhang, H. Tong, **G. Y. Liu**, J. A. Herbsommer, G. S. Huang, and N. Tansu, “Characterizations of Seebeck Coefficients and Thermoelectric Figures of Merit for AlInN Alloys with Various In-Contents,” *J. Appl. Phys.*, vol. 109 (5), Art. 053706, March 2011.

38. H. Zhao, J. Zhang, T. Toma, **G. Liu**, J. D. Poplawsky, V. Dierolf, and N. Tansu, “MOCVD Growths of LinearlyShaped Staggered InGaN Quantum Wells Light-Emitting Diodes,” in Proc. of *the American Physical Society (APS) Annual March Meeting 2011*, Dallas, Texas, March 2011.

39. H. P. Zhao, J. Zhang, **G. Y. Liu**, and N. Tansu, “Surface Plasmon Dispersion Engineering via Double-Metallic Au / Ag Layers for Nitride Light-Emitting Diodes,” in Proc. of *the IEEE/OSA Conference on Lasers and Electro-Optics (CLEO) 2011*, Paper CWF5, Baltimore, MD, May 2011.

40. **G. Y. Liu**, H. P. Zhao, J. Zhang, and N. Tansu, “Growths of InGaN-Based Light-Emitting Diodes with AlInN Thin Barrier for Efficiency Droop Suppression,” in Proc. of *the IEEE/OSA Conference on Lasers and Electro-Optics (CLEO) 2011*, Paper CMDD6, Baltimore, MD, May 2011.

41. G. B. Xu, G. Sun, Y. J. Ding, H. P. Zhao, **G Y. Liu**, J. Zhang, and N. Tansu, “Investigation of Blueshift of Photoluminescence Emission Peak in InGaN/GaN Multiple Quantum Wells,” in Proc. of *the IEEE/OSA Conference on Lasers and Electro-Optics (CLEO) 2011*, Paper JWA70, Baltimore, MD, May 2011.

42. G. Sun, G. B. Xu, Y. J. Ding, H. P. Zhao, **G. Y. Liu**, J. Zhang, and N. Tansu, “High-Power Terahertz Generation due to Dipole Radiation within InGaN/GaN Multiple Quantum Wells,” in

Proc. of *the IEEE/OSA Conference on Lasers and Electro-Optics (CLEO) 2011*, Paper CMM4, Baltimore, MD, May 2011.

43. **G Y. Liu**, H. P. Zhao, J. Zhang, J. H. Park, L. J. Mawst, and N. Tansu, "Selective Area Epitaxy of Ultra-High Density InGaN Quantum Dots by Diblock Copolymer," *Nanoscale Res. Lett.*, vol. 6, Art. 342, April 2011.
44. H. P. Zhao, J. Zhang, **G. Y. Liu**, and N. Tansu, "Surface Plasmon Dispersion Engineering via Double-Metallic Au / Ag Layers for III-Nitride Based Light-Emitting Diodes," *Appl. Phys. Lett.*, vol. 98, Art. 151115, April 2011.
45. **(Invited Journal Paper)** H. P. Zhao, **G. Y. Liu**, J. Zhang, J. D. Poplawsky, V. Dierolf, and N. Tansu, "Approaches for High Internal Quantum Efficiency Green InGaN Light-Emitting Diodes with Large Overlap Quantum Wells," Optics Express, vol. 19 (S4), pp. A991-A1007, July 2011.
46. J. Zhang, S. Kutlu, **G. Y. Liu**, and N. Tansu, "High-Temperature Characteristics of Seebeck Coefficients for AlInN Alloys Grown by Metalorganic Vapor Phase Epitaxy," J. Appl. Phys., vol. 110, Art. 043710, August 2011.
47. G. Sun, G. B. Xu, Y. J. Ding, H. P. Zhao, **G. Y. Liu**, J. Zhang, and N. Tansu, "Investigation of Fast and Slow Decays in InGaN/GaN Quantum Wells," *Appl. Phys. Lett*., vol. 99, Art. 081104, August 2011.
48. **G. Y. Liu**, J. Zhang, H. P. Zhao, and N. Tansu, "Device Characteristics of InGaN Quantum Well Light-Emitting Diodes with AlInN Thin Barrier Insertion," *Proc. of the SPIE Photonics West 2012, Gallium Nitride Materials and Devices VII*, San Francisco, CA, Jan 2012.
49. **G. Y. Liu**, J. D. Poplawsky, J. Zhang, V. Dierolf, H. P. Zhao, and N. Tansu, "Quantum Efficiency Characterizations of Staggered InGaN Quantum Wells Light-Emitting Diodes by Temperature-Dependent Electroluminescence Measurement," Proc. of the SPIE Photonics West 2012, LEDs: Materials, Devices, and Applications for Solid State Lighting XVI, San Francisco, CA, Jan 2012.
50. **G. Y. Liu**, J. Zhang, X. H. Li, G. S. Huang, T. Paskova, K. R. Evans, H. P. Zhao, and N. Tansu, "Metalorganic Vapor Phase Epitaxy and Characterizations of Nearly-Lattice-Matched AlInN Alloys on GaN / Sapphire Templates and Free-Standing GaN Substrates," *J. Crys. Growth*, vol. 340 (1), pp. 66-73, February 2012.
51. **G. Y. Liu**, J. Zhang, C. K. Tan, and N. Tansu, "Characteristics of InGaN Quantum Wells Light-Emitting Diodes with Thin AlGaInN Barrier Layers," Proc. of the IEEE Photonics Conference 2012, Burlingame, CA, Sept 2012.
52. C. K. Tan, J. Zhang, X. H. Li, **G. Y. Liu**, and N. Tansu, "Dilute-As GaNAs Semiconductor for Visible Emitters," Proc. of the IEEE Photonics Conference 2012, Burlingame, CA, September 2012.
53. P. F. Zhu, J. Zhang, **G. Y. Liu**, and N. Tansu, "FDTD Modeling of InGaN-Based Light-Emitting Diodes with Microsphere Arrays," Proc. of the IEEE Photonics Conference 2012, Burlingame, CA, September 2012.
54. **G. Y. Liu**, J. Zhang, C. K. Tan, and N. Tansu, "InGaN-Delta-InN Quantum Well Light-Emitting Diodes with Carrier Transport Effect" *Proc. of the SPIE Photonics West 2013,* San Francisco, CA, Feb 2013.
55. C. K. Tan, J. Zhang, **G. Y. Liu**, and N. Tansu, "Effect of Interband Energy Separation on the Interband Auger Processes in III-Nitride Semiconductors," *Proc. of SPIE Photonics West 2013,* San Francisco, CA, Feb 2013.
56. P. F. Zhu, P. O. Weigel, **G. Y. Liu**, J. Zhang , A. L. Weldon , T. Muangnaphor, J. F. Gilchrist, and N. Tansu, "Optimization of Deposition Conditions for Silica / Polystyrene Microlens and Nanolens Arrays for Light Extraction Enhancement in GaN Light-Emitting Diodes," *Proc. of SPIE Photonics West 2013,* San Francisco, CA, Feb 2013.
57. G. Sun, R. Chen, Y. Ding, H. Zhao, **G. Liu**, J. Zhang, and N. Tansu, "Strikingly Different Behaviors of Photoluminescence and Terahertz Generation in InGaN/GaN Quantum Wells," IEEE J. Sel. Top. Quantum Electron., vol. 19, no. 1, Art. 8400106, January / February 2013. DOI: 10.1109/JSTQE.2012.2218093

58. G. Xu, G. Sun, Y. J. Ding, H. P. Zhao, **G. Y. Liu**, J. Zhang, and N. Tansu, “Investigation of Large Stark Shifts in InGaN / GaN Multiple Quantum Wells”, J. Appl. Phys., vol 113, Art. 033104, January 2013. DOI: 10.1063/1.4775605
59. H. P. Zhao, **G. Y. Liu**, J. Zhang, R. A. Arif, and N. Tansu, “Analysis of Internal Quantum Efficiency and Current Injection Efficiency in Nitride Light-Emitting Diodes”, Journal of Display Technology, vol. 9, no. 4, pp. 212-225, April 2013. DOI: 10.1109/JDT.2013.2250252
60. C. K. Tan, J. Zhang, X. H. Li, **G. Y. Liu**, B. O. Tayo, and N. Tansu, “First-Principle Electronic Properties of Dilute-As GaNAs Alloy for Visible Light Emitters”, Journal of Display Technology, vol. 9, no. 4, pp. 272-279, April 2013. DOI: 10.1109/JDT.2013.2248342
61. **G. Y. Liu**, J. Zhang, C. K. Tan, and N. Tansu, “Efficiency-Droop Suppression by Using Large-Bandgap AlGaInN Thin Barrier Layers in InGaN Quantum Wells Light-Emitting Diodes”, IEEE Photonics Journal, vol. 5, no. 2, Art. 2201011, April 2013. DOI: 10.1109/JPHOT.2013.2255028.
62. P. F. Zhu, **G. Y. Liu**, J. Zhang, and N. Tansu, “FDTD Analysis on Extraction Efficiency of GaN Light-Emitting Diodes with Microsphere Arrays”, Journal of Display Technology, vol. 9, no. 5, pp. 317-323, May 2013. DOI: 10.1109/JDT.2013.2250253
63. X. H. Li, P. F. Zhu, **G. Y. Liu**, J. Zhang, R. B. Song, Y. K. Ee, P. Kumnorkaew, and J. F. Gilchrist, and N. Tansu, “Light Extraction Efficiency Enhancement of III-Nitride Light-Emitting Diodes by using 2-D Close-Packed TiO_2 Microsphere Arrays”, Journal of Display Technology, vol. 9, no. 5, pp. 324-332, May 2013. DOI: 10.1109/JDT.2013.2246541
64. **(Invited Conference Paper)** N. Tansu, J. Zhang, **G. Y. Liu**, C. K. Tan, P. F. Zhu, and H. P. Zhao, “Internal and External Efficiency in InGaN-Based Light-Emitting Diodes,” Proc. of the ICMAT Conference 2013, Material Research Society (MRS), Singapore, July 2013.
65. **(Invited Conference Paper)** C. K. Tan, J. Zhang, **G. Y. Liu**, and N. Tansu, “Exploration of New Materials for Visible Light-Emitting Diodes and Lasers – Dilute-As GaNAs Alloy,” Proc. of the *SPIE Optics + Photonics 2012*, NanoEpitaxy : Materials and Devices V, San Diego, CA, August 2013.

Submitted Refereed Journal and Conference Publications

66. **G. Y. Liu** J. Zhang, C. K. Tan, and N. Tansu, “Charateristics of InGaN-Delta-InN Quantum Wells Light-Emitting Diodes for Green, Yellow and Red Emission”, IEEE Photonics Journal (submitted).
67. Y. K. Ee, X. H. Li, J. Zhang, **G. Y. Liu**, H. P. Zhao, J. M. Biser, W. Cao, H. M. Chan, R.. P. Vinci, and N. Tansu, “Nano-pattern Pitch Dimension Dependence and Time-resolved Photoluminescence Study of InGaN Quantum Well Light-Emitting Diodes Grown by Abbreviated Growth Mode on Nano-patterned AGOG Substrate”, Journal of Display Technology (submitted).
68. C. K. Tan, B. Tayo, J. Zhang, **G. Y. Liu** and N. Tansu, “First-Principle Natural Band Alignment of Dilute-As GaNAs Alloy”, Journal of Display Technology (submitted).

Patents

1. Nelson Tansu, **Guangyu Liu**, and Hongping Zhao, “Ultrahigh Density InGaN-Based Quantum Dots for Optoelectronics Devices” (US Patent Pending).
2. Nelson Tansu, Hongping Zhao, and **Guangyu Liu**, “Novel Surface Plasmon Based Light-Emitting Diodes” (US Patent Pending).
3. Nelson Tansu, Hongping Zhao, **Guangyu Liu**, and Ronald A. Arif, “Methods to Suppress Efficiency-Droop for High-Power Nitride Light-Emitting Diodes Applicable for Solid State Lighting” (US Patent Pending).
4. Nelson Tansu, Hongping Zhao, **Guangyu Liu**, and Gensheng Huang, “Staggered InGaN Quantum Well with InN Delta-Layer” (US Patent Pending).
5. Nelson Tansu, Hua Tong, Jing Zhang, **Guangyu Liu**, and Gensheng Huang, “Novel techniques to achieve high thermoelectric figure of merit based on nitride semiconductor” (US Patent Pending).

6. Nelson Tansu, Xiao-Hang Li, Hongping Zhao, **Guangyu Liu**, Gensheng Huang, James F. Gilchrist, and Pisist Kumnorkaew, “Novel Supercontinuum Broadband White Light-Emitting Diodes” (US Patent Pending).

Selected Research Works Featured in Magazine / Newspapers

1. **“You build yourself into what you do”** in ***Lehigh News Center Highlight***, August 15th, 2012.
   http://www4.lehigh.edu/news/newsarticle.aspx?Channel=%2fChannels%2fNews%3a+2012&WorkflowItemID=aab27191-029a-43fa-9abe-198d4e34aea2
2. **“A Revolution in Lighting”** in Feature Section of **Resolve magazine**, vol. 2, Fall 2012.
   http://www.nxtbook.com/nxtbooks/lehigh/resolve_2012vol2/#/20
3. **“Nanoscale Work Yields Greener Lighting”** in Research Section of ***Lehigh Alumni Bulletin***, Winter 2012-2013.
   http://www.nxtbook.com/nxtbooks/lehigh/alumni_2013winter/#/14

Professional and Synergistic Services

1. **Journal Reviewer:**
   - ✓ **Optics Express**
   - ✓ **IEEE Photonics Journal**
   - ✓ **Optical Materials Express**
   - ✓ **Nanoscale Research Letters**
   - ✓ **IEEE/OSA Journal of Display Technology**
   - ✓ **Materials Research Bulletin**
   - ✓ **Journal of Photonics for Energy**
   - ✓ **Photonics Technology Letters**
2. **Vice President, SPIE Student Chapter at Lehigh University,** May 2010 – May 2011.
3. **President, SPIE Student Chapter at Lehigh University,** May 2011 – present.

Internal Scientific Lectures & Seminars (Non-Refereed)

1. N. Tansu, R. A. Arif, H. Zhao, Y. K. Ee, G. S. Huang, **G. Liu**, and X. Li, “High Efficiency III-Nitride Light-Emitting Diodes for Solid State Lighting,” Oral Presentation in Lehigh Center for Optical Technologies (COT) Open House 2008, COT Workshop on Solid State Materials for Energy Applications, *Lehigh University*, Bethlehem, Pennsylvania, USA, October 2008.
2. N. Tansu, M. Jamil, H. Zhao, **G. Liu**, and G. S. Huang, “Toward InGaN-Based Solar Cells,” Oral Presentation in Lehigh Center for Optical Technologies (COT) Open House 2008, COT Workshop on Solid State Materials for Energy Applications, *Lehigh University*, Bethlehem, Pennsylvania, USA, October 2008.
3. H. Zhao, **G. Liu**, X. H. Li, R. A. Arif, G. S. Huang, S. Tafon Penn, V. Dierolf, and N. Tansu, “Enhancement of Radiative Efficiency via Staggered InGaN Quantum Well Light Emitting Diodes,” Invited Poster Presentation in Transformation in Lighting 2009, *DOE R&D Workshop on Solid State Lighting 2009*, San Francisco, CA, USA, February 2009.
4. H. Zhao, **G. Liu**, X. H. Li, G. S. Huang, J. Poplawsky, V. Dierolf, and N. Tansu, “Staggered InGaN Quantum-Well Light-Emitting Diodes,” Oral Presentation in Lehigh Center for Optical Technologies (COT) Open House 2009, COT Workshop on NanoPhotonics, *Lehigh University*, Bethlehem, Pennsylvania, USA, October 2009.
5. **G. Liu**, H. Zhao, G. S. Huang, and N. Tansu, “Electron-Photon and Electron-Phonon Intersubband Scatterings in AlN / GaN and AlInN / GaN Quantum Wells,” Poster Presentation in Lehigh Center for Optical Technologies (COT) Open House 2009, COT Workshop on NanoPhotonics, *Lehigh University*, Bethlehem, Pennsylvania, USA, October 2009.

6. H. Zhao, **G. Liu**, X. H. Li, G. S. Huang, J. Poplawsky, S. Tafon Penn, V. Dierolf, and N. Tansu, "Growths of Staggered InGaN Quantum Wells Light-Emitting Diodes Emitting at 520-525 nm Employing Graded Growth-Temperature Profile," Poster Presentation in Lehigh Center for Optical Technologies (COT) Open House 2009, COT Workshop on NanoPhotonics, *Lehigh University*, Bethlehem, Pennsylvania, USA, October 2009.
7. H. Zhao, **G. Liu**, R. A. Arif, and N. Tansu, "Current Injection Efficiency and Efficiency-Droop of InGaN Quantum Well Light-Emitting Diodes," Poster Presentation in Lehigh Center for Optical Technologies (COT) Open House 2009, COT Workshop on NanoPhotonics, *Lehigh University*, Bethlehem, Pennsylvania, USA, October 2009.
8. H. Zhao, **G. Liu**, J. Zhang, T. Toma, G. S. Huang, J. D. Poplawsky, V. Dierolf, and N. Tansu, "Enhancement of Internal Quantum Efficiency with Staggered InGaN Quantum Wells Light-Emitting Diodes," Poster Presentation in Nano-Energy Workshop 2010, *Lehigh University*, Bethlehem, Pennsylvania, USA, September 2010.
9. H. Zhao, **G. Liu**, J. Zhang, T. Toma, G. S. Huang, J. D. Poplawsky, V. Dierolf, and N. Tansu, "Enhancement of Internal Quantum Efficiency with Staggered InGaN Quantum Wells Light-Emitting Diodes," Poster Presentation in Lehigh Center for Optical Technologies (COT) Open House 2010, COT Workshop on NanoPhotonics, *Lehigh University*, Bethlehem, Pennsylvania, USA, October 2010.

Outreach Lectures and Seminars (for Middle School and High School Students)

1. Nelson Tansu, Ronald A. Arif, Hongping Zhao, Hua Tong, Yik Khoon Ee, Xiaohang Li, and **Guangyu Liu**, "Semiconductor Nanotechnology for High Energy Efficient Applications," Outreach Program, OptoCamp 2008 – Center for Optical Technologies, ***Lehigh University***, Bethlehem, Pennsylvania, USA, August 2008.
2. Nelson Tansu, Hongping Zhao, Hua Tong, Yik Khoon Ee, Xiaohang Li, and **Guangyu Liu**, "Semiconductor Nanotechnology for High Energy Efficient Applications," Outreach Program, OptoCamp 2009 – Center for Optical Technologies, ***Lehigh University***, Bethlehem, Pennsylvania, USA, August 2009.

References

1. **Prof. Nelson Tansu (PhD Advisor)**
New Century Endowed Chair Associate Professor in Engineering and Applied Science
Center for Photonics and Nanoelectronics
Department of Electrical and Computer Engineering
P. C. Rossin College of Engineering and Applied Science
Lehigh University
Bethlehem, PA 18015, USA
Email: Tansu@Lehigh.Edu
Phone: (610) 758-2678, Fax: (610) 758-2605
Research Group: http://www.ece.lehigh.edu/~tansu

2. **Prof. Filbert J. Bartoli**
Chandler Weaver Chair Professor, and ECE Department Chair
Department of Electrical and Computer Engineering
Lehigh University
Bethlehem, PA 18015, USA
Email: fjb205@Lehigh.Edu
Phone: (610) 758-4069
http://www.ece.lehigh.edu/index.php?page=filbert-j-bartoli

3. **Prof. Yujie Ding**
   Professor
   Department of Electrical and Computer Engineering
   Lehigh University, Bethlehem, PA 18015, USA
   Email: yud2@Lehigh.Edu Phone: (610) 758-4582
   http://www.ece.lehigh.edu/index.php?page=yujie-ding

4. **Prof. Michael J. Stavola**
   Sherman Fairchild Chair Professor of Physics
   Department of Physics
   Lehigh University
   Bethlehem, PA 18015, USA
   Email: mjsa@Lehigh.Edu
   Phone: (610) 758-4282
   http://www.lehigh.edu/~mjsa/mjsa.html

5. **Prof. Luke J. Mawst**
   Professor
   Department of Electrical and Computer Engineering
   Reed Center for Photonics
   University of Wisconsin-Madison
   1415 Engineering Dr., Madison, WI 53706, USA
   Email: mawst@engr.wisc.edu
   Phone: (608) 263-1705
   http://www.engr.wisc.edu/ece/faculty/mawst_luke.html

6. **Prof. Hongping Zhao**
   Assistant Professor
   Department of Electrical Engineering and Computer Science
   Case Western Reserve University
   Cleveland, OH 44106, USA
   Email: hongping.zhao@case.edu
   Phone: (216) 368-4120
   http://engineering.case.edu/profiles/hxz168